



UNIL | Université de Lausanne

Unicentre

CH-1015 Lausanne

<http://serval.unil.ch>

Year : 2018

Resolving thermo-hydro-mechanical coupling: Spontaneous porous fluid and strain localisation

Räss Ludovic

Räss Ludovic, 2018, Resolving thermo-hydro-mechanical coupling: Spontaneous porous fluid and strain localisation

Originally published at : Thesis, University of Lausanne

Posted at the University of Lausanne Open Archive <http://serval.unil.ch>

Document URN : urn:nbn:ch:serval-BIB_03FB255652A92

Droits d'auteur

L'Université de Lausanne attire expressément l'attention des utilisateurs sur le fait que tous les documents publiés dans l'Archive SERVAL sont protégés par le droit d'auteur, conformément à la loi fédérale sur le droit d'auteur et les droits voisins (LDA). A ce titre, il est indispensable d'obtenir le consentement préalable de l'auteur et/ou de l'éditeur avant toute utilisation d'une oeuvre ou d'une partie d'une oeuvre ne relevant pas d'une utilisation à des fins personnelles au sens de la LDA (art. 19, al. 1 lettre a). A défaut, tout contrevenant s'expose aux sanctions prévues par cette loi. Nous déclinons toute responsabilité en la matière.

Copyright

The University of Lausanne expressly draws the attention of users to the fact that all documents published in the SERVAL Archive are protected by copyright in accordance with federal law on copyright and similar rights (LDA). Accordingly it is indispensable to obtain prior consent from the author and/or publisher before any use of a work or part of a work for purposes other than personal use within the meaning of LDA (art. 19, para. 1 letter a). Failure to do so will expose offenders to the sanctions laid down by this law. We accept no liability in this respect.



UNIL | Université de Lausanne

Unicentre

CH-1015 Lausanne

<http://serval.unil.ch>

Year : 2018

Resolving thermo-hydro-mechanical coupling: Spontaneous porous fluid and strain localisation

Räss Ludovic

Räss Ludovic, 2018, Resolving thermo-hydro-mechanical coupling: Spontaneous porous fluid and strain localisation

Originally published at : Thesis, University of Lausanne

Posted at the University of Lausanne Open Archive <http://serval.unil.ch>

Document URN : urn:nbn:ch:serval-BIB_03FB255652A92

Droits d'auteur

L'Université de Lausanne attire expressément l'attention des utilisateurs sur le fait que tous les documents publiés dans l'Archive SERVAL sont protégés par le droit d'auteur, conformément à la loi fédérale sur le droit d'auteur et les droits voisins (LDA). A ce titre, il est indispensable d'obtenir le consentement préalable de l'auteur et/ou de l'éditeur avant toute utilisation d'une oeuvre ou d'une partie d'une oeuvre ne relevant pas d'une utilisation à des fins personnelles au sens de la LDA (art. 19, al. 1 lettre a). A défaut, tout contrevenant s'expose aux sanctions prévues par cette loi. Nous déclinons toute responsabilité en la matière.

Copyright

The University of Lausanne expressly draws the attention of users to the fact that all documents published in the SERVAL Archive are protected by copyright in accordance with federal law on copyright and similar rights (LDA). Accordingly it is indispensable to obtain prior consent from the author and/or publisher before any use of a work or part of a work for purposes other than personal use within the meaning of LDA (art. 19, para. 1 letter a). Failure to do so will expose offenders to the sanctions laid down by this law. We accept no liability in this respect.

Faculté des géosciences et de l'environnement

Institut des sciences de la Terre

RESOLVING THERMO-HYDRO-MECHANICAL COUPLING: SPONTANEOUS POROUS FLUID AND STRAIN LOCALISATION

THÈSE DE DOCTORAT

présentée à la Faculté des géosciences et de l'environnement de l'Université de Lausanne
pour l'obtention du grade de Docteur en sciences de la Terre par

LUDOVIC RÄSS

Maîtrise ès Sciences en géosciences de l'environnement de l'Université de Lausanne

Jury

Prof. Dr. Michel Jaboyedoff	Université de Lausanne	Président du jury
Prof. Dr. Yury Y. Podladchikov	Université de Lausanne	Directeur de thèse
Prof. Dr. Stefan M. Schmalholz	Université de Lausanne	Expert interne
Prof. Dr. Paul J. Tackley	ETH Zürich	Expert externe

Lausanne, 2018

IMPRIMATUR

Vu le rapport présenté par le jury d'examen, composé de

Président de la séance publique :	M. le Professeur Michel Jaboyedoff
Président du colloque :	M. le Professeur Michel Jaboyedoff
Directeur de thèse :	M. le Professeur Yury Podladchikov
Expert interne:	M. le Professeur Stefan Schmalholz
Expert externe:	M. le Professeur Paul J. Tackley

Le Doyen de la Faculté des géosciences et de l'environnement autorise l'impression de la thèse de

Monsieur Ludovic Räss

Titulaire d'une
*Maîtrise universitaire ès Sciences en géosciences de l'environnement
de l'Université de Lausanne*

intitulée

Resolving thermo-hydro-mechanical coupling: spontaneous porous fluid and strain localisation

Lausanne, le 21 mars 2018

Pour le Doyen de la Faculté des géosciences et de l'environnement


Professeur Michel Jaboyedoff

In dedication to my parents, my sister and Simone

Contents

1	Introduction	1
1.1	Rationale	2
1.2	Objectives	5
1.2.1	Motivations	7
1.2.2	Open questions	9
1.3	Approach	9
1.4	Thesis structure	12
2	Spontaneous formation of fluid escape pipes from subsurface reservoirs	25
2.1	Results	30
2.2	Discussion	32
2.3	Methods	34
2.3.1	Mathematical model	34
2.3.2	Numerical implementation	35
	Appendix	35
2.A	Supplementary methods	35
2.A.1	Hydro-mechanical coupled model formulation	35
2.A.2	Simulation details and initial conditions	37
2.A.3	Solving strategy	38
2.A.4	Scaling relationships	39

3	M2Di: Concise and efficient MATLAB 2-D Stokes solvers using the finite-difference method	45
3.1	Introduction	47
3.2	Methods	48
3.2.1	The mathematical model	48
3.2.2	Numerical Implementation	50
3.3	The results	54
3.3.1	The validation of the linear Stokes flow solver	54
3.3.2	The validation of the power law Stokes flow solver	55
3.3.3	The algorithms' performance	56
3.4	Examples of instantaneous flow field calculations	59
3.4.1	Direct numerical simulations of crystal-melt dynamics	59
3.4.2	Pressure variations around viscous inclusions	60
3.4.3	The deformation of heterogenous power law viscous materials	61
3.4.4	Mantle flow and dynamic topography	62
3.5	Conclusions	64
	Appendix	65
3.A	The Stokes flow equation in cylindrical coordinates	65
4	Resolving hydro-mechanical coupling in two and three dimensions: Spontaneous channelling of porous fluids owing to decompaction weakening	71
4.1	Introduction	73
4.2	Mathematical model and hydro-mechanical coupling	75
4.3	Model setup	77
4.4	Numerical implementation and solving strategies	79
4.4.1	The direct-iterative solver	81
4.4.2	The pseudo-transient solver	83
4.4.3	Comparison of the DI and PT solvers	87
4.4.4	The performance of the solvers	90
4.5	Results	94
4.5.1	Hydro-mechanical fluid focussing in 2-D: A systematic study	94
4.5.2	Selected end-member runs	99
4.5.3	Data-collapse	99
4.6	Discussion	100

4.6.1	The genesis of high-porosity channels	100
4.6.2	Prediction of localised flow regimes	101
4.6.3	Extension to power law shear viscosity in 3-D	101
4.6.4	The influences of far-field tectonic regimes	104
4.6.5	Benefits and limitations of the pseudo-transient method	104
4.7	Conclusions	106
	Appendix	107
4.A	The direct-iterative scheme	107
4.B	Numerical transient time	108
5	Resolving thermo-mechanical coupling in two and three dimensions: Spontaneous strain localisation owing to strain heating	117
5.1	Introduction	119
5.2	The mathematical model	120
5.2.1	Thermo-mechanical coupling	120
5.3	The numerical methods	121
5.3.1	The direct-iterative method	122
5.3.2	The pseudo-transient method	122
5.3.3	Time integration	124
5.4	A comparison of the direct-iterative and the pseudo-transient methods	125
5.4.1	The reference model's configuration	125
5.4.2	The temperatures and strain rates inside the shear zones	127
5.4.3	The non-linear solvers' accuracy	127
5.4.4	The conservation of energy	128
5.4.5	Performance	129
5.4.6	Explicit and implicit coupling strategies	131
5.4.7	Time integration	133
5.5	Thermally activated shear localisation: Applications	133
5.5.1	Thermo-mechanical strain localisation in 2-D: A systematic study	133
5.5.2	The development of shear zones in 3-D	134
5.6	Discussion	137
5.6.1	Benefits of the pseudo-transient method and perspectives	137
5.7	Conclusions	138
	Appendix	138
5.A	The direct-iterative scheme	138

6	Chimneys, channels, pathway flow or water-conducting features: An explanation from numerical modelling and implications for CO₂ storage	143
6.1	Introduction	145
6.1.1	The need for numerical modelling	145
6.1.2	The Sleipner example	145
6.1.3	Localised fluid flow	146
6.1.4	Reservoir rheology	146
6.2	Model equations	147
6.2.1	Basic formulation	147
6.2.2	Model parameters	148
6.2.3	Flow instability and chimney formation	150
6.3	Numerical implementation	150
6.3.1	The numerical setup of the model	151
6.4	Results and discussion	152
6.4.1	Fluid flow in deforming rocks and channel-formation	152
6.4.2	Model development, improvements and goals	152
6.4.3	Porosity waves in 1-D and rock properties' effects	153
6.4.4	Examples of 3-D simulations	155
6.5	Conclusions	157
7	The quantification of viscous creep's influence on caprock's storage capacity	163
7.1	Introduction	165
7.2	Background	166
7.3	Methods	167
7.3.1	Experimental technique	167
7.3.2	Numerical methods	169
7.3.3	Material	170
7.4	Results and discussion	170
7.5	Conclusions	174
8	Perspectives	179
8.1	Summarising discussion	180
8.1.1	Fluid flow localisation arising from multi-physics coupling	180
8.1.2	Applicability of two-phase models to shallow environments	182
8.1.3	Supercomputing and algorithm performance	183
8.1.4	Outlook	187
8.2	Conclusion	188

Abstract

Localisation of deformation and flow is ubiquitously observed on Earth, spanning from subterraneous locations both in the deep interior and towards the shallow surface. Ductile strain localisation in tectonic processes or channelling and focusing of fluids in porous rocks are widely reported expressions of strain and flow localisation, governed by hydraulic, thermal and mechanical interactions. The intrinsic coupling of these different physical processes provides additional localisation mechanisms to well-established single-process physics. Models that address interactions between different physical processes must include non-linear feedbacks that may potentially trigger new and non-intuitive characteristic length and time scales. Accurately resolving this complex non-linear interplay resulting from coupled physics permits us to better understand the nature of multiphysics processes and to provide more accurate predictions on how, when and where to expect localisation. In many anthropogenic activities related to achieving a carbon-free energy transition, accurate predictions of mid-term to long-term behaviour for geosystems are vital. Engineered waste disposal solutions such as CO₂ sequestration and nuclear waste deposits require coupled models in order to predict the complexities of the evolving system. However, there is a current lack in model capability to address the non-linear interactions resulting from multiphysics coupling. Available models often fail to reproduce major first-order field observations of localisation, mainly owing to poor coupling strategies and a lack of affordable resolution needed to resolve very local non-linear features, especially in three spatial dimensions. In this thesis, I address these issues using a supercomputing approach to resolve sufficiently high-resolution strain and flow localisation in non-linearly deforming porous media, relying on a thermodynamically consistent model formulation. The developed graphical processing unit-based parallel algorithms show close to linear weak scaling on the world's third-largest supercomputer and are benchmarked against classical direct-iterative type solvers. The high-resolution computations are needed for the convergence of the calculations. The results confirm that a strong coupling between solid deformation, fluid flow and heat diffusion provides a viable mechanism for 'chimney' formation or strain localisation. Flow localisation in high-permeability chimneys provides efficient pathways for fast vertical fluid migration. By using model parameters relevant for sedimentary rocks, natural observations and their main characteristic features could be reproduced. In summary, this thesis provides an extensive study on hydro-mechanical interaction in fluid-saturated and non-linearly deforming porous rocks. Further, the predicted high-permeability pathways are vital to understand the formation of potential leakage pathways and are a prerequisite for reliable risk assessment in long-term waste storage. Finally, the developed solution strategy is successfully utilised to resolve strain localisation in thermo-mechanically coupled processes.

Résumé

La localisation de la déformation et des fluides est observée à l'échelle du Globe, allant des couches profondes jusqu'à la subsurface. Des phénomènes géologiques tels que la localisation de la déformation ductile ou la chenalisation des fluides dans les roches poreuses témoignent d'amplifications locales de la déformation et de la porosité et résultent d'interactions entre des processus hydrauliques, thermiques et mécaniques. Le couplage de ces divers processus physiques génère des rétroactions non-linéaires et aboutit à des nouvelles grandeurs caractéristiques non-triviales. Une résolution précise de ces interactions complexes permet de mieux comprendre la nature des processus multi-physiques et permet d'établir de meilleures prédictions quant à de possibles occurrences de localisation. Passablement d'activités anthropogéniques liées à la transition énergétique reposent sur des prédictions précises de l'évolution à long terme des géo-systèmes. La séquestration du CO₂ ainsi que le stockage des déchets nucléaires requièrent l'utilisation de modèles couplés afin de prédire l'évolution des systèmes de confinement. Toutefois, les modèles actuels peinent à reproduire les observations de premier ordre, notamment les évidences de localisation des fluides et de la déformation. Les principales raisons sont le traitement des problèmes trop souvent effectué en deux dimensions, le manque de rigueur dans les stratégies de couplage entre les différents processus ainsi que l'utilisation de résolutions insuffisantes dans les modèles. Dans cette thèse, je propose une approche basée sur le calcul à haute performance permettant de résoudre avec des résolutions élevées les processus de localisation dans des milieux poreux déformables en utilisant des modèles thermodynamiquement consistants. Les algorithmes parallèles développés utilisent des processeurs graphiques disponibles entre autres sur le troisième plus performant superordinateur du monde et reportent un temps de calcul identique lorsque la taille du problème à résoudre grandit proportionnellement avec le nombre de ressources disponibles. Les résultats attestent de la convergence de la méthode et confirment le fait qu'un couplage important entre déformation, écoulement des fluides et diffusion de la chaleur permet la formation de chenaux à perméabilité élevée ainsi que la localisation de la déformation. Ces chenaux, ou drains, permettent l'écoulement focalisé ainsi qu'une migration verticale rapide des fluides. En prenant en compte les paramètres pétrophysiques caractéristiques des roches situées dans des bassins sédimentaires, ces écoulements préférentiels reproduisent les observations naturelles. La prédiction d'occurrence de chenaux à perméabilité élevée est vitale afin de mieux prévenir de potentiels risques de fuites et de fournir des solutions sûres pour les générations futures en termes de stockage de déchets à risque. Pour conclure, cette thèse propose une étude extensive sur les interactions hydromécaniques dans des roches poreuses saturées avec des fluides. De manière analogue, la stratégie de solution développée a été appliquée pour étudier la localisation de la déformation ductile résultant d'un couplage thermomécanique.

CHAPTER 1

Introduction

1.1 Rationale

Fluid flow in porous rocks is a process common in a wide range of different rock types on Earth. Low-permeability rocks in the Earth's deep interior host dehydration reactions of aqueous minerals in ductile rocks (Figure 1.1), preventing fluids (mainly water) from escaping the Earth's surface in active subduction zones (Connolly and Podladchikov, 1998, 2000; Iyer et al., 2013; Miller et al., 2003; Skarbek and Rempel, 2016). In low-crustal regions, evidence of fluid circulation triggered by metasomatic processes are observed in exhumed rocks showing localised reaction patterns or veins (Omlin et al., 2017; Plümper et al., 2017a,b). Migration of melt into partially molten and deforming regions of the lithosphere suggests evidence of important fluid transfer that provides source fluids for active magmatism on Earth (Cai and Bercovici, 2013; Connolly and Podladchikov, 2007a; Keller et al., 2013; Liang et al., 2011; McKenzie, 1984; Rudge et al., 2011; Schiemenz et al., 2011; Scott and Stevenson, 1984; Simpson et al., 2010a,b). At mid-ocean ridges, black smokers and hydrothermal venting are additionally well-observed processes of fluid expulsion that reflect fluids' generalised tendency to migrate within porous rocks (Katz and Weatherley, 2012; Keller and Katz, 2016; Keller et al., 2017). In shallower crustal environments, fluid-saturated porous rocks compose a large majority of sedimentary formations around the world. These sedimentary basins are mainly located on continental shelves and are of major economic interest, since their pore volume is vital for the transportation and storage of global oil and gas reserves.

Over the past decades, sedimentary rock formations have gained attention owing to their close link to the ongoing development of a society whose economy still relies on fossil fuels. Besides this, sedimentary and porous rock formations may also play a key role in various engineered waste sequestration solution types, such as carbon dioxide (CO_2) capture and storage (CCS) or nuclear waste storage (Dupray et al., 2013; McCartney et al., 2016; Rutqvist et al., 2009). To remediate greenhouse gas emissions, large amounts of CO_2 need to be captured and stored underground (IEA, 2013). Saline aquifers and depleted oil fields found in places

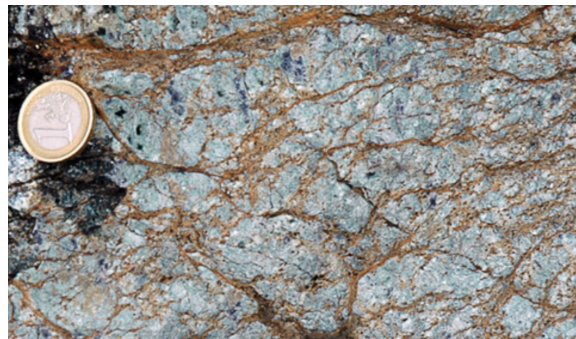


Figure 1.1: Vein formation during dehydration in the Erro-Tobbio meta-serpentinite, Ligurian Alps, Italy. Adapted from Plümper et al. (2017b).

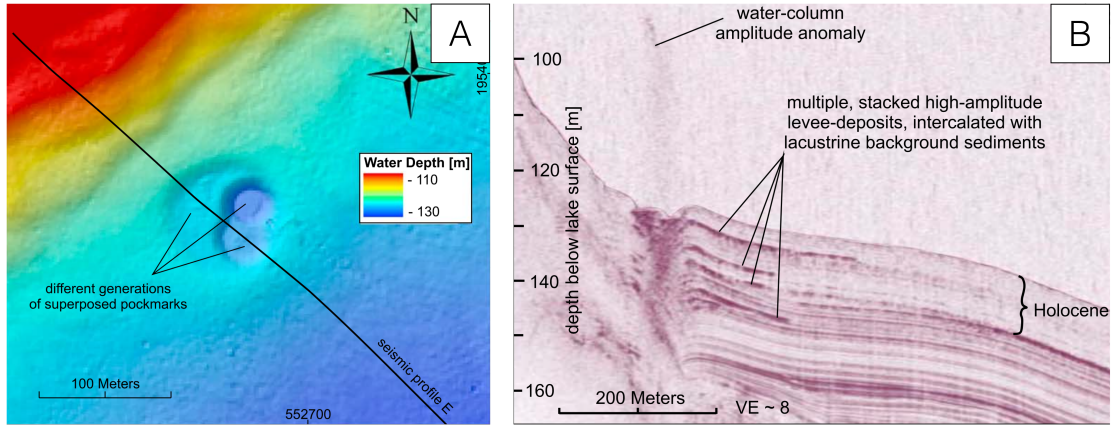


Figure 1.3: Multibeam-derived bathymetric maps showing (a) Treytel pockmark in lake Neuchâtel, Switzerland. (b) Corresponding seismic profiles, obtained by seismic reflection (3.5 kHz pinger seismic) of Treytel pockmark, enhanced amplitude in water column. Adapted from Reusch et al. (2015).

and compacted transition zones between the chimney's exterior and interior (the so-called chimney rims). Expressions of these vertical chimneys on a horizontal plane are visible via bathymetry and sonar data (Figure 1.2b). Entire fields of blowout craters and so-called pockmarks are visible on the seafloor and represent the top end of seismic chimneys (Berndt, 2005; Cartwright and Santamarina, 2015; Cathles et al., 2010; Hustoft et al., 2010; Judd and Hovland, 2007; Løseth et al., 2011; Mazzini et al., 2017; Plaza-Faverola et al., 2010, 2011). Recently, identical features (Figure 1.3) were also discovered in Swiss lacustrine environments (Reusch et al., 2015). Interestingly, similar seismic signature types have also been observed in reservoir operation environments, such in Norway's Sleipner field. After the start of CO₂ injection at the bottom of the reservoir, seismic vertical chimneys appeared, and have become increasingly evident over the years (Berndt, 2005; Chadwick et al., 2009). The coloured horizontal layers are caused by CO₂ reflectance (Figure 1.4) and show the extent of the CO₂ plume within the Utsira formation. Geophysical measurements indicate that CO₂ is safely contained below the main caprock and that the pressure at the well-head is stable. While attempts have been made to correlate these observations at Sleipner using conventional reservoir simulations (Cavanagh, 2013; Cavanagh and Rostron, 2013; Cavanagh and Haszeldine, 2014; Cavanagh et al., 2015; Chadwick et al., 2016; Singh et al., 2010), these have failed to capture some of the major first-order observations, such as enhanced vertical flow cutting through intermediate low-permeable shale layers (e.g. Foschi et al., 2014), a rapid lateral spreading under the caprock, and the formation or utilisation of localised flow-path or chimneys. The current conclusion concerning vertical buoyancy-driven flow in the Utsira formation proposes that CO₂ migration occurs via some pathway flow, becoming more effective and numerous with time. However, the nature of these pathways remains uncertain. The Sleipner example

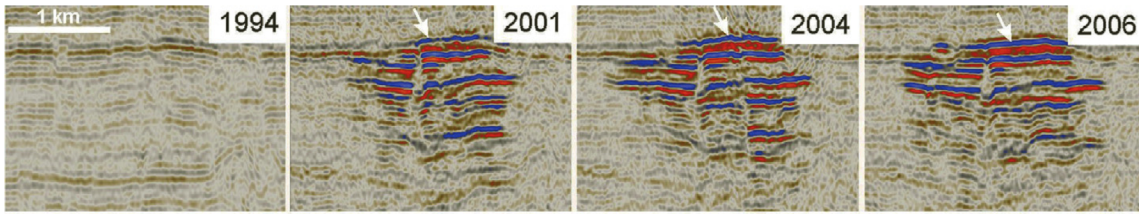


Figure 1.4: Seismic images of the Sleipner plume showing its development to 2006. North-South seismic section through the plume. Topmost CO₂ layer arrowed. Adapted from Chadwick et al. (2009).

shows among others that, besides the large amount of available observations and field data regarding pockmarks and chimneys, no current model is capable of explaining the physical behaviour of such two-phase systems.

Understanding the interplay of fluid-filled porous rocks with their pore-fluid requires that one combining the governing of physical relationships of single-phase rock deformation and porous fluid flow. The pore-fluid may affect the system's overall response, since pore pressure modifies the skeleton's stress response and the skeleton sustains pressure gradients that drive fluid flow. Also, temperature effects and chemical reactions may further influence the system's evolution. The interactions (thus, coupling) between these various hydraulic, thermal, chemical and mechanical processes are crucial to understanding the bulk behaviour of complex systems, targeted by engineered waste disposals, among others. Thus, the lack of models that can reproduce and predict key observations arising from multiphysics coupling sets an important precedent to further develop models capable of providing accurate predictions on the long-term evolution of porous rock formations and their interacting pore-fluids (Rutqvist et al., 2001, 2002; Zhang et al., 2011).

1.2 Objectives

In this thesis, I focus on modelling hydro-mechanical (HM) and thermo-mechanical (TM) coupled processes in the Earth's subsurface. The aim is to gain a deeper understanding of the dynamics of fluid flow localisation in non-linearly deforming porous rocks, motivated by the abundant evidence of focussed flow patterns in sedimentary basins, forming so-called seismic chimneys. I will use a numerical modelling approach based on continuum mechanics in one, two and three spatial dimensions (1-D, 2-D and 3-D), to explore the underlying physical mechanisms that lead to the formation and propagation of high-porosity chimneys. Major first-order qualitative field observations (Figure 1.5a) that are summarised by Løseth et al. (2011) combined with quantitative geophysical data will provide important information used to constrain the numerical models. To resolve the formation of these multiscale features with accuracy in space and time, high-resolution models are mandatory. Insufficient numerical res-

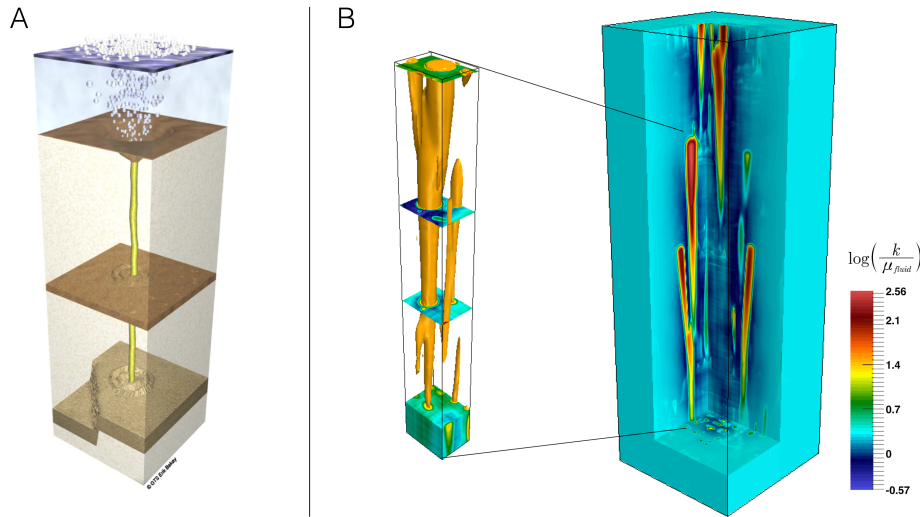


Figure 1.5: (a) Illustration and summary sketch of the major field observation concerning fluid focussing and channelling in sedimentary basin (Løseth et al., 2011). (b) Permeability field of a 3-D high-resolution numerical simulation of focussing fluid flow as a natural outcome of random initial porosity and permeability distribution.

olution may lead to erroneous results or no localisation at all. This need for high resolution is especially challenging for 3-D calculations, owing to the large number of grid-points involved. The mandatory memory requirements and fairly sequential processing workflow of standard computer processors invokes a supercomputing approach as the only viable option to achieve a solution within a reasonable timeframe, or even a solution at all. The recent development of hardware accelerators such as graphical processing units (GPUs) has significantly democratised the accessibility of many core computing devices, unlocking new potential for parallel computing. However, there is a lack of software (i.e. numerical models) capable of efficiently utilising these many core architectures.

Understanding the controlling parameters and conditions that allow fluids to propagate in a localised and rapid fashion instead of migrating and spreading in a diffuse and slow way within the subsurface is necessary to increase the predictive power of two-phase coupled models. In this context, the main objectives of this work are to: (1) develop numerical models capable of resolving sudden localisation of fluid flow and strain on various temporal and spatial ranges and, (2) make optimal usage of current supercomputers, ensuring algorithms to perform close to the limits of the hardware. Both are challenging because:

- appropriate coupling between fluid flow and porous matrix deformation is required
- complex non-linear rheology must be considered
- material properties such as permeability and viscosity range over several orders of magnitude

- sufficient numerical resolution is mandatory to accurately resolve localisation
- we currently lack 3-D numerical codes capable of optimally running in parallel on modern supercomputers.

1.2.1 Motivations

Fluid-filled sedimentary rocks have been extensively studied since the middle of the twentieth century owing to their potential as hydrocarbon reservoirs (Biot, 1941, 1955, 1956a,b, 1962, 1963; Gassmann, 1951; Geertsma, 1957; Rice and Cleary, 1976; Verruijt, 1969). The so-called porous medium is a combination of a matrix or skeleton and its pore-fluid, which can consist of one or more distinct phases. The presence of fluid in the rock's pores leads to pore pressure and may significantly affect the way the porous rock deforms under an applied load (Rozhko et al., 2007; Skempton, 1954; Terzaghi, 1923). Thus, the single-phase behaviour of both the pore-fluid and the solid skeleton are affected by the presence of the other phases, resulting in a two-phase or multiphase and multiphysics behaviour of the porous media.

An abundant variety of numerical models that couple thermal, hydraulic, chemical and mechanical processes are currently available in order to investigate multiphysics processes in porous media. They couple diffusion-like processes (thermal, hydraulic, chemical) to mechanics (e.g. Bea et al., 2015; Rutqvist, 2011; Rutqvist et al., 2002; Tsang, 1999). However, their predictive potential is fairly limited in some cases, since they often only address distributed percolation in non-deformable skeletons, or assume a linear elastic response of the porous media (Jha and Juanes, 2014; Kim et al., 2011a,b; Minkoff et al., 2003; Rutqvist, 2012; Settari and Walters, 2001). Although some of these models include plastic failure to predict faults and fractures, they don't explain the formation of localised tube-shaped chimneys.

In geodynamic applications, hydro-mechanical coupling is addressed by two-phase (solid + fluid) flow. Early models were derived for magma migration and account for time-dependent viscous deformation of the porous matrix (Fowler, 1990a,b; McKenzie, 1984; Scott and Stevenson, 1984; Simpson et al., 2010a,b). Viscous bulk rheology combined with non-linear Darcian fluid flow allows the existence and propagation of solitary waves (soliton) (Barcilon and Richter, 1986; Scott and Stevenson, 1984; Stevenson and Scott, 1991; Wiggins and Spiegelman, 1995). Analogous to solitary waves, porosity waves (Vasilyev et al., 1998; Yarushina and Podladchikov, 2015) refer to soliton generated by local decompaction and compaction of the porous matrix (Figure 1.6). Specifically, they are a buoyancy-driven fluid motion mechanism driven by a difference between the fluid pressure and the total pressure (or mean stress), here defined as the effective pressure. The effective pressure induces decompaction of the porous matrix if negative (i.e. when fluid pore pressure overcomes the local mean stress) and compaction if positive (i.e. when the fluid pore pressure is less than the confining total pressure or mean stress).

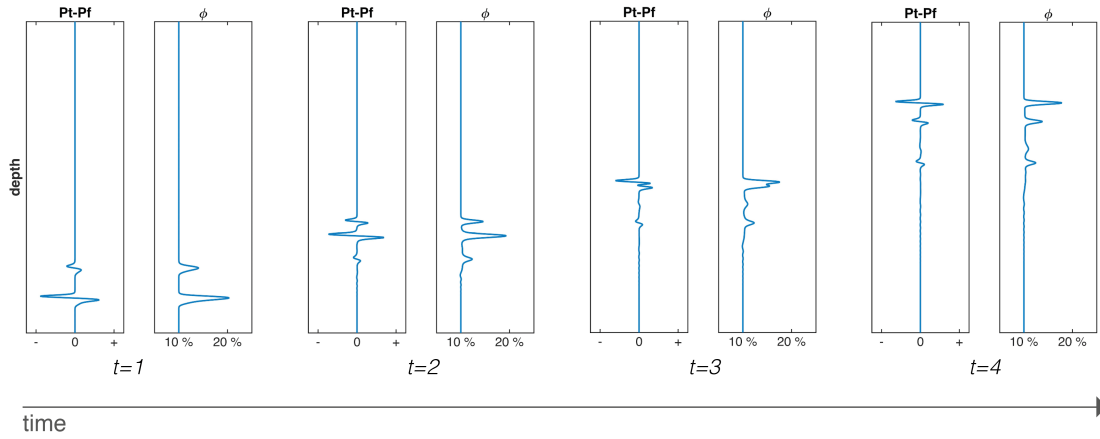


Figure 1.6: Snapshots in time of buoyant rise of a solitary wave of porosity (i.e. porosity wave) in a 1-D poro-viscous medium filled with buoyant pore-fluid. The left-hand panel is the effective pressure and the right-hand panel the porosity fraction. ($t=1$) initial setup of two high-porosity anomalies. ($t=2$) upward motion of the elevated porosity pulse driven by negative effective pressure at the front (decompaction) and positive effective pressure at the tail (compaction). ($t=3$) Particularity of solitary waves showing travel speed proportional to their amplitude; the bottom wave ‘overtakes’ the upper one. ($t=4$) Final stage; each individual wave is recovering its shape and is continuing a buoyant rise.

Although porosity waves provide an efficient mechanism for enhanced fluid transfers within the subsurface, neither their shape nor their propagation velocity shows a pertinent match to major field observations of localised flow-paths. An example from recent studies (Appold and Nunn, 2002; Joshi and Appold, 2016) that utilises porosity waves as a mechanism for fluid and hydrocarbon transfer in shallow reservoirs also struggles to match appropriate flow rates. An additional focussing mechanism, decompaction weakening, provides the “blob to channel” transition, modifying the porosity wave’s initial blob shape into elongated channels (Connolly and Podladchikov, 2007b). Decompaction weakening represents an asymmetry between the decompaction and the compaction regimes, reflecting rocks’ tendency to sustain less extensional than compressional loads. Thus, a drastic drop in bulk viscosity values in decompacting regions significantly increases the porous matrix’s ability to creep locally. Although low-crustal environments are assumed to be warm enough for viscous rheology to be active, shallow reservoir rocks are commonly assumed to undergo elastic or elasto-plastic deformation. However, recent laboratory experiments on major reservoir rock types suggest a fairly fluid-like rather than solid-like behaviour of saturated sedimentary porous rocks; thus, time-dependant deformation (creep) of the skeleton must be considered (Brantut et al., 2013; David et al., 2015; Hagin and Zoback, 2004a,b; Kong et al., 2009; Sone and Zoback, 2013, 2014). Viscous effects cannot be neglected; thus, the mechanical model needs to include a poro-visco-elasto-plastic rheology. By accounting for viscous rheology, the porous matrix deformation is no longer limited to small strain, as predicted by elastic deformation. This

invokes additional challenges in terms of modelling, since large strains (i.e. important shear and bulk deformation) may need to be handled by the numerical models.

The current lack of performant numerical applications must be addressed by providing simple yet robust algorithms capable of resolving multiphysics-coupled processes that provide accurate predictions for a wide range of key unanswered questions in the Earth Sciences. This motivates the spreading of HPC in the Earth Sciences.

1.2.2 Open questions

Although several studies have investigated localisation mechanisms in non-linear rheologies via hydro-mechanical and thermo-mechanical couplings, several questions remain unanswered, namely:

1. Does fluid flow localise in channels or pipes as a natural outcome of hydro-mechanical coupling?
2. Which mechanism mainly governs the primary characteristics of high-porosity chimneys (spacing, size, velocity)?
3. Is this model applicable to shallow environments such as reservoirs and sedimentary basins?
4. What numerical resolution is mandatory to accurately resolve localised flow patterns in 2-D and 3-D?
5. Is there an efficient strategy to numerically resolve diffusion processes coupled to mechanics in 3-D on modern hardware?

1.3 Approach

I propose addressing these questions utilising thermodynamically admissible models to perform state-of-the-art numerical modelling of coupled hydro-mechanical and thermo-mechanical processes that lead to flow and strain localisation in 2-D and 3-D. I propose combining the modelling activity with laboratory experiments on the long-term behaviours of major reservoir rock types, moving towards more accurate rheological constrains of shallow sedimentary reservoir rocks, namely sandstone, limestone and shale.

Porosity waves are a hydro-mechanical instability type I aim to explore, to explain chimney generation in low-permeability environments. Also, I am interested in exploring the applicability of algorithms designed to resolve the coupling of a diffusion-like process (such as fluid

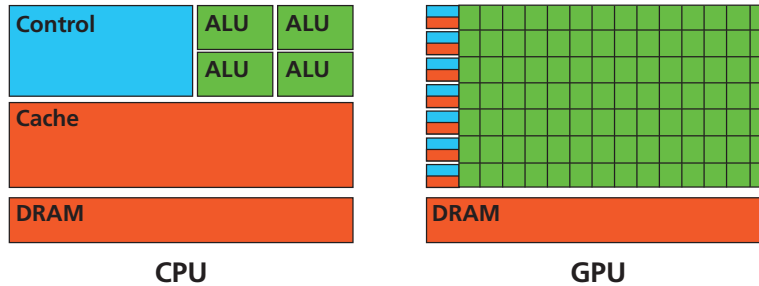


Figure 1.7: Conceptual difference between a central processing unit (CPU) vs. a graphical processing unit (GPU) chip design. On the CPU, most of the on-chip space is devoted to controlling units and cache memory; little space is left for the arithmetic and logical units (ALU). On the GPU, cache memory and controlling units are reduced to the strict minimum, allowing most of the on-chip area to host several thousand ALUs.

pressure diffusion or heat diffusion) to mechanical deformation (Stokes). I plan to tackle the numerical resolution of shear-heating instabilities. Shear-heating induces strain localisation in specific regimes of thermo-mechanical coupling (Duretz et al., 2014; Schmalholz and Duretz, 2015), resulting in mechanical softening. Shear-heating may trigger important and highly localised strain-localisations (as investigated by Jaquet and Schmalholz, 2017) and therefore must be accurately resolved in numerical models that for instance address lithospheric dynamics.

The growing number of mandatory features to be included for the numerical models sets major challenges in the development of the next generation of numerical models. In addition to the model’s physics-based features and capabilities, challenging technicalities that unlock near peak performance execution of the algorithms on modern supercomputing must be considered. An important part of the work makes use of developed solutions to address technical challenges inherent in the development of real-world high-performance computing (HPC) applications. Optimal algorithm performance results in minimal time-to-solution for a given problem on specific hardware. There are two motivations for utilising performant algorithms. First, more problems can be solved in the same amount of time. Second, power consumption is reduced, a strong argument when several thousands of computer nodes are utilised in parallel to achieve a solution. Both the nature of the physical problem (e.g. equations, number of spatial dimensions) to be solved and the specificities of current hardware may significantly influence the appropriate strategy to find the best solution.

Classical approaches to achieve an implicit solution of a set of governing equations are to collect the coefficient multiplying the unknowns in a coefficient matrix. Applying the inverse (e.g. by a Gauss elimination) of the latter allows one to retrieve the solution vector. The advantages of a so-called direct method reside in implicit solutions that are fairly insensitive to large variations in material properties (e.g. viscosity jumps across an interface). How-

ever, such an approach is only viable for restricted system sizes and mainly for 1-D setups, since the time-to-solution grows exponentially with problem size; the length of the coefficient matrix's main diagonal equals the total number of grid-points involved in the computation. Thus, the linear system of equations grows linearly for 1-D setups, but quadratically for 2-D ones. Also, direct methods are not a viable solution for resolving 3-D setups. An optimised direct method resides in a factorisation of subparts from the global coefficient matrix and to iteratively retrieve a global solution by explicitly performing few well-defined steps of the Gauss elimination and back-substitutions. The resulting direct-iterative (DI) method allows one to substitute the expensive Gauss elimination on the entire coefficient matrix with the factorisation of smaller matrices, for instance using a Cholesky factorisation on symmetric and positive defined objects (e.g. Dabrowski et al., 2008). Using this approach, 2-D setups show much closer to linear time-to-solution with increasing problem size. Although DI methods greatly improve matrix-based solution approaches, they still don't perform well when addressing 3-D setups.

In this work, I further investigate the viability of an iterative solver based on a matrix-free implementation to resolve coupled problems. Pseudo-transient (PT) continuation allows one to minimise a given system's residuals without having to build a coefficient matrix (e.g. Yang and Mittal, 2014). Matrix-free approaches combine well with the staggered grid discretisation, reported since the 1960s in the broader computational fluid dynamics (CFD) literature (e.g. Patankar, 1980). The subsequent finite-difference (FD) method relies on the staggered grid discretisation, for which variables are defined at different location on the computational grid; for the Stokes flow it results in defining pressure at the cells centre and fluxes or velocities at the cells boundaries. This contrasts with other implementations of Stokes flow using non-staggered finite-difference grids and various CFD flow problems using a finite-volume approach. I will principally consider solid Earth dynamics in this work, whereas staggered grid discretisation and FD methods have also been extensively utilised since the 1990s to model 3-D Stokes flow, mainly in the mantle convection community (e.g. Kameyama et al., 2005; Ogawa et al., 1991; Ratcliff et al., 1995; Tackley, 1996).

Combining the PT approach with the FD stencil-based method on a regular staggered grid provides numerous advantages that enable parallel 2-D and 3-D algorithms to maximise the utilisation of modern hardware such as GPUs. GPUs are many-core accelerators (Figure 1.7) capable of performing the same simple instruction concurrently on each of their enormous numbers of threads (or workers). Thus, every grid-point of the numerical domain can be simultaneously computed by an individual thread. It is therefore straightforward to solve a given set of equations in parallel on the entire domain. This approach requires access only to neighbouring values of every cell in order to perform the stencil-based derivative evaluation. The locality of data access combined with a mostly regular memory access pattern allows one to reduce to the strict minimum the mandatory memory transfers for every arithmetic

operation. Thus, the resulting algorithm performance is significantly increased, reflecting the status of actual processors to transfer memory at a much lower rate than when performing arithmetic operations (leading to memory-bounded applications). An additional benefit of using a regular grid and regular memory access is a simple message-passing interface (MPI) parallelisation, enabling the routine to run on distributed memory machines (such GPU-based supercomputers). In this context, only local boundaries need to be exchanged with neighbouring processes, leading to optimal performance.

1.4 Thesis structure

My aim in this thesis is to provide at least partial answers to the different open questions I have introduced. In Chapter 2, I provide a concise overview on the importance of resolving hydro-mechanical (HM) coupling with application to fluid flow localisation in the subsurface. In Chapter 3, I familiarise the reader with linear and non-linear Stokes flow in 2-D, providing efficient solving approaches of single-phase mechanics streamlining direct-iterative solver types. In Chapter 4, I consider the extension of single-phase mechanics to two-phase flow. I explore hydro-mechanical (HM) coupling and consider both a DI and a matrix-free PT solver type. I benchmark the accuracy of the PT GPU-based routines using a classical DI approach. I show flow localisation to be a natural outcome of accurate HM coupling for specific parameter combinations. In Chapter 5, I provide the analogy of HM coupling in terms of thermo-mechanical (TM) coupling. The matrix-free PT approach I develop in Chapter 4 successfully ports to investigate strain-localisation resulting from TM coupling. In Chapter 6, I suggest HM coupling and decompaction weakening as main mechanisms to explain high-permeability pathways imaged as seismic chimneys at the world's largest CO₂ storage pilot (Sleipner Norway). In Chapter 7, I link numerical modelling and laboratory experiments on rock mechanics to further constrain the viscous bulk rheology of major reservoir rock types (sandstone, limestone and shale) with application to caprock integrity in the framework of CO₂ storage. In Chapter 8, I conclude this thesis with a summary that highlights the primary results from every chapter. I propose future research avenues involving mainly HM-coupled physics, discussing the performance of HPC implementation of HM-coupled solvers on modern supercomputers.

This thesis contains a collection of articles published or under review in peer-reviewed ISI journals. Chapter 3 was published in *Geochemistry, Geophysics, Geosystems* and Chapters 6 and 7 were published in *Energy Procedia*. Chapter 2 is based on a submitted scientific report to *Nature*. Chapters 4 and 5 are based on submitted manuscripts to *Geophysical Journal International*. I will now provide some information about these publications, including the main scientific contributions.

- *Chapter 2: Spontaneous formation of fluid escape pipes from subsurface reservoirs*

This scientific report to *Nature* addresses channelised fluid flow in the shallow subsurface and the related pipes or chimney-like features observed ubiquitously in sedimentary rocks. These fluid-conductive chimneys constitute evidence for significant transient permeability-generation events responsible for spontaneous flow localisation. Understanding their dynamics is vital concerning both natural fluid migration and anthropogenic fluid and gas operations, or in waste sequestration. We provide a physical mechanism of such chimney formation. We use novel high-resolution numerical calculations in three-dimensions to address the current lack of predictive models in this field. Resolving both fluid flow and shear deformation of the matrix in three dimensions permits us to predict fluid flux and matrix stress distribution over time. The chimneys constitute efficient pathways that show more than three orders of magnitude enhanced permeability. Our study points out that accurate predictions are vital to understand the formation and evolution of leakage pathways in natural gas emissions and are a prerequisite for reliable risk assessment when planning long-term subsurface waste storage.

As first author, I contributed to writing the final manuscript together with N.S.C. Simon. I developed the numerical algorithm together with Y.Y. Podladchikov. All authors contributed to the overall study's design.

- *Chapter 3: M2Di: Concise and efficient MATLAB 2-D Stokes solvers using the Finite Difference Method*

This paper provides a set of routines for 2-D linear and power law incompressible viscous flow based on finite-difference discretisation. The MATLAB codes can achieve a time-to-solution of 22 seconds for linear viscous flow on 1000^2 grid-points using a personal computer. The DI solver type includes both a Newton and Picard iteration scheme. Application examples spanning from finely resolved crystal-melt dynamics, deformation of heterogeneous power law viscous fluids to instantaneous models of mantle flow in cylindrical coordinates are provided. I validate the routines against analytical solutions for linear viscous flow with highly variable viscosity and compare them to analytical and numerical solutions of power law viscous folding and necking.

As first author, I am the main contributor to this study, with co-author T. Duretz. I implemented the majority of the MATLAB routines, with the exception of the analytical Newton Jacobian (T. Duretz). I realised the performance benchmark and drafted the manuscript, with T. Duretz. I completed the manuscript with minor contributions from the co-authors.

- *Chapter 4: Resolving hydro-mechanical coupling in two and three dimensions: Spontaneous channelling of porous fluids owing to decompaction weakening*

In this paper, I numerically investigate a physical mechanism, decompaction weakening, which leads to the formation and propagation of localised flow-paths in fluid-saturated porous media. I use high-resolution 2-D and 3-D numerical modelling to solve non-linear Darcian porous flow in a viscously deforming matrix using a non-linear Stokes flow. I implement matrix-free pseudo-transient approaches on graphical processing units. The PT routines converge towards identical solutions compared to DI solving strategies. The results suggest that high-porosity channels may be a dynamic and natural outcome of sufficiently resolved hydro-mechanical coupling and decompaction weakening.

As first author, I am the main contributor to this study. I implemented the DI MATLAB solvers as well as the PT MATLAB and C-CUDA (GPU) solvers. I designed the setup of the numerical model, realised the simulations and performance benchmarks, and drafted the manuscript, including tables and figures. The co-authors suggested the figure outline and helped to improve the manuscript's quality. T. Duretz helped to design the early version of the DI workflow for HM-coupled equations.

- *Chapter 5: Resolving thermo-mechanical coupling in two and three dimensions: Spontaneous strain localisation owing to strain heating*

This paper provides 2-D codes based on an implicit FD discretisation. The DI method relies on a classical Newton iteration cycle, while the PT method uses pseudo-time marching. Both methods are able to capture the thermo-mechanical instability leading to shear localisation and to deliver coherent results both in terms of non-linear accuracy and conservativeness. The PT method is an attractive alternative, since it can deliver similar accuracy to the standard DI method but is based on a much simpler algorithm and enables high-resolution 3-D simulations. The results provide a systematic investigation of the dimensionless parameters that control 2-D shear localisation. Shear zone propagation in 3-D using the PT method is finally modelled.

The main contributor to this study is T. Duretz. As second author, I implemented the PT version of the TM code and provided both the 2-D and the 3-D C-CUDA GPU routines. I participated in the manuscript's design and realised parts of the figures and the performance benchmarks. The other co-authors helped to formulate the final set of dimensionless equations and suggested investigations discussed in the results section.

- *Chapter 6: Chimneys, channels, pathway flow or water conducting features - an explanation from numerical modelling and implications for CO₂ storage*

This paper reports on the development and application of coupled HM codes in the context of CO₂ storage in the Sleipner field (offshore Norway). A stress-dependent poro-visco-elasto-plastic deformation in accordance with field observations and laboratory measurements is considered. The simulations predict the spontaneous formation of self-localising high-porosity channels (or pathway flow) under conditions applicable to CO₂

storage in reservoirs. These channels form owing to mechanical instabilities that occur as a natural outcome of buoyancy-driven flow in visco-plastically deforming rocks. The results indicate that viscous deformation may explain the formation of chimneys such as those observed at the Sleipner pilot, and that non-linear effects strongly impact the fluid's velocity and distribution as well as on stress and deformation of the rock matrix.

As first author, I was the main contributor to this study. I designed and realised the numerical experiments and drafted the manuscript, with N. S. C. Simon and V. M. Yarushina. The co-authors provided the literature review and the mathematical model (V. M. Yarushina and Y. Y. Podladchikov).

- *Chapter 7: Quantification of viscous creep influence on storage capacity of caprock*

This paper focusses on the ease of creep of Opalinus clay (Jurassic shale) under shallow geological storage conditions and predicts the possible propagation of high-porosity channels at operational time scales in wastewater reservoirs. The effective poro-visco-elastic parameters of rocks are inferred from the novel laboratory experiments that allow evaluation of time-dependent deformation. The shale's bulk viscosity is found to be $\sim 10^{14} - 10^{15}$ Pa.s and decreases with increasing temperature and pore-fluid pressure to total mean stress ratio. Further, the propagation speed of high-porosity channels (porosity waves) is calculated to be centimetres per year.

As first author, I am one of the main contributors to this study. I realised the design of the numerical experiments and worked with the co-authors on the conceptual design of relevant setups for the laboratory experiments. I also calculated the channels' propagation speeds. R. Y. Makhnenko designed and conducted experiments at the Laboratory of Soil Mechanics, EPFL. I drafted part of the manuscript and finalised the submission. All co-authors helped to improve the manuscript's quality.

Bibliography

- Appold, M. S., Nunn, J. A., 2002. Numerical models of petroleum migration via buoyancy-driven porosity waves in viscously deformable sediments. *Geofluids* 2 (3), 233–247.
- Barcion, V., Richter, F. M., 1986. Nonlinear waves in compacting media. *Journal of Fluid Mechanics* 164 (1), 429.
- Bea, S., Mayer, U., MacQuarrie, K., 2015. Reactive transport and thermo-hydro-mechanical coupling in deep sedimentary basins affected by glaciation cycles: model development, verification, and illustrative example. *Geofluids* 16 (2), 279–300.

- Berndt, C., 2005. Focused fluid flow in passive continental margins. *Philosophical Transactions of the Royal Society of London A: Mathematical, Physical and Engineering Sciences* 363 (1837), 2855–2871.
- Biot, M. A., 1941. General theory of three-dimensional consolidation. *Journal of applied physics* 12 (2), 155–164.
- Biot, M. A., 1955. Theory of elasticity and consolidation for a porous anisotropic solid. *Journal of applied physics* 26 (2), 182–185.
- Biot, M. A., 1956a. General solutions of the equation of elasticity and consolidation for a porous material. *Journal of Applied Mechanics* 78, 91–96.
- Biot, M. A., 1956b. Thermoelasticity and irreversible thermodynamics. *Journal of Applied Physics* 27 (3), 240–253.
- Biot, M. A., 1962. Mechanics of deformation and acoustic propagation in porous media. *Journal of Applied Physics* 33 (4), 1482–1498.
- Biot, M. A., 1963. Theory of stability and consolidation of a porous medium under initial stress. *Journal of Mathematics and Mechanics*, 521–541.
- Brantut, N., Heap, M., Meredith, P., Baud, P., 2013. Time-dependent cracking and brittle creep in crustal rocks: A review. *Journal of Structural Geology* 52 (1), 17–43.
- Bünz, S., Polyanov, S., Vadakkepuliambatta, S., Consolaro, C., Mienert, J., 2012. Active gas venting through hydrate-bearing sediments on the Vestnesa Ridge, offshore W-Svalbard. *Marine Geology* 332-334, 189–197.
- Cai, Z., Bercovici, D., 2013. Two-phase damage models of magma-fracturing. *Earth and Planetary Science Letters* 368, 1–8.
- Cartwright, J., Santamarina, C., 2015. Seismic characteristics of fluid escape pipes in sedimentary basins: Implications for pipe genesis. *Marine and Petroleum Geology* 65, 126–140.
- Cathles, L., Su, Z., Chen, D., 2010. The physics of gas chimney and pockmark formation, with implications for assessment of seafloor hazards and gas sequestration. *Marine and Petroleum Geology* 27 (1), 82–91.
- Cavanagh, A., 2013. Benchmark Calibration and Prediction of the Sleipner CO₂ Plume from 2006 to 2012. *Energy Procedia* 37, 3529–3545.
- Cavanagh, A., Rostron, B., 2013. High-resolution simulations of migration pathways and the related potential well risk at the IEAGHG WeyburnMidale CO₂ storage project. *International Journal of Greenhouse Gas Control* 16, S15–S24.

- Cavanagh, A. J., Haszeldine, R. S., 2014. The Sleipner storage site: Capillary flow modeling of a layered CO₂ plume requires fractured shale barriers within the Utsira Formation. *International Journal of Greenhouse Gas Control* 21, 101–112.
- Cavanagh, A. J., Haszeldine, R. S., Nazarian, B., 2015. The Sleipner CO₂ storage site: using a basin model to understand reservoir simulations of plume dynamics. *First Break* 33 (June), 61–68.
- Chadwick, R., Noy, D., Arts, R., Eiken, O., 2009. Latest time-lapse seismic data from Sleipner yield new insights into CO₂ plume development. *Energy Procedia* 1 (1), 2103–2110.
- Chadwick, R., Williams, G., White, J., 2016. High-resolution imaging and characterization of a CO₂ layer at the Sleipner CO₂ storage operation, North Sea using time-lapse seismics. *First break* 34 (February), 79–88.
- Chadwick, R., Zweigel, P., Gregersen, U., Kirby, G., Holloway, S., Johannessen, P., 2004. Geological reservoir characterization of a CO₂ storage site: The Utsira Sand, Sleipner, northern North Sea. *Energy* 29 (9-10), 1371–1381.
- Connolly, J., Podladchikov, Y., 2007a. Decompaction weakening and channeling instability in ductile porous media: Implications for asthenospheric melt segregation. *Journal of Geophysical Research: Solid Earth* 112 (B10).
- Connolly, J., Podladchikov, Y. Y., 1998. Compaction-driven fluid flow in viscoelastic rock. *Geodinamica Acta* 11 (2-3), 55–84.
- Connolly, J., Podladchikov, Y. Y., 2000. Temperature-dependent viscoelastic compaction and compartmentalization in sedimentary basins. *Tectonophysics* 324 (3), 137–168.
- Connolly, J. A. D., Podladchikov, Y. Y., 2007b. Decompaction weakening and channeling instability in ductile porous media: Implications for asthenospheric melt segregation. *Journal of Geophysical Research* 112 (B10), B10205.
- Dabrowski, M., Krotkiewski, M., Schmid, D. W., 2008. MILAMIN: MATLAB-based finite element method solver for large problems. *Geochemistry, Geophysics, Geosystems* 9 (4).
- David, C., Dautriat, J., Sarout, J., Delle Piane, C., Menéndez, B., Macault, R., Bertauld, D., 2015. Mechanical instability induced by water weakening in laboratory fluid injection tests. *Journal of Geophysical Research: Solid Earth* 120 (6), 4171–4188.
- Dupray, F., Li, C., Laloui, L., 2013. THM coupling sensitivity analysis in geological nuclear waste storage. *Engineering Geology* 163, 113–121.

- Duretz, T., Schmalholz, S. M., Podladchikov, Y. Y., Yuen, D. A., 2014. Physics-controlled thickness of shear zones caused by viscous heating: Implications for crustal shear localization. *Geophysical Research Letters* 41 (14), 4904–4911.
- Foschi, M., Cartwright, J. A., Peel, F. J., 2014. Vertical anomaly clusters: Evidence for vertical gas migration across multilayered sealing sequences. *AAPG Bulletin* 98 (9), 1859–1884.
- Fowler, A. C., 1990a. A compaction model for melt transport in the Earth’s asthenosphere, part I, The basic model. *Magma Transport and Storage*, 1–14.
- Fowler, A. C., 1990b. A compaction model for melt transport in the Earth’s asthenosphere, part II, Applications. *Magma Transport and Storage*, 15–32.
- Gassmann, F., 1951. Elastic waves through a packing of spheres. *Geophysics* 16 (4), 673–685.
- Geertsma, J., 1957. The effect of fluid pressure decline on volumetric changes of porous rocks.
- Hagin, P. N., Zoback, M. D., 2004a. Viscous deformation of unconsolidated reservoir sandsPart 1: Time-dependent deformation, frequency dispersion, and attenuation. *geophysics* 69 (3), 731–741.
- Hagin, P. N., Zoback, M. D., 2004b. Viscous deformation of unconsolidated reservoir sandsPart 2: Linear viscoelastic models. *geophysics* 69 (3), 742–751.
- Hustoft, S., Bünz, S., Mienert, J., 2010. Three-dimensional seismic analysis of the morphology and spatial distribution of chimneys beneath the Nyegga pockmark field, offshore mid-Norway. *Basin Research* 22 (4), 465–480.
- IEA, 2013. *Technology Roadmap - Carbon capture and storage*, 2013 edition. Report.
- Ingebritsen, S. E., Manning, C. E., 2010. Permeability of the continental crust: dynamic variations inferred from seismicity and metamorphism. *Geofluids* 10 (1-2), 193–205.
- Iyer, K., Rüpke, L., Galerne, C. Y., 2013. Modeling fluid flow in sedimentary basins with sill intrusions: Implications for hydrothermal venting and climate change. *Geochemistry, Geophysics, Geosystems* 14 (12), 5244–5262.
- Jaquet, Y., Schmalholz, S. M., 2017. Spontaneous ductile crustal shear zone formation by thermal softening and related stress, temperature and strain rate evolution. *Tectonophysics*.
- Jha, B., Juanes, R., 2014. Coupled multiphase flow and poromechanics: A computational model of pore pressure effects on fault slip and earthquake triggering. *Water Resources Research* 50 (5), 3776–3808.
- Joshi, A., Appold, M. S., 2016. Potential of porosity waves for methane transport in the Eugene Island field of the Gulf of Mexico basin. *Marine and Petroleum Geology* 75, 1–13.

- Judd, A., Hovland, M., 2007. *Seabed Fluid Flow*. Cambridge University Press, Cambridge.
- Kameyama, M., Kageyama, A., Sato, T., 2005. Multigrid iterative algorithm using pseudo-compressibility for three-dimensional mantle convection with strongly variable viscosity. *Journal of Computational Physics* 206, 162–181.
- Katz, R. F., Weatherley, S. M., 2012. Consequences of mantle heterogeneity for melt extraction at mid-ocean ridges. *Earth and Planetary Science Letters* 335-336, 226–237.
- Keller, T., Katz, R. F., 2016. The role of volatiles in reactive melt transport in the asthenosphere. *Journal of Petrology* 57 (6), 1073–1108.
- Keller, T., Katz, R. F., Hirschmann, M. M., 2017. Volatiles beneath mid-ocean ridges: Deep melting, channelised transport, focusing, and metasomatism. *Earth and Planetary Science Letters* 464, 55–68.
- Keller, T., May, D. A., Kaus, B. J. P., 2013. Numerical modelling of magma dynamics coupled to tectonic deformation of lithosphere and crust. *Geophysical Journal International* 195 (3), 1406–1442.
- Kim, J., Tchelepi, H., Juanes, R., 2011a. Stability and convergence of sequential methods for coupled flow and geomechanics: Drained and undrained splits. *Computer Methods in Applied Mechanics and Engineering* 200 (23-24), 2094–2116.
- Kim, J., Tchelepi, H., Juanes, R., 2011b. Stability and convergence of sequential methods for coupled flow and geomechanics: Fixed-stress and fixed-strain splits. *Computer Methods in Applied Mechanics and Engineering* 200 (13-16), 1591–1606.
- Kong, X.-Z., Kinzelbach, W., Stauffer, F., 2009. Migration of air channels: An instability of air flow in mobile saturated porous media. *Chemical Engineering Science* 64 (7), 1528–1535.
- Liang, Y., Schiemenz, A., Hesse, M. A., Parmentier, E. M., 2011. Waves, channels, and the preservation of chemical heterogeneities during melt migration in the mantle. *Geophysical Research Letters* 38 (20), 1–5.
- Løseth, H., Wensaas, L., Arntsen, B., Hanken, N.-M., Basire, C., Graue, K., 2011. 1000 m long gas blow-out pipes. *Marine and Petroleum Geology* 28 (5), 1047–1060.
- Mazzini, A., Svensen, H. H., Forsberg, C. F., Linge, H., Lauritzen, S.-E., Haffidason, H., Hammer, Ø., Planke, S., Tjelta, T. I., 2017. A climatic trigger for the giant Troll pockmark field in the northern North Sea. *Earth and Planetary Science Letters* 464 (May), 24–34.
- McCartney, J. S., Sánchez, M., Tomac, I., 2016. Energy geotechnics: Advances in subsurface energy recovery, storage, exchange, and waste management. *Computers and Geotechnics* 75, 244–256.

- McKenzie, D., 1984. The generation and compaction of partially molten rock. *Journal of Petrology* 25 (3), 713–765.
- Miller, S. A., van der Zee, W., Olgaard, D. L., Connolly, J. A. D., 2003. A fluid-pressure feedback model of dehydration reactions: experiments, modelling, and application to subduction zones. *Tectonophysics* 370 (1), 241–251.
- Minkoff, S. E., Stone, C., Bryant, S., Peszynska, M., Wheeler, M. F., 2003. Coupled fluid flow and geomechanical deformation modeling. *Journal of Petroleum Science and Engineering* 38 (1-2), 37–56.
- Ogawa, M., Schubert, G., Zebib, A., 1991. Numerical Simulations Of 3-Dimensional Thermal-Convection In a Fluid with Strongly Temperature-Dependent Viscosity. *Journal of Fluid Mechanics* 233, 299–328.
- Omlin, S., Malvoisin, B., Podladchikov, Y. Y., 2017. Pore Fluid Extraction by Reactive Solitary Waves in 3-D. *Geophysical Research Letters*.
- Patankar, S., 1980. Numerical heat transfer and fluid flow. CRC press.
- Plaza-Faverola, A., Bünz, S., Mienert, J., 2010. Fluid distributions inferred from P-wave velocity and reflection seismic amplitude anomalies beneath the Nyegga pockmark field of the mid-Norwegian margin. *Marine and Petroleum Geology* 27 (1), 46–60.
- Plaza-Faverola, A., Bünz, S., Mienert, J., 2011. Repeated fluid expulsion through sub-seabed chimneys offshore Norway in response to glacial cycles. *Earth and Planetary Science Letters* 305 (3), 297–308.
- Plümper, O., Botan, A., Los, C., Liu, Y., Malthe-Sørenssen, A., Jamtveit, B., 2017a. Fluid-driven metamorphism of the continental crust governed by nanoscale fluid flow. *Nature geoscience* 10 (9), 685.
- Plümper, O., John, T., Podladchikov, Y. Y., Vrijmoed, J. C., Scambelluri, M., 2017b. Fluid escape from subduction zones controlled by channel-forming reactive porosity. *Nature Geoscience* 10 (2), 150–156.
- Ratcliff, J. T., Schubert, G., Zebib, A., 1995. Three-dimensional variable viscosity convection of an infinite Prandtl number Boussinesq fluid in a spherical shell. *Geophysical Research Letters* 22 (16), 2227–2230.
- Reusch, A., Loher, M., Bouffard, D., Moernaut, J., Hellmich, F., Anselmetti, F. S., Bernasconi, S. M., Hilbe, M., Kopf, A., Lilley, M. D., Meinecke, G., Strasser, M., 2015. Giant lacustrine pockmarks with subaqueous groundwater discharge and subsurface sediment mobilization. *Geophysical Research Letters* 42 (9), 3465–3473.

- Rice, J. R., Cleary, M. P., 1976. Some basic stress diffusion solutions for fluid-saturated elastic porous media with compressible constituents. *Reviews of Geophysics* 14 (2), 227–241.
- Rozhko, A. Y., Podladchikov, Y. Y., Renard, F., 2007. Failure patterns caused by localized rise in pore-fluid overpressure and effective strength of rocks. *Geophysical Research Letters* 34 (L22304).
- Rudge, J. F., Bercovici, D., Spiegelman, M., 2011. Disequilibrium melting of a two phase multicomponent mantle. *Geophysical Journal International* 184 (2), 699–718.
- Rutqvist, J., 2011. Status of the TOUGH-FLAC simulator and recent applications related to coupled fluid flow and crustal deformations. *Computers & Geosciences* 37 (6), 739–750.
- Rutqvist, J., 2012. The geomechanics of CO₂ storage in deep sedimentary formations. *Geotechnical and Geological Engineering* 30 (3), 525–551.
- Rutqvist, J., Barr, D., Birkholzer, J. T., Fujisaki, K., Kolditz, O., Liu, Q. S., Fujita, T., Wang, W., Zhang, C. Y., 2009. A comparative simulation study of coupled THM processes and their effect on fractured rock permeability around nuclear waste repositories. *Environmental Geology* 57 (6), 1347–1360.
- Rutqvist, J., Börgesson, L., Chijimatsu, M., Kobayashi, A., Jing, L., Nguyen, T., Noorishad, J., Tsang, C.-F., 2001. Thermohydromechanics of partially saturated geological media: governing equations and formulation of four finite element models. *International Journal of Rock Mechanics and Mining Sciences* 38 (1), 105–127.
- Rutqvist, J., Wu, Y.-S., Tsang, C.-F., Bodvarsson, G., 2002. A modeling approach for analysis of coupled multiphase fluid flow, heat transfer, and deformation in fractured porous rock. *International Journal of Rock Mechanics and Mining Sciences* 39 (4), 429–442.
- Schiemenz, A., Liang, Y., Parmentier, E. M., 2011. A high-order numerical study of reactive dissolution in an upwelling heterogeneous mantle-I. Channelization, channel lithology and channel geometry. *Geophysical Journal International* 186 (2), 641–664.
- Schmalholz, S. M., Duretz, T., 2015. Shear zone and nappe formation by thermal softening, related stress and temperature evolution, and application to the Alps. *Journal of Metamorphic Geology* 33 (8), 887–908.
- Scott, D. R., Stevenson, D. J., 1984. Magma solitons. *Geophysical Research Letters* 11 (11), 1161–1164.
- Settari, A., Walters, D., 2001. Advances in Coupled Geomechanical and Reservoir Modeling With Applications to Reservoir Compaction. *SPE Journal* 6 (3), 14–17.

- Simpson, G., Spiegelman, M., Weinstein, M. I., 2010a. A multiscale model of partial melts: 1. Effective equations. *Journal of Geophysical Research* 115 (B4), B04410.
- Simpson, G., Spiegelman, M., Weinstein, M. I., 2010b. A multiscale model of partial melts: 2. Numerical results. *Journal of Geophysical Research* 115 (B4), B04411.
- Singh, V. P., Cavanagh, A., Hansen, H., Nazarian, B., Iding, M., Ringrose, P. S., 2010. Reservoir Modeling of CO₂ Plume Behavior Calibrated Against Monitoring Data From Sleipner, Norway. In: *SPE Annual Technical Conference and Exhibition*. Society of Petroleum Engineers.
- Skarbek, R. M., Rempel, A. W., 2016. Dehydration-induced porosity waves and episodic tremor and slip. *Geochemistry, Geophysics, Geosystems* 17 (2), 442–469.
- Skempton, A. W., 1954. The Pore-Pressure Coefficients A and B. *Géotechnique* 4 (4), 143–147.
- Sone, H., Zoback, M. D., 2013. Mechanical properties of shale-gas reservoir rocks Part 2: Ductile creep, brittle strength, and their relation to the elastic modulus. *geophysics* 78 (5), D393–D402.
- Sone, H., Zoback, M. D., 2014. Time-dependent deformation of shale gas reservoir rocks and its long-term effect on the in situ state of stress. *International Journal of Rock Mechanics and Mining Sciences* 69, 120–132.
- Stevenson, D. J., Scott, D. R., 1991. Mechanics of Fluid-Rock Systems. *Annual Review of Fluid Mechanics* 23 (1), 305–339.
- Tackley, P. J., 1996. Effects of strongly variable viscosity on three-dimensional compressible convection in planetary mantles. *Journal of Geophysical Research: Solid Earth* 101 (B2), 3311–3332.
- Terzaghi, K., 1923. Die berechnung der durchlässigkeitsziffer des tones aus dem verlauf der hydrodynamischen spannungserscheinungen. *Sitzungsberichte der Akademie der Wissenschaften in Wien, Mathematisch-Naturwissenschaftliche Klasse, Abteilung IIa* 132, 125–138.
- Tsang, C.-f., 1999. Linking thermal, hydrological, and mechanical processes in fractured rocks. *Annual Review of Earth and Planetary Sciences* 27 (1), 359–384.
- Vasilyev, O. V., Podladchikov, Y. Y., Yuen, D. A., 1998. Modeling of compaction driven flow in poro-viscoelastic medium using adaptive wavelet collocation method. *Geophysical Research Letters* 25 (17), 3239–3242.
- Verruijt, A., 1969. Elastic storage of aquifers. *Flow through porous media*, 331–376.

-
- Wiggins, C., Spiegelman, M., 1995. Magma migration and magmatic solitary waves in 3-D. *Geophysical Research Letters* 22 (10), 1289–1292.
- Yang, X. I., Mittal, R., 2014. Acceleration of the Jacobi iterative method by factors exceeding 100 using scheduled relaxation. *Journal of Computational Physics* 274, 695–708.
- Yarushina, V. M., Podladchikov, Y. Y., 2015. (De)compaction of porous viscoelastoplastic media: Model formulation. *Journal of Geophysical Research: Solid Earth* 120 (6), 4146–4170.
- Zhang, K., Moridis, G., Pruess, K., 2011. TOUGH+CO₂: A multiphase fluid-flow simulator for CO₂ geologic sequestration in saline aquifers. *Computers & Geosciences* 37 (6), 714–723.

CHAPTER 2

Spontaneous formation of fluid escape pipes from subsurface reservoirs

Ludovic Räss^{1,2}, Nina S. C. Simon³, and Yury Y. Podladchikov^{1,2}

¹Faculté des géosciences et de l'environnement, Institut des Sciences de la Terre, University of Lausanne,
Lausanne, Switzerland.

²Swiss Geocomputing Centre, University of Lausanne, Lausanne, Switzerland.

³SignificaNS, Oslo, Norway.

Abstract

Ubiquitous observations of channelised fluid flow in the form of pipes or chimney-like features in sedimentary sequences provide strong evidence for significant transient permeability-generation in the subsurface. Understanding the mechanisms and dynamics for spontaneous flow localisation into fluid conductive chimneys is vital for natural fluid migration and anthropogenic fluid and gas operations, and in waste sequestration, yet no model exists that can predict how, when, or where these chimneys form. Here we propose a physical mechanism and show that chimneys form spontaneously through hydro-mechanical coupling between fluid flow solid deformation. By resolving both fluid flow and shear deformation of the matrix in three dimensions, we predict fluid flux and matrix stress distribution over time. The chimneys constitute efficient fluid pathways with permeability enhancement exceeding three orders of magnitude. We find that in essentially impermeable shale (10^{-19} m²), vertical fluid migration rates in the high-permeability chimneys approach rates expected in permeable sandstones (10^{-15} m²). This previously unidentified mechanism for overcoming and destroying assumed impermeable barriers has a profound impact on assessing the evolution of leakage pathways in natural gas emissions, for reliable risk assessment for long-term subsurface waste storage, or CO₂ sequestration.

Fluid and melt extraction from porous rocks occurs at many scales on Earth, from the mantle to the shallow subsurface (Connolly and Podladchikov, 2007; Elger et al., 2018; Ingebritsen and Manning, 2011; John et al., 2012; Koulakov et al., 2013; Marschall and Schumacher, 2012; McGary et al., 2014; Plümper et al., 2017; Sumita et al., 1996; Taetz et al., 2018; Tian et al., 2018). In the shallow subsurface, distinct features are observed (Cartwright and Santamarina, 2015; Judd and Hovland, 2007; Løseth et al., 2008; Mazzini et al., 2017) of vertical chimneys associated with localised continuous or episodic buoyancy-driven fluid flow. These vertical fluid migration pathways are located in most of the studied sedimentary basins. As these regions are of economic interest, they are widely screened with geophysical methods, which provide excellent data that clearly exhibit fluid migration pathways in three dimensions (Petersen et al., 2010). These features are particularly recognisable by their specific signature on seismic cross-sections (Figure 2.1a), while pockmarks and circular-shaped craters (Figure 2.1b) are their related expression on the seafloor (Figure 2.5). These focussed flow pathways provide an important and efficient transport mechanism for fluid migration, yet the physical controls on their formation are not well understood and still debated.

We propose hydro-mechanical coupling as the dominant underlying physical process for the formation of high-permeability pathways, based on the following observations: 1) Vertical

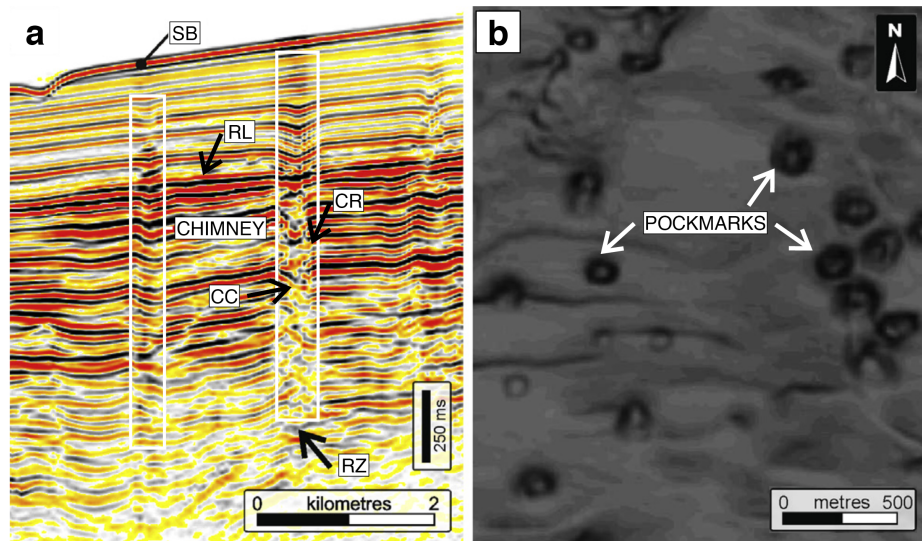


Figure 2.1: Seismic expression of chimneys and pockmarks. Figure modified from Cartwright and colleagues (Cartwright and Santamarina, 2015; Moss and Cartwright, 2010). (a) Vertical seismic profile through fluid migration pathways from offshore Namibia. SB = seabed, RL = reflective horizontal sedimentary layer, CR = chimney downward-bending compacted rim, CC = chimney core, RZ = root zone and diffuse base of the chimney. (b) Horizontal slice through a group of chimneys displaying the typical circular craters or pockmarks.

chimneys occur in various sedimentary basin lithologies (Foschi et al., 2014) and appear unaffected by rock composition, refuting chemical reactions as the main formation mechanism. 2) The vertical chimneys develop through existing formations and are not influenced by sedimentary layering or structural features such as faults (Foschi et al., 2014; Løseth et al., 2008; Moss and Cartwright, 2010). These observations also suggest that they do not form by reactivation of pre-existing structures, but are the outcome of a self-sustaining dynamic process independent of the inherited geological setting. Since chimney formation cannot be inferred from static models nor geological history, there is a need to develop predictive models to resolve their spontaneous formation and to better constrain the parameters that govern their propagation.

We address this issue by considering a poro-visco-elastic model of rock deformation and flow to quantify the process of channelised fluid migration associated with the deformation of permeable rocks (Yarushina and Podladchikov, 2015). We use a continuum mechanics model to compute the porous matrix deformation using a non-linear bulk and shear rheology. Resolving the mechanics is required to calculate the total pressure, strain rates and corresponding stresses, which implies evaluating the entire deviatoric stress tensor. We couple the mechanical solver with a Darcy flow solver and calculate the fluid fluxes using the non-linear Carman-Kozeny relation (Costa, 2006) for dynamic permeability. We streamline a super-computing approach to resolve the coupled fluid-rock interactions in high resolution (Omlin et al., 2017). This hydro-mechanical model permits us to predict high-permeability chimney formation and propagation and the stress distribution in the deforming poro-visco-elastic matrix in three dimensions (Figure 2.2). The fully resolved hydro-mechanical coupling generates and propagates solitary waves (Barcilon and Richter, 1986; Scott, 1988; Scott et al., 1986; Wiggins and Spiegelman, 1995) of porosity within a specific parameter range. A pressure sensitive viscous bulk rheology further triggers a significant flow focussing mechanism, ‘decompaction weakening’ (Connolly and Podladchikov, 2007), at the top of the solitons. The usual spherically shaped solitons (Scott, 1988; Wiggins and Spiegelman, 1995) turn into elongated chimney-shaped features (Omlin et al., 2017) (Figure 2.2).

Solitary waves have been proposed as mechanism for enhanced fluid transport in deep crustal and mantle rocks, as well as for primary hydrocarbon and methane migration from source rocks into sedimentary basins (Appold and Nunn, 2002; Connolly and Podladchikov, 2007; Joshi and Appold, 2016; Scott and Stevenson, 1984; Sumita et al., 1996; Wiggins and Spiegelman, 1995). These deep rock formations are generally considered to exhibit viscous or creep behaviour, in contrast to shallow sedimentary rocks, which are believed to deform in a more elastic and brittle way. However, recent laboratory experiments on major sedimentary reservoir rock types indicate that time-dependent deformation must be considered (Räss et al., 2017; Sone and Zoback, 2014). The clay content of sediments strongly enhances creep and self-sealing capabilities while hindering the propagation of brittle fractures (Omlin et al.,

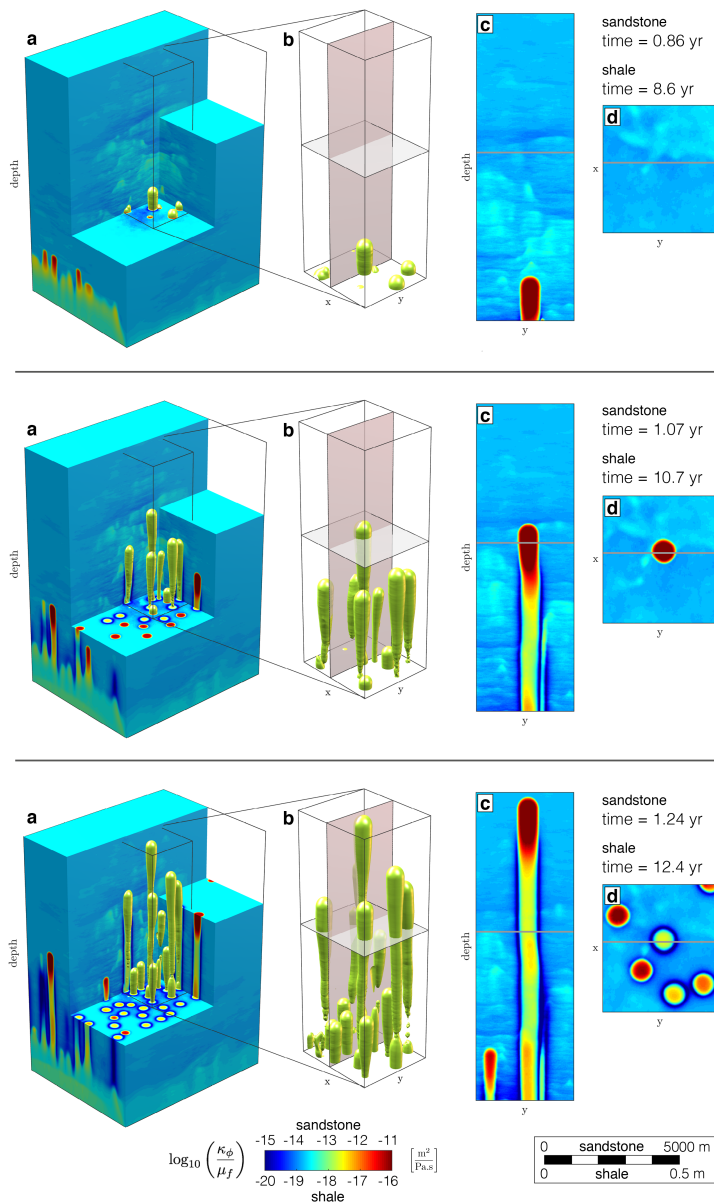


Figure 2.2: High-permeability chimney genesis out of a source region (reservoir) in three dimensions. Colour plot (logarithmic scale) of dynamic permeability (κ_{ϕ} / μ_f) for two different lithologies, conductive sandstone and impermeable shale. Contoured values show a 1.5 order of magnitude increase in κ_{ϕ} / μ_f representative for the chimneys. (a) Insight into the hydro-mechanical model unveiling the existence of high-permeability chimneys as tubular shaped features in three dimensions. (b) Enlargement of the centre of the model, selectively displaying the contoured chimneys. (c) Vertical two-dimensional slice of b) displaying a colour plot of the permeability field of an isolated chimney. (d) Horizontal slice of b) displaying a colour plot of the permeability field, resulting in rounded craters or pockmarks. Effective permeability, time and length scale are given for both permeable sandstones and low-permeability shales (Räss et al., 2017).

2017). Thus, ‘soft’ clay-rich rocks are regarded as natural barriers (Arts et al., 2004; Foschi et al., 2014; Räss et al., 2017) and are recommended as caprock for storage operations. However, although brittle processes are inhibited, a time-dependent creep rheology may lead to localised flow of the sedimentary material in response to applied stress, proportional to bulk viscosity values in the range of $10^{16} - 10^{13}$ Pa.s (Räss et al., 2017, 2014).

2.1 Results

We show the spontaneous development of high-permeability (> 3 orders of magnitude over background values) chimneys from a fluid-enriched source region in three dimensions (Figure 2.2). The buoyant pore-fluid triggers local decompaction of the porous medium and enables upward-migration within self-organised chimneys. This contrasts with Darcian flow models in non-deforming porous media that predict diffusive fluid flow and spreading of fluids. The focussed flow patterns have a tubular shape (Figures 2.2a and 2.2b), which can only be resolved by 3-D models. Both the vertical and horizontal 2-D expression (Figures 2.2c and 2.2d) of the contoured high-permeable regions (Figure 2.2b) reproduce natural seismic chimney (Figure 2.1) and pockmark observations (Figure 2.5). The physical mechanism leading to chimney formation is a natural outcome of time-dependent creep deformation of the fluid-rich porous matrix interacting with the non-linear flow of the pore-fluid. The difference between total pressure and fluid pressure (Figure 2.3c) affects the bulk viscosity distribution (Figure 2.3b) in a non-linear way and leads to a significant permeability increase (Figure 2.3a).

The upward-migration of the highly permeable chimneys is sustained by active fluid drainage from the immediate surrounding regions, leading to localised compaction. The resulting consolidated chimney rim is characterised by decreased permeability and increased viscosity values (Figures 2.3a, 2.3b, 2.3e and 2.3f). We propose that the consolidated rims correspond to the downward-bending horizontal reflectors diagnostic for chimney occurrence in seismic cross-sections (Figure 2.1). The consolidated rim confines pressure deviations (Figure 2.3c) and high fluid fluxes to within the chimney. Thus, pressure measurements outside the chimneys may show no significant perturbations. In contrast to pressure, the localised shear deformation may be detected outside of the chimneys, and the stress envelope runs slightly ahead of the propagating chimney. The second invariant of the deviatoric stress tensor (τ_{II}) quantifies the magnitude of shear deformation recorded by the porous matrix (Figure 2.3d). Variations in stresses may be measurable with seismic methods and their increase in time may further trigger micro-seismic events. The transient fluid expulsion pulse induces irreversible alteration of the permeability and bulk viscosity distributions. These alterations are responsible for the preservation of the dormant features recognisable in the field (Figure 2.5). In contrast, variation in pressure and stresses are restricted to the transient deformation accompanying the fluid pulse.

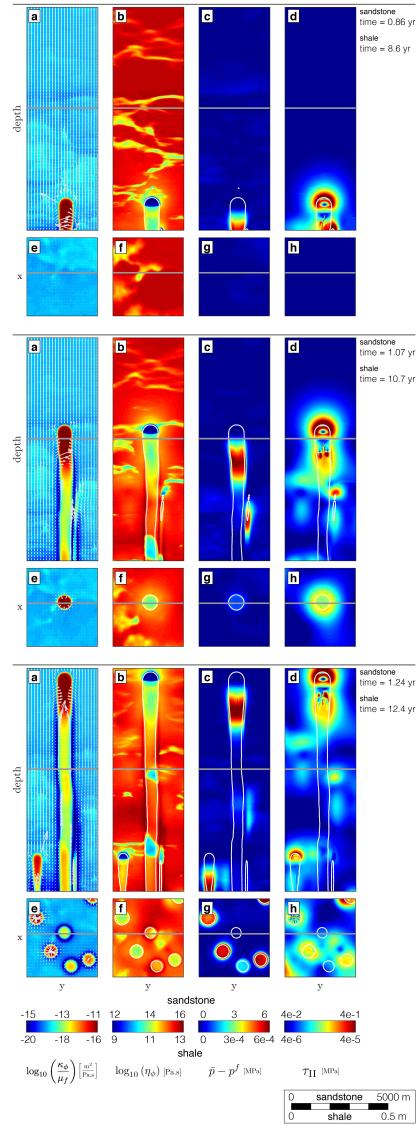


Figure 2.3: Chimney formation mechanism. Three successive time laps of two-dimensional vertical (a to d) and horizontal (e to f) slices from Figure 2.1b. (a) and (e) Dynamic permeability (logarithmic scale) field. The white arrows represent the fluid flux vectors, scaled by the maximal flux over time and directed into the chimney in the local drainage area, showing flux from outside to inside the chimneys. (b) and (f) Strain rate-dependent non-linear bulk viscosity values (logarithmic scale). (c) and (g) Effective pressure ($\bar{p} - p^f$) distribution. (d) and (h) Shear stress deformation magnitude (second invariant of the deviatoric stress tensor). Results are scaled for low-permeable shale ($\kappa_{\text{shale}} = 10^{-19} \text{ m}^2$) and permeable sandstone ($\kappa_{\text{sand}} = 10^{-14} \text{ m}^2$) and display downward-bending compacted chimney rims, permeable chimney cores and circular pockmarks; the characteristic chimney attributes observed in nature. White contour lines (b) to (d) and (f) to (h) represent the chimney extend, characterised by a significant increase (1.5 order of magnitude) in dynamic permeability.

Recording the fluid flux over time at a specific horizontal cross-section of the model confirms the ability of high-permeability chimneys to enhance vertical flow rates (Figure 2.4). Using an initial permeability value of 10^{-19} m^2 , representative of typical clay-rich sealing sequences (Räss et al., 2017), we predict that the formation of high-permeability chimneys leads to maximal flow rates up to 0.1 m/yr (mean flow rates of about 0.01 m/yr) through a 1 m^2 horizontal cross-section of clay-rich shale (Figure 2.4a). Thus, the preferential flow paths (chimneys) within clay-rich rocks enable flow rates of only one order of magnitude below expected diffusive Darcian flow through typical reservoir-quality sandstones with a permeability of 10^{-15} m^2 (Figure 2.4a). Prior to first chimney arrival, vertical fluid flux values are constant over time and reflect the four orders of magnitude discrepancy in background permeability values. At first chimney breakthrough (Figure 2.4b), vertical fluid fluxes in the shale significantly increase and reach their maximal value over an extremely short time (Figure 2.4c). Although the flow rates through the chimneys in the shale horizon decreased during the last year of the simulation (Figure 2.4d), the highly conductive chimneys continuously enable high fluid fluxes at rates three orders of magnitude higher than the background.

2.2 Discussion

Our results show that non-linear hydro-mechanical coupling provides a self-consistent mechanism for rapid and localised fluid expulsion even through a priori impermeable rocks. The chimneys are tubular features generated by transient fluid pulses that exhibit an increased permeability core and a compacted rim, which are preserved in the geological record. They display a characteristic size, spacing and propagation velocity. This stands in contrast to brittle fractures, which are planar features that occur instantaneously. Further, hydro-fractures require high fluid pressure to initiate and remain open, maintaining fluid conductivity. Hydro-fracturing results in a fluid pressure gradient that pushes fluid from the fracture interior into the host rock. Chimneys do not require an over-pressured source region and grow by collecting surrounding fluids into their under-pressured core. This self-sustained fluid collection process results in efficient fluid drainage (the white arrows in Figures 2.3a and 2.3e), and the associated shear deformation generates a characteristic transient stress pattern.

Our results reproduce the natural observations of fluid migration conduits in many different locations (Figures 2.1 and 2.5) and geological settings (Judd and Hovland, 2007; Mazzini et al., 2017; Moss and Cartwright, 2010; Plaza-Faverola et al., 2011; Reusch et al., 2015). Our findings show that the dominant mechanisms responsible of the spontaneous formation of fluid escape pipes in the subsurface are viscous creep of the porous matrix, decompaction weakening, and hydro-mechanical coupling. Numerical simulations predict that the activated creep leads to the rapid formation of chimneys in low-viscosity shales, expected to be natural flow barriers (Foschi et al., 2014; Løseth et al., 2008). Thus, resolving the variations in flow

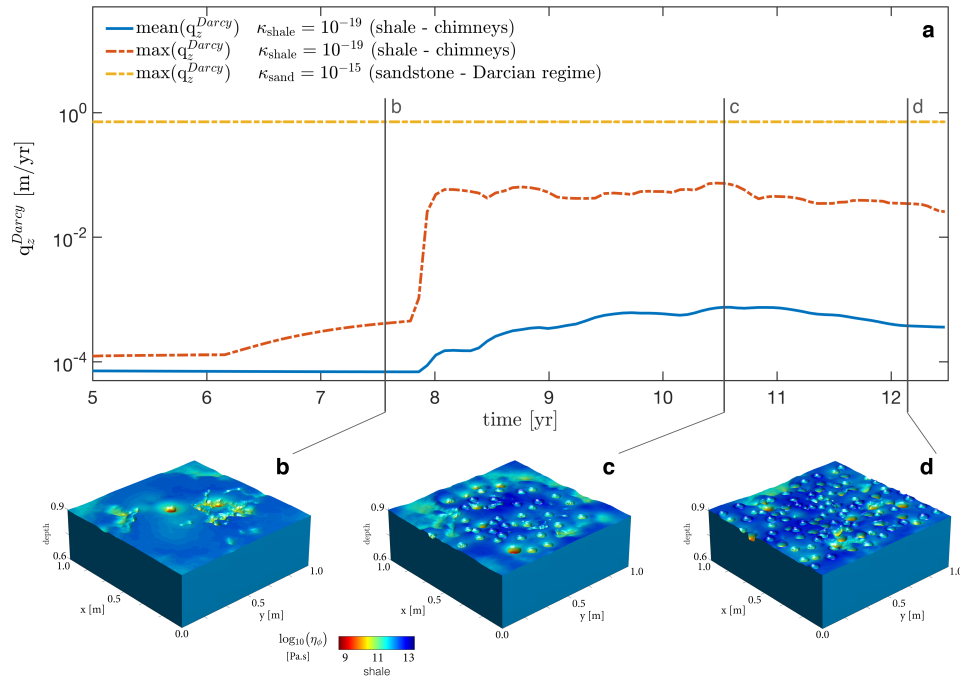


Figure 2.4: Fluid flux through a horizontal slice of 1 m² of low-permeable shale ($\kappa_{\text{shale}} = 10^{-19}$ m²) located at 1 m above the source region showing corresponding typical circular craters or pockmarks. (a) Mean fluid flux ($\text{mean}(q_z^{Darcy})$) and maximal fluid flux ($\text{max}(q_z^{Darcy})$) values in m/yr through the contributing area (1 m²) as a function of time for chimney populated shale. Comparison with fluid flux through 1 m² of four orders of magnitude more permeable sandstone ($\kappa_{\text{sand}} = 10^{-15}$ m²) in pure diffusive Darcian regime without chimneys. Mean and maximal fluid flux values are identical for homogenous permeability distribution in sandstone. (b) to (d) Expression of craters resulting from flow focusing in high-permeability chimneys. Surface and colour plot of bulk viscosity (η_ϕ) reflecting the geological records of contrasting material parameters, by analogy to Figure 2.1b. (b) First chimney break through after 8 years. (c) Vertical flow peak after 10.5 years. (d) Lowered flux and dormant chimneys after 12 years.

patterns, viscous compaction and associated stresses is vital to evaluate storage potential and geological barrier integrity in oil and gas operations (de Waal et al., 2015; Løseth et al., 2008) and waste sequestration (Arts et al., 2004). Our results also suggest chimneys and pockmarks to be the expression of rapid migration of natural gas such as methane out of hydrate-rich sediments (Andreassen et al., 2017; Elger et al., 2018; Mazzini et al., 2017). Understanding the migration mechanism is a prerequisite for accurately constraining these natural greenhouse gas fluxes towards the atmosphere, with major implications for long-term climate modification, the evolution of Earth and for society.

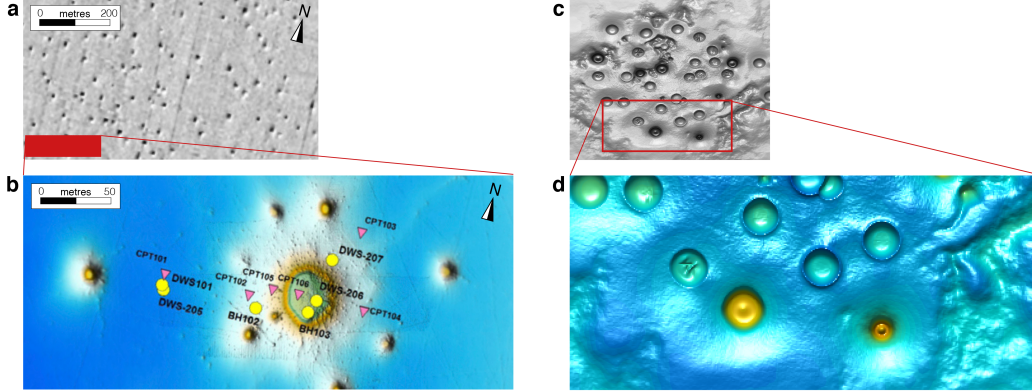


Figure 2.5: Comparison of the numerical results to pockmarks observed on the seafloor. (a) Natural data showing pockmarks on the seafloor in part of the Troll field area, offshore Norway. Figure modified from Mazzini and colleagues (Mazzini et al., 2017). (b) Multibeam line across the red rectangular region from a), displaying high-resolution seafloor mapping of pockmarks. (c) Numerical result from the simulation described in the main text (Figures 2.4b to 2.4d), reoriented to fit the natural data aspect ratios. (d) Magnification of a specific region of the numerical model results (red rectangle) showing crater distribution, size variation and topography.

2.3 Methods

2.3.1 Mathematical model

We utilised a thermodynamically consistent set of two-phase equations coupling non-linear Darcian flow with a mechanical poro-visco-elastic solver (Yarushina and Podladchikov, 2015). We adopted a Carman-Kozeny relation (Costa, 2006) to capture the non-linear porosity-dependent permeability using a power-law exponent of 3. We utilised a viscous bulk and shear rheology for the matrix. The bulk viscosity η_ϕ is inversely proportional to the porosity and reduced by a factor R in the regions of fluid overpressure to account for decompaction weakening (Connolly and Podladchikov, 2007):

$$\eta_\phi = \begin{cases} \eta_C, & \text{if fluid pressure} < \text{total pressure.} \\ \frac{\eta_C}{R}, & \text{if fluid pressure} > \text{total pressure.} \end{cases} \quad (2.1)$$

The bulk shear viscosity μ_s is a non-linear function of the strain rate and tends to a reference value for negligible strain rates.

2.3.2 Numerical implementation

We discretised the system of coupled hydro-mechanical partial differential equations using the Finite Difference Method on a regular Cartesian grid in 3-D. We reached an implicit solution of the stencil-based algorithm using an iterative approach in parallel on graphical processing units (GPUs). We utilised a high-resolution numerical grid of 500 x 500 x 1,000 grid points in x, y and z direction, respectively, required to accurately resolve chimney formation and propagation.

Further technicalities regarding the methods and the numerical implementation are discussed in the Appendix.

Acknowledgments

We thank S. M. Schmalholz, T. Duretz and E. Moulas for discussion and suggestions that improved early versions of the manuscript. We thank S. Miller for suggestions that improved the final version of the manuscript. We thank S. Omlin and P. Logean for long-term collaboration on HPC code and infrastructure development. We acknowledge the University of Lausanne for hosting the octopus supercomputer.

Appendix

2.A Supplementary methods

2.A.1 Hydro-mechanical coupled model formulation

We utilised a set of two-phase equations to model (Yarushina and Podladchikov, 2015) the formation and the evolution of high-porosity chimneys over time as a natural outcome of the coupling of fluid flow to the deformation of a viscous porous matrix. The mass balances for fluid and solid phases, assuming constant fluid and solid densities, were:

$$\begin{aligned} \nabla_k v_k^s &= -\frac{d \log(1 - \phi)}{dt}, \\ \nabla_k \left[\phi \left(v_k^f - v_k^s \right) \right] &= \frac{d \log(1 - \phi)}{dt}, \end{aligned} \tag{2.A.1}$$

where $\frac{d}{dt} = \frac{\partial}{\partial t} + v_k^s \nabla_i$ is the material derivative with respect to the solid. The momentum balance equations for the matrix and the pore-fluid were:

$$\begin{aligned} \nabla_j (\bar{\tau}_{ij} - \bar{p} \delta_{ij}) - \bar{\rho} g_i &= 0, \\ \phi \left(v_i^f - v_i^s \right) + \frac{k_\phi}{\mu^f} \left(\nabla_i p_i^f + \rho^f g_i \right) &= 0, \end{aligned} \tag{2.A.2}$$

where $\bar{\tau}_{ij}$ are the components of the stress deviator, δ_{ij} is the Kronecker delta, g_i are the components of the downward pointing gravity acceleration vector, $\phi (v_i^f - v_i^s)$ is the Darcy flux vector (the relative flux of the fluid relative to the solid), μ^f is the pore fluid viscosity and \bar{p} , p^f are the total and fluid pressures, respectively. The total porosity averaged density:

$$\bar{\rho} = (1 - \phi) \rho^s + \phi \rho^f, \quad (2.A.3)$$

includes constant solid and fluid densities ρ^s and ρ^f , respectively. The Carman-Kozeny relation (Costa, 2006) defines the porosity ϕ dependent permeability k_ϕ :

$$k_\phi = k_0 \left(\frac{\phi}{\phi_0} \right)^3, \quad (2.A.4)$$

where k_0 is the reference permeability and ϕ_0 the reference porosity. The strain rate tensor and non-linear viscous creep rheology are expressed as:

$$\dot{\epsilon}_{ij} = \frac{1}{2} (\nabla_i v_j^s + \nabla_j v_i^s) - \frac{1}{3} \delta_{ij} \nabla_k v_k^s = \frac{1}{2} A \tau_{II}^{n-1} \bar{\tau}_{ij}, \quad (2.A.5)$$

where $\dot{\epsilon}_{ij}$ is the strain rate tensor, δ_{ij} is the Kronecker-delta, $\bar{\tau}_{ij}$ and τ_{II} are the deviatoric stress tensor and the square root of its second invariant, respectively, n is the stress exponent and A is a pre-exponential constant that is equal to the inverse of the solid shear viscosity in the linear viscous case $n = 1$. The system is closed by a final constitutive equation accounting for viscous (de)compaction:

$$\nabla_k v_k^s = - \frac{p_e}{\eta_\phi (1 - \phi)}, \quad (2.A.6)$$

where η_ϕ is the bulk viscosity. The reference bulk compaction viscosity, η_C , at reference porosity ϕ_0 and $\bar{p} \gg p^f$ is:

$$\eta_C = \frac{\mu_s}{C \phi_0}, \quad (2.A.7)$$

where C is the pore geometry dependent coefficient. At other porosity and fluid pressure values, the bulk viscosity η_ϕ is inversely proportional to the porosity and drops with the increase of the effective pressure $p_e = \bar{p} - p^f$ to account for decompaction weakening, parametrised by a hyperbolic tangent function in the numerical implementation:

$$\eta_\phi = \eta_C \frac{\phi_0}{\phi} \left[1 + \frac{1}{2} \left(\frac{1}{R} - 1 \right) \left(1 + \tanh \left[- \frac{p_e}{\lambda_p} \right] \right) \right], \quad (2.A.8)$$

where λ_p is the sharpness of transition zone between the decompacting and compacting regime and R is a rheological constant (Connolly and Podladchikov, 2007) that quantifies the ratio

of compaction (η_C) over decompaction (η_D) bulk viscosity. The effective solid shear viscosity μ_s is a non-linear function of the strain rate and is implemented as:

$$\mu_s = \frac{1}{2A^{\frac{1}{n}} \epsilon_{II}^{\frac{n-1}{n}} + \frac{1}{\mu_0}}, \quad (2.A.9)$$

where ϵ_{II} is the square root of the second invariant of the deviatoric strain rate, n is the power-law exponent (here $n = 3$) and μ_0 the reference viscosity for negligible strain rates.

2.A.2 Simulation details and initial conditions

The hydro-mechanical simulation initial setup consists of a rectangular box with a dimensionless extent of 30 x 30 x 60 in the x, y (horizontal) and z (depth) directions, respectively. The initial porosity follows an anisotropic Gaussian random-field distribution, with a standard deviation equal to 1, and correlation lengths of 5, 5, 1 in the x, y and z directions, respectively. Further, a high-porosity cylindrical ellipse is located at the first 1/4 of the domain height and represents a fluid-rich source region or reservoir. Permeability values within the source region

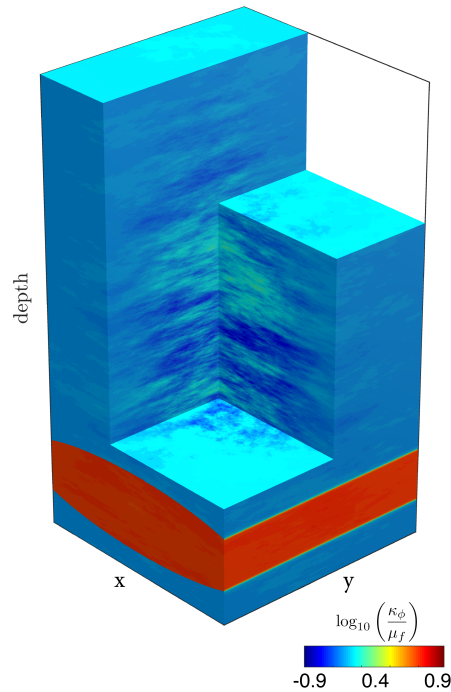


Figure 2.A.1: Initial conditions for the numerical simulation. Permeability distribution is set as an anisotropic Gaussian random field throughout the model. A cylindrical ellipse of close to one order of magnitude higher dynamic permeability values (logarithmic scale) compared to the background dimensionless value of 1 is located at 1/4 from the bottom of the domain. Gravity is acting downwards and the pore fluid is twice as buoyant as the solid matrix.

Description	Symbol	Dimensionless Value
Fluid density	ρ^f	1.0
Solid density	ρ^s	2.0
Gravity acceleration [x, y, z]	g_i	[0, 0, 1]
Background permeability	k_0	1.0
Fluid viscosity	μ^f	1.0
Bulk compaction viscosity	η_C	1.0
Background porosity	ϕ_0	0.01
Background solid shear viscosity	μ_0	1.0
Carman-Kozeny power-law exponent	n^{perm}	3
Compaction/Decompaction bulk viscosity	R	500
Shear viscosity power-law exponent	n	3
Effective pressure transition zone	λ_p	0.01

Table 2.A.1: Dimensionless physical values used in the computation.

were nine times higher compared to normalised background values of 1 (Figure 2.A.1). The computational domain was subjected to the downward-pointing gravity field and affected by a background horizontal strike-slip shear-deformation of similar magnitude than buoyancy forces. The pore-fluid is twice as buoyant as the solid. The mechanical problem was solved using free-slip (no shear stress) boundary conditions on all sides of the box. For the fluid flow problem, we applied no flux boundary conditions on all vertical sides of the box, and fixed flux value at the bottom and top boundaries to satisfy the condition $p_e = 0$ (no compaction or decompaction). A total number of 10,000 time steps was necessary to obtain the results. The dimensionless parameters used in the code (Table 2.A.1) allowed us to optimally converge the numerical simulation.

2.A.3 Solving strategy

We reached an implicit solution of the coupled set of equations using an iterative pseudo-transient relaxation approach. Acceleration of the residual convergence rates was achieved via a problem-specific damping strategy (Cundall, 1982, 1987; Poliakov et al., 1993; Yang and Mittal, 2014). The numerical algorithm was written in C-CUDA and ran on Nvidia GPUs to efficiently process in parallel 0.25 billion grid points. We relied on Message Passing Interface (MPI) libraries to parallelise the application on distributed memory machines and supercomputers. We calculated the presented high-resolution numerical results in a five-day run on 128 GPUs (Nvidia GTX Titan X) in parallel on the octopus supercomputer, in-house

Description	Symbol	Shale	Limestone	Sandstone	Units
Bulk viscosity	η_ϕ	1e13	1e15	1e16	[Pa.s]
Permeability	k_ϕ	1e-19	1e-16	1e-15	[m ²]
Fluid viscosity	μ_f	8e-4	8e-4	8e-4	[Pa.s]
Channel width		0.1 - 1	10 - 100	100 - 500	[m]
Propagation speed		0.3	300	1'000	[m/yr]

Table 2.A.2: Scaling of the numerical results to values for reservoir rocks (Hagin and Zoback, 2004; Räss et al., 2017, 2014).

designed for such high-performance computations, hosted by the Institute of Earth sciences, University of Lausanne, Switzerland.

2.A.4 Scaling relationships

We used three independent scales:

$$\begin{aligned}
 \delta_c &= \sqrt{k_\phi \frac{\eta_C}{\mu^f}}, \\
 p_c &= (\rho^s - \rho^f) g \delta_c, \\
 \tau_c &= \frac{\eta_C}{p_c},
 \end{aligned}
 \tag{2.A.10}$$

and their dependent combinations such the characteristic velocity $v_c = \delta_c / \tau_c$ to normalise all the variables, resulting in a dimensionless form of the governing equations. The characteristic length scale δ_c is also referred to as the compaction length (McKenzie, 1984). τ_c is the characteristic time and p_c is the characteristic pressure or stress (buoyancy force). Using the scaling relations (equations (2.A.10)), the dimensionless model results were scaled to dimensional values representative of reservoir-type rocks: shale, limestone and sandstone. The spacing and the width of the chimneys were mainly controlled by the compaction length δ_c . The effective size and propagation speed of high-permeability chimneys ranged from centimetre-sized to metre-sized features in low-permeable shale to features in the hundreds of metres in permeable sandstones. The propagation speed varied from 30 centimetres per year in shale representative for caprock to 1 kilometre per year in permeable sandstones (Table 2.A.2).

Bibliography

- Andreassen, K., Hubbard, A., Winsborrow, M., Patton, H., Vadakkepuliymbatta, S., Plaza-Faverola, A., Gudlaugsson, E., Serov, P., Deryabin, A., Mattingsdal, R., Mienert, J., Büinz, S., 2017. Massive blow-out craters formed by hydrate-controlled methane expulsion from the Arctic seafloor. *Science* 356 (6341), 948 – 953.
- Appold, M. S., Nunn, J. A., 2002. Numerical models of petroleum migration via buoyancy-driven porosity waves in viscously deformable sediments. *Geofluids* 2 (3), 233–247.
- Arts, R., Eiken, O., Chadwick, A., Zweigel, P., van der Meer, L., Zinszner, B., 2004. Monitoring of CO₂ injected at Sleipner using time-lapse seismic data. *Energy* 29 (9-10), 1383–1392.
- Barcion, V., Richter, F. M., 1986. Nonlinear waves in compacting media. *Journal of Fluid Mechanics* 164 (1), 429.
- Cartwright, J., Santamarina, C., 2015. Seismic characteristics of fluid escape pipes in sedimentary basins: Implications for pipe genesis. *Marine and Petroleum Geology* 65, 126–140.
- Connolly, J. A. D., Podladchikov, Y. Y., 2007. Decompaction weakening and channeling instability in ductile porous media: Implications for asthenospheric melt segregation. *Journal of Geophysical Research* 112 (B10), B10205.
- Costa, A., 2006. Permeability-porosity relationship: A reexamination of the Kozeny-Carman equation based on a fractal pore-space geometry assumption. *Geophysical Research Letters* 33 (2), L02318.
- Cundall, P. A., 1982. Adaptive density-scaling for time-explicit calculations. *Proc. of the 4th Int. Con. on Numerical Methods in Geomechanics, Edmonton, S*, 23–26.
- Cundall, P. A., 1987. Distinct element models of rock and soil structure. *Analytical and Computational Methods in Engineering Rock Mechanics, Allen & Unwin, London*, 129–163.
- de Waal, J. A., Muntendam-Bos, A. G., Roest, J. P. A., 2015. Production induced subsidence and seismicity in the Groningen gas field – can it be managed? *Proceedings of the International Association of Hydrological Sciences* 372, 129–139.
- Elger, J., Berndt, C., Rüpke, L., Krastel, S., Gross, F., Geissler, W. H., 2018. Submarine slope failures due to pipe structure formation. *Nature Communications* 9 (1), 715.
- Foschi, M., Cartwright, J. A., Peel, F. J., 2014. Vertical anomaly clusters: Evidence for vertical gas migration across multilayered sealing sequences. *AAPG Bulletin* 98 (9), 1859–1884.

- Hagin, P. N., Zoback, M. D., 2004. Viscous deformation of unconsolidated reservoir sands Part 1: Time-dependent deformation, frequency dispersion, and attenuation. *geophysics* 69 (3), 731–741.
- Ingebritsen, S. E., Manning, C. E., 2011. Permeability of the Continental Crust: Dynamic Variations Inferred from Seismicity and Metamorphism. *Frontiers in Geofluids*, 193–205.
- John, T., Gussone, N., Podladchikov, Y. Y., Bebout, G. E., Dohmen, R., Halama, R., Klemm, R., Magna, T., Seitz, H.-M., 2012. Volcanic arcs fed by rapid pulsed fluid flow through subducting slabs. *Nature Geoscience* 5 (7), 489–492.
- Joshi, A., Appold, M. S., 2016. Potential of porosity waves for methane transport in the Eugene Island field of the Gulf of Mexico basin. *Marine and Petroleum Geology* 75, 1–13.
- Judd, A., Hovland, M., 2007. *Seabed Fluid Flow*. Cambridge University Press, Cambridge.
- Koulakov, I., West, M., Izbekov, P., 2013. Fluid ascent during the 2004-2005 unrest at Mt. Spurr inferred from seismic tomography. *Geophysical Research Letters* 40 (17), 4579–4582.
- Løseth, H., Gading, M., Wensaas, L., 2008. Hydrocarbon leakage interpreted on seismic data. *Marine and Petroleum Geology* 26 (7), 1304–1319.
- Marschall, H. R., Schumacher, J. C., 2012. Arc magmas sourced from mélange diapirs in subduction zones. *Nature Geoscience* 5 (12), 862–867.
- Mazzini, A., Svensen, H. H., Forsberg, C. F., Linge, H., Lauritzen, S.-E., Haffidason, H., Hammer, Ø., Planke, S., Tjelta, T. I., 2017. A climatic trigger for the giant Troll pockmark field in the northern North Sea. *Earth and Planetary Science Letters* 464 (May), 24–34.
- McGary, R. S., Evans, R. L., Wannamaker, P. E., Elsenbeck, J., Rondenay, S., 2014. Pathway from subducting slab to surface for melt and fluids beneath Mount Rainier. *Nature* 511 (7509), 338–340.
- McKenzie, D., 1984. The generation and compaction of partially molten rock. *Journal of Petrology* 25 (3), 713–765.
- Moss, J. L., Cartwright, J., 2010. 3D seismic expression of km-scale fluid escape pipes from offshore Namibia. *Basin Research* 22 (4), 481–501.
- Omlin, S., Räss, L., Podladchikov, Y. Y., 2017. Simulation of three-dimensional viscoelastic deformation coupled to porous fluid flow. *Tectonophysics*.
- Petersen, C. J., Büinz, S., Hustoft, S., Mienert, J., Klaeschen, D., 2010. High-resolution P-Cable 3D seismic imaging of gas chimney structures in gas hydrated sediments of an Arctic sediment drift. *Marine and Petroleum Geology* 27 (9), 1981–1994.

- Plaza-Faverola, A., Bünz, S., Mienert, J., 2011. Repeated fluid expulsion through sub-seabed chimneys offshore Norway in response to glacial cycles. *Earth and Planetary Science Letters* 305 (3-4), 297–308.
- Plümper, O., John, T., Podladchikov, Y. Y., Vrijmoed, J. C., Scambelluri, M., 2017. Fluid escape from subduction zones controlled by channel-forming reactive porosity. *Nature Geoscience* 10 (2), 150–156.
- Poliakov, A. N. B., Cundall, P. A., Podladchikov, Y. Y., Lyakhovsky, V. A., 1993. An Explicit Inertial Method for the Simulation of Viscoelastic Flow: An Evaluation of Elastic Effects on Diapiric Flow in Two- and Three- Layers Models. Springer Netherlands, Dordrecht, pp. 175–195.
- Räss, L., Makhnenko, R. Y., Podladchikov, Y., Laloui, L., 2017. Quantification of Viscous Creep Influence on Storage Capacity of Caprock. *Energy Procedia* 114, 3237–3246.
- Räss, L., Yarushina, V. M., Simon, N. S. C., Podladchikov, Y. Y., 2014. Chimneys, channels, pathway flow or water conducting features - An explanation from numerical modelling and implications for CO₂ storage. *Energy Procedia* 63, 3761–3774.
- Reusch, A., Loher, M., Bouffard, D., Moernaut, J., Hellmich, F., Anselmetti, F. S., Bernasconi, S. M., Hilbe, M., Kopf, A., Lilley, M. D., Meinecke, G., Strasser, M., 2015. Giant lacustrine pockmarks with subaqueous groundwater discharge and subsurface sediment mobilization. *Geophysical Research Letters* 42 (9), 3465–3473.
- Scott, D. R., 1988. The competition between percolation and circulation in a deformable porous medium. *Journal of Geophysical Research: Solid Earth* 93 (B6), 6451–6462.
- Scott, D. R., Stevenson, D. J., 1984. Magma solitons. *Geophysical Research Letters* 11 (11), 1161–1164.
- Scott, D. R., Stevenson, D. J., Whitehead, J. A., 1986. Observations of solitary waves in a viscously deformable pipe. *Nature* 319, 27.
- Sone, H., Zoback, M. D., 2014. Time-dependent deformation of shale gas reservoir rocks and its long-term effect on the in situ state of stress. *International Journal of Rock Mechanics and Mining Sciences* 69, 120–132.
- Sumita, I., Yoshida, S., Kumazawa, M., Hamano, Y., 1996. A model for sedimentary compaction of a viscous medium and its application to inner-core growth. *Geophysical Journal International* 124 (2), 502–524.
- Taetz, S., John, T., Bröcker, M., Spandler, C., Stracke, A., 2018. Fast intraslab fluid-flow events linked to pulses of high pore fluid pressure at the subducted plate interface. *Earth and Planetary Science Letters* 482, 33–43.

- Tian, M., Ague, J. J., Chu, X., Baxter, E. F., Dragovic, N., Chamberlain, C. P., Rumble, D., 2018. The Potential for Metamorphic Thermal Pulses to Develop During Compaction-Driven Fluid Flow. *Geochemistry, Geophysics, Geosystems*.
- Wiggins, C., Spiegelman, M., 1995. Magma migration and magmatic solitary waves in 3-D. *Geophysical Research Letters* 22 (10), 1289–1292.
- Yang, X. I., Mittal, R., 2014. Acceleration of the Jacobi iterative method by factors exceeding 100 using scheduled relaxation. *Journal of Computational Physics* 274, 695–708.
- Yarushina, V. M., Podladchikov, Y. Y., 2015. (De)compaction of porous viscoelastoplastic media: Model formulation. *Journal of Geophysical Research: Solid Earth* 120 (6), 4146–4170.

CHAPTER 3

M2Di: Concise and efficient MATLAB 2-D Stokes solvers using the
finite-difference method

**Ludovic Räss¹, Thibault Duretz¹, Yury Y. Podladchikov¹, and Stefan M.
Schmalholz¹**

¹Faculté des géosciences et de l'environnement, Institut des Sciences de la Terre, University of Lausanne,
Lausanne, Switzerland.

Abstract

The recent development of many multiphysics modelling tools reflects the currently growing interest in studying coupled processes in the Earth Sciences. The core of such tools should rely on fast and robust mechanical solvers. Here, we provide M2Di, a set of routines for 2-D linear and power law incompressible viscous flow based on finite-difference discretisation. The 2-D codes are written in a concise vectorised MATLAB fashion and can achieve a time-to-solution of 22 seconds for linear viscous flow on 1000^2 grid-points using a standard personal computer. We provide application examples ranging from finely resolved crystal-melt dynamics, deformation of heterogeneous power law viscous fluids, to instantaneous models of mantle flow in cylindrical coordinates. The routines are validated against an analytical solution for linear viscous flow with highly variable viscosity and compared against analytical and numerical solutions of power law viscous folding and necking. In the power law case, both Picard and Newton iterations schemes are implemented. For linear Stokes flow and Picard linearisation, the discretisation results in symmetric positive-definite matrix operators on Cartesian grids with either regular or variable grid-spacing, allowing for an optimised solving procedure. For Newton linearisation, the matrix operator is no longer symmetrical, and an adequate solving procedure is provided. The reported performance of linear and power law Stokes flow is finally analysed in terms of wall-time. All MATLAB codes are provided and can readily be used for both educational and research purposes.

3.1 Introduction

Efficient and concise numerical algorithms are well-suited tools to study physical processes in the Earth Sciences, enhancing clarity and portability without lacking in performance. Such routines can be used to independently explore specific processes, and turn out to be key building blocks that can be employed to further address coupled processes involving multiphysics. These coupled processes are mainly grouped into four major categories, which are referred as thermo-hydro-chemico-mechanical (THCM) processes (e.g. Bea et al., 2015; Rutqvist, 2011; Rutqvist et al., 2006; Weatherley and Katz, 2012). While THC processes can be represented by scalar Poisson equations, mechanical processes involve vectorial and tensorial components, which are more challenging to consider. Thus, we investigate an efficient and accurate method using the finite-difference approach to solve the mechanical problem (M) for linear and non-linear rheologies in 2-D. The proposed framework will be extended in a future step to couple the mechanics to diffusion-like processes (THC) in powerful predictive tools.

With M2Di (Mechanics 2-D iterative), here, we provide a simple yet efficient framework to solve linear and power law viscous Stokes flow with Picard and Newton linearisation. While existing tools can efficiently model these processes in three-dimensions using high-performance computing (Kaus et al., 2016; May et al., 2014), our motivation is to deliver a set of concise and performant routines for research application that may also be used for educational purposes. The M2Di routines allow for simulating 2-D steady state flow at high resolution in a short time on modern personal computers. We focus on finite-difference discretisation using a direct solver strategy on shared memory devices. In contrast to body-fitting finite-element discretisation, finite-difference discretisation have a limited geometrical flexibility (Deubelbeiss and Kaus, 2008; Schmeling et al., 2008). However, it has been shown that finite-difference discretisation is successful for modelling large deformations of heterogeneous materials (Gerya and Yuen, 2003, 2007; Yamato et al., 2012b). High numerical resolution is needed to overcome the discretisation errors of the staggered grid, which is feasible with current hardware. Further, the simplicity of the Cartesian staggered grid discretisation makes it extremely well suited for educational purposes.

Here, we describe MATLAB-based implementations of Stokes solvers on Cartesian grids (regular and variable grid-spacing) and cylindrical staggered grids, with an emphasis on linear and power law viscous constitutive equations. The M2Di algorithms are optimised to take advantage of MATLAB-vectorised operations, Cholesky factorisation for the direct solve (Dabrowski et al., 2008), and Newton iterations for power law viscous flow. The M2Di routines were validated against the analytical solution of Schmid and Podladchikov (2003) for linear viscous flow with sharp viscosity contrast, and against analytic and numerical solutions computed with Folder (Adamuszek et al., 2016). Performance and calculation times are reported us-

ing the wall-time metric. The hardware we used in this study is a MacBook Pro hosting a dual-core Intel Core i7 @ 3.1 GHz processor with 16 GB memory (RAM) and running MATLAB R2016a. The MATLAB codes are available in the supporting information for full reproducibility.

3.2 Methods

3.2.1 The mathematical model

The incompressible Stokes equations in 2-D Cartesian coordinates are:

$$\begin{aligned}\frac{\partial \sigma_{xx}}{\partial x} + \frac{\partial \sigma_{xy}}{\partial y} &= 0, \\ \frac{\partial \sigma_{yx}}{\partial x} + \frac{\partial \sigma_{yy}}{\partial y} &= -\rho g, \\ \frac{\partial v_x}{\partial x} + \frac{\partial v_y}{\partial y} &= 0,\end{aligned}\tag{3.1}$$

where x and y are the spatial coordinates, v_x and v_y correspond to the components of the velocity vector, p is the pressure, ρ is the density and g is the vertical gravity acceleration component. σ_{xx} , σ_{yy} and σ_{xy} are the components of the total stress tensor and are:

$$\begin{aligned}\sigma_{xx} &= -P + 2\eta \frac{\partial v_x}{\partial x}, \\ \sigma_{yy} &= -P + 2\eta \frac{\partial v_y}{\partial y}, \\ \sigma_{xy} &= \eta \left(\frac{\partial v_x}{\partial y} + \frac{\partial v_y}{\partial x} \right),\end{aligned}\tag{3.2}$$

where η represents the dynamic fluid viscosity. A solution of the Stokes problem is achieved on the domain Γ for the given set of boundary conditions:

$$\begin{aligned}v_i &= v_i^{\text{BC}} \text{ on } \Gamma_{\text{Dirichlet}} \\ \sigma_{ij}n_j &= T_i^{\text{BC}} \text{ on } \Gamma_{\text{Neumann}},\end{aligned}\tag{3.3}$$

where n_j is the unit outward normal vector to the domain boundary; v_i^{BC} and T_i^{BC} represent velocity and traction vectors boundary values, applied on corresponding non-overlapping parts of the domain boundary ($\Gamma_{\text{Dirichlet}}$, Γ_{Neumann}). If no pressure boundary condition is supplemented (e.g. free surface), the pressure null space causes the pressure field to be defined up to a constant value.

Linear and power law viscous Stokes flow

Newtonian, or linear viscous, shear rheology is used to describe systems for which the stresses linearly depend on the strain rates, the viscosity being the factor of proportionality. Although the viscosity can be highly variable in space, its values do not depend on the strain rate.

In a power law viscous model, stresses exhibit a non-linear dependence on the magnitude of strain rate. We quantify the strain rate ($\dot{\epsilon}_{II}$) with the square root of the second invariant of the deviatoric strain rate tensor:

$$\dot{\epsilon}_{II} = \sqrt{\frac{1}{2} (\dot{\epsilon}_{xx}^2 + \dot{\epsilon}_{yy}^2) + \dot{\epsilon}_{xy}^2}, \quad (3.4)$$

where $\dot{\epsilon}_{xx} = \frac{\partial v_x}{\partial x}$, $\dot{\epsilon}_{yy} = \frac{\partial v_y}{\partial y}$ and $\dot{\epsilon}_{xy} = \frac{1}{2} \left(\frac{\partial v_x}{\partial y} + \frac{\partial v_y}{\partial x} \right)$ are, respectively, the x and y normal and the shear strain rates. The power law viscous rheological model is of particular interest for geodynamic modelling, since it can be used to model numerous ductile creep mechanisms (e.g. diffusion, dislocation and exponential creep) (see Montési and Zuber, 2002; Schmalholz and Fletcher, 2011). The effective viscosity takes the form of:

$$\eta_{\text{pwl}} = \eta_{\text{ref}} \left(\frac{\dot{\epsilon}_{II}}{\dot{\epsilon}_{\text{ref}}} \right)^{\frac{1}{n}-1}, \quad (3.5)$$

where n and η_{ref} corresponds to the stress exponent and the reference viscosity evaluated for a reference bulk strain rate $\dot{\epsilon}_{\text{ref}}$, respectively. However, the power law model can lead to unrealistically low or large viscosities in the limits of infinite and zero strain rates. Thus, it is convenient to employ constitutive models that allow for power law behaviour over a limited range of strain rate magnitudes.

The Carreau fluid model (Allen, 1999) offers this regularisation type (e.g. Adamuszek et al., 2016) and provides a flow law with the following form:

$$\eta_{\text{Carreau}} = \eta_{\infty} + (\eta_0 - \eta_{\infty}) \left[1 + \left(\xi \frac{\dot{\epsilon}_{II}}{\dot{\epsilon}_{\text{ref}}} \right)^2 \right]^{\frac{1}{2} \left(\frac{1}{n} - 1 \right)}, \quad (3.6)$$

where η_{∞} and η_0 are the values of viscosities for infinite and zero strain rates. The parameter ξ is:

$$\xi = \left(\frac{\eta_{\text{ref}}}{\eta_0 - \eta_{\infty}} \right)^{\frac{1}{n-1}}. \quad (3.7)$$

3.2.2 Numerical Implementation

The system of partial differential equations describing Stokes flow (3.1) and (3.2) can readily be discretised using the finite-difference method on a regular Cartesian staggered grid. The staggered grid relies on second-order conservative finite-differences (Patankar, 1980) and is inherently devoid of oscillatory pressure modes (Shin and Strikwerda, 1997). The pressure null space arising from the absence of boundary conditions on the pressure equation can be circumvented by subtracting the mean value of pressure in a segregated solve (May and Moresi, 2008).

Pressure nodes are defined at cell centres while nodes corresponding to velocity components are defined at cells' mid-faces. Normal and shear components of the strain rate tensor are not collocated and are computed at cell centres and vertices, respectively. As a result, stress evaluations require viscosity to be defined at both cell centres and vertices (Gerya and Yuen, 2003). In the linear viscous case, the stencil corresponding to the discrete X-momentum Stokes equations is the symmetrical Picard linearised operator, composed of 11 entries (Figure 3.1a). In the power law viscous case, viscosity is a function of the magnitude of the strain rate. Thus, it is necessary to evaluate shear strain rate tensor components on cell centres and normal strain rate components on vertices. This can be achieved by either averaging neighbouring strain rate components or averaging the second invariant contributions (Kaus et al., 2016). Both implementations were tested and are referred to as “inv 0” and “inv 1”, respectively. Thus, the corresponding finite-difference stencil requires information from additional neighbouring nodes (Figure 3.1b). As a result, the discrete operator (i.e. stiffness matrix) representing the Newton linearisation of Stokes equations (Jacobian) is denser (19 entries) than its linear viscous counterpart (or Picard linearised operator) and is asymmetrical.

The solving procedure

The solution of finite-difference discretisation of the incompressible Stokes equations for velocity \mathbf{u} and pressure \mathbf{p} as primitive variables can be obtained by solving the following system expressed in defect correction form to conveniently handle linear and non-linear problems (e.g. Spiegelman et al., 2016):

$$\underbrace{\begin{bmatrix} \mathbf{M} & \mathbf{G} \\ -\mathbf{G}^T & \mathbf{0} \end{bmatrix}}_{\mathbf{M}_{\text{Stokes}}} \underbrace{\begin{bmatrix} \delta \mathbf{u} \\ \delta \mathbf{p} \end{bmatrix}}_{\delta \mathbf{x}} = - \underbrace{\begin{bmatrix} \mathbf{f}_u \\ \mathbf{f}_p \end{bmatrix}}_{\mathbf{f}}, \quad (3.8)$$

where \mathbf{M} either stands for the symmetrical positive-definite Picard linearised operator \mathbf{K} or the asymmetrical Jacobian matrix \mathbf{J} (Newton linearisation). $\delta \mathbf{u}$ and $\delta \mathbf{p}$ are the velocity and pressure iterative corrections. The vectors \mathbf{f}_u and \mathbf{f}_p represent the velocity and pressure

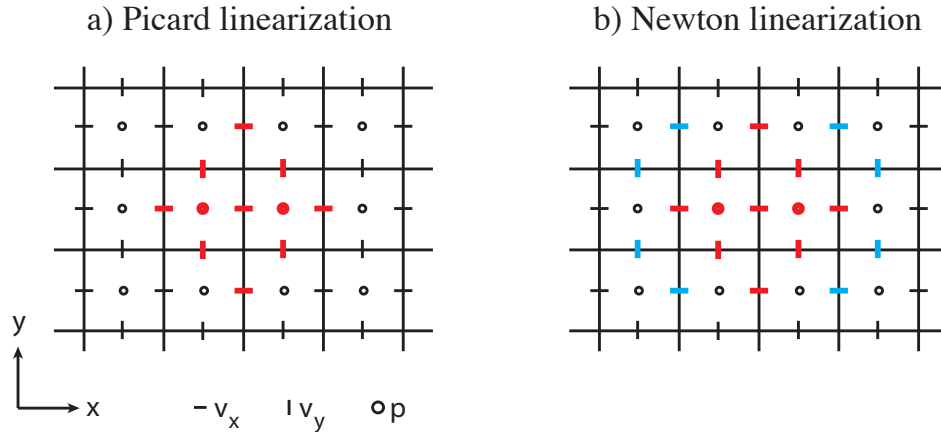


Figure 3.1: Examples of finite-difference stencils used for discretising the X-momentum equation. (a) The standard linear Stokes stencil (Picard linearisation) and (b) the stencil arising from the Newton linearisation of the Stokes equation with power law rheology. The red symbols outline the degrees of freedom involved in the Picard linearisation, and the blue symbols correspond to additional degrees of freedom required for the Newton linearisation (i.e. stencil growth).

residuals, which we seek to minimise. These residuals also include the velocity and pressure force vectors \mathbf{b}_u and \mathbf{b}_p , which contain the contributions of both body forces and boundary conditions (BC). The coefficients of the \mathbf{J} matrix were derived analytically (see the appended Maple script `JacobianStokes.mw`). Notably, the discrete divergence operator is equivalent to minus the transposed gradient operator $-\mathbf{G}^T$ after applying boundary conditions (see section 3.2.2). For the variable grid-spacing case, matrix operators remain symmetrical only if equations are scaled by their corresponding control volume (see Section 3.3.3). For pressure-independent viscous flow laws, the $-\mathbf{G}^T$ and \mathbf{G} blocks are not affected by the choice of linearisation, and symmetry is retained. The global correction vector $\delta\mathbf{x}$ can be obtained via a straightforward direct factorisation of the $\mathbf{M}_{\text{Stokes}}$ matrix. Nonetheless, such an approach is likely not to be optimal, since the $\mathbf{M}_{\text{Stokes}}$ matrix has a missing diagonal for the pressure block. To overcome this, as preconditioner \mathbf{P} , we use a weakly compressible Stokes formulation, adding a numerical bulk modulus γ to the pressure block diagonal, resulting in:

$$\mathbf{P} = \begin{bmatrix} \mathbf{M} & \mathbf{G} \\ -\mathbf{G}^T & \gamma^{-1}\mathbf{I} \end{bmatrix}, \quad (3.9)$$

where the pressure correction $\delta\mathbf{p}$ can be substituted in the momentum equations resulting in the following velocity Schur complement $\tilde{\mathbf{M}} = [\mathbf{M} + \mathbf{G}(\gamma\mathbf{I}\mathbf{G}^T)]$, where $\gamma\mathbf{I} = (\gamma^{-1}\mathbf{I})^{-1}$ is a trivial inverse. Note that the \mathbf{P} matrix is not symmetrical but positive-definite; multiplying the second block row by -1 would make the matrix symmetrical although indefinite. The velocity and pressure corrections can then be iteratively retrieved within Powell-Hestenes

iterations (Cuvelier et al., 1986) by applying the action of $\tilde{\mathbf{M}}^{-1}$, the inverse of the velocity Schur complement to $\tilde{\mathbf{f}}_u$:

$$\delta \mathbf{u} = \tilde{\mathbf{M}}^{-1} \underbrace{[\mathbf{f}_u - \mathbf{G} (\gamma \mathbf{I} \mathbf{f}_p + \delta \mathbf{p})]}_{\tilde{\mathbf{f}}_u}, \quad (3.10)$$

and subsequently computing the pressure corrections:

$$\delta \mathbf{p} = \delta \mathbf{p} + \gamma \mathbf{I} (\mathbf{f}_p + \mathbf{G}^T \delta \mathbf{u}). \quad (3.11)$$

The pressure null space is handled by ensuring that pressure corrections have a zero mean, $\int_{\Omega} \delta p dV = 0$. To ensure incompressibility, the Powell-Hestenes iterations are performed until the amount of flow divergence reaches the tolerance of the linear solver $\max \|\mathbf{G}^T \delta \mathbf{u}\|_{L2} < \text{tol}_{\text{lin}}$. The solution is subsequently updated using the corresponding velocity and pressure corrections. A global overview of the linear solving strategy is detailed in Algorithm (3.1), applying to both Picard and Newton schemes.

Algorithm 3.1 Iterative Powell-Hestenes procedure

```

1:  $\tilde{\mathbf{K}} = \mathbf{K} - \mathbf{G} (\gamma \mathbf{I} \mathbf{G}^T)$  ▷ Construct the Stokes Schur Complement
2: if Newton then
3:    $\tilde{\mathbf{J}} = \mathbf{J} - \mathbf{G} (\gamma \mathbf{I} \mathbf{G}^T)$  ▷ Construct the Jacobian Schur Complement
4: end if
5:  $[\mathbf{Lc}, e, \mathbf{s}] = \text{chol}(\tilde{\mathbf{K}}, 'lower', 'vector')$  ▷ Cholesky factorisation with permutation vector
6:  $\delta \mathbf{p} = 0$ 
7: while ( $\max \|\mathbf{G}^T \delta \mathbf{u}\|_{L2} < \text{tol}_{\text{lin}}$ ) do
8:    $\tilde{\mathbf{f}}_u = \mathbf{f}_u - \mathbf{G} (\gamma \mathbf{I} \mathbf{f}_p + \delta \mathbf{p})$  ▷ Construct the velocity residual Schur Complement
9:   if Picard then
10:      $\delta \mathbf{u}(\mathbf{s}) = \text{cs\_lsolve}(\mathbf{Lc}, \text{cs\_lsolve}(\mathbf{Lc}, \tilde{\mathbf{f}}_u(\mathbf{s})))$  ▷ Computing velocity corrections
11:   else if Newton then
12:      $\delta \mathbf{u}(\mathbf{s}) = \text{kspgcr\_m}(\tilde{\mathbf{J}}, \tilde{\mathbf{f}}_u, \delta \mathbf{u}, \mathbf{Lc}, \mathbf{s}, \dots)$  ▷ Computing velocity corrections
13:   end if
14:    $\delta \mathbf{p} = \delta \mathbf{p} + \gamma \mathbf{I} (\mathbf{f}_p - \mathbf{G}^T \delta \mathbf{u})$  ▷ Computing pressure corrections
15: end while
16:  $[\alpha] = \text{Linesearch}(\mathbf{u}, \delta \mathbf{u}, \dots)$  ▷ Searching for a globalization parameter
17:  $\mathbf{u} = \mathbf{u} + \alpha \delta \mathbf{u}$  ▷ Updating solution
18:  $\mathbf{p} = \mathbf{p} + \alpha \delta \mathbf{p}$ 

```

The iterative Powell-Hestenes workflow (Algorithm 3.1) avoids an expensive direct factorisation of the $\mathbf{M}_{\text{Stokes}}$ by applying the inverse of the Schur complements $\tilde{\mathbf{K}}$ and $\tilde{\mathbf{J}}$. This leads to an efficient solve of the linear system of equations (3.8) in the incompressible limit. Since $\tilde{\mathbf{K}}$ is a symmetrical positive-definite matrix, a Cholesky factorisation can be achieved. Being mainly based on vector-vector operations type, this factorisation optimally exploits

modern CPU capabilities. We employ the CHOLMOD routine, an efficient sparse supernodal Cholesky factorisation package developed by T. Davis (Chen et al., 2008) that relies on highly optimised libraries of BLAS2 operations (multiplication of dense matrices). In MATLAB, it is accessible via the `chol()` function.

Back-substitutions need to be performed iteratively in a different way depending whether the Picard or the Newton scheme is used. For Picard, Dabrowski et al. (2008) proposed an efficient routine using the SuiteSparse `cs_ltsolve` and `cs_lsolve` functions as follows: $\mathbf{u}(\mathbf{s}) = \text{cs_ltsolve}(\mathbf{L}, \text{cs_lsolve}(\mathbf{L}, \mathbf{rhs}(\mathbf{s})))$. A possible alternative without these functions would be to use the Backslash “\” command as following $\mathbf{u}(\mathbf{s}) = \mathbf{L}' \backslash (\mathbf{L} \backslash \mathbf{rhs}(\mathbf{s}))$. The CHOLMOD related and optimised functions are available by installing the entire SuiteSparse package from the developer’s website (<http://faculty.cse.tamu.edu/davis/suitesparse>). For Newton, since $\tilde{\mathbf{J}}$ is not symmetrical and is therefore not a candidate for Cholesky factorisation. We approximate the application of the inverse Jacobian velocity Schur complement via successive Krylov Subspace iterations (generalised conjugate residuals) (Eisenstat et al., 1983) and use the Cholesky factorisation of $\tilde{\mathbf{K}}$ for preconditioning.

In the power law case, the linear solver (Algorithm 3.1) is embedded into a non-linear iteration loop. In this case, \mathbf{f} is the non-linear residual that must be minimised (equation (3.8)), thus specifying the exit condition of the non-linear loop according to $\|\mathbf{f}_u\|_{L2} < \|\mathbf{f}_u\|_{L2}^{\text{initial}} \text{tol}_{\text{nonlin}}$. A line-search algorithm determines the optimal globalisation parameter via direct search after convergence of the linear solver. To do so, non-linear residuals ($\mathbf{f}_u, \mathbf{f}_p$) are explicitly evaluated (matrix-free approach) for n values of $\alpha =]0 ; \alpha_{\text{max}}]$. For Newton linearisation, we set $\alpha_{\text{max}} = 1.0$, while for Picard linearisation, we let $\alpha_{\text{max}} > 1.0$. The value of α that yields to:

$$\min \|\mathbf{f}_u + \alpha \delta \mathbf{x}\|_{L2} \quad (3.12)$$

is retained as the optimal globalisation parameter. In the linear case, a global optimisation parameter equal to 1 is applied and the problem converges in a single non-linear iteration.

Optimised assembly and boundary conditions

In the previous sections, optimised solving strategies were presented, assuming a global system of linear equations for the linear or non-linear Stokes flow. Prior to solve, the subsystems’ matrices must be assembled, and boundary conditions should be applied. Taking full advantage of MATLAB, the assembly of the submatrices should be performed in a vectorised fashion, instead of using loops. Transparency and optimal performance are the major outcomes of this choice. In a first step, the 2-D fields of the stiffness matrix coefficients are saved in submatrices, considering the appropriate staggering. Equation numbering is also implemented following this strategy. In a second step, these fields are saved in a sparse triplet

vector format using MATLAB's `sparse()` function or a more efficient `sparse2()` function if the SuiteSparse package is installed.

In the solver, both Dirichlet and Neumann type BC are implemented for nodes that either conform or don't conform to the domain boundaries. For conforming Dirichlet BC (fixed normal velocity), scaled BC values are injected into the right-hand-side vector, while corresponding lines of the stiffness matrix are cancelled and diagonal values are set to the appropriate scaling factor. All related matrix coefficients connecting to these nodes are multiplied by corresponding Dirichlet BC values and are subtracted from the right-hand-side prior to cancellation. For non-conforming Dirichlets BC, a modified stencil accounting for fixed tangential velocity (ghost node approach) is assembled. These constraints induce modifications of both the diagonal of the stiffness matrix and the corresponding entry of the right-hand-side vector. Similarly, conforming Neumann type BC are constructed in order to impose fixed tangential stresses. Such assembly maintains a symmetrical and positive-definite stiffness matrix, making it a good candidate for Cholesky factorisation.

3.3 The results

3.3.1 The validation of the linear Stokes flow solver

The linear Stokes flow solver can be validated by performing a grid convergence analysis. To this end, we evaluate the magnitude of velocity and pressure truncation errors ($e_{\mathbf{u}}, e_{\mathbf{p}}$) for decreasing spatial discretisation steps h . In practice, a truncations error is calculated by subtracting numerically calculated solution fields from analytically calculated solutions ($\mathbf{u}_{\text{analytic}}, \mathbf{p}_{\text{analytic}}$). We characterise the magnitude of truncation errors by their L_1 norms:

$$\begin{aligned} e_{\mathbf{u}} &= \|\mathbf{u}_{\text{analytic}} - \mathbf{u}\|_1, \\ e_{\mathbf{p}} &= \|\mathbf{p}_{\text{analytic}} - \mathbf{p}\|_1. \end{aligned} \tag{3.13}$$

The analytical solution of Schmid and Podladchikov (2003) provides full 2-D flow and pressure fields for incompressible Stokes flow, incorporating a viscous circular inclusion subjected to background shear. Confronting our numerical solution to this analytical solution is particularly challenging, since Cartesian grids cannot conform to the circular geometry of inclusions. Nonetheless, numerical solutions for velocity and pressure exhibit first-order spatial accuracy. In other words, truncation error magnitudes decrease by a factor of k as the grid-spacing is reduced by the same factor (Figure 3.2). These results are in agreement with previous studies (e.g. Duretz et al., 2011) that reported first-order spatial accuracy of the staggered grid for similar model configurations.

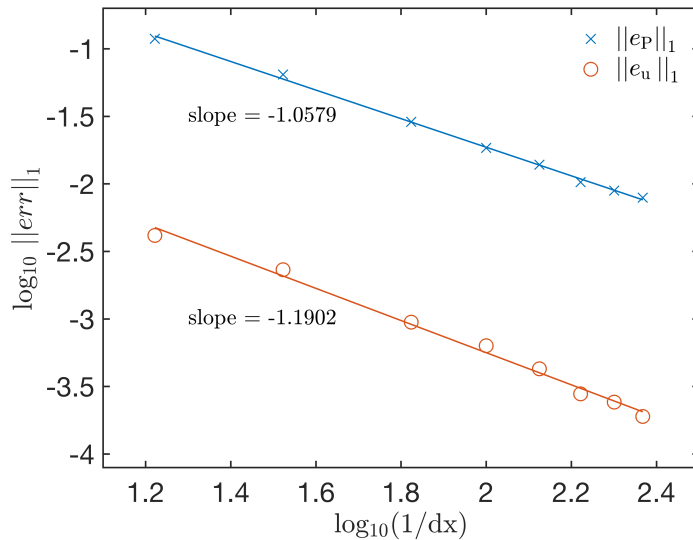


Figure 3.2: Evolution of velocity and pressure truncation errors (L1-norm) upon mesh refinement. The finite-difference scheme is first-order accurate in space for both velocity and pressure. The symbols correspond to numerical runs, and the lines correspond to linear interpolants. We set the domain size to $[-3, 3] \times [-3, 3]$, the inclusion radius to 1, the matrix viscosity to 1, and the inclusion viscosity to 10^4 . Boundary conditions for the analytical solution were set to far-field pure-shear. For the numerical solution, we use full Dirichlet boundary conditions where normal and tangential velocity components were analytically evaluated. These results can be reproduced using the appended script M2Di_Dani.m.

3.3.2 The validation of the power law Stokes flow solver

To validate the power law Stokes solver, we calculate numerical growth rates for folding and necking instabilities and compared them to reference solutions. We use the Folder software (Adamuszek et al., 2016) to compute both a reference numerical solution (body-fitted finite-element method) as well as analytical solutions (thick plate finite matrix thickness). For both folding and necking, model configurations consist of a layer embedded in a matrix subjected to either compression or stretching. To initiate mechanical instabilities, the position of layer/matrix interface requires a geometrical perturbation (sinusoidal). As in Section (3.3.1), this test is challenging when making use of regularly spaced Cartesian grids, because the amplitude of the perturbation must be resolved over several nodal points in order to influence the flow field. Subsequently successful finite-difference solutions require a large number of nodal points in both spatial dimensions (see Figure 3.3 caption). As an alternative, variable grid-spacing or arbitrary mesh refinement (i.e. Gerya et al. (2013)) could be used to achieve relatively finer resolution along material interfaces. For simplicity, we do not introduce this additional complexity level at this point. We have carried out simulations for the folding of a linear viscous layer (Figure 3.3a), power law viscous layer (Figure 3.3b), and necking of a power law viscous layer (Figure 3.3c) in a linear viscous matrix. Growth rates were measured

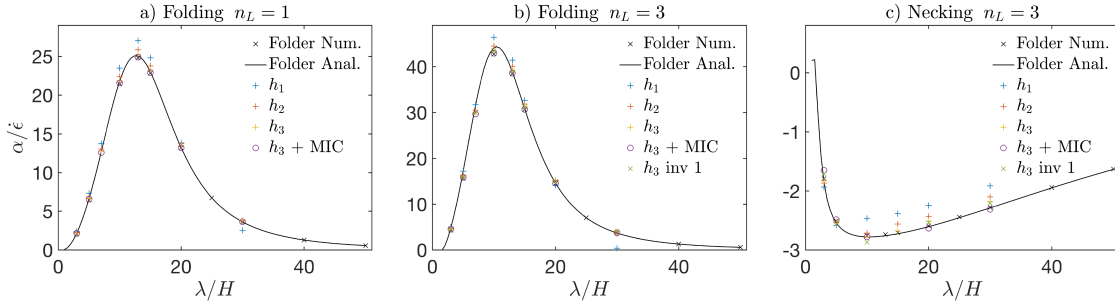


Figure 3.3: Numerically calculated growth rates $\alpha/\dot{\epsilon}$ for various mechanical instability types: (a) linear viscous folding, (b) power law viscous folding, and (c) power law viscous necking. The results are compared to those obtained with the Folder toolbox (Adamuszek et al., 2016) (black dot and line). The domain dimensions were set to $[-\lambda/2, \lambda/2] \times [-3, 3]$, where λ corresponds to the wavelength of the sinusoidal perturbation. The layer thickness $H = 1$, the amplitude of the perturbation is set to 0.0500, and the reference viscosity contrast is 200. Growth rates were calculated using three different grid resolutions, and vertical and horizontal grid-spacings were kept equal ($h_1 = 0.0500$, $h_2 = 0.0250$, $h_3 = 0.0125$). The highest resolution benchmark run, h_3 , was also performed using a marker-in-cell (MIC) viscosity interpolation at the material interface and using the “inv 1” invariant formulation. The appended scripts can be used to reproduce these results (M2Di_Newton_Folding.m and M2Di_Newton_Necking.m).

for different wavelengths and using three different grid-spacings ($h_1 > h_2 > h_3$) and “inv 0” invariant formulation. For all tests, overall grid convergence is observed as numerical solutions tend to benchmark solutions with decreasing grid-spacing. We have also run simulations that account for marker-in-cell type viscosity evaluation (volume-average arithmetic interpolation) and the finest grid spacing h_3 . Such an approach introduces sensitivity at the subgrid level and manages to better reproduce the benchmark growth rate solutions at lower resolutions. Growth rate calculation on the finest level (h_3) was also run with the “inv 1” second strain rate invariant formulation. The resulting growth rates show very little dependence on the type of invariant formulation. However, the “inv 1” formulation requires fewer Newton iterations to converge.

3.3.3 The algorithms’ performance

Overall performance

In this study, we propose an efficient approach using the efficient sparse Cholesky factorisation to solve 2-D Stokes flow in the minimal amount of time on MATLAB, focussing on ease-of-use rather than on ultimate performance. Thus, to estimate the performance of our routines, we performed the related timings on a MacBook Pro laptop running OS X 10.11 equipped with 16 GB of memory (RAM) and a dual-core Intel Core i7 processor @ 3.1 GHz. MATLAB R2016a with SuiteSparse V4.5.3 were installed. We use the wall-time reported in Figure 3.4, or

overall time-to-solution, as performance indicator. Two reasons motivate this choice. First, since MATLAB is an interpreted language, it is fairly complicated to determine the exact memory usage, or the accurate number of flops involved for the entire workflow. Second, the end-user is mainly interested in the approximate time-to-solution, rather than in a complex metric that would depend on hardware technicalities beyond the scope of this technical brief.

The linear solver's performance

The performance of our linear Stokes flow solver is reported in Figure 3.4a. The model configuration is identical to that used for the linear solver validation (section 3.3.1), featuring a circular inclusion located in the centre of a square domain under pure-shear with background strain rate value set to 1. Viscosity values for the inclusion and the matrix are 10^4 and 1, respectively. The square domain has a size of 6×6 , and the radius of the inclusion is 1. The straightforward solve, a direct factorisation of the stiffness matrix (dashed bars) using the UMFPACK solver, could be sustained up to 1.92 MDoF, which represents a 2-D domain of 800^2 grid-points. The 16 GB of available RAM were then saturated, while the time-to-solution seriously deviates from any linear trend. Moving towards an optimised solving strategy involving a sparse Cholesky factorisation and Powell-Hestenes iterations (plain bars), both the time-to-solution and the maximal problem size could be greatly improved. A solution of 5.88 MDoF, representing a 2-D domain size of 1400^2 grid-points could fit in the 16 GB of RAM, while the dependence of the solving time on the resolution is weakly non-linear.

Since the straightforward implementation gave unsatisfactory and fairly limiting results, we will highlight some key parts of the successful optimisations. A closer look at the wall-time reveals a linear scaling for the vectorised matrix assembly as well as back-substitutions, the scaling of the Cholesky factorisation is close to linear. This behaviour type was also reported by Dabrowski et al. (2008). We reach MATLAB limits in term of efficiency with a vectorised assembly and the usage of SuiteSparse optimised `sparse2()`, `cs_ltsolve()`, and `cs_lsolve` functions. Thus, the only computationally expensive part of the optimised solving procedure should reduce to the Cholesky factorisation. In terms of memory requirement, the Cholesky approach performs fairly well, since only the lower part of the stiffness matrix must be assembled, factorised and stored, reducing the demand on the RAM by a factor close to 2. Finally, the efforts of using a symmetrical and positive-definite stiffness matrix appropriate for a Cholesky solver type with iterative back-substitutions, resulting in faster solving times for a 1400^2 (72 s) vs. a 600^2 (84 s) grid-points domain for the straightforward approach.

As a general remark, the reported timing demonstrates that the iterative penalty (Powell-Hestenes) approach combined with the use of Cholesky factorisation (restricted to symmetrical and positive-definite matrices) is a powerful approach and further confirms the trend observed by Dabrowski et al. (2008).

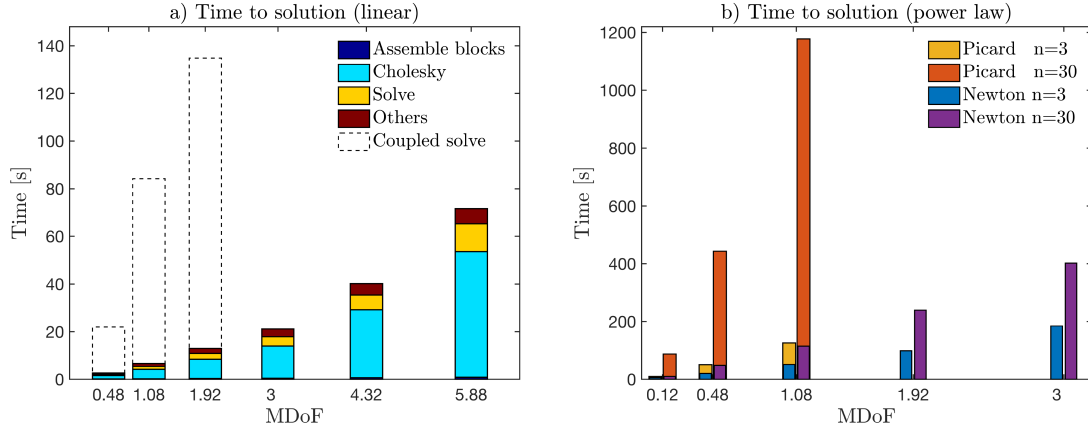


Figure 3.4: Times-to-solution in seconds for (a) the linear Stokes solver and (b) the power law Stokes solver for both Picard and Newton operators as a function of millions of degrees of freedom (MDoF), computed for the 2-D setup as $n_x \times n_y \times 3 \times 10^{-6}$). In Figure 3.4a, the wall-time of the optimised solve (plain bars) is compared to the wall-time of a coupled solve (dashed bars). The optimised solve is detailed in four parts and consists of a vectorised block assembly (Assemble blocks), a Cholesky factorisation, iterative Powell-Hestenes back-substitutions using the SuiteSparse functions (Solve) and some other required operations. The post-processing is excluded from the reported timings. The coupled solve is performed using MATLAB’s backslash (calling UMFPACK) for the direct solve. In Figure 3.4b, the wall-times for non-linear power law exponents $n = 3$ and $n = 30$ are shown as a function of MDoF. The setup used in both Figure 3.4a and Figure 3.4b cases is a cylindrical inclusion of high viscosity located in the centre of a square domain under simple shear with a background strain rate value set to 1. In Figure 3.4a, the viscosity of the matrix and of the inclusion is 1 and 10^4 , respectively. In Figure 3.4b, the matrix has a reference viscosity of 1 and a power law exponent of n , the minimum and maximum viscosities were set to 10^{-6} and 10^3 , respectively. The viscosity of the inclusion was set to 10^3 .

The power law solver’s performance

The performance of both the Picard and the Newton non-linear solver is reported in Figure 3.4b for two different values of the power law exponent n (see Section 3.2.1) per reported DoF. The model configuration is identical to that used for the linear solver performance (section 3.3.3) evaluation. A background strain rate of 1 is applied, and the reference matrix viscosity is set to 1. The minimum and maximum viscosity values for the Carreau model were set to $\eta_\infty = 10^{-6}\eta_{\text{ref}}$ and $\eta_0 = 10^3\eta_{\text{ref}}$, respectively (see Section 3.2.1). Introducing a non-linear rheology impacts on the solving time, since now several linear solves must be performed in the non-linear iteration loop, until the non-linear residual tolerance $\text{tol}_{\text{nonlin}}$ is reached. The wall-time increases owing to this requirement. The performance of the direct factorisation approach, or coupled solve, is not reported for the non-linear case, since it shows an order of magnitude lower performance compared to the optimised solving strategies, and only up to 400^2 grid-points could be resolved with the available 16 GB of RAM.

For the Newton linearisation, the stencil gets additional DoFs (Figure 3.1b), thus reducing the global domain size that can reside in memory. The Newton linearisation is less sensitive to the increase in non-linearity. Moving from $n = 3$ to $n = 30$, the time-to-solution increased by an approximately constant factor 3 for the five tested grid resolutions (ranging from 0.12 to 3 MDoF). This is mainly due to the superlinear scaling of the Cholesky factorisation together with a slight increase in the number of Newton steps to converge the non-linear residual.

The Picard linearisation has a reduced stencil (Figure 3.1a) and therefore uses less memory for a similar domain size than the Newton linearisation. Nonetheless, the main limitation of the linearised Picard non-linear solver resides in its sensitivity to the problem’s non-linearity. Even if every linear solve is performed faster than in the Newton case, their number tends to drastically increase with increase in the non-linear exponent n . In highly non-linear setups, the non-linear iteration ratio between Picard and Newton solver type reaches factors in the range of 200:10. While the Newton solver is a powerful tool, it is more sensible regarding the tuning parameters and may fail to converge in some cases, while the Picard non-linear solver, although requiring a growing number of iterations with increasing non-linearity, will not. Notably, in the provided Newton routines, the user has the possibility to perform a number of Picard steps before switching to Newton iterations.

3.4 Examples of instantaneous flow field calculations

To demonstrate the flexibility of the Stokes solvers described above, we provide four examples of flow field calculations that are relevant for different geodynamics problem types and that highlight several technical aspects described above.

3.4.1 Direct numerical simulations of crystal-melt dynamics

The dynamics of systems consisting of multiple material phases of distinct rheologies and densities can be studied using direct numerical simulations. Magmatic suspensions and crystal mushes are often considered as laminar fluids (Glazner, 2014) and processes such as phase separation, mixing and segregation can to some extent be investigated using Stokes flow models (Suckale et al., 2012; Yamato et al., 2015, 2012a). However, numerical models require high resolution in order to render the hydrodynamic interactions between crystals and the net effect of the crystalline load on the overall flow. We provide a high-resolution instantaneous flow model of crystal settling under gravity using the Stokes flow solver described above (Section 3.2.1). Three populations of prismatic crystals characterised by various dimensions, aspect ratios and densities were distributed quasi-randomly across the model domain. The crystals are considered to be highly viscous inclusions and are therefore characterised by regions of low strain rate (Figure 3.5a–3.5c). In contrast, the interstitial liquid accommodates

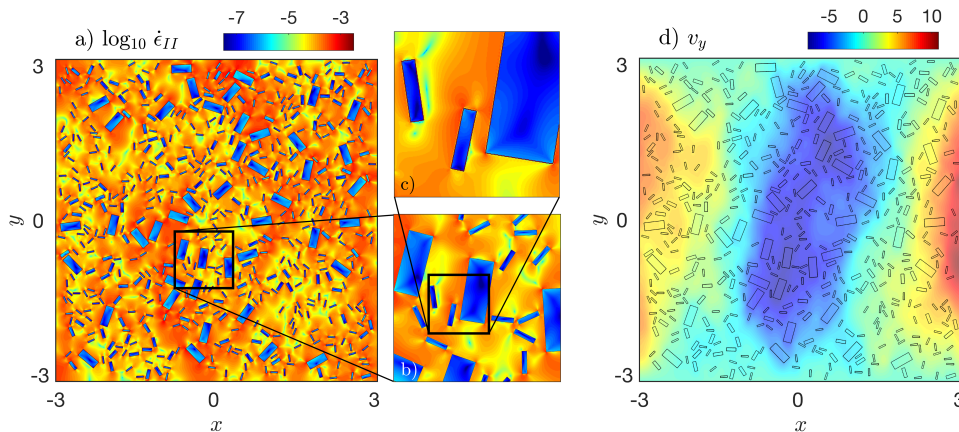


Figure 3.5: High resolution (5000^2 cells) instantaneous model of crystal/melt settling using a random crystal distribution. (a) The strain rate over the entire model domain (dimensionless). (b) and (c) different figure enlargements and the black frames correspond to the respective areas. (d) The vertical velocity component (dimensionless), each individual crystal is outlined by a black contour line. The crystals have different aspect ratios (2.5:1, 3:1, 3:1) and densities (1.350, 1.3750, 1.400). The fluid has a density of 1.3 and a viscosity of 1. The viscosity ratio between the crystals and the fluid is set to 10^3 and the gravity is set to -1 . The crystal fraction reaches 18%. A 500^2 resolution example is provided by the appended script M2Di_crystals.m.

the strain induced by the sinking of the denser crystals and thus exhibits a large strain rate (Figures 3.5a to 3.5c). The fraction of crystals is larger in the centre of the domain than towards the domain's lateral sides. Thus, the effective density is greater in the centre of the domain, which induces a convection flow pattern (Figures 3.5a and 3.5d). Here, we observe that crystals have a collective sinking behaviour (e.g. Hernandez-Ortiz et al., 2005) in the centre of the domain in response to hydrodynamic interactions (i.e. viscous drag).

3.4.2 Pressure variations around viscous inclusions

The prediction of pressure and flow field variations around viscous inclusions has numerous geological implications (Moulas et al., 2014; Schmid and Podladchikov, 2003). For an isolated inclusion, the quality of the numerical solution can be improved by increasing the grid resolution close to the material boundary (e.g. Gerya et al., 2013). Here, we present numerical models of a single inclusion embedded in constant viscosity matrix subjected to far-field pure-shear (see Section 3.3.1) and show the benefits of using variable grid-spacing. Pressure fields were computed using numerical resolutions of 500^2 cells using regular (Figure 3.6a) and variable grid-spacings (Figure 3.6b). Variable grid-spacing drastically improves the quality of the pressure field at the inclusion/matrix interface, which is known to be oscillatory for staggered grids (Deubelbeiss et al., 2011) in the absence of a specific material jump treatment (e.g. the ghost fluid method) Suckale et al. (2010). Further, we could show a better reduc-

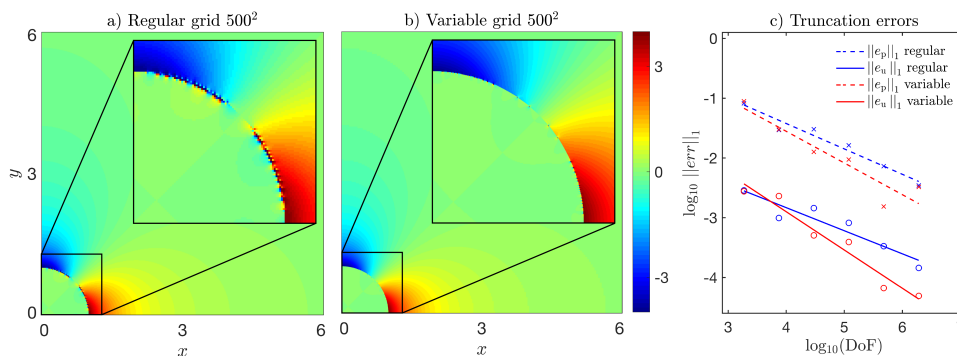


Figure 3.6: (a) And (b) computed pressure fields for a single viscous inclusion embedded in constant viscosity matrix using a resolution of 500^2 nodes. The domain dimensions are set to $[0, 6] \times [0, 6]$, the inclusion radius to 1, the matrix viscosity to 1, and the inclusion viscosity to 10^4 . (a) Solution obtained with regular grid-spacing. (b) Solution computed with variable grid-spacing in x and y dimensions and refined in the vicinity of the inclusion. (c) Evolution of pressure and velocity truncation errors (L1-norm) as a function of the number of degrees of freedom (DoF). The results can be reproduced using the appended script `M2Di_Linear_varxdy.m`.

tion of pressure and velocity truncation errors upon mesh refinement when using variable grid-spacing (Figure 3.6c).

3.4.3 The deformation of heterogenous power law viscous materials

Rocks often consist of different mineral phases and are therefore heterogeneous. If heterogeneities provide a strength contrast, they can act as stress concentrators. Experimentally derived flow laws characterising the rheology of single mineral phases often exhibit a power law behaviour. Modelling the deformation of heterogenous power law viscous materials allows one to unravel the dynamics of shear localisation and the formation of rock fabrics (Dabrowski et al., 2012; Deubelbeiss et al., 2011; Jessell et al., 2009; Le Pourhiet et al., 2013; Mancktelow, 2002). We have set up a power law model consisting in randomly located highly viscous elliptical inclusions. The viscosity of the inclusions is constant, and the matrix rheology follows a Carreau model (Section 3.2.1). Horizontal pure-shear compression is applied at the boundaries of the domain, and gravity is deactivated (see Figure 3.7 caption for model parameters). The model depicts the establishment of heterogeneous shear zone patterns in the vicinity of the inclusions. Areas of reduced viscosity (Figure 3.7a) develop in the regions of increased strain rate (Figure 3.7b). The shear zones develop at an angle of 45° to the compression direction, and are locally intensified by the proximity and orientation of the inclusions. Both second strain rate invariant formulations (“inv 0” and “inv 1”) (see Section 3.2.2) were tested. While computed non-linear viscosities and strain rate patterns do not differ significantly, the number of non-linear iterations needed to converge is greatly reduced using “inv 1” formulation (18 for “inv 1”, 36 for “inv 0”) (Figure 3.7c).

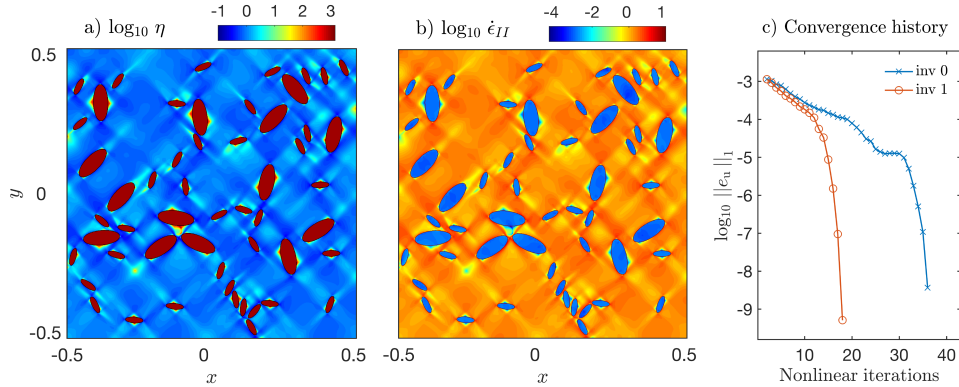


Figure 3.7: Horizontal compression of a material composed of randomly located highly viscous elliptical inclusions in a power law matrix (resolution 1000^2 cells). The non-linear solver ran until it reaches a relative residual of 10^{-8} . (a) The resulting effective viscosity (dimensionless) and (b) the corresponding strain rate (dimensionless). The matrix has a reference viscosity of 1 and a power law exponent of 10, the minimum and maximum viscosities were set to 10^{-3} and 10^3 , respectively. The viscosity of the inclusions was set to 10^3 . The background strain rate is set to 1. The non-linear solver (using the Newton linearisation) converged to relative $\text{tol}_{\text{nonlin}} < 10^{-8}$ in 18 iterations. (c) shows the \log_{10} of the corresponding convergence history for the two different definitions of the second strain rate invariant $\dot{\epsilon}_{II}$ as a function of non-linear iteration count. inv 0 refers to a linear interpolation of the missing strain rate components while inv 1 refers to a linear interpolation of the second invariant contributions.

3.4.4 Mantle flow and dynamic topography

Instantaneous flow models are a powerful tool for improving our knowledge of the viscosity and density structure of the Earth’s mantle (e.g. Billen et al. (2003), G erault et al. (2015)). At this scale, it is convenient to solve the flow problem in cylindrical coordinates. This framework allows one to account for the non-negligible role of the Earth’s curvature (Jarvis, 1993), for instance in slab-mantle interaction (Morra et al., 2009). The Stokes equations (equation (3.1)) can be formulated in cylindrical coordinates in a form suitable for staggered grid discretisation (Appendix A). Since the corresponding discrete operator conserves the properties of the Cartesian discretisation (symmetrical positive-definite), similar linear flow solvers can be used efficiently (see Section 3.2.1). To demonstrate our approach’s flexibility, we have designed an instantaneous mantle flow model in cylindrical coordinates using linear (constant) viscosity (Figure 3.8). The model configuration incorporates a 120 km thick plate, a detached negatively buoyant slab, and a non-smooth radial viscosity structure. Here, viscous drag exerted by the sinking detached slab induces longitudinal plate motion ($v_\theta \approx 5$ cm/yr, Figure 3.8a) and positive-dynamic topography ($h_d \approx 150$ m, Figure 3.8b). This model illustrates the role of the slab suction force in inducing plate motions well (Conrad and Lithgow-Bertelloni, 2002).

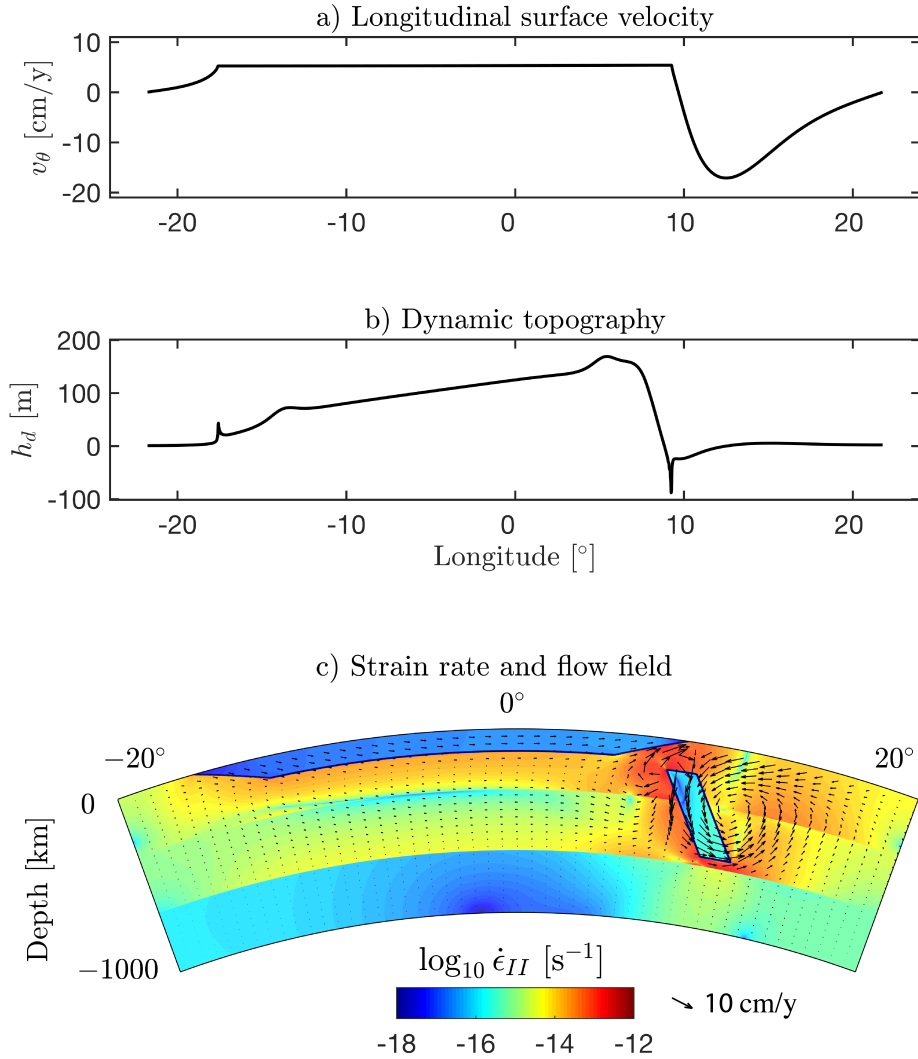


Figure 3.8: Instantaneous model of mantle flow induced by the sinking of a detached slab in cylindrical coordinates (Resolution 1000×2000 cells). (a) The longitudinal velocity along the surface. (b) The dynamic topography induced by the mantle flow. (c) A colour plot of the effective strain rate; arrows correspond to velocity vectors and grey contours outline the location of a continental plate and the slab. The dynamic topography (h_d) was calculated according to the relationship $h_d = \frac{-\sigma_{rr}}{g_r \Delta \rho}$, where σ_{rr} is the total radial stress measured along the surface, g_r is the radial component of gravity, and $\Delta \rho$ is the density difference between the lithosphere and the air (assumed to be equal to 0 kg/m^3). The mantle density was set to 3250 kg/m^3 , its viscosity varies from 10^{19} Pa.s down to -330 km , 10^{20} Pa.s down to -660 km , and 10^{22} Pa.s down to 1000 km . The slab and plate densities were set to 3275 kg/m^3 and 3245 kg/m^3 , respectively. Their viscosities were set to 10^{23} Pa.s . All boundary conditions were set to free slip. This simulation can be reproduced using the appended script M2Di_cyl_slab.m.

3.5 Conclusions

We developed and provide M2Di, an efficient set of routines that solve linear and non-linear Stokes flow on a personal computer using MATLAB. We report a wall-time of 22 seconds for the linear solver and both 180 and 400 seconds for the non-linear Newton solver with power law exponent $n = 3$ and $n = 30$ (single inclusion setup), respectively, on a 1000^2 2-D domain (3 MDoF) (Figure 3.4). These times-to-solution could be obtained using vectorised assembly of matrix operators and solvers that rely on efficient sparse Cholesky factorisation routines provided in T. Davis' SuiteSparse library (accessible in native MATLAB directly via the `chol()` function). The routines were validated by comparing our numerical results to analytical and benchmark numerical solutions for both linear and power law viscous flow. Here, we only considered Dirichlet and Neumann boundary conditions; however, the routines could also be extended to account for free surface flow (Duretz et al., 2016).

Multiphysics applications necessitate coupling between a mechanical solver and diffusion-type solvers (fluid pressure, heat, compositional) as well as accurate resolution of non-linearities. In this perspective, the development of 2-D THCM models will benefit from the presented mechanical solvers (M). The latter will be used as the main building block to further tackle studies of thermo-mechanical shear localisation (Duretz et al., 2014) (TM coupling), two-phase flow (Yarushina and Podladchikov, 2015) leading to fluid channelling instabilities (Räss et al., 2014; Yarushina et al., 2015) (HM coupling), reactive porosity waves (Malvoisin et al., 2015) (HCM coupling) or THCM coupling (Keller and Katz, 2016; Weatherley and Katz, 2012). Features arising from THCM coupling are often localised in space, close to material interfaces (e.g. shear zones, fluid channelling) and may depend on the local pressure field. Our results indicate that variable grid-spacing (Cartesian grid) can greatly improve the solution of pressure fields close to material boundaries and may therefore be considered in multiphysics applications.

Acknowledgments

The authors are grateful to Marcin Dabrowski and Anton Popov for their constructive review, which helped to significantly improve the work's quality and content. We thank Dave A. May for his constructive comments on the earlier version of the draft, which considerably improved the final manuscript. The authors acknowledge P. J. Yamato, who provided the script used for generating the random particle distributions in Figures 3.5 and 3.7.

Appendix

3.A The Stokes flow equation in cylindrical coordinates

To perform the model presented in section 3.4.4, the momentum and continuity equations (equation (3.1)) were reformulated in cylindrical coordinates (r, θ) :

$$\begin{aligned} \frac{1}{r} \frac{\partial \sigma_{\theta\theta}}{\partial \theta} + \frac{\partial \sigma_{r\theta}}{\partial r} + 2 \frac{\sigma_{r\theta}}{r} &= 0, \\ \frac{\partial \sigma_{rr}}{\partial r} + \frac{1}{r} \frac{\partial \sigma_{r\theta}}{\partial \theta} + \frac{\sigma_{rr}}{r} - \frac{\sigma_{\theta\theta}}{r} &= -\rho g_r, \\ \frac{1}{r} \frac{\partial v_\theta}{\partial x} + \frac{1}{r} \frac{\partial (rv_r)}{\partial y} &= 0. \end{aligned} \tag{3.A.1}$$

To allow discretisation on a staggered grid, the above equations were rewritten using the product rule and multiplied by r :

$$\begin{aligned} \frac{\partial \sigma_{\theta\theta}}{\partial \theta} - r \frac{\partial \sigma_{r\theta}}{\partial r} + 2 \frac{\partial (r\sigma_{r\theta})}{\partial r} &= 0, \\ \frac{\partial (r\sigma_{rr})}{\partial r} + r \frac{\partial \sigma_{\theta\theta}}{\partial r} - \frac{\partial (r\sigma_{\theta\theta})}{\partial r} + \frac{\partial \sigma_{r\theta}}{\partial \theta} &= -r\rho g_r, \\ \frac{\partial v_\theta}{\partial x} + \frac{\partial (rv_r)}{\partial y} &= 0. \end{aligned} \tag{3.A.2}$$

In this form, the gradients of stress tensor components and the value of the components do not have to be spatially collocated. Thus, the finite-difference discretisation involves no stress interpolations, and the stencil involves the same number of points (no stencil growth) as in the Cartesian formulation (see Section 3.2.1). Similarly, the stress tensor components were expressed as:

$$\begin{aligned} \sigma_{\theta\theta} &= -P + 2\eta \left(\frac{v_r}{r} + \frac{1}{r} \frac{\partial v_\theta}{\partial \theta} \right) = -P + 2\eta \left(\frac{1}{r} \frac{\partial (rv_r)}{\partial r} - \frac{\partial v_r}{\partial r} + \frac{1}{r} \frac{\partial v_\theta}{\partial \theta} \right), \\ \sigma_{rr} &= -P + 2\eta \left(\frac{\partial v_r}{\partial r} \right), \\ \sigma_{r\theta} &= \eta \left(\frac{\partial v_\theta}{\partial r} + \frac{1}{r} \frac{\partial v_r}{\partial \theta} - \frac{v_\theta}{r} \right) = \eta \left(2 \frac{\partial v_\theta}{\partial r} - \frac{1}{r} \frac{\partial (rv_\theta)}{\partial r} - \frac{1}{r} \frac{\partial v_r}{\partial \theta} \right), \end{aligned} \tag{3.A.3}$$

where v_θ and v_r , respectively, correspond to the longitudinal and radial velocity vector components.

Bibliography

- Adamuszek, M., Dabrowski, M., Schmid, D. W., 2016. Folder: A numerical tool to simulate the development of structures in layered media. *Journal of Structural Geology* 84, 85 – 101.
- Allen, G. M., 1999. Rheology of polymeric systems, principles and applications. *AIChE Journal* 45 (8), 1836–1837.
- Bea, S., Mayer, U., MacQuarrie, K., 2015. Reactive transport and thermo-hydro-mechanical coupling in deep sedimentary basins affected by glaciation cycles: model development, verification, and illustrative example. *Geofluids* 16 (2), 279–300.
- Billen, M. I., Gurnis, M., Simons, M., 2003. Multiscale dynamics of the Tonga-Kermadec subduction zone. *Geophysical Journal International* 153 (2), 359–388.
- Chen, Y., Davis, T. A., Hager, W. W., Rajamanickam, S., 2008. Algorithm 887: CHOLMOD, supernodal sparse Cholesky factorization and update/downdate. *ACM Transactions on Mathematical Software (TOMS)* 35 (3), 22.
- Conrad, C. P., Lithgow-Bertelloni, C., 2002. How Mantle Slabs Drive Plate Tectonics. *Science* 298 (5591), 207–209.
- Cuvelier, C., Segal, A., Van Steenhoven, A. A., 1986. Finite element methods and Navier-Stokes equations. Vol. 22. Springer Science & Business Media.
- Dabrowski, M., Krotkiewski, M., Schmid, D. W., 2008. MILAMIN: MATLAB-based finite element method solver for large problems. *Geochemistry, Geophysics, Geosystems* 9 (4).
- Dabrowski, M., Schmid, D. W., Podladchikov, Y. Y., 2012. A two-phase composite in simple shear: Effective mechanical anisotropy development and localization potential. *Journal of Geophysical Research: Solid Earth* 117 (B8).
- Deubelbeiss, Y., Kaus, B., 2008. Comparison of Eulerian and Lagrangian numerical techniques for the Stokes equations in the presence of strongly varying viscosity. *Physics of the Earth and Planetary Interiors* 171 (1), 92–111.
- Deubelbeiss, Y., Kaus, B. J. P., Connolly, J. A. D., Caricchi, L., 2011. Potential causes for the non-newtonian rheology of crystal-bearing magmas. *Geochemistry, Geophysics, Geosystems* 12 (5).
- Duretz, T., May, D., Yamato, P., 2016. A free surface capturing discretization for the staggered grid finite difference scheme. *Geophysical Journal International* 204 (3), 1518–1530.

- Duretz, T., May, D. A., Gerya, T. V., Tackley, P. J., 2011. Discretization errors and free surface stabilization in the finite difference and marker-in-cell method for applied geodynamics: A numerical study. *Geochemistry, Geophysics, Geosystems* 12 (7).
- Duretz, T., Schmalholz, S., Podladchikov, Y., Yuen, D., 2014. Physics-controlled thickness of shear zones caused by viscous heating: Implications for crustal shear localization. *Geophysical Research Letters* 41 (14), 4904–4911.
- Eisenstat, S. C., Elman, H. C., Schultz, M. H., 1983. Variational iterative methods for nonsymmetric systems of linear equations. *SIAM Journal on Numerical Analysis* 20 (2), 345–357.
- Gérault, M., Husson, L., Miller, M. S., Humphreys, E. D., 2015. Flat-slab subduction, topography, and mantle dynamics in southwestern Mexico. *Tectonics* 34 (9), 1892–1909.
- Gerya, T. V., May, D. A., Duretz, T., 2013. An adaptive staggered grid finite difference method for modeling geodynamic stokes flows with strongly variable viscosity. *Geochemistry, Geophysics, Geosystems* 14 (4), 1200–1225.
- Gerya, T. V., Yuen, D. A., 2003. Characteristics-based marker-in-cell method with conservative finite-differences schemes for modeling geological flows with strongly variable transport properties. *Physics of the Earth and Planetary Interiors* 140 (4), 293–318.
- Gerya, T. V., Yuen, D. A., 2007. Robust characteristics method for modelling multiphase visco-elasto-plastic thermo-mechanical problems. *Physics of the Earth and Planetary Interiors* 163 (1), 83–105.
- Glazner, A. F., 2014. Magmatic life at low reynolds number. *Geology* 42 (11), 935–938.
- Hernandez-Ortiz, J. P., Stoltz, C. G., Graham, M. D., 2005. Transport and Collective Dynamics in Suspensions of Confined Swimming Particles. *Phys. Rev. Lett.* 95, 204501.
- Jarvis, G. T., 1993. Effects of curvature on two-dimensional models of mantle convection: Cylindrical polar coordinates. *Journal of Geophysical Research: Solid Earth* 98 (B3), 4477–4485.
- Jessell, M. W., Bons, P. D., Griera, A., Evans, L. A., Wilson, C. J., 2009. A tale of two viscosities. *Journal of Structural Geology* 31 (7), 719 – 736.
- Kaus, B. J., Popov, A. A., Baumann, T., Püsök, A. E., 2016. Forward and inverse modelling of lithospheric deformation on geological timescales. In: *Proceedings NIC Symposium*.
- Keller, T., Katz, R. F., 2016. The role of volatiles in reactive melt transport in the asthenosphere. *Journal of Petrology* 57 (6), 1073–1108.

- Le Pourhiet, L., Huet, B., Labrousse, L., Yao, K., Agard, P., Jolivet, L., 2013. Strain localisation in mechanically layered rocks beneath detachment zones: insights from numerical modelling. *Solid Earth* 4 (1), 135–152.
- Malvoisin, B., Podladchikov, Y. Y., Vrijmoed, J. C., 2015. Coupling changes in densities and porosity to fluid pressure variations in reactive porous fluid flow: Local thermodynamic equilibrium. *Geochemistry, Geophysics, Geosystems* 16 (12), 4362–4387.
- Mancktelow, N. S., 2002. Finite-element modelling of shear zone development in viscoelastic materials and its implications for localisation of partial melting. *Journal of Structural Geology* 24 (6–7), 1045 – 1053.
- May, D. A., Brown, J., Pourhiet, L. L., 2014. pTatin3D: High-Performance Methods for Long-Term Lithospheric Dynamics. In: *SC14: International Conference for High Performance Computing, Networking, Storage and Analysis*. pp. 274–284.
- May, D. A., Moresi, L., 2008. Preconditioned iterative methods for Stokes flow problems arising in computational geodynamics. *Physics of the Earth and Planetary Interiors* 171 (1), 33–47.
- Montési, L. G. J., Zuber, M. T., 2002. A unified description of localization for application to large-scale tectonics. *Journal of Geophysical Research: Solid Earth* 107 (B3).
- Morra, G., Chatelain, P., Tackley, P., Koumoutsakos, P., 2009. Earth curvature effects on subduction morphology: Modeling subduction in a spherical setting. *Acta Geotechnica* 4 (2), 95–105.
- Moulas, E., Burg, J.-P., Podladchikov, Y., 2014. Stress field associated with elliptical inclusions in a deforming matrix: Mathematical model and implications for tectonic overpressure in the lithosphere. *Tectonophysics* 631, 37 – 49, observational and Modelling perspectives on the Mechanical properties of the Lithosphere.
- Patankar, S., 1980. *Numerical heat transfer and fluid flow*. CRC press.
- Räss, L., Yarushina, V. M., Simon, N. S., Podladchikov, Y. Y., 2014. Chimneys, channels, pathway flow or water conducting features-an explanation from numerical modelling and implications for CO₂ storage. *Energy Procedia* 63, 3761–3774.
- Rutqvist, J., 2011. Status of the TOUGH-FLAC simulator and recent applications related to coupled fluid flow and crustal deformations. *Computers & Geosciences* 37 (6), 739–750.
- Rutqvist, J., Feng, X., Hudson, J., Jing, L., Kobayashi, A., Koyama, T., Pan, P., Lee, H., Rinne, M., Sonnenthal, E., et al., 2006. Multiple-code benchmark simulation study of coupled THMC processes in the excavation disturbed zone associated with geological nuclear waste repositories. Lawrence Berkeley National Laboratory.

- Schmalholz, S. M., Fletcher, R. C., 2011. The exponential flow law applied to necking and folding of a ductile layer. *Geophysical Journal International* 184 (1), 83–89.
- Schmeling, H., Babeyko, A., Enns, A., Faccenna, C., Funiciello, F., Gerya, T., Golabek, G., Grigull, S., Kaus, B., Morra, G., et al., 2008. A benchmark comparison of spontaneous subduction models – Towards a free surface. *Physics of the Earth and Planetary Interiors* 171 (1), 198–223.
- Schmid, D. W., Podladchikov, Y. Y., 2003. Analytical solutions for deformable elliptical inclusions in general shear. *Geophysical Journal International* 155 (1), 269–288.
- Shin, D., Strikwerda, J. C., 1997. Inf-sup conditions for finite-difference approximations of the Stokes equations. *The Journal of the Australian Mathematical Society. Series B. Applied Mathematics* 39 (01), 121–134.
- Spiegelman, M., May, D. A., Wilson, C. R., 2016. On the solvability of incompressible stokes with viscoplastic rheologies in geodynamics. *Geochemistry, Geophysics, Geosystems* 17 (6), 2213–2238.
- Suckale, J., Nave, J.-C., Hager, B. H., 2010. It takes three to tango: 1. Simulating buoyancy-driven flow in the presence of large viscosity contrasts. *Journal of Geophysical Research: Solid Earth* 115 (B7), B07409.
- Suckale, J., Sethian, J. A., Yu, J.-d., Elkins-Tanton, L. T., 2012. Crystals stirred up: 1. direct numerical simulations of crystal settling in nondilute magmatic suspensions. *Journal of Geophysical Research: Planets* 117 (E8).
- Weatherley, S., Katz, R., 2012. Melting and channelized magmatic flow in chemically heterogeneous, upwelling mantle. *Geochemistry, Geophysics, Geosystems* 13 (5).
- Yamato, P., Duretz, T., May, D., Tartèse, R., 2015. Quantifying magma segregation in dykes. *Tectonophysics* 660, 132 – 147.
- Yamato, P., Tartèse, R., Duretz, T., May, D., 2012a. Numerical modelling of magma transport in dykes. *Tectonophysics* 526, 97 – 109, modelling in Geosciences.
- Yamato, P., Tartèse, R., Duretz, T., May, D. A., 2012b. Numerical modelling of magma transport in dykes. *Tectonophysics* 526, 97–109.
- Yarushina, V. M., Podladchikov, Y. Y., 2015. (De)compaction of porous viscoelastoplastic media: Model formulation. *Journal of Geophysical Research: Solid Earth* 120 (6), 4146–4170.

Yarushina, V. M., Podladchikov, Y. Y., Connolly, J. A., 2015. (De)compaction of porous viscoelastoplastic media: Solitary porosity waves. *Journal of Geophysical Research: Solid Earth* 120 (7), 4843–4862.

CHAPTER 4

Resolving hydro-mechanical coupling in two and three dimensions: Spontaneous channelling of porous fluids owing to decompaction weakening

Ludovic Räss^{1,2}, Thibault Duretz^{1,3}, and Yury Y. Podladchikov^{1,2}

¹Faculté des géosciences et de l'environnement, Institut des Sciences de la Terre, University of Lausanne,
Lausanne, Switzerland.

²Swiss Geocomputing Centre, University of Lausanne, Lausanne, Switzerland.

³Géosciences Rennes, Univ. Rennes 1, UMR CNRS 6118, France.

Abstract

Fingering, veining, channelling and focussing of porous fluids are widely observed phenomena in the Earth's interior, driving a range of geo-processes across all scales. While observations suggest fairly localised flow patterns induced by fractures, the classical Darcian model predicts diffusive behaviour that leads to never-ending spreading and delocalisation. We numerically investigate an alternative physical mechanism without the need to involve fractures. Decompaction weakening leads to the formation and propagation of localised flow-pathways in fluid-saturated porous media. We use high-resolution 2-D and 3-D numerical modelling to predict non-linear porous flow in a non-linearly viscously deforming matrix. We use a high-performance computing approach to accurately resolve strong localisation in space and time. In particular, we streamline a matrix-free pseudo-transient numerical method and usage of graphical processing units to solve Darcy and Stokes flow coupled equations. The pseudo-transient routines converge towards identical solutions compared to direct-iterative solving strategies. We discuss performance benefits of the matrix-free method on modern parallel hardware. We show that high-porosity channels may be a dynamic and natural outcome of sufficiently resolved hydro-mechanical coupling and decompaction weakening. Further, we systematically study the channel propagation velocity as a function of bulk and shear viscosity ratios. We show that the fluid flow rate in the channels is up to three orders of magnitude higher than expected by pure Darcian flow regimes. Finally, we include strain rate-dependent shear rheology and predict channel emplacement in three dimensions. We provide both the two-dimensional MATLAB-based direct-iterative and pseudo-transient routines for full reproducibility of the presented results and suggest our model setup as a key benchmark case to validate the implementation of hydro-mechanical coupling in 2-D and 3-D numerical codes.

4.1 Introduction

Evidence of localised fluid flow in saturated porous media are observed in various geosystems on Earth. Their expression in the interior of deep Earth relates to metasomatism and dehydration of aqueous minerals in ductile rocks (Ague, 2011; Connolly and Podladchikov, 1998, 2000; Iyer et al., 2013; Miller et al., 2003; Omlin et al., 2017a; Skarbek and Rempel, 2016) and migration of melt into deforming partially molten regions of the lithosphere (Cai and Bercovici, 2013; Connolly and Podladchikov, 2007; Katz and Weatherley, 2012; Keller et al., 2017, 2013; Liang et al., 2011; McKenzie, 1984; Rudge et al., 2011; Schiemenz et al., 2011; Scott and Stevenson, 1984; Simpson et al., 2010a,b). At shallower levels, vertical chimneys or pipe structures are populating sedimentary basins in continental shelves (Judd and Hovland, 2007). These structures are inferred from their distinct signatures on seismic cross-sections and are often related to pockmarks on the seafloor. Their presence is especially well documented in regions of economic interest (Berndt, 2005; Cartwright and Santamarina, 2015; Cathles et al., 2010; Minakov et al., 2017; Räss et al., 2014). Indications suggest that some vertical pipes may act as preferential fluid pathways, while other structures appear to be dormant. The expression of these subseabed pipes is well reported for instance on the Nigerian continental shelf and in the Norwegian North Sea (Huq et al., 2017; Hustoft et al., 2010; Løseth et al., 2011; Mazzini et al., 2017; Plaza-Faverola et al., 2010, 2011), as well as in lacustrine environments (Reusch et al., 2015). Understanding the physical process that leads to the formation and evolution of these pipes is essential to accurately constrain subsurface fluid flow. Most field observations are qualitatively explained by conceptual models, and only a few recent studies address the physics of gas-rich and fluid-rich chimneys (e.g. Cartwright and Santamarina, 2015; Cathles et al., 2010, and references therein); however, they mainly involve capillary forces and fracture mechanics that lead to a potential blowout scenario.

In this study, we use numerical modelling to resolve prediction, rather than prescription, of the *spontaneous* formation and propagation of pipe structures in viscously deforming porous media. Our model is based on non-linear and coupled two-phase flow equations (Yarushina and Podladchikov, 2015) and allows for the existence of solitary or porosity waves and decompaction weakening as a flow-focussing mechanism. Solitary waves require non-linear porosity-dependent permeability, here a Carman-Kozeny relationship (Costa, 2006) in order to form blob-shaped propagating porosity waves, but not yet reproducing the first-order natural data. Decompaction weakening results in the *blobs to channels* transition in better agreement with field observations. Such numerical models are numerically and computationally challenging because 1) the spatial occurrence of these structures is not known in advance; 2) the material properties such as permeability and viscosity range over several orders of magnitude; 3) important contrasts in spatial and temporal scales must be resolved, ranging from channel spacing down to the decompacting area at the tip of each propagating channel. Thus,

the strong non-linear coupling between the different physical processes requires appropriate numerical treatment. The computational domain size must be large enough to resolve spontaneous spacing between the channels, and the numerical resolution must be sufficiently high to resolve the channel's tip areas mandatory for accurate predictions of the propagation velocity and growth of the channels.

To date, most porosity wave models (Appold and Nunn, 2002; Barcilon and Richter, 1986; Connolly and Podladchikov, 2007, 1998, 2000; Joshi and Appold, 2016; Olson and Christensen, 1986; Scott, 1988; Skarbek and Rempel, 2016; Tian and Ague, 2014; Wiggins and Spiegelman, 1995) decouple fluid flow from shear deformation by assuming lithostatic total pressure gradient. The fully coupled model utilises appropriate geomechanics to predict stresses and pressure distribution in the porous matrix. The fully coupled approach has two major benefits; first, total pressure no longer needs to be assumed to follow a lithostatic gradient; second, the shear deformation of the porous matrix is resolved. Most importantly, the dynamics and morphology of porosity waves become sensitive to the shear rheology of the rock matrix. The fully coupled approach's importance has been discussed concerning industry-related simulators based on Biot's poro-elasticity theory (Prevost, 2013; Settari and Walters, 2001). There, the standard solution to simulate fluid-flow porous media relies on a direct coupling approach, in which fluid pressure is transferred to the geomechanical module, but the geomechanics don't affect the fluid pressure. Such an approach does not include any non-linear iteration, mainly owing to time constraints, and results in an explicit coupling. More advanced workflows iteratively couple a fluid flow-solver to a geomechanical solver (e.g. Minkoff et al., 2003; Rutqvist, 2011, 2012). In such an approach, data must often be explicitly transferred from one software package to another, hindering the maximal affordable numerical resolution. Both solution strategies mainly don't verify non-linear convergence, owing to the large number of iterations needed, resulting in long simulation times. The computed solutions may not be accurate, and non-linear features may be underresolved. An alternative solution is to fully couple fluid flow and Stokes matrix flow in a single solver (Dannberg and Heister, 2016; Dymkova and Gerya, 2013; Gradmann and Beaumont, 2012; Gradmann et al., 2012; Keller et al., 2013; Morency et al., 2007; Omlin et al., 2017b; Scott, 1988; Stevenson and Scott, 1991; Zheng et al., 2016). Further, none of the previous studies, with the exception of Omlin et al. (2017b), have considered decompaction weakening while coupling Darcian and Stokes flows in 3-D.

Recently, Yarushina and Podladchikov (2015) presented a general system of thermodynamically admissible equations for fluid flow in deformable visco-elastic porous media. The well-established Biot poro-elastic model (Wang, 2000) is recovered in the linear elastic limit, valid at low stress levels. A number of numerical studies (e.g. Haga et al., 2012; Phillips and Wheeler, 2008; Wheeler et al., 2014, and references therein), have explored linear poro-elastic coupling. At higher stress levels, rock deformation deviates significantly from a linear elastic

rheology. The non-linear instantaneous response is typically characterised using an elasto-plastic rheology (Baud et al., 2000; Vajdova et al., 2012; Wong and Baud, 2012). Lewis and Schrefler (1987) and more recently Cacace and Jacquey (2017) or Wheeler et al. (2014) numerically investigated poro-elasto-plastic deformation coupled to fluid flow. Pure elastic and elasto-plastic matrix rheologies are beyond this study’s scope.

In this contribution, we utilise the viscous limit of Yarushina and Podladchikov (2015) model to investigate the importance of decompaction weakening while coupling Darcian and Stokes flows. Viscous rheology is expected to operate in the rock matrix at high (comparable to melting) temperatures and is usually neglected in lower-temperature environments. However, even at low (ambient) temperatures, rock deformation experiments on sandstones, limestones and shales show that major reservoir rock types exhibit non-negligible time-dependent creep deformation (Brantut et al., 2013; David et al., 2015; Sone and Zoback, 2014; Spiers et al., 1990). Recent studies (Makhnenko and Labuz, 2016; Räss et al., 2017a) suggest that the porosity-dependent bulk viscosity is a non-linear function of the effective pressure. This strong non-linear interaction may lead to a drastic decrease in bulk viscosity values for regions of elevated pore-fluid pressure. Thus, the viscosity drop from the compaction to the decompaction regime, the decompaction weakening, suggested on theoretical grounds (Connolly and Podladchikov, 2007; Yarushina and Podladchikov, 2015) is thus experimentally confirmed.

We numerically simulate the formation and propagation of high-porosity channels (Keller et al., 2013; Omlin et al., 2017b; Räss et al., 2017a, 2016; Räss et al., 2014) utilising decompaction weakening as a flow-focussing mechanism. We use the finite-difference method with two different solving approaches. We perform both 2-D and 3-D forward simulations and present a systematic study based on more than 400 forward 2-D simulations at various high resolutions and four 3-D simulations involving more than 2 billion grid-points. We suggest our model result as benchmark for future numerical two-phase poro-viscous implementations, augmenting the existing poro-elastic (Rozhko, 2008) benchmark and the analytical solution of compacting flow past a sphere (Rudge, 2014). We highlight that accurate convergence may lead to the formation of porosity waves and discuss the influence of the decompaction over compaction viscosity and the bulk to shear viscosity ratios in terms of maximal wave velocities and some performance-related outcomes. Finally, we explore the impacts of non-linear shear rheology on channel size and distribution in 3-D.

4.2 Mathematical model and hydro-mechanical coupling

We utilise a set of two-phase equations to model the formation and evolution of high-porosity channels over time as a natural outcome of the coupling of fluid flow and the deformation of a viscous porous matrix (Räss et al., 2014; Yarushina et al., 2015b).

The mass balance for fluid and solid phases assuming constant fluid and solid densities are:

$$\begin{aligned}\nabla_k v_k^s &= -\frac{d \log(1 - \phi)}{dt}, \\ \nabla_k \left[\phi \left(v_k^f - v_k^s \right) \right] &= \frac{d \log(1 - \phi)}{dt},\end{aligned}\tag{4.1}$$

where $\frac{d}{dt} = \frac{\partial}{\partial t} + v_k^s \nabla_k$ is the material derivative with respect to the solid.

The momentum balance equations for the matrix (Stokes) and the pore-fluid (Darcy) are:

$$\begin{aligned}\nabla_j (\bar{\tau}_{ij} - \bar{p} \delta_{ij}) - \bar{\rho} g_i &= 0, \\ \phi \left(v_i^f - v_i^s \right) + \frac{k_\phi}{\mu^f} \left(\nabla_i p_i^f + \rho^f g_i \right) &= 0,\end{aligned}\tag{4.2}$$

where $\bar{\tau}_{ij}$ are the components of the stress deviator, δ_{ij} is the Kronecker delta, g_i are the components of downward-pointing gravity acceleration vector, $\phi \left(v_i^f - v_i^s \right)$ is the Darcy flux vector (the relative flux of the fluid relative to the solid), μ^f is the pore-fluid viscosity and \bar{p} , p^f are the total and fluid pressures, respectively. The total porosity-averaged density:

$$\bar{\rho} = (1 - \phi) \rho^s + \phi \rho^f,\tag{4.3}$$

includes constant solid and fluid densities ρ^s and ρ^f , respectively. The Carman-Kozeny relationship (Costa, 2006) defines the porosity ϕ dependent permeability k_ϕ :

$$k_\phi = k_0 \left(\frac{\phi}{\phi_0} \right)^3,\tag{4.4}$$

where k_0 is the reference permeability and ϕ_0 the reference porosity.

The strain rate tensor and non-linear viscous creep rheology are expressed as:

$$\dot{\epsilon}_{ij} = \frac{1}{2} (\nabla_i v_j^s + \nabla_j v_i^s) - \frac{1}{3} \delta_{ij} \nabla_k v_k^s = \frac{1}{2} A \tau_{II}^{n-1} \bar{\tau}_{ij},\tag{4.5}$$

where $\dot{\epsilon}_{ij}$ is the strain rate tensor, δ_{ij} is the Kronecker-delta, $\bar{\tau}_{ij}$ and τ_{II} are the deviatoric stress tensor and the square root of its second invariant, respectively, n is the stress exponent and A is a pre-exponential constant that is equal to the inverse of the solid shear viscosity in the linear viscous case $n = 1$.

The system is closed by a final constitutive equation that accounts for viscous (de)compaction:

$$\nabla_k v_k^s = -\frac{p_e}{\eta_\phi (1 - \phi)},\tag{4.6}$$

where η_ϕ is the bulk viscosity. The reference bulk compaction viscosity, η_C , at reference porosity ϕ_0 and $\bar{p} \gg p^f$, is:

$$\eta_C = \frac{\mu_s}{C\phi_0} \quad (4.7)$$

where C is the pore geometry dependent coefficient. At other porosity and fluid pressure values, the bulk viscosity η_ϕ is inversely proportional to the porosity and drops with the decrease of the effective pressure $p_e = \bar{p} - p^f$ to account for decompaction weakening, here parametrised by a hyperbolic tangent function:

$$\eta_\phi = \eta_C \frac{\phi_0}{\phi} \left[1 + \frac{1}{2} \left(\frac{1}{R} - 1 \right) \left(1 + \tanh \left[-\frac{p_e}{\lambda_p} \right] \right) \right], \quad (4.8)$$

where λ_p is the transition zone sharpness between the decompacting and compacting regime and R is a rheological constant (Connolly and Podladchikov, 2007, 1998) quantifying the ratio of compaction (η_C) bulk viscosity (at $p_e \gg \lambda_p$) over decompaction (η_D) bulk viscosity (at $p_e \ll -\lambda_p$).

Several non-linearities arise from the set of equations described above, both owing to coupling and porosity-dependent parameters. These non-linearities will require proper treatment in the solving procedure.

We use three independent scales:

$$\begin{aligned} \delta_c &= \sqrt{k_\phi \frac{\eta_C}{\mu^f}}, \\ p_c &= \left(\rho^s - \rho^f \right) g \delta_c, \\ \tau_c &= \frac{\eta_C}{p_c}, \end{aligned} \quad (4.9)$$

and their dependent combinations such as the characteristic velocity $v_c = \delta_c/\tau_c$ to normalise all the variables, resulting in a dimensionless form of the governing equations. The characteristic length scale δ_c is also referred to as the compaction length (Connolly and Podladchikov, 2014; McKenzie, 1984). τ_c is the characteristic time and p_c is the characteristic pressure or stress.

4.3 Model setup

The initial conditions we used in this study consist of a column of saturated porous media with an initial normalised background porosity value $\phi/\phi_0 = 1$. An elliptical region of $\phi/\phi_0 = 3$ is located at the first one-quarter above the computational domain's base. The computational 2-D or 3-D domain dimensions (x, depth (vertical) or x, y, depth (vertical), respectively) are

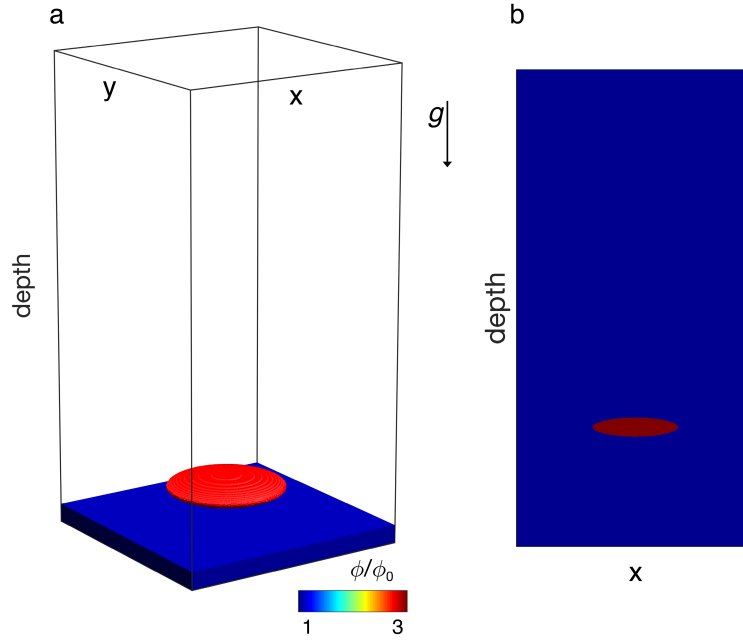


Figure 4.1: Schematic initial model configuration for (a) the 3-D and (b) the 2-D calculations. The high-porosity anomaly is located at the first one-quarter of the model depth and the values are three times higher than background normalised porosity (ϕ/ϕ_0).

normalised by the characteristic length scale δ_c . We report the main parameters used in this study, and not subject to change, in Table 4.1.

The viscous medium undergoes progressive compaction in response to the downward-pointing gravity acceleration. Since the fluid density is twice as low as the solid density, the fluid excess in the high-porosity anomaly tends to travel upwards as buoyancy-driven flow. As further discussed in this study, the flow tends to focus in high-porosity channels if the decompaction weakening is significant, $R \gg 1$. The resulting flow rate and propagation velocities are therefore significantly enhanced. Figure 4.2 shows three stages of a reference 2-D simulation of buoyancy-driven propagating porosity waves in a low-porosity region. For significant decompaction weakening, $R \gg 1$, the coupling of fluid flow and solid matrix deformation naturally rearranges into high-porosity channels. In this case, the resulting vertical fluid transfer rates are significantly higher than diffusive Darcian flow (Figure 4.2a-c). The corresponding effective pressure p_e values show, at each stage, which part of the domain is in the compaction ($p_e > 0$) or decompaction ($p_e < 0$) regime (Figure 4.2d-f). The high-porosity channels evolve and propagate upwards in a self-sustained mechanism, collecting the surrounding fluid via lower fluid pressure inside compared to outside the channels. Since mass is conserved, the regions surrounding the vertical channels compact owing to fluid depletion. The resulting increased bulk viscosity values in low-porosity regions turn out to freeze the channel wall geometry and potentially provide preferential flow-paths for future fluid release.

Description	Symbol	Value	
		2-D	3-D
Domain size	x, (y), depth	20 x 40	20 x 20 x 40
Ellipsoid axis length	x, (y), depth	2 x 8	2 x 2 x 8
Reference porosity	ϕ_0	0.01	
Reference permeability	k_0	1	
Fluid shear viscosity	μ^f	1	
Solid shear viscosity power law exponent	n	1	3
Compaction bulk viscosity	η_C	1	
Gravity acceleration	g	[0,1]	[0,0,1]
Solid density	ρ^s	2	
Fluid density	ρ^f	1	
Effective pressure transition zone	λ_p	0.01	

Table 4.1: Non-dimensional simulation parameters. Notably, the 3-D setup, Y is the second horizontal axis and is equal to the X-axis, which represents the domain width in 2-D and 3-D. Also, values identical for both 2-D and 3-D setups are not repeated in the 3-D column.

4.4 Numerical implementation and solving strategies

We investigate two approaches are investigated to solve the coupled system of non-linear equations; i) a so-called direct-iterative (DI) solver workflow that includes a coupled or decoupled linear solve (matrix assembly for linearised operator) and performing Picard iterations type for converging the non-linearities, and ii) a matrix-free pseudo-transient (PT) alternative. The porosity time derivative is approximated either by a backward Euler or a Crank-Nicolson scheme. The dimensionless solid shear viscosity μ_s is a non-linear function of the strain rate and is expressed as:

$$\mu_s = \frac{1}{2A^{\frac{1}{n}} \epsilon_{II}^{\frac{n-1}{n}} + \frac{1}{\mu_0}}, \quad (4.10)$$

where ϵ_{II} is the square root of the second invariant of the deviatoric strain rate and μ_0 is the reference viscosity for negligible strain rates.

The DI solving strategy (i) is based on extending the developed M2Di single-phase Stokes flow routines (Räss et al., 2017b) for two-phase flow and made available as part of these routines under the HM2Di moniker. The Stokes equations are now coupled to a non-linear Darcy flow in order to compute the additional fluid pressure. The alternative PT solving strategy (ii) relies on a matrix-free approach that does not require a matrix assembly for the linear operator. Thus, the memory requirements scale linearly with increasing problem size. Minimising the residuals is performed iteratively using a numerical time-stepping (relaxation) strategy. In this communication, we will demonstrate that both PT and DI methods allow

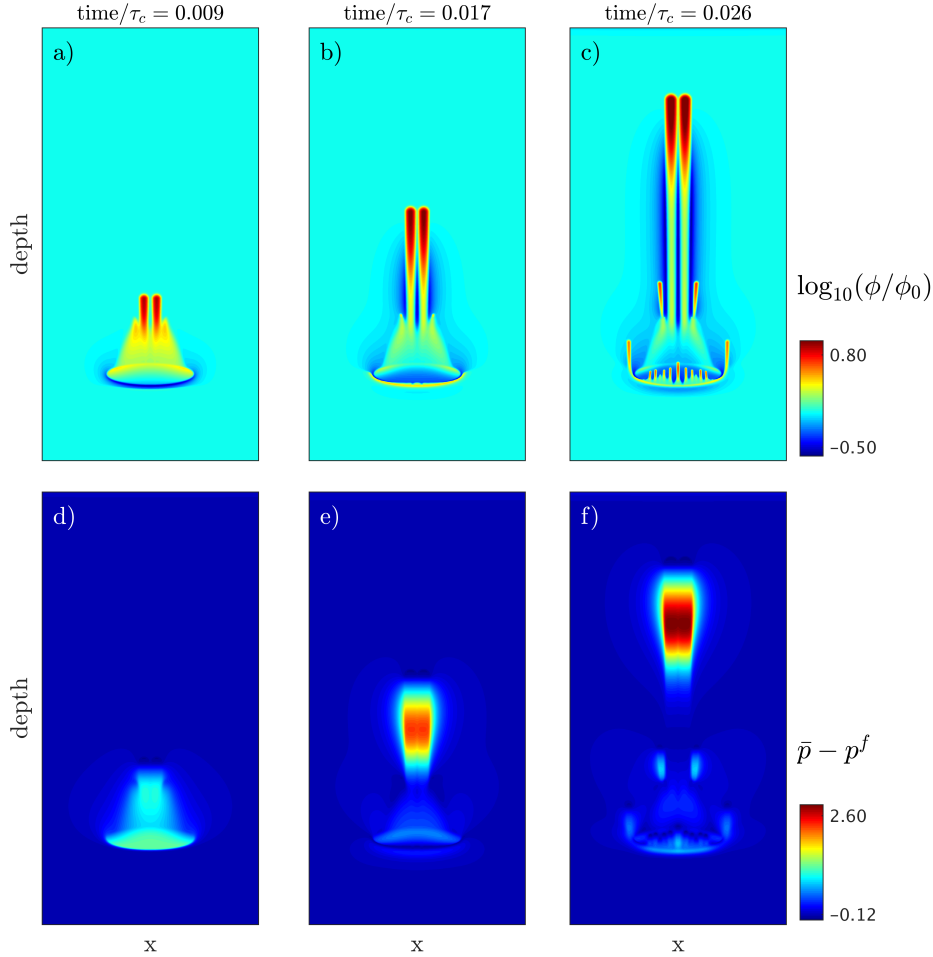


Figure 4.2: Evolution in a 2-D setup of the formation and propagation of high-porosity channels for three snapshots in dimensionless time. (a) to (c) The \log_{10} of the normalised porosity $\log_{10}(\phi/\phi_0)$ distribution. (d) to (f) The corresponding distribution of effective pressure $\bar{p} - p^f$. The initial condition used for this simulation is the one presented in Figure 4.1b, and we used following parameters: $\eta_D/\eta_C = 500$, $\frac{\mu_s}{\eta_C \phi_0} = 0.1$. The simulation runs until the high-porosity channels reaches 85% of the domain depth. The grid resolution is of $511 \times 1,023$ grid-points and a few hours were needed to perform the close to 2,000 time-steps on a Nvidia Titan Xp GPU.

us to obtain an implicit solution of the coupled system of equations; thus, fluxes and source terms are evaluated at physical time $(t + \Delta t)$. To achieve this, we collect the coefficient matrix of the linearised system of equation in the DI procedure and perform a direct solve. In

contrast, we don't assemble any coefficient matrix in the PT procedure, but iteratively reach the solution in a pseudo-time loop.

The system of partial differential equations (Section 4.2) that describes the two-phase poro-viscous flow is discretised using the finite difference method on a regular Cartesian staggered grid. This staggering is inherently devoid of oscillatory pressure modes (Shin and Strikwerda, 1997) and relies on second-order conservative finite differences (Patankar, 1980). Further technicalities regarding spatial discretisation and staggering are discussed in Räss et al. (2017b), Section 2.2. The introduced fluid pressure nodes are located in the cell centres. Additional material properties, namely porosity and bulk viscosity, also reside in this location.

To solve the two-phase flow problem, we apply free-slip boundary conditions for the Stokes problem (no shear stress on the boundaries). For the fluid flow part (i.e. the Darcy problem), we assign fixed flux boundary conditions. Fluxes in X direction are set to 0 on both sides of the computational domain. Vertical inflow and outflow values (bottom and top boundaries) are chosen to satisfy the condition $p_e = 0$, leading to no compaction or decompaction of the porous matrix. Similar boundary condition types are used and further discussed in Rhebergen et al. (2015).

In a classical approach, solving the set of time-dependent non-linear equations described above requires a five-step procedure (Figure 4.3i) that includes: 1) an update of the non-linearly dependent parameters (listed in Section 4.2), 2) the check of the non-linear residual, 3) the assembly of the linear matrix operator, 4) a solve of the linearised system, 5) updating the solution and repeating (1) to (5) until convergence is reached. This procedure is then applied in a time-loop. We will follow such an approach in the direct-iterative solver, using either a coupled or decoupled linear solving strategy for the linear system (4), and a Picard scheme for the non-linear iterations. Alternatively, the five-step procedure is rearranged in a single iteration loop that combines steps (3) to (5) in the pseudo-transient solver type (Figure 4.3ii), thus simultaneously converging both the linear and the non-linear problem for each time-step.

4.4.1 The direct-iterative solver

In this section, we describe how a DI solver approach is used to solve the Stokes equations coupled to fluid flow. The velocity \mathbf{u} , total pressure $\bar{\mathbf{p}}$ and fluid pressure \mathbf{p}^f solution vectors are the primitive variables and can be obtained by solving the system (equation (4.11)) expressed in a defect correction form:

$$\underbrace{\begin{bmatrix} \mathbf{M} & \mathbf{G} & \mathbf{0} \\ -\mathbf{G}^T & \mathbf{PP} & \mathbf{PPF} \\ \mathbf{0} & \mathbf{PFP} & \mathbf{PF} \end{bmatrix}}_{\mathbf{M}_{\text{HM}}} \underbrace{\begin{bmatrix} \delta \mathbf{u} \\ \delta \bar{\mathbf{p}} \\ \delta \mathbf{p}^f \end{bmatrix}}_{\delta \mathbf{x}} = - \underbrace{\begin{bmatrix} \mathbf{f}_u \\ \mathbf{f}_p \\ \mathbf{f}_{p^f} \end{bmatrix}}_{\mathbf{f}}, \quad (4.11)$$

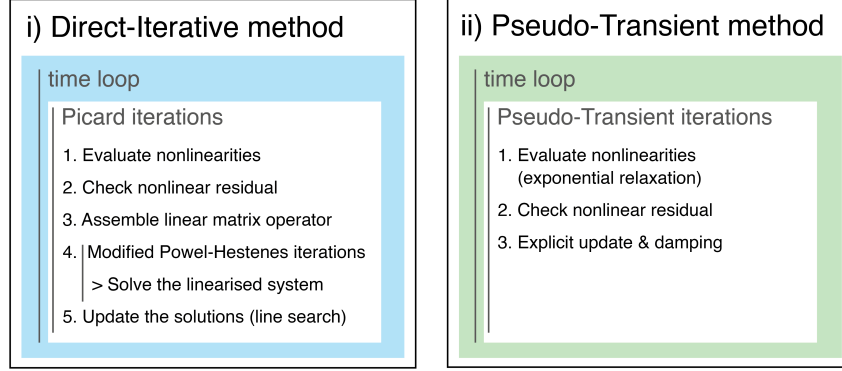


Figure 4.3: Algorithmic flowchart for both solving methods investigated in this study: (i) the direct-iterative solver (HM2Di code) and (ii) the pseudo-transient solver.

where the symmetric positive-definite \mathbf{M} block represents the Picard linearised operator. $\delta\mathbf{u}$, $\delta\bar{\mathbf{p}}$ and $\delta\mathbf{p}^f$ are the velocity, total pressure and fluid pressure iterative correction vectors, respectively. \mathbf{f}_u , \mathbf{f}_p and \mathbf{f}_{p^f} represent the velocity, total pressure and fluid pressure residuals that we aim to minimise. The contributing boundary conditions and body forces are both included in the \mathbf{f} vector. The \mathbf{PP} diagonal block takes values of $[\eta_\phi(1-\phi)]^{-1}$, naturally and physically solving the issues of the missing diagonal entries encountered in the incompressible Stokes formulation, as discussed in Räss et al. (2017b). The \mathbf{PF} block is a Poisson operator for the fluid pressure diffusion. Its main diagonal is augmented with the $[\eta_\phi(1-\phi)]^{-1}$ values, the symmetric counterpart of the \mathbf{PP} diagonal block. The two \mathbf{PPF} and \mathbf{PFP} diagonal blocks contain the symmetric pressure coupling terms, total-to-fluid and fluid-to-total respectively. They arise from splitting the p_e variable in equation (4.6) into total and fluid pressures.

Iterative Picard corrections are obtained by the application of the inverse of \mathbf{M}_{HM} to the current non-linear residual vector:

$$\delta\mathbf{x} = \mathbf{M}_{\text{HM}}^{-1}\mathbf{f}. \quad (4.12)$$

Details of the combined direct-iterative approach used to achieve the solution appear in the Appendices. A direct search is performed after convergence of the linear solver to determine the optimal globalisation parameter.

The non-linear residuals (\mathbf{f}_u , \mathbf{f}_p , \mathbf{f}_{p^f}) are explicitly evaluated in a line search algorithm (matrix-free approach) for n values of $\alpha =]0; \alpha_{\text{max}}]$, where $\alpha_{\text{max}} > 1.0$ for Picard linearisation. The optimal globalisation parameter yielding to:

$$\min \|\mathbf{f}_{p^f} + \alpha \delta\mathbf{p}^f\|_{L2} \quad (4.13)$$

is retained. An accurate solve is only achieved if all the non-linearities are included in the non-linear iteration loop and updated after each solve of the linear system. The strong and inherent coupling arising from equation (4.1) in terms of pressures must also be appropriately handled, i.e. avoiding a so-called one-way coupling (Prevost, 2013; Settari and Walters, 2001). Thus, we involve additional discrete operators to describe the coupled system (**PPF** and **PPF**), and will generate new non-zero entries in the global system.

The same symmetry and positive-definite constraints, as discussed in Räss et al. (2017b), are enforced for the linear system of the Stokes equations coupled to a Poisson solver (equation (4.11)). The assembly of a well-conditioned system allows the application of an optimal solving strategy using a Cholesky factorisation in the decoupled linear solve. For performance issues in MATLAB, all the operation performed in the routines are vectorised.

4.4.2 The pseudo-transient solver

An alternative solving approach to the DI routines resides in performing a pseudo-transient or relaxation method. While the DI solvers type can handle important contrasts in material properties such as viscosity, the memory requirements and the time-to-solution do not scale with an increase in the number of degrees of freedom (DoF). Further, DI solvers may be complex to develop when the physical problem requires one to include several non-linearities and are not a viable solution when investigating 3-D setups. Resolving 3-D setups on high spatial resolution is the main motivation to develop pseudo-transient-based solvers, since they are capable of addressing these limitations. The relaxation method is a classical numerical technique to solve stationary (elliptic) problems (Frankel, 1950). The method was extended in the 1960s to elastic problems (Otter et al., 1966) and more recently to elasto-plastic (Cundall, 1982) and visco-elastic problems (Poliakov et al., 1993). Unfortunately, the most straightforward update algorithm (first order scheme) requires order of n^2 iterations to converge to the stationary solution, where n is the total number of unknowns or grid points in a 1-D problem. However, a second order scheme permits to reach enhanced convergence rates when selecting the appropriate relaxation parameters.

We show that the PT iterative solving strategy allows one to avoid an expensive assembly of a matrix for the linearised operator, resulting in a matrix-free approach. The combination of PT solvers with a matrix-free implementation of the finite-difference method shows by construction a linear scaling between memory usage and computed problem size (DoF). Further, such an approach is well suited for parallel execution on modern hardware accelerators such as graphical processing units (GPUs), since the same instruction set is performed at every grid-point in the numerical domain. The addition of message passing interface (MPI) protocols to the PT routines permits a non-expensive internal boundary values exchange by point-to-point

MPI communication. Thus, a close-to-linear scaling of the routines on distributed-memory machines is expected.

Further, a PT-based iterative solver can be designed to simultaneously minimise both the linear and the non-linear problem in a single iteration loop. This can be achieved by the relaxation of the non-linearities during the iterative procedure used to converge the linearised problem. Such an approach may significantly reduce the overall number of iterations needed to converge one physical time-step, once optimal relaxation parameters are found. Additional details regarding the PT continuation method with application to a generic example is appear in the Appendices.

Application of the pseudo-transient continuation

The system of non-linear partial differential two-phase flow equations (equations (4.1), (4.2) and (4.6)) can be rearranged and rewritten, augmented with numerical pseudo-time derivatives $d/d\tau$, in order to be solved using the PT continuation approach:

$$\begin{aligned} \nabla (\bar{\tau}_{ij} - \bar{p}\delta_{ij}) - \bar{\rho}\hat{g} &= \frac{dv_i^s}{d\tau_v}, \\ \nabla_k v_k^s + \frac{p_e}{\eta_\phi(1-\phi)} &= \frac{d\bar{p}}{d\tau_{\bar{p}}}, \\ \nabla_k \left[\phi \left(v_k^f - v_k^s \right) \right] - \frac{p_e}{\eta_\phi(1-\phi)} &= \frac{dp^f}{d\tau_{p^f}}. \end{aligned} \quad (4.14)$$

The system of equations (equation (4.14)) can be rearranged, substituting the left-hand-side terms:

$$\begin{aligned} \frac{dv_i^s}{d\tau_v} &= f_u, \\ \frac{d\bar{p}}{d\tau_{\bar{p}}} &= f_{\bar{p}}, \\ \frac{dp^f}{d\tau_{p^f}} &= f_{p^f}, \end{aligned} \quad (4.15)$$

where f_u , $f_{\bar{p}}$ and f_{p^f} are the momentum, the total pressure and the fluid pressure equation residuals, respectively. Expanding the numerical time derivatives from equation (4.15), it is now possible to explicitly iterate on the three primitive variables v_i^s , \bar{p} and p^f until the numerical time derivatives vanish, thereby converging to an implicit steady state solution

of the system. The PT time-steps required to integrate the momentum and mass balance equations (equation (4.15)) are formulated as:

$$\begin{aligned}\Delta\tau_v &= v_{sc} \frac{\max(\Delta x, \Delta y)^2}{2.1 n_{\text{dim}} \mu_s (1 + \eta_b)}, \\ \Delta\tau_{\bar{p}} &= \bar{p}_{sc} \frac{2.1 n_{\text{dim}} \mu_s (1 + \eta_b)}{\max(nx, ny)}, \\ \Delta\tau_{p^f} &= p_{sc}^f \frac{\max(\Delta x, \Delta y)^2}{2.1 n_{\text{dim}} k_\phi / \mu^f},\end{aligned}\tag{4.16}$$

where η_b is a numerical bulk viscosity, Δx and Δy are the grid step sizes, n_{dim} the number of spatial dimensions and v_{sc} , \bar{p}_{sc} and p_{sc}^f some adjustable scaling or relaxation factors for their respective primitive variables. Both $\Delta\tau_v$ and $\Delta\tau_{p^f}$ refer to slightly modified explicit CFL diffusive time-step limiter. We chose $\Delta\tau_{\bar{p}}$ to optimise the solution procedure by minimising the number of performed non-linear iterations, and balancing the viscosity term μ_s introduced in $\Delta\tau_v$. We also highlight that both μ_s and k_ϕ / μ^f refer to entire fields (local to every grid-point) and are analogous to diagonal preconditioners in matrix-based solvers.

Accelerating the convergence

A successful solve of the system of non-linear equations (equation (4.15)) using the PT continuation requires an optimal numerical (or iterative) time-stepping strategy. Further, a damping of the residuals can significantly accelerate the convergence of the system, making the PT method competitive on a large range of numerical resolutions in 1-D, 2-D and 3-D.

Damping acts like a successive over-relaxation of the residual in the pseudo-time iterations loop (Yang and Mittal, 2014). Adding to the current (k) residual an important fraction of the previous ($k-1$) residual strongly impacts the overall convergence rate. We more precisely – and successfully – apply damping or over-relaxation on both the momentum and the fluid pressure equations:

$$\begin{aligned}\Delta v_i^s{}^k &= \Delta\tau_{v_i} f_u^k + \left(1 - \frac{\nu}{n_i}\right) \Delta v_i^s{}^{k-1}, \\ \Delta\bar{p}{}^k &= \Delta\tau_{\bar{p}} f_{\bar{p}}^k, \\ \Delta p^f{}^k &= \Delta\tau_{p^f} f_{p^f}^k + c \left(1 - \frac{\nu}{n_i}\right) \Delta p^f{}^{k-1},\end{aligned}\tag{4.17}$$

where optimal values of ν reside within the range ($1 \leq \nu \leq 10$). Values of c vary between 0.75 and 1.0 while increasing spatial grid resolution n_i in the direction i . The velocity and both total and fluid pressures fields are computed at each iteration using the following update rule:

$$\begin{aligned} v_i^s{}^k &= v_i^s{}^{k-1} + \Delta v_i^s{}^k, \\ \bar{p}{}^k &= \bar{p}{}^{k-1} + \Delta \bar{p}{}^k, \\ p^f{}^k &= p^f{}^{k-1} + \Delta p^f{}^k. \end{aligned} \tag{4.18}$$

Such a problem-specific damping strategy significantly accelerates the residual convergence rates (Cundall, 1982, 1987; Poliakov et al., 1993). Notably, the elastic analogy of this approach Cundall and Strack (1979) is successfully used in FLAC geotechnical software (Cundall et al., 1993).

Finally, we added an additional numerical compressibility η_b that multiplies the total pressure residual $f_{\bar{p}}$ in the stress definition to accelerate convergence by counterbalancing the divergence-free strain rate definition. Since $f_{\bar{p}}$ vanishes once convergence is reached, this numerical treatment does not impact the physical solution. The described implementation refers to the code appended to this work as supplementary material.

Parallel implementation on GPUs

One underlying reason to explore iterative and matrix-free solving approaches is such methods' ability to deliver the best performance in parallel implementation. Since no global matrix needs to be assembled at any point in the solving procedure, all operations are identical on each grid-point in the computational domain. The finite-difference derivatives are constructed by stencil operation, where only neighbouring values accesses are mandatory. We successfully implemented the PT solver to perform the computation on GPUs, using the CUDA extension to C language. GPUs are multiple-core processors, initially designed to refresh screen pixels at high frame-rates. In the CUDA framework, each small GPU core can concurrently execute several threads. Thus, we assign to each thread one single cell of the computational domain, making it is possible to perform in parallel the same operation simultaneously on the entire domain. A careful implementation of synchronisation barriers avoids race conditions and prevents reading from an array that is not yet fully updated.

An additional step towards parallel implementation can be achieved by porting the single-GPU-based routines to run on several GPUs simultaneously, via message-passing interface (MPI) libraries. Thus, we enable the routines to be executed on distributed-memory machines, multiple-GPU workstations and the largest GPU-based supercomputers. Such an approach is particularly relevant for high resolution 3-D computations involving more than 1 billion grid-points. We expect efficient MPI implementation of the developed PT solver, since only

internal boundaries need to be exchanged using MPI point-to-point communication. Thus, a close to linear weak scaling is ensured by construction, and optimal parallel efficiency is expected.

4.4.3 Comparison of the DI and PT solvers

To validate the two solving strategies, we propose a set of benchmark simulations. The goal is to evaluate the solution’s sensitivity on both the non-linear residual threshold and the spatial resolution. The results we report in this section use the setup described in Section 4.3 as initial conditions. The simulation runs until the high-porosity channel, also called porosity wave, reaches 85% of the domain depth. In this study, we report results for the PT solver using single-precision arithmetic performed on a Nvidia GTX Titan Xp (Pascal) GPU. The DI solver is an extension to the M2Di routines and is implemented in MATLAB, running on an Intel i5 processor using double-precision arithmetic.

The influences of non-linear iterations

The influences of the non-linear threshold are more pronounced in the PT than in the DI approach (Figure 4.4). Both the linear and the non-linear residuals are considered in the PT approach, while in the DI solving procedure, each non-linear step encounters an accurate solve of the linearised problem. The reported end-members of tested absolute non-linear tolerance ($\text{tol}_{\text{nonlin}}$) start at $\text{tol}_{\text{nonlin}} = 1\text{e-}3$ and spread over five orders of magnitude for the DI solver, and over two for the PT solver. Since the PT simulations are performed on a GPU using single-precision arithmetic, the lowest achievable value is $\text{tol}_{\text{nonlin}} = 1\text{e-}5$ (Figure 4.4c). The double-precision arithmetic used in the MATLAB framework for the DI solve allows the absolute non-linear tolerance $\text{tol}_{\text{nonlin}} = 1\text{e-}8$ (Figure 4.4f). At values of $\text{tol}_{\text{nonlin}} = 1\text{e-}3$, both PT and DI solvers show deviations from converged solutions, even though the DI solver shows less dramatic deviation than the PT solver (Figure 4.4b and Figure 4.4e, respectively). The line plots show the evolution over dimensionless time of the maximum normalised porosity values (Figure 4.4a) and for the vertical location of the maximal porosity region (Figure 4.4d). The PT results (lines) show important discrepancy as a function of $\text{tol}_{\text{nonlin}}$, while the DI results (square and triangular markers) are less affected. The major outcome of this sensitivity analysis reports single-precision ($\text{tol}_{\text{nonlin}} = 1\text{e-}5$) PT results that match the best-converged double-precision DI ($\text{tol}_{\text{nonlin}} = 1\text{e-}8$) results. Discrepancy in the non-converged runs ($\text{tol}_{\text{nonlin}} = 1\text{e-}3$) arises from the fact that the DI solver type relies on a converged linearised problem for each non-linear step. In contrast, both linear and non-linear residuals are converged simultaneously in the PT workflow, resulting in different results for non-converged simulations.

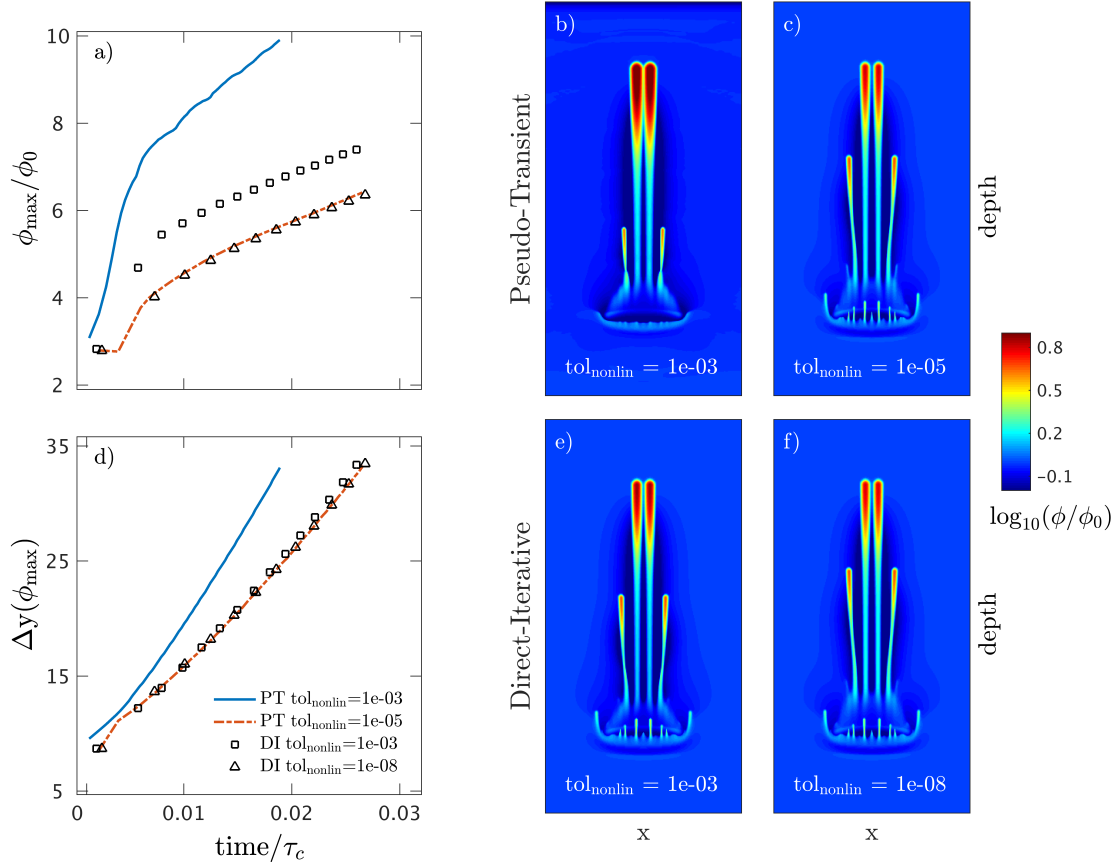


Figure 4.4: Non-linear accuracy of the DI (HM2Di code) and PT (GPU-based) solving approaches for two sets of non-linear tolerances (tol_{nonlin}). (a) The normalised maximal values of porosity (ϕ_{max}/ϕ_0) and (d) the vertical distance from initial perturbation ($\Delta y(\phi_{max})$), both plotted against dimensionless time ($time/\tau_c$). The lines represent the PT solver and the markers the DI solver. The corresponding 2-D final steps are reported for the PT solver for the poorly (b) and accurately (c) converged results, and by analogy (e) and (f) for the DI method, respectively. Since the PT implementation is computed on GPUs using single-precision arithmetic, the lowest achievable non-linear tolerance is $tol_{nonlin} = 1e - 5$. The colour axis represents the \log_{10} of the normalised porosity (ϕ/ϕ_0).

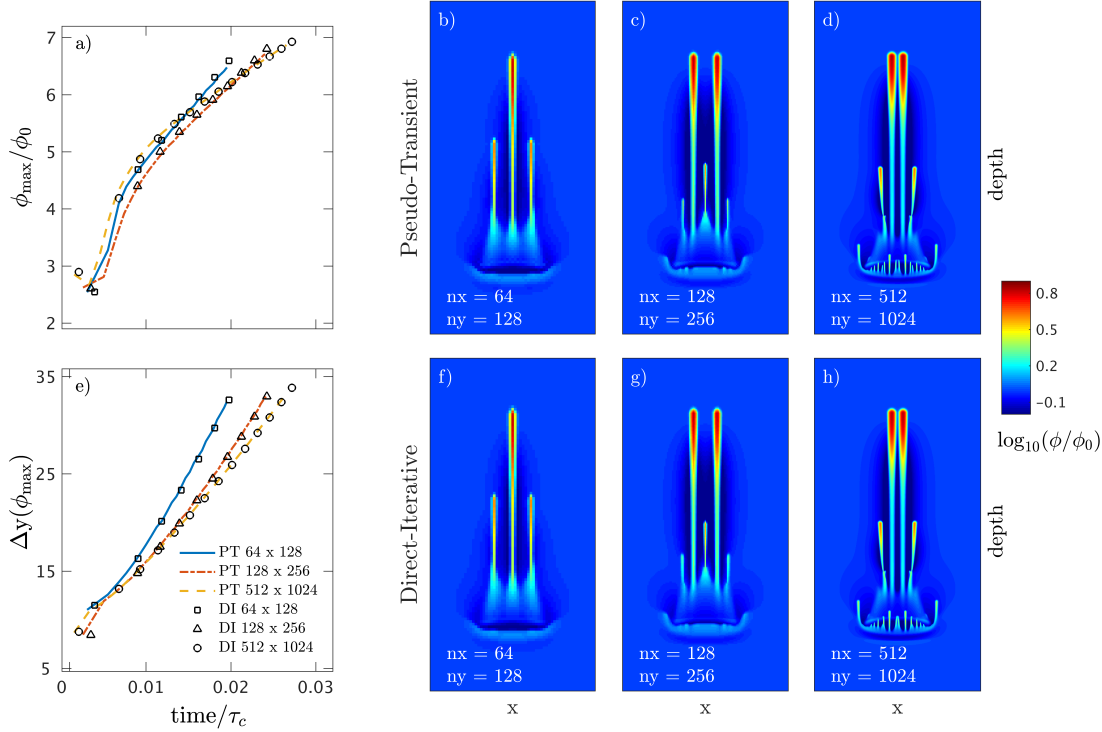


Figure 4.5: Sensitivity analysis of the results on the grid resolution for both the DI (HM2Di code) and the PT (GPU-based) solving approaches. We report a) the normalised maximal values of porosity (ϕ_{max}/ϕ_0) and d) the vertical distance from initial perturbation ($\Delta y(\phi_{max})$), both plotted against dimensionless time ($time/\tau_c$) for three tested resolutions. The lines represent the PT solver and the markers the DI solver. We report the corresponding 2-D final steps for the PT solver for the low- (b), medium- (c) and high- (d) resolution runs, and - by analogy - (f), (g) and (h) for the DI method. The colour axis represents the \log_{10} of the normalised porosity (ϕ/ϕ_0).

The influences of spatial resolution

The continuous increase in computing power allows high spatial resolution simulations to become feasible within reasonable execution times. Investigating the impacts of resolution increase on a given problem allows us to assess whether such high resolution is required and allows us to find the optimal resolution, leading to a physically converged solution. Here, we report the influences of variations in grid resolution for two-phase flow using both PT and DI solver types. The three tested resolutions show different results, but tend to converge towards a stable solution while increasing the number of grid-points (Figure 4.5). Both the PT (Figure 4.5b-d) and DI (Figure 4.5f-h) runs clearly confirm that high spatial resolution is mandatory in order to accurately converge towards a stable solution. The line plots show

the evolution over dimensionless time of the maximum values of normalised porosity (Figure 4.5a) and the vertical location of the maximal porosity region (Figure 4.5e). In contrast to the non-linear tolerance benchmark, the spatial resolution test shows identical behaviour for both DI and PT solving approaches; thus, the markers (DI solver) are located on top of the lines (PT solver) for all tested resolutions (Figure 4.5).

A comparison of 2-D and 3-D runs

We extended the two-phase flow-solver to compute the coupled physics in three spatial dimensions. Thus, the resulting 3-D routines are based on the PT matrix-free implementation and combine C-CUDA to MPI running in parallel on GPU-based distributed-memory supercomputers. The resulting final stages are reported (Figure 4.6) for three different resolutions for both the 2-D and 3-D comparative resolutions. The 3-D setup is identical to the 2-D initial configuration, with an additional y dimension being equivalent to the x dimension (as described in Figure 4.1). The 2-D ellipse is converted to a 3-D ellipsoid, with an identical major/minor axis ratio. A cross-section in the middle of the Y-axis (at $y/2$) is extracted from the 3-D cube in order to be compared to the 2-D setup. The results clearly show a significant yet systematic discrepancy between the 2-D and the 3-D simulations. While the 2-D simulation results (Figure 4.6b-d) tend towards a stable solution that shows two thin distinct channels, the 3-D analogous runs (Figure 4.6f-h) organise high-porosity regions into one single and larger channel. This systematic difference in shape mainly result from the 3-D nature of the investigated process, as discussed in Omlin et al. (2017b). In contrast to other strain localisation mechanisms such as viscous shear-heating or folding and necking, porosity waves cannot be assumed infinite in the third (out-of-plane) dimension when computed in 2-D. The resulting drainage area and available fluid fluxes in 3-D are much more important. Thus, the increased availability of fluid already in the initial condition impacts the overall dynamic. The results' dependence on the number of spatial dimensions must be carefully assessed, since implications in terms of transported volume of fluids and propagation speeds are not negligible.

4.4.4 The performance of the solvers

We use two distinct metrics to report the solvers' performance, the effective memory throughput ($MTP_{\text{effective}}$) and the wall-time. We first evaluate both the MATLAB CPU-based and the C-CUDA GPU-based 2-D PT solver implementations in terms of $MTP_{\text{effective}}$. We then compare the 2-D GPU-based PT solver to the MATLAB-based HM2Di DI solver using the wall-time metric to time the convergence of one non-linear time-step.

The memory access rather than the floating-point operations per second (FLOPs) limit the performance of the PT algorithm, which is designed to perform stencil operation in a matrix-

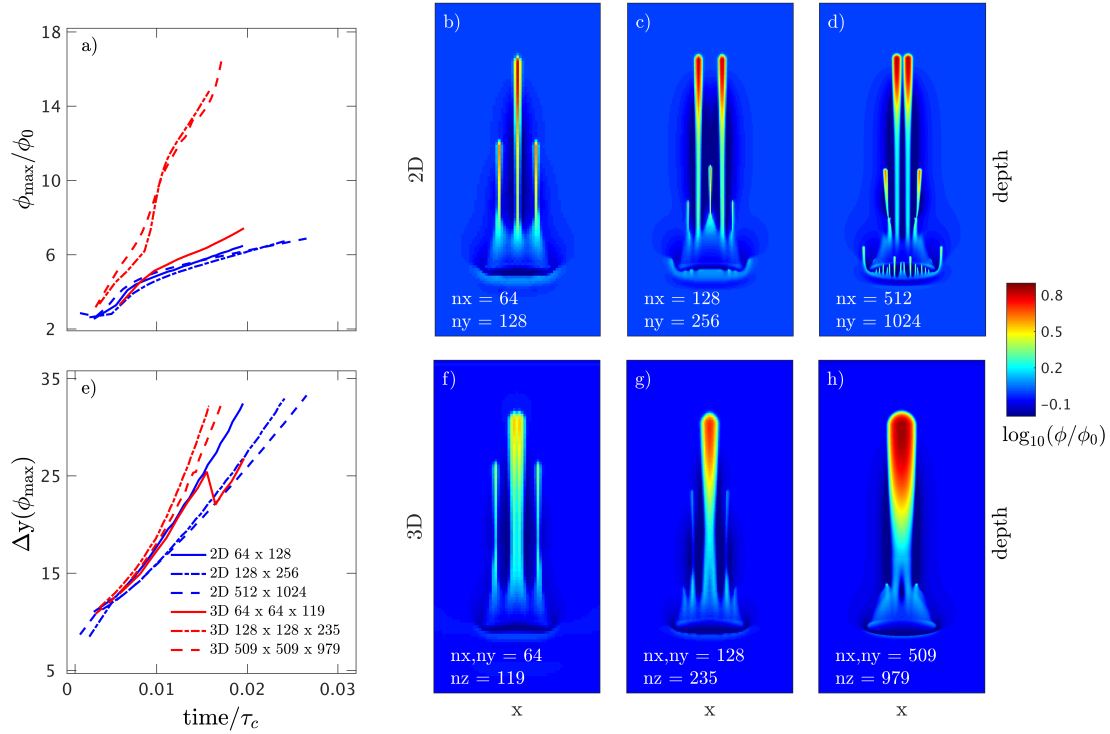


Figure 4.6: Sensitivity analysis of the PT (GPU-based) results on the grid resolution for both the 2-D and the 3-D implementations. (a) the normalised maximal values of porosity (ϕ_{max}/ϕ_0) and (d) the vertical distance from initial perturbation ($\Delta y(\phi_{max})$), both plotted against dimensionless time ($time/\tau_c$) for three tested resolutions. The blue coloured lines represent the 2-D setup and the red coloured lines the 3-D setup. We report the corresponding 2-D final steps for the PT solver for the low- (b), medium- (c) and high- (d) resolution runs. The analogous 3-D setup results (f), (g) and (h) represent a slice of the 3-D domain at $y/2$. The grid resolution in the Y direction is identical to the resolution in the X direction for the 3-D runs. Thus, the high-resolution 3-D runs involve more than $2.5 \cdot 10^8$ grid-points. The colour axis represents the \log_{10} of the normalised porosity (ϕ/ϕ_0).

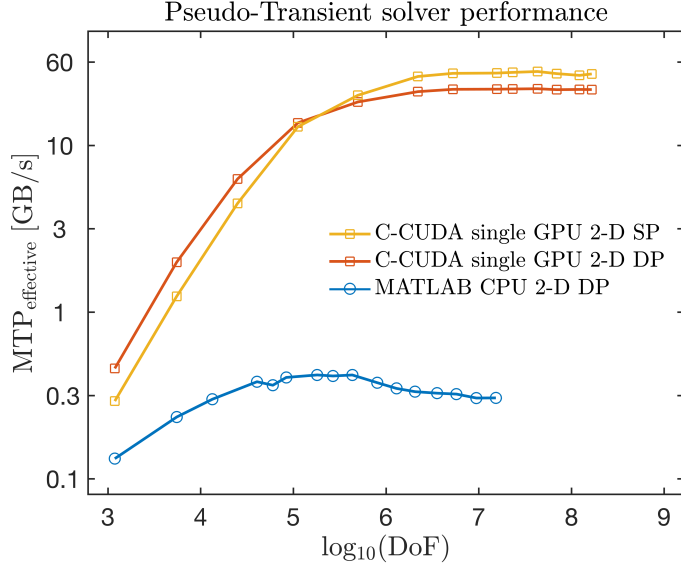


Figure 4.7: Performance evaluation of the PT-based hydro-mechanically coupled solvers in terms of effective memory throughput $\text{MTP}_{\text{effective}}$ in GB/s. We compare the 2-D MATLAB-based implementation running on an Intel i5 (2016) processor (CPU) with 16GB of RAM with 2-D GPU-based implementation using both SP and DP arithmetic, respectively. The GPU is a Nvidia Titan Xp (Pascal) with 16 GB of on-chip RAM. The DoF represents four variables in 2-D (v_x, v_y, \bar{p} and p^f) multiplied by the respective number of grid-points.

free approach. For this reason, we chose the $\text{MTP}_{\text{effective}}$ metric (Omlin et al., 2017c) to evaluate how efficiently data is transferred between the memory and the computation units, in gigabytes per second (GB/s):

$$\text{MTP}_{\text{effective}} = \frac{n_{\text{gridpoints}} \cdot nt \cdot n_{\text{IO}} \cdot \text{precis}}{1e9 \cdot \text{time}_{nt}}, \quad (4.19)$$

where $n_{\text{gridpoints}}$ is the total grid resolution, nt is the number of time-steps or iterations performed, n_{IO} is the number of memory accesses performed, precis is the floating-point precision (either 4 or 8 bytes), and time_{nt} is the time in seconds needed to perform the nt steps. The number of memory accesses (n_{IO}) defines the minimum number of read-and-write or read-only operations required to solve the specific physics. For 2-D coupled hydro-mechanics, the read-and-write operations correspond to the updates of the DoFs (v_x, v_y, \bar{p}, p^f), and three additional read-only operations for converging the non-linear viscosity; in our case, $n_{\text{IO}} = 11$.

The performance benchmark runs are performed using double-precision floating-point arithmetic ($\text{precis} = 8$ bytes) for a fair comparison in particular between MATLAB and C-CUDA implementations. However, we also report $\text{MTP}_{\text{effective}}$ using single-precision arithmetic for the C-CUDA PT solver implementation ($\text{precis} = 4$ bytes). One motivation is the identical accuracy of the converged results (Figure 4.4 & Figure 4.5) for twice lower memory usage and twice faster execution time than double-precision. The $\text{MTP}_{\text{effective}}$ values reported in

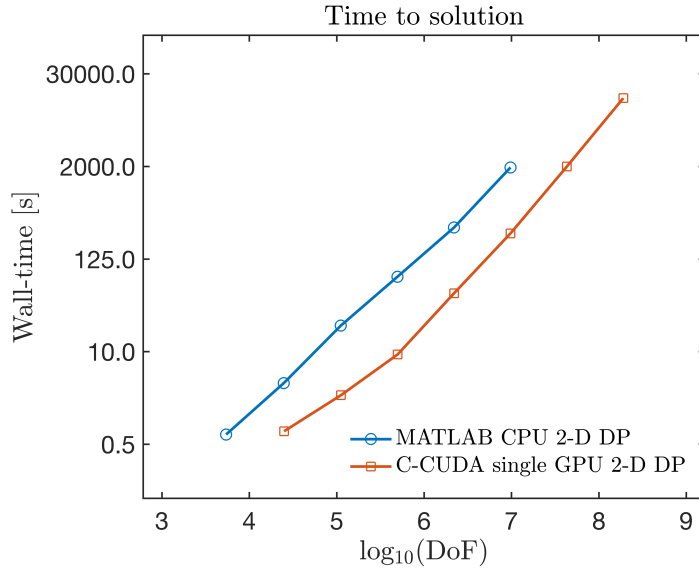


Figure 4.8: Performance evaluation of the PT-based hydro-mechanically coupled solvers in terms of time-to-converge (in seconds) one non-linear step to $\text{tol}_{\text{nonlin}} = 1e - 8$ (wall-time). We compare the PT GPU-based solver (C-CUDA) to the DI CPU (MATLAB) based solver and report only DP arithmetic times.

Figure 4.7 represent the efficiency of memory access for both the vectorised MATLAB CPU and C-CUDA single GPU PT solver implementations. The reported numbers are to be compared to the peak memory throughput values (MTP_{peak}) for the specific hardware, here an Intel i5 CPU and a Nvidia Titan Xp (Pascal) GPU. MTP_{peak} values are measured performing memory copy only, without any computation. Values of MTP_{peak} are in the order of 20 GB/s for the Intel i5 CPU and in the order of 390 GB/s for the Titan Xp GPU. The MATLAB CPU implementation runs at about 2% of the MTP_{peak} , while the C-CUDA GPU codes run about 15% of the MTP_{peak} . The overall performance gain of the parallel GPU implementation vs. the serial CPU routines is more than two orders of magnitude. Some optimisation steps are still possible, to bring the GPU $\text{MTP}_{\text{effective}}$ values closer to MTP_{peak} values. Such considerations are beyond the scope of this study, but may include an increased number of on-the-fly computations, kernel rearranging and register queues (Omlin et al., 2017c).

The effective memory throughput metric reports the efficiency of hardware utilisation for a specific implementation of the hydro-mechanical solver. But to compare the memory-bounded stencil PT iterative approach to the DI solver HM2Di, we use a more relevant measure. Thus, we chose the wall-time metric to assess the overall time-to-solution of a single non-linear step converged to $\text{tol}_{\text{nonlin}} = 1e-8$. The DI solver shows a close to linear increase of wall-time with increasing problem size (DoF). It is implemented in MATLAB and we use an Intel i5 (2016) CPU on a system equipped with 16 GB of RAM for computations. The maximal 2-D problem size fitting in 16 GB RAM represent a numerical domain of 1,024 x 2,048 grid-points,

solved in a wall-time close to 32 minutes, requiring 17 Picard iterations. In comparison, only 4.5 minutes were needed to converge the same problem using the C-CUDA GPU-based PT solver, on a Nvidia Titan Xp (Pascal) accelerator. The speedup vs. the DI implementation is close to one order of magnitude. The PT method's additional key benefit is the maximal problem size that can be resolved using the available 12 GB of GPU on-chip RAM; 134 MDoF represent a numerical 2-D domain size of 4,096 x 8,192 grid-points. On all tested resolutions, the GPU implementation of the PT method outperforms the DI solver (HM2Di) in terms of wall-time. Further, for fair comparison, we realised the study using double-precision arithmetic calculation on the GPU. Moving towards single-precision arithmetic, a domain that is twice as large may fit in the 12 GB of on-chip GPU RAM, and computation efficiency is enhanced, since the GPU's compute chip is largely populated with single-precision arithmetic units. However, the calculations would not allow one to reach the target accuracy of $\text{tol}_{\text{nonlin}} = 1\text{e}-8$.

4.5 Results

4.5.1 Hydro-mechanical fluid focussing in 2-D: A systematic study

We performed a systematic investigation to understand the parameters that influence key properties of the two-phase flow channels, such as their propagation velocity and their shape. We realised more than 400 high-resolution forward 2-D runs, varying the bulk viscosity decompaction over compaction ratio ($R = \frac{\eta D}{\eta C}$) and the bulk to shear viscosity ratio ($C = \frac{\mu_s}{\eta_C \phi_0}$). For each simulation, the computational domain size was discretised in 512 x 1,024 grid-points, and the simulation lasted until the channel reached 85% of the domain depth. We performed single-precision computations on a Nvidia Titan Xp GPU using single-precision arithmetic. The achieved non-linear convergence threshold was 10^{-5} for every run. We realised the entire systematic sequentially on a single GPU, which took about one week for the reported resolution. For each simulation, we monitored (Figure 4.9) the maximal velocity of the upward-propagating porosity wave $\max(V_{\text{wave}})$, the maximal Darcy flux normalised over background Darcy velocity $\frac{\max(\phi[V_y^f - V_y^s])}{V_{\text{BG}}^{\text{Darcy}}}$, and both the minimal and maximal solid velocities $\frac{\min(V_y^s)}{V_{\text{BG}}^{\text{Darcy}}}$ and $\frac{\max(V_y^s)}{V_{\text{BG}}^{\text{Darcy}}}$, respectively. The 2-D systematic maps report an increasing wave velocity, while decreasing both the decompaction over compaction bulk viscosity ratio ($\frac{\eta D}{\eta C}$) and the bulk to shear viscosity ratio ($\frac{\mu_s}{\eta_C \phi_0}$). The normalised Darcy flux partly follows a similar trend, while both the solid minimum and maximum velocities are mainly influenced by the bulk to shear viscosity ratio.

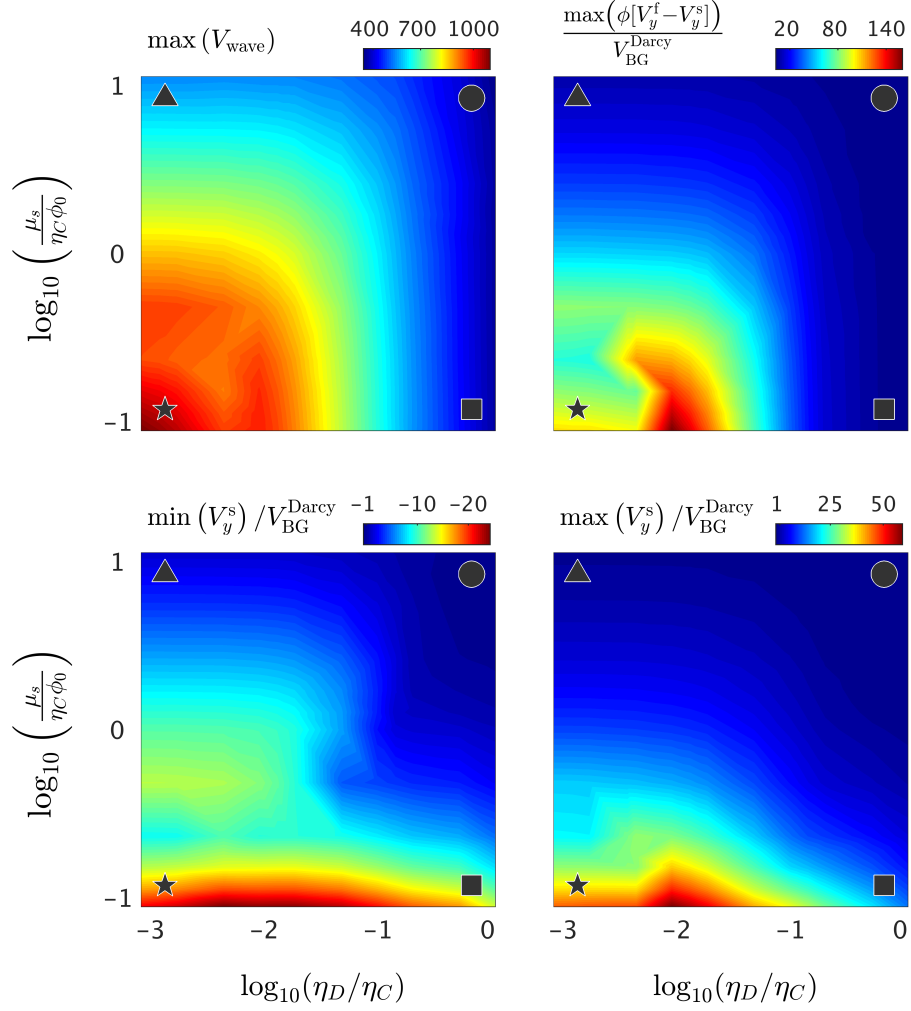


Figure 4.9: Systematic study of decompaction's relative importance over compaction bulk viscosity (η_D/η_C) and shear over bulk viscosity ($\frac{\mu_s}{\eta_C\phi_0}$) ratios. In the upper left panel, we report maximal wave velocities $\max()V_{\text{wave}}$; in the upper right panel, maximal fluid fluxes $\frac{\max(\phi[V_y^f - V_y^s])}{V_{\text{BG}}^{\text{Darcy}}}$; in the lower left panel, the minimal solid velocities values $\min(V_y^s)/V_{\text{BG}}^{\text{Darcy}}$; in the lower right panel, the maximal solid velocities values $\max(V_y^s)/V_{\text{BG}}^{\text{Darcy}}$. The symbols represent four end-member runs for which spatial distribution of $\log_{10}(\phi/\phi_0)$, $\log_{10}\left(\frac{\max(\phi[V_y^f - V_y^s])}{V_{\text{BG}}^{\text{Darcy}}}\right)$ and $\log_{10}(\eta_D/\eta_C)$ are reported in Figure 4.10, Figure 4.11 and Figure 4.12, respectively. The forward model used for this systematic study has a grid resolution of 511 x 1,023 grid-points in 2-D.

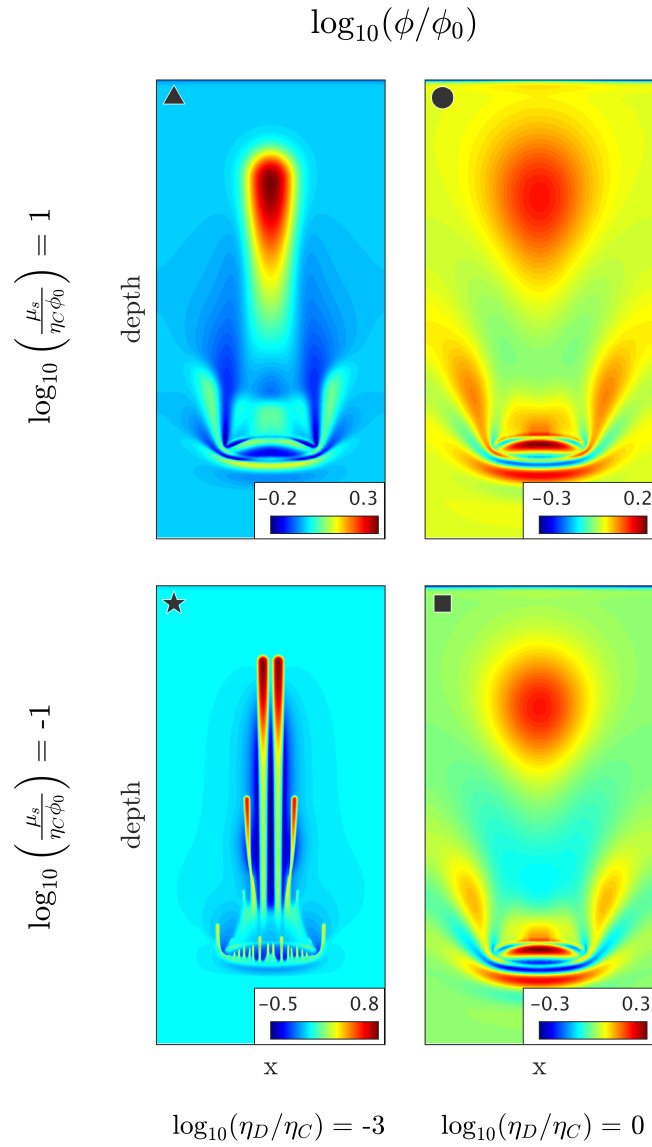


Figure 4.10: We report spatial distribution of normalised porosity $\log_{10}(\phi/\phi_0)$ for the end-member runs in the explored parameter space (Figure 4.9). The final stage (i.e. when the porosity wave reached 85% of the domain depth) is shown with individual colour axis for every parameter combination to encounter the important variations between the different regimes.

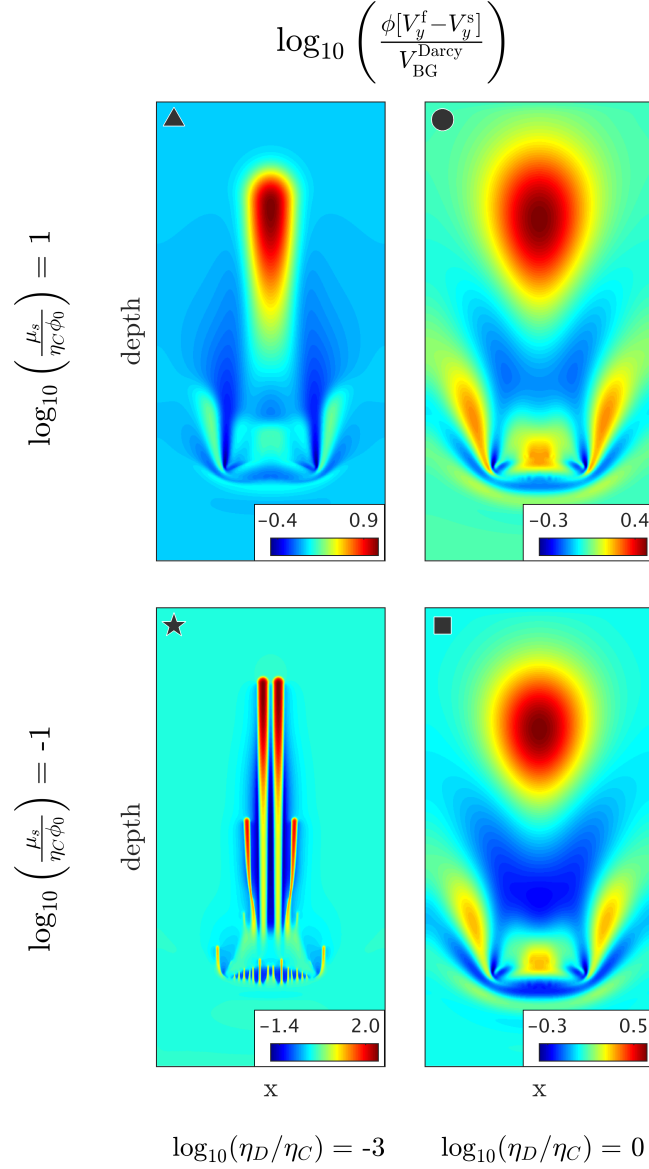


Figure 4.11: We report spatial distribution of normalised vertical fluid flux $\log_{10} \left(\frac{\max(\phi[V_y^f - V_y^s])}{V_{BG}^{Darcy}} \right)$ for the end-member runs in the explored parameter space (Figure 4.9). The final stage (i.e. when the porosity wave reached 85% of the domain depth) is shown with individual colour axes for every parameter combination to encounter the key variations between the different regimes.

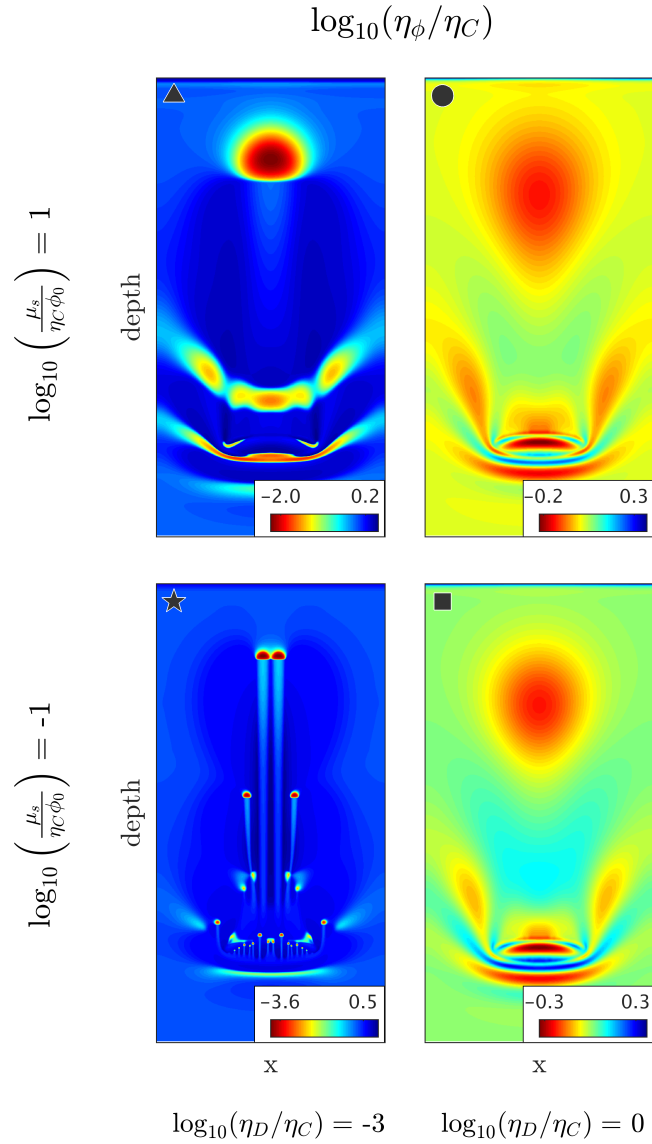


Figure 4.12: We report spatial distribution of normalised bulk viscosity $\log_{10}(\eta_\phi/\eta_C)$ for the end-member runs in the explored parameter space (Figure 4.9). The final stage (i.e. when the porosity wave reached 85% of the domain depth) is shown with an individual colour axis for every parameter, to encounter the key variations between the different regimes. Notably, the colour axes are reversed for this figure; the red values represent low bulk viscosities - enhanced ability to encounter for fast viscous matrix deformation.

4.5.2 Selected end-member runs

Four end-member simulations of this systematic study are highlighted, providing insights into the 2-D spatial distribution of normalised porosity (Figure 4.10), the vertical fluid flux (Figure 4.11) and the non-linear bulk viscosity (Figure 4.12). We report the 2-D field and plot the last time-step for every simulation, where the location and the symbols correspond to those on the systematic maps (Figure 4.9). The selected runs show important variations in the reported end-member combination of parameters, leading to significant changes in propagation regimes. For decompaction over compaction bulk viscosity ratios and bulk to shear viscosity ratios close to 1, the initial high-porosity anomaly propagates upwards in a blob-shaped soliton (circle symbol). The opposite end-member combination of parameters (star symbol) triggers the formation of sharply defined high-porosity channels (Figure 4.9) with locally high fluid fluxes (Figure 4.10) and extremely localised low values of non-linear bulk viscosity (Figure 4.11). Notably, the colour axis is different for every subplot and is therefore reported, since the important changes in regimes induce large variations in the parameter range and may saturate some plots.

4.5.3 Data-collapse

Finally, we represent the maximal wave velocity values of the entire systematic study as a function of the combined decompaction over compaction bulk viscosity $\left(\frac{\eta_D}{\eta_C}\right)$ and bulk to shear viscosity ratios $\left(\frac{\mu_s}{\eta_C\phi_0}\right)$. A naive linear combination of the two parameters shows diverging trends and does not explain the maximal wave velocities (Figure 4.13a). A more elaborate combination of the two investigated parameters, as reported in the X label (Figure 4.13b), shows the relative importance of $\frac{\eta_D}{\eta_C}$ and $\frac{\mu_s}{\eta_C\phi_0}$ on explaining the increasing wave velocity. The plotted data can be cast into three major regimes. Most runs exhibit a single-channel-like mode, tending towards more pronounced focussing and faster propagation rates with an increase in the problem's non-linearity. At some critical point, the single-channel modes transform into a two-channel-like motion. The impact of this macroscopically different behaviour is the shift in the reported maximal velocity values from the displayed fitting curve ($y = 370x^{0.22}$). This major change in propagation regime reflects the underlying non-linearities of the investigated coupled physics. With an increasing viscosity ratio, the effective compaction length (or characteristic length scale) tends to reduce, developing narrower channels. The observed shift in maximal wave velocities is also reflected in the maximal values of fluid fluxes (Figure 4.9).

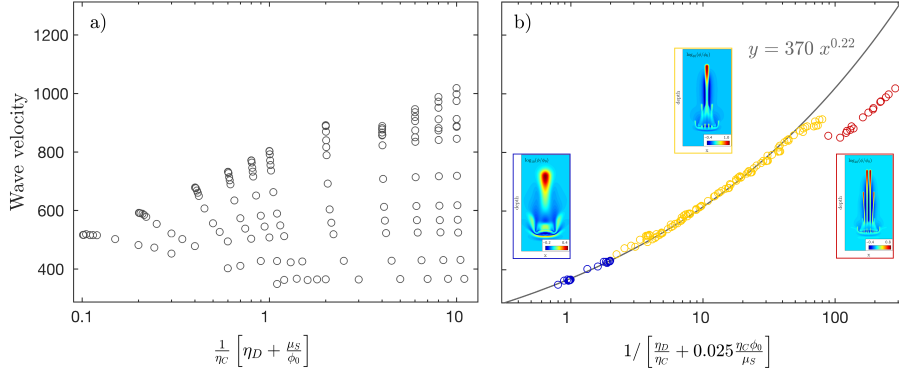


Figure 4.13: Wave velocity represented as function of combined systematically varied parameters, the bulk viscosity and bulk to shear viscosity ratios. (a) Wave velocity plotted against linear combination of bulk decompaction η_D and solid shear viscosity μ_s normalised over compaction viscosity η_C . (b) Wave velocity after data collapse: the formula shown as X-label allows us to collapse the entire systematic study result onto a single power law trend $y = 370x^{0.22}$. The three regimes are highlighted by colours, ranging from diffuse blobs to single-focussed channels, and finally, splitting into two channels towards the X-axis range end.

4.6 Discussion

4.6.1 The genesis of high-porosity channels

Numerically accurate resolving of coupled and non-linear two-phase flow and including decompaction weakening as focussing mechanism allows one to predict the *spontaneous* formation and propagation of high-porosity channels (Figure 4.2), developing from an initial region of elevated porosity, such as a fluid reservoir or a region containing partial melt. The buoyant fluid generates forces on the upper part of the reservoir, leading to increase in fluid pressure. The effective pressure decreases accordingly and decompaction occurs, permitting the fluid anomaly to move upwards. Pressure-sensitive bulk rheology further results in lower bulk viscosity values in the regions affected by decompaction, leading to enhanced upward-migration. Decompaction weakening is responsible for orders of magnitude faster decompaction (opening of pores) at the top of the channels compared to compaction (closure of pores) at the tail of the channel. The fluid pressure gradient decreases from regions outside the channels towards the inside of the channels, resulting in fluid drainage from the surrounding regions affected by the presence of a propagating channel. This mechanism enables the self-sustenance of the propagation of the porosity waves and results in fluid depletion in the rims of the channels. To ensure mass-balance, those rims thus compact and turn into high viscosity regions. Thus, the channels' structure may remain detectable even if the channels are dormant.

Both the channel spacing and the channel width are mainly controlled by the compaction length. Thus, the three introduced scales (equation (4.9)) can be used to predict the effective

Description	Shale	Limestone	Sandstone	Crustal rocks	Units
Bulk viscosity (η_ϕ)	1e13	1e15	1e16	1e16	[Pa.s]
Permeability (k_ϕ)	1e-19	1e-16	1e-14	1e-13	[m ²]
Fluid viscosity (μ_f)	8e-4	8e-4	8e-4	1	[Pa.s]
Channel width	0.1 - 1	10 - 100	100 - 500	100 - 500	[m]
Propagation speed	0.3	300	10'000	100	[m/yr]

Table 4.2: Scaling of the numerical results to representative values for reservoir rocks (Räss et al., 2017a; Räss et al., 2014, and references therein) and crustal environments (McKenzie, 1984).

size and propagation speed of high-porosity channels for different reservoir or metamorphic environments, ranging from kilometre to metre size features, with propagation velocities from metres per year in low-permeable shales to kilometres per years in permeable sandstones (Table 4.2).

4.6.2 Prediction of localised flow regimes

The power law relationship between maximal wave velocities and the combination of viscosity ratios (Figure 4.13b) allows one to give an estimate on potential flow enhancement for relevant and well-defined rheological parameters. Further, a closer analysis of the various maximal velocity values shows a distinct trend, supporting the wave-like behaviour of porosity waves. The maximal dimensionless wave velocity is close to 1,000. The maximal recorded vertical fluid fluxes are about one order of magnitude lower, with values of close to 140. The solid velocities are even one order of magnitude lower than the fluid fluxes; thus, two orders of magnitude lower than wave velocities. This clearly shows that fast-propagating high-porosity channels trigger minor solid displacement and moderate to high fluid fluxes. It is interesting to note the similarity in maximal positive and negative values for the solid velocity components' characteristics for percolation flow instead of circulation observed in diapirism regimes (Scott, 1988).

4.6.3 Extension to power law shear viscosity in 3-D

In this study, we solved the coupled two-phase flow model for non-linear bulk viscosity (η_ϕ), dependent on effective pressure (p_e) and porosity (ϕ). To better understand the relative importance of the shear viscosity (μ_s) compared to the bulk viscosity ($\frac{\mu_s}{\eta_C \phi_0}$), we used a linear (thus, constant) shear viscosity and varied it systematically in comparison to the bulk viscosity. We conclude on an enhanced focussing, narrower channels and faster wave velocities the lower $\frac{\mu_s}{\eta_C \phi_0}$ is. In fact, some parameters may significantly influence the solid shear viscosity,

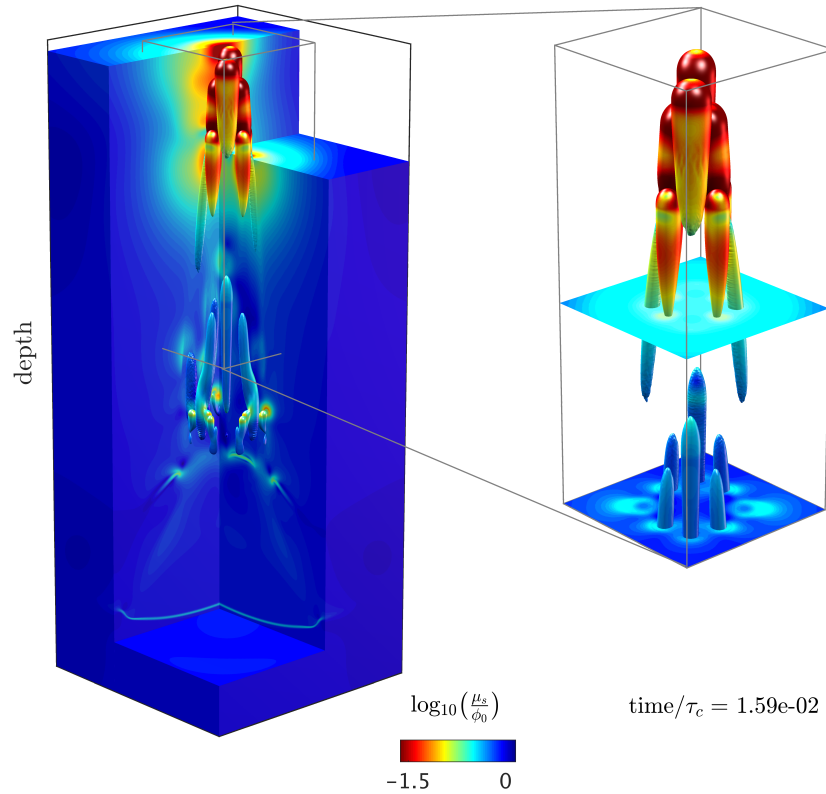


Figure 4.14: Strain rate-dependant non-linear solid shear viscosity normalised over background porosity (μ_s/ϕ_0) resulting from the propagation of high-porosity channels in three dimensions. The initial condition used for this simulation is presented in Figure 4.1b with $\eta_D/\eta_C = 500$. The numerical resolution is $1,023 \times 1,023 \times 2,048$ grid-points in 3-D, which represents a total of $2 \cdot 10^9$ grid-points. The simulation took three weeks to perform the close to 10,000 time-steps on 128 Nvidia Titan X GPUs, using the entire octopus GPU-based supercomputer designed by the Scientific Computing Group and hosted by the Institute of Earth Sciences at the University of Lausanne. The tube-shaped isosurface contours 1.5 order of magnitude permeability increase from background values. The subplot magnifies the central part of the computational domain ($290 \times 290 \times 760$ grid-points) and provides a detailed view of strain distribution of and around the developing fluid-conducting chimneys. Regions of elevated strain rates exhibit a close to two orders of magnitude decreases in solid shear viscosity values.

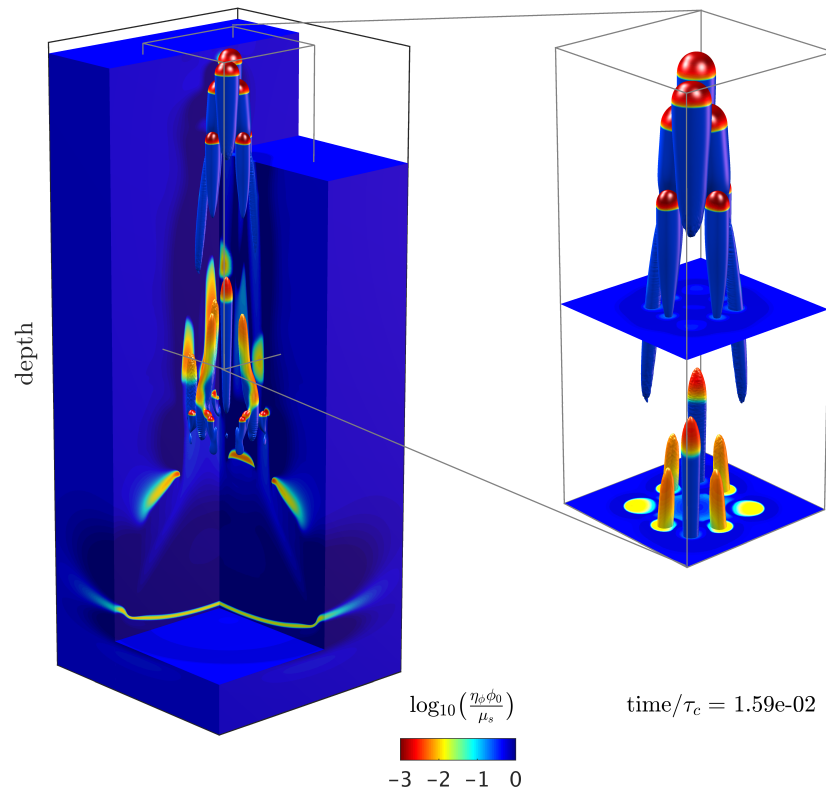


Figure 4.15: Non-linear bulk viscosity normalised over solid shear viscosity values $\left(\frac{\eta_{\phi}\phi_0}{\mu_s}\right)$ for the simulation described in Figure 4.14. The spatial distribution of viscosity ratios shows low values concentrated at the tip of the channels, and highlight the non-linear dependence of both bulk and shear viscosity on effective pressure $(\bar{p} - p^f)$.

such as strain rates or temperature. Thus, we performed high-resolution 3-D simulation with power law solid shear viscosity, having $n = 3$ (equation (4.10)). Here, the resulting solid shear viscosity (Figure 4.14) non-linearly depends on the second strain rate invariant. The upward-propagating porosity waves generate highly focussed matrix strain rates, which tend to locally lower the background shear viscosity by about one order of magnitude. It is a physical mechanism to locally decrease the $\frac{\mu_s}{\eta_\phi \phi_0}$ ratio used in the systematic study. The non-linear bulk viscosity (η_ϕ) is sensitive to both the porosity averaged shear viscosity and the effective pressure (p_e). In the present scenario, the solid shear viscosity (μ_s) is also sensitive to the matrix strain rate. Thus, the spatial distribution of $\frac{\eta_\phi \phi_0}{\mu_s}$ ratio (Figure 4.15) confirms an enhanced dependence of η_ϕ on p_e .

4.6.4 The influences of far-field tectonic regimes

Preliminary studies on the influences of far-field tectonic regimes on two-phase environments (Figure 4.16) show channel distribution to be sensitive to shear deformation, while channel geometry remains mostly unaffected. Propagation speed or channel extent is maximal in extensional regimes, intermediate in shear regimes, and minimal in compressional regimes. Further, vertical channel connectivity seems maximal in horizontal shear regimes. Total pressure values reflect the mean stress state in the model. The results clearly show deviation from lithostatic pressure conditions. Changes in non-lithostatic pressure conditions in time and space have major implications in application to hydro-chemical and metamorphic reactions, such as methane hydrate expulsion in sedimentary basins.

4.6.5 Benefits and limitations of the pseudo-transient method

The pseudo-transient and direct-iterative solvers implemented here both us to accurately resolve the non-linear coupled two-phase flow physics, in reasonable wall-time. Modern CPUs and the current amount of RAM present on modern desktop systems enable to compute numerical domains of up to 2 million grid-points using DI solvers that are robust and handle large contrasts in material properties such as variable viscosity fairly well. Although the DI solver types are efficient in addressing 2-D models, it is not viable to utilise them to resolve high-resolution 3-D setups.

The current development of hardware accelerators such as GPUs enables new possibilities for iterative methods. The massive number of arithmetic units of multiple-core computing devices such as GPUs allows one to perform computations at almost no cost. Further, the constant increase in memory bandwidth enables rapid memory transfers between on-chip memory and computing cores. Thus, these latest hardware developments put matrix-free iterative methods in the spotlight and make PT solvers fully competitive with matrix-based solvers,

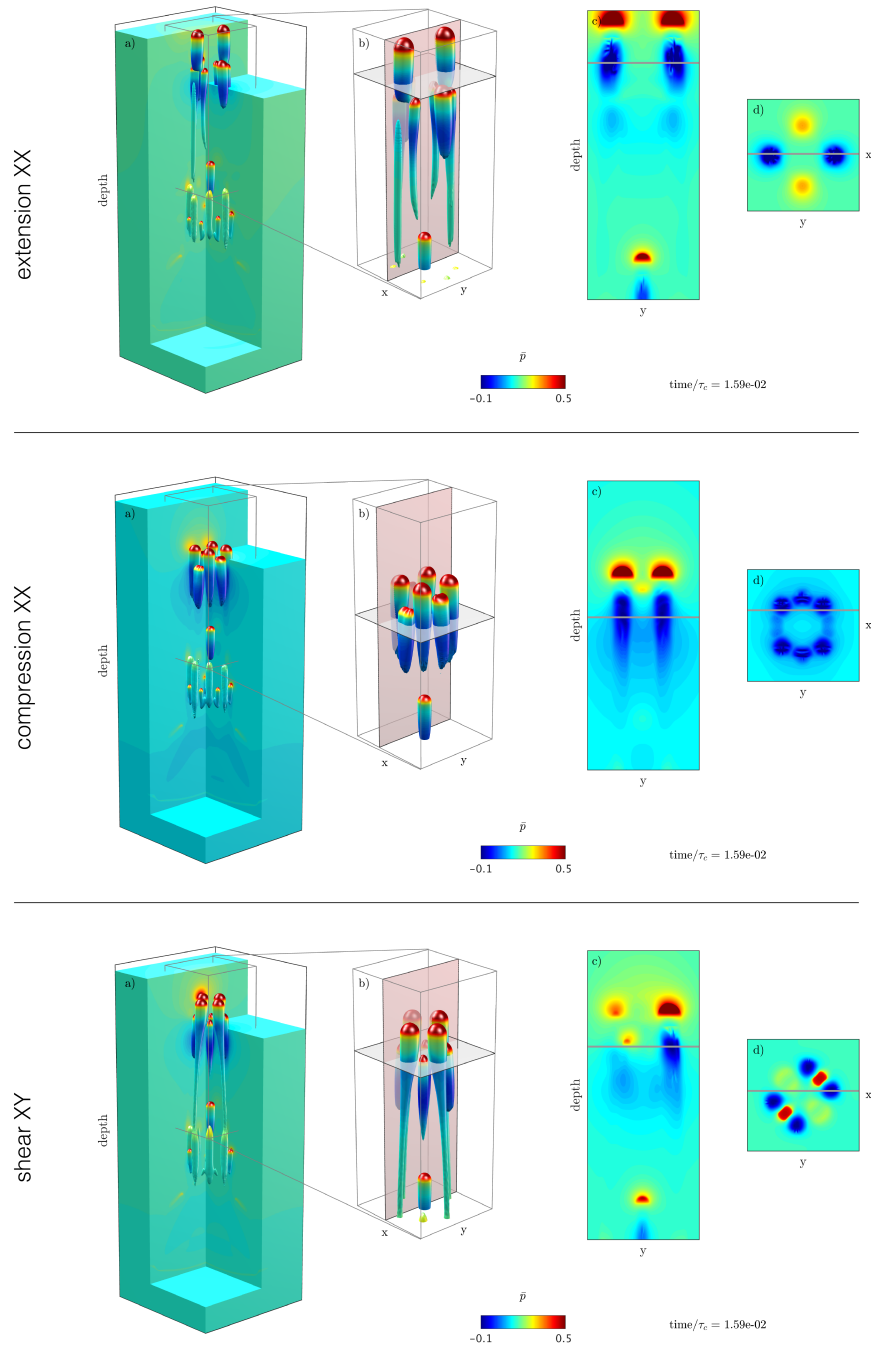


Figure 4.16: Total pressure distribution after dimensionless time = $1.59e-02$ for the 3-D setup described in Figure 4.14, as a function of three far-field tectonic regime, namely extension along the X-axis, compression along the X-axis, and shear in the XY horizontal plane. (a) Overview of the high-porosity channels' distribution. (b) Zoom-in on the region of interest, showing total pressure values interpolated onto a isosurface of 1.5 order of magnitude increase in permeability. (c) YZ slice at $x/2$ of the b) plot. (d) XY slice at given depth as shown on b).

even on 2-D setups. Since PT-based solvers using finite-difference stencils to evaluate the partial derivatives by construction access only neighbouring values, PT solvers show a close-to-optimal parallel efficiency, and remain valid in 3-D. The addition of point-to-point MPI communication directly enables the PT solvers to run on distributed-memory supercomputers. Thus, we were able to produce the 3-D results (Section 4.6.3) in less than 72 hours, calculating more than 10,000 time-steps on more than $2 \cdot 10^8$ grid-points. We involved 128 Titan X GPUs available in the octopus GPU-based supercomputer, hosted by the Institute of Earth Sciences at University of Lausanne.

In sum, the key benefits of the PT method are as follows: i) we obtain identical results as the DI method, ii) the implementation of PT solver types using the finite-difference method is straightforward and results in short, readable codes (see the MATLAB PT codes in the supplementary material), iii) PT solver types outperform DI solver types when ported to GPUs, and are therefore fully competitive, and iv) PT solvers are a viable option when investigating 3-D setups; further, MPI parallelisation can readily be implemented for distributed-memory parallelisation. Finally, the approach's limitations reside mainly in deprecated convergence rates for large material parameter contrasts over narrow spatial extent and the need for additional effort finding optimal numerical parameters for highly non-linear setups.

4.7 Conclusions

We successfully developed 2-D and 3-D routines to solve coupled hydro-mechanical problems. We benchmarked both the pseudo-transient-based and direct-iterative-based two-phase flow-solvers and report their relative sensitivity on the non-linear threshold and the numerical grid resolution. We conclude that both methods are in agreement, since the GPU-based pseudo-transient matrix-free solver and the CPU-based direct-iterative solver unveil identical results. We further highlight the strong impacts of non-sufficient grid resolution and non-linear threshold on physical results after a large number of time-steps. We performed a systematic investigation of hydro-mechanical coupled flow in deforming porous media. The outcome of the data collapse is a scaling power law that predicts the propagating wave velocity as a combination of viscous bulk and shear rheology. The 3-D results show that the shape of the high-permeability chimney is not sensitive to the far-field tectonic regime. Instead, the regional deformation affects the spatial distribution of chimneys and has a non-negligible effect on their propagation speed.

We also show that the MPI-based and GPU-based implementation of the PT routines allowed us to realise extremely high-resolution 3-D simulations involving over $2 \cdot 10^9$ grid-points. This significant increase in affordable resolution enabled us to tackle mega-pixel resolution in all three dimensions. The 3-D results provide novel insights towards better understanding the physics of chimney formation, including strain rate dependant non-linear solid shear rheology.

Acknowledgments

The authors thank Nina Simon, Stefan Schmalholz and Viktoryia Yarushina for enlightening discussion during the entire project, and are grateful to Samuel Omlin for his long participation in developing the HPC application related to the current research. We acknowledge Philippe Logean for his constant support and development with the GPU-based octopus supercomputer.

Appendix

4.A The direct-iterative scheme

For each linear step, the global correction vector $\delta\mathbf{x}$ can be obtained by performing a direct factorisation of the entire \mathbf{M}_{HM} matrix. This approach is referred to as a coupled solve and results in a long solving time. It also does not scale very well with an increase in physical domain size. An alternative is to proceed to a decoupled linear solve, by designing a two step substitution procedure; thus, precomputing two separate Schur complements (denoted by $\widetilde{}$):

$$\begin{aligned}\widetilde{\mathbf{P}\mathbf{P}} &= \left[\mathbf{P}\mathbf{P} - \mathbf{P}\mathbf{P}\mathbf{F} \left(\widehat{\mathbf{P}\mathbf{F}} \mathbf{P}\mathbf{F}\mathbf{P} \right) \right], \\ \widetilde{\mathbf{M}} &= \left[\mathbf{M} + \mathbf{G} \left(\widetilde{\mathbf{P}\mathbf{P}} \mathbf{G}^T \right) \right],\end{aligned}\tag{4.A.1}$$

where $\widehat{\mathbf{P}\mathbf{F}} = \text{diag}^{-1}(\mathbf{P}\mathbf{F})$ and $\widetilde{\mathbf{P}\mathbf{P}} = \text{diag}^{-1}(\widehat{\mathbf{P}\mathbf{P}})$ are the approximation (diagonal preconditioner, denoted by $\widehat{}$) of the inverse of $\mathbf{P}\mathbf{F}$ and $\mathbf{P}\mathbf{P}$, respectively. The velocity as well as the total and fluid pressure corrections can be iteratively retrieved by applying the action of $\widetilde{\mathbf{M}}^{-1}$, $\widetilde{\mathbf{P}\mathbf{P}}^{-1}$ and $\mathbf{P}\mathbf{F}^{-1}$, the inverse of the velocity, the total pressure and the fluid pressure blocks, to $\widetilde{\mathbf{f}}_{\mathbf{u}}$, $\widetilde{\mathbf{f}}_{\mathbf{p}}$ and $\mathbf{f}_{\mathbf{p}^f}$:

$$\begin{aligned}\delta\delta\mathbf{u} &= \widetilde{\mathbf{M}}^{-1} \underbrace{\left[\mathbf{f}_{\mathbf{u}} - \mathbf{G} \widetilde{\mathbf{P}\mathbf{P}}^{-1} \underbrace{(\mathbf{f}_{\mathbf{p}} - \mathbf{P}\mathbf{P}\mathbf{F}^{-1}\mathbf{f}_{\mathbf{p}^f})}_{\widetilde{\mathbf{f}}_{\mathbf{p}}} \right]}_{\widetilde{\mathbf{f}}_{\mathbf{u}}}, \\ \delta\delta\mathbf{p} &= \widetilde{\mathbf{P}\mathbf{P}}^{-1} \left[\widetilde{\mathbf{f}}_{\mathbf{p}} - \mathbf{G}^T \delta\delta\mathbf{u} \right], \\ \delta\delta\mathbf{p}^f &= \mathbf{P}\mathbf{F}^{-1} \left[\mathbf{f}_{\mathbf{p}^f} - \mathbf{P}\mathbf{P}\mathbf{F} \delta\delta\mathbf{p} \right].\end{aligned}\tag{4.A.2}$$

The global correction vector $\delta\mathbf{x}$ is retrieved by iteratively updating the computed velocity, total pressure and fluid pressure corrections increments $\delta\delta\mathbf{u}$, $\delta\delta\mathbf{p}$ and $\delta\delta\mathbf{p}^f$, respectively, until

the linear residuals reach the tolerance threshold of the linear solver $\|\mathbf{f}\|_{L_2} < \text{tol}_{\text{lin}}$. Taking advantage of symmetrical and positive-definite velocity Schur complement and fluid pressure blocks ($\widetilde{\mathbf{M}}$ and \mathbf{PF}), a Cholesky factorisation followed by iterative back-substitutions can be performed to compute the corrections increments (equation (4.A.2)). Since the total pressure Schur complement ($\widetilde{\mathbf{PP}}$) is a diagonal block, its trivial inverse can readily be used in the solving procedure.

The Cholesky factorisation optimally exploits the modern CPU capabilities, since it relies on highly optimised libraries of BLAS2 operations and is therefore a powerful approach to address the solve of a linear system. The routines are either available from the CHOLMOD functions included in the SuiteSparse package developed by T. Davis (Chen et al., 2008) and are now also accessible via the MATLAB `chol()` function. An optimised back-substitution routine is available using the SuiteSparse functions `cs_ltsolve()` and `cs_lsolve()` instead of MATLAB's native `\` command. The linear operators can be assembled out of the triplet vectors using the optimised `sparse2()` function. The SuiteSparse package can be downloaded from the developer's website (<http://faculty.cse.tamu.edu/davis/suitesparse.html>).

The non-linearities listed at the end of Section 4.2 require an appropriate treatment in the solving procedure. Thus, the linear solve performed using the linearised operators (equation (4.12)) must to be repeated until the non-linear residuals, in this case \mathbf{f} , reaches the desired threshold value according to $\|\mathbf{f}\|_{L_2} < \|\mathbf{f}\|_{L_2}^{\text{initial}} \text{tol}_{\text{nonlin}}$.

4.B Numerical transient time

The essence of the PT continuation method resides in introducing a transient or numerical time derivative to the equation of interest and to iterate on until the steady state is reached. At that stage, the time derivative vanishes and the equation is solved. The following generic 1-D example illustrates this basic workflow. Assuming one must find the solution to the elliptic problem (equation (4.B.1)):

$$C = \frac{\partial^2 A}{\partial x^2}, \quad (4.B.1)$$

without performing a direct solve. The first step is to rearrange the equation, sending all the terms to the right-hand-side, assembling the residual:

$$0 = \frac{\partial^2 A}{\partial x^2} - C = \mathbf{f}_A. \quad (4.B.2)$$

It is now possible to introduce a numerical time derivative on the left-hand-side of the equation (4.B.2):

$$\frac{dA}{d\tau} = \mathbf{f}_A, \quad (4.B.3)$$

and use it to iteratively reach the steady state of the system:

$$A^k = A^{k-1} + \Delta\tau f_A, \quad (4.B.4)$$

where k and $\Delta\tau$ are the pseudo-transient iteration count and time-step, respectively. Once A stops changing over successive iterations, the numerical time derivative vanishes. Thus, the residual f_A has converged towards machine precision, and the equation (4.B.1) is solved. Notably, first, the method is also applicable if f_A contains non-linear terms – as present in the two-phase flow equations described here. Second, the solution of parabolic equation using the PT continuation leads to an implicit solution, since both the temporal and the spatial derivative are included in the residual. The solution of the unknown field satisfies the equation at time $(t + dt)$. Additional details regarding the PT continuation approach can be found in a non-exhaustive selected contribution (Kelley and Keyes, 1998; Kelley and Liao, 2013) and references therein.

In the PT continuation iterations, we implemented relaxation of non-linear quantities such as bulk viscosity η_ϕ , effective permeability over fluid shear viscosity $\frac{k_\phi}{\mu_f}$ and non-linear solid shear viscosity μ_s using the following generic relaxation approach:

$$\xi^k = \exp \left[(1 - \text{rel}_\xi) \ln \left(\xi^{k-1} \right) + \text{rel}_\xi \ln \left(\xi^{\text{phys}} \right) \right], \quad (4.B.5)$$

where rel_ξ ($0 \leq \text{rel}_\xi \leq 1$) is the relaxation parameters. ξ is the non-linear quantity we seek to solve for, presently $\xi = \left(\eta_\phi, \frac{k_\phi}{\mu_f}, \mu_s \right)$. We iteratively approached the physical non-linear quantities ξ^{phys} in k iterations. The procedure has converged when the difference between the iterative quantities and the physical one vanishes; thus:

$$\left\| \text{abs} \left(\xi^{\text{phys}} - \xi^k \right) \right\|_{L2} \leq \text{tol}_{\text{nonlin}}. \quad (4.B.6)$$

Bibliography

- Ague, J. J., 2011. Extreme channelization of fluid and the problem of element mobility during Barrovian metamorphism. *American Mineralogist* 96 (2-3), 333–352.
- Appold, M. S., Nunn, J. A., 2002. Numerical models of petroleum migration via buoyancy-driven porosity waves in viscously deformable sediments. *Geofluids* 2 (3), 233–247.
- Barcilon, V., Richter, F. M., 1986. Nonlinear waves in compacting media. *Journal of Fluid Mechanics* 164 (1), 429.
- Baud, P., Schubnel, A., Wong, T.-f., 2000. Dilatancy, compaction, and failure mode in Solnhofen limestone. *Journal of Geophysical Research: Solid Earth* 105 (B8), 19289–19303.

- Berndt, C., 2005. Focused fluid flow in passive continental margins. *Philosophical Transactions of the Royal Society of London A: Mathematical, Physical and Engineering Sciences* 363 (1837), 2855–2871.
- Brantut, N., Heap, M., Meredith, P., Baud, P., 2013. Time-dependent cracking and brittle creep in crustal rocks: A review. *Journal of Structural Geology* 52, 17–43.
- Cacace, M., Jacquy, A. B., 2017. Flexible parallel implicit modelling of coupled thermal–hydraulic–mechanical processes in fractured rocks. *Solid Earth* 8 (5), 921.
- Cai, Z., Bercovici, D., 2013. Two-phase damage models of magma-fracturing. *Earth and Planetary Science Letters* 368, 1–8.
- Cartwright, J., Santamarina, C., 2015. Seismic characteristics of fluid escape pipes in sedimentary basins: Implications for pipe genesis. *Marine and Petroleum Geology* 65, 126–140.
- Cathles, L., Su, Z., Chen, D., 2010. The physics of gas chimney and pockmark formation, with implications for assessment of seafloor hazards and gas sequestration. *Marine and Petroleum Geology* 27 (1), 82–91.
- Chen, Y., Davis, T. A., Hager, W. W., Rajamanickam, S., 2008. Algorithm 887: CHOLMOD, supernodal sparse Cholesky factorization and update/downdate. *ACM Transactions on Mathematical Software (TOMS)* 35 (3), 22.
- Connolly, J., Podladchikov, Y., 2007. Decompaction weakening and channeling instability in ductile porous media: Implications for asthenospheric melt segregation. *Journal of Geophysical Research: Solid Earth* 112 (B10).
- Connolly, J., Podladchikov, Y. Y., 1998. Compaction-driven fluid flow in viscoelastic rock. *Geodinamica Acta* 11 (2-3), 55–84.
- Connolly, J., Podladchikov, Y. Y., 2000. Temperature-dependent viscoelastic compaction and compartmentalization in sedimentary basins. *Tectonophysics* 324 (3), 137–168.
- Connolly, J. A. D., Podladchikov, Y. Y., 2014. An analytical solution for solitary porosity waves: dynamic permeability and fluidization of nonlinear viscous and viscoplastic rock. *Geofluids* 15 (1-2), 269–292.
- Costa, A., 2006. Permeability-porosity relationship: A reexamination of the Kozeny-Carman equation based on a fractal pore-space geometry assumption. *Geophysical Research Letters* 33 (2), L02318.
- Cundall, P., Coetzee, M., Hart, R., Varona, P., 1993. *FLAC users manual*. Itasca Consulting Group, USA.

- Cundall, P. A., 1982. Adaptive density-scaling for time-explicit calculations. Proc. of the 4th Int. Con. on Numerical Methods in Geomechanics, Edmonton, S, 23–26.
- Cundall, P. A., 1987. Distinct element models of rock and soil structure. Analytical and Computational Methods in Engineering Rock Mechanics, Allen & Unwin, London, 129–163.
- Cundall, P. A., Strack, O. D., 1979. A discrete numerical model for granular assemblies. *geotechnique* 29 (1), 47–65.
- Dannberg, J., Heister, T., 2016. Compressible magma/mantle dynamics: 3-D, adaptive simulations in ASPECT. *Geophysical Journal International* 207 (3), 1343–1366.
- David, C., Dautriat, J., Sarout, J., Delle Piane, C., Menéndez, B., Macault, R., Bertauld, D., 2015. Mechanical instability induced by water weakening in laboratory fluid injection tests. *Journal of Geophysical Research: Solid Earth* 120 (6), 4171–4188.
- Dymkova, D., Gerya, T., 2013. Porous fluid flow enables oceanic subduction initiation on Earth. *Geophysical Research Letters* 40 (21), 5671–5676.
- Frankel, S. P., 1950. Convergence rates of iterative treatments of partial differential equations. *Mathematical Tables and Other Aids to Computation* 4 (30), 65–75.
- Gradmann, S., Beaumont, C., 2012. Coupled fluid flow and sediment deformation in margin-scale salt-tectonic systems: 2. Layered sediment models and application to the northwestern Gulf of Mexico. *Tectonics* 31 (4).
- Gradmann, S., Beaumont, C., Ings, S. J., 2012. Coupled fluid flow and sediment deformation in margin-scale salt-tectonic systems: 1. Development and application of simple, single-lithology models. *Tectonics* 31 (4).
- Haga, J. B., Osnes, H., Langtangen, H. P., 2012. A parallel block preconditioner for large-scale poroelasticity with highly heterogeneous material parameters. *Computational Geosciences* 16 (3), 723–734.
- Huq, F., Smalley, P. C., Mørkved, P. T., Johansen, H., Johansen, I., Yarushina, V., 2017. International Journal of Greenhouse Gas Control The Longyearbyen CO2 Lab : Fluid communication in reservoir and caprock. *International Journal of Greenhouse Gas Control* 63 (May), 59–76.
- Hustoft, S., Bünz, S., Mienert, J., 2010. Three-dimensional seismic analysis of the morphology and spatial distribution of chimneys beneath the Nyegga pockmark field, offshore mid-Norway. *Basin Research* 22 (4), 465–480.

- Iyer, K., Rüpke, L., Galerne, C. Y., 2013. Modeling fluid flow in sedimentary basins with sill intrusions: Implications for hydrothermal venting and climate change. *Geochemistry, Geophysics, Geosystems* 14 (12), 5244–5262.
- Joshi, A., Appold, M. S., 2016. Potential of porosity waves for methane transport in the Eugene Island field of the Gulf of Mexico basin. *Marine and Petroleum Geology* 75, 1–13.
- Judd, A., Hovland, M., 2007. *Seabed Fluid Flow*. Cambridge University Press, Cambridge.
- Katz, R. F., Weatherley, S. M., 2012. Consequences of mantle heterogeneity for melt extraction at mid-ocean ridges. *Earth and Planetary Science Letters* 335-336, 226–237.
- Keller, T., Katz, R. F., Hirschmann, M. M., 2017. Volatiles beneath mid-ocean ridges: Deep melting, channelised transport, focusing, and metasomatism. *Earth and Planetary Science Letters* 464, 55–68.
- Keller, T., May, D. A., Kaus, B. J. P., 2013. Numerical modelling of magma dynamics coupled to tectonic deformation of lithosphere and crust. *Geophysical Journal International* 195 (3), 1406–1442.
- Kelley, C. T., Keyes, D. E., 1998. Convergence Analysis of Pseudo-Transient Continuation. *SIAM Journal on Numerical Analysis* 35 (2), 508–523.
- Kelley, C. T., Liao, L.-Z., 2013. Explicit pseudo-transient continuation. *Pacific Journal of Optimization* 9 (1), 77–91.
- Lewis, R., Schrefler, B., 1987. *The finite element method in the deformation and consolidation of porous media*. John Wiley and Sons Inc., New York, NY.
- Liang, Y., Schiemenz, A., Hesse, M. A., Parmentier, E. M., 2011. Waves, channels, and the preservation of chemical heterogeneities during melt migration in the mantle. *Geophysical Research Letters* 38 (20), 1–5.
- Løseth, H., Wensaas, L., Arntsen, B., Hanken, N.-M., Basire, C., Graue, K., 2011. 1000 m long gas blow-out pipes. *Marine and Petroleum Geology* 28 (5), 1047–1060.
- Makhnenko, R. Y., Labuz, J. F., 2016. Elastic and inelastic deformation of fluid-saturated rock. *Phil. Trans. R. Soc. A* 374 (2078), 20150422.
- Mazzini, A., Svensen, H. H., Forsberg, C. F., Linge, H., Lauritzen, S.-E., Haffidason, H., Hammer, Ø., Planke, S., Tjelta, T. I., 2017. A climatic trigger for the giant Troll pockmark field in the northern North Sea. *Earth and Planetary Science Letters* 464 (May), 24–34.
- McKenzie, D., 1984. The generation and compaction of partially molten rock. *Journal of Petrology* 25 (3), 713–765.

- Miller, S. A., van der Zee, W., Olgaard, D. L., Connolly, J. A. D., 2003. A fluid-pressure feedback model of dehydration reactions: experiments, modelling, and application to subduction zones. *Tectonophysics* 370 (1), 241–251.
- Minakov, A., Yarushina, V., Faleide, J. I., Krupnova, N., Sakoulina, T., Dergunov, N., Glebovsky, V., 2017. Dyke emplacement and crustal structure within a continental large igneous province, northern Barents Sea. Geological Society, London, Special Publications (March), SP460.4.
- Minkoff, S. E., Stone, C., Bryant, S., Peszynska, M., Wheeler, M. F., 2003. Coupled fluid flow and geomechanical deformation modeling. *Journal of Petroleum Science and Engineering* 38 (1-2), 37–56.
- Morency, C., Huismans, R. S., Beaumont, C., Fullsack, P., 2007. A numerical model for coupled fluid flow and matrix deformation with applications to disequilibrium compaction and delta stability. *Journal of Geophysical Research: Solid Earth* 112 (B10).
- Olson, P., Christensen, U., 1986. Solitary wave propagation in a fluid conduit within a viscous matrix. *Journal of Geophysical Research: Solid Earth* 91 (B6), 6367–6374.
- Omlin, S., Malvoisin, B., Podladchikov, Y. Y., 2017a. Pore Fluid Extraction by Reactive Solitary Waves in 3-D. *Geophysical Research Letters*.
- Omlin, S., Räss, L., Podladchikov, Y. Y., 2017b. Simulation of three-dimensional viscoelastic deformation coupled to porous fluid flow. *Tectonophysics*.
- Omlin, S., Räss, L., Podladchikov, Y. Y., 2017c. Simulation of three-dimensional viscoelastic deformation coupled to porous fluid flow. *Tectonophysics*.
- Otter, J. R. H., Cassell, A. C., Hobbs, R. E., 1966. Dynamic relaxation. *Proceedings of the Institution of Civil Engineers* 35 (4), 633–656.
- Patankar, S., 1980. Numerical heat transfer and fluid flow. CRC press.
- Phillips, P. J., Wheeler, M. F., 2008. A coupling of mixed and discontinuous Galerkin finite-element methods for poroelasticity. *Computational Geosciences* 12 (4), 417–435.
- Plaza-Faverola, A., Büinz, S., Mienert, J., 2010. Fluid distributions inferred from P-wave velocity and reflection seismic amplitude anomalies beneath the Nyegga pockmark field of the mid-Norwegian margin. *Marine and Petroleum Geology* 27 (1), 46–60.
- Plaza-Faverola, A., Büinz, S., Mienert, J., 2011. Repeated fluid expulsion through sub-seabed chimneys offshore Norway in response to glacial cycles. *Earth and Planetary Science Letters* 305 (3), 297–308.

- Poliakov, A. N. B., Cundall, P. A., Podladchikov, Y. Y., Lyakhovsky, V. A., 1993. An Explicit Inertial Method for the Simulation of Viscoelastic Flow: An Evaluation of Elastic Effects on Diapiric Flow in Two- and Three- Layers Models. Springer Netherlands, Dordrecht, pp. 175–195.
- Prevost, J. H., 2013. One-way versus two-way coupling in reservoir-geomechanical models. In: *Poromechanics V: Proceedings of the Fifth Biot Conference on Poromechanics*. pp. 517–526.
- Räss, L., Makhnenko, R. Y., Podladchikov, Y., Laloui, L., 2017a. Quantification of Viscous Creep Influence on Storage Capacity of Caprock. *Energy Procedia* 114, 3237–3246.
- Räss, L., Makhnenko, R. Y., Podladchikov, Y., Laloui, L., 2017b. Quantification of Viscous Creep Influence on Storage Capacity of Caprock. *Energy Procedia* 114, 3237–3246.
- Räss, L., Yarushina, V., Duretz, T., Podladchikov, Y., 2016. High-resolution Numerical Modelling to Resolve the Dynamics of Pipe Structures in Porous Media. In: *ECMOR XV-15th European Conference on the Mathematics of Oil Recovery*.
- Räss, L., Yarushina, V. M., Simon, N. S., Podladchikov, Y. Y., 2014. Chimneys, channels, pathway flow or water conducting features-an explanation from numerical modelling and implications for CO₂ storage. *Energy Procedia* 63, 3761–3774.
- Reusch, A., Loher, M., Bouffard, D., Moernaut, J., Hellmich, F., Anselmetti, F. S., Bernasconi, S. M., Hilbe, M., Kopf, A., Lilley, M. D., Meinecke, G., Strasser, M., 2015. Giant lacustrine pockmarks with subaqueous groundwater discharge and subsurface sediment mobilization. *Geophysical Research Letters* 42 (9), 3465–3473.
- Rhebergen, S., Wells, G. N., Wathen, A. J., Katz, R. F., 2015. Three-field block preconditioners for models of coupled magma/mantle dynamics. *SIAM Journal on Scientific Computing* 37 (5), A2270–A2294.
- Rozhko, A. Y., 2008. Benchmark for poroelastic and thermoelastic numerical codes. *Physics of the Earth and Planetary Interiors* 171 (1), 170–176.
- Rudge, J., 2014. Analytical solutions of compacting flow past a sphere. *Journal of Fluid Mechanics* 746, 466–497.
- Rudge, J. F., Bercovici, D., Spiegelman, M., 2011. Disequilibrium melting of a two phase multicomponent mantle. *Geophysical Journal International* 184 (2), 699–718.
- Rutqvist, J., 2011. Status of the TOUGH-FLAC simulator and recent applications related to coupled fluid flow and crustal deformations. *Computers & Geosciences* 37 (6), 739–750.

- Rutqvist, J., 2012. The geomechanics of CO₂ storage in deep sedimentary formations. *Geotechnical and Geological Engineering* 30 (3), 525–551.
- Schiemenz, A., Liang, Y., Parmentier, E. M., 2011. A high-order numerical study of reactive dissolution in an upwelling heterogeneous mantle-I. Channelization, channel lithology and channel geometry. *Geophysical Journal International* 186 (2), 641–664.
- Scott, D. R., 1988. The competition between percolation and circulation in a deformable porous medium. *Journal of Geophysical Research: Solid Earth* 93 (B6), 6451–6462.
- Scott, D. R., Stevenson, D. J., 1984. Magma solitons. *Geophysical Research Letters* 11 (11), 1161–1164.
- Settari, A., Walters, D., 2001. Advances in Coupled Geomechanical and Reservoir Modeling With Applications to Reservoir Compaction. *SPE Journal* 6 (3), 14–17.
- Shin, D., Strikwerda, J. C., 1997. Inf-sup conditions for finite-difference approximations of the Stokes equations. *The Journal of the Australian Mathematical Society. Series B. Applied Mathematics* 39 (01), 121–134.
- Simpson, G., Spiegelman, M., Weinstein, M. I., 2010a. A multiscale model of partial melts: 1. Effective equations. *Journal of Geophysical Research* 115 (B4), B04410.
- Simpson, G., Spiegelman, M., Weinstein, M. I., 2010b. A multiscale model of partial melts: 2. Numerical results. *Journal of Geophysical Research* 115 (B4), B04411.
- Skarbek, R. M., Rempel, A. W., 2016. Dehydration-induced porosity waves and episodic tremor and slip. *Geochemistry, Geophysics, Geosystems* 17 (2), 442–469.
- Sone, H., Zoback, M. D., 2014. Time-dependent deformation of shale gas reservoir rocks and its long-term effect on the in situ state of stress. *International Journal of Rock Mechanics and Mining Sciences* 69, 120–132.
- Spiers, C., Schutjens, P., Brzesowsky, R., Peach, C., Liezenberg, J., Zwart, H., 1990. Experimental determination of constitutive parameters governing creep of rocksalt by pressure solution. *Geological Society, London, Special Publications* 54 (1), 215–227.
- Stevenson, D. J., Scott, D. R., 1991. Mechanics of Fluid-Rock Systems. *Annual Review of Fluid Mechanics* 23 (1), 305–339.
- Tian, M., Ague, J. J., 2014. The impact of porosity waves on crustal reaction progress and CO₂ mass transfer. *Earth and Planetary Science Letters* 390, 80–92.
- Vajdova, V., Baud, P., Wu, L., Wong, T.-f., 2012. Micromechanics of inelastic compaction in two allochemical limestones. *Journal of Structural Geology* 43, 100–117.

- Wang, H., 2000. Theory of linear poroelasticity with applications to geomechanics and hydrogeology. Princeton University Press.
- Wheeler, M., Xue, G., Yotov, I., 2014. Coupling multipoint flux mixed finite element methods with continuous galerkin methods for poroelasticity. *Computational Geosciences* 18 (1), 57–75.
- Wiggins, C., Spiegelman, M., 1995. Magma migration and magmatic solitary waves in 3-D. *Geophysical Research Letters* 22 (10), 1289–1292.
- Wong, T.-f., Baud, P., 2012. The brittle-ductile transition in porous rock: A review. *Journal of Structural Geology* 44, 25–53.
- Yang, X. I., Mittal, R., 2014. Acceleration of the Jacobi iterative method by factors exceeding 100 using scheduled relaxation. *Journal of Computational Physics* 274, 695–708.
- Yarushina, V. M., Podladchikov, Y. Y., 2015. (De)compaction of porous viscoelastoplastic media: Model formulation. *Journal of Geophysical Research: Solid Earth* 120 (6), 4146–4170.
- Yarushina, V. M., Podladchikov, Y. Y., Connolly, J. A., 2015b. (De)compaction of porous viscoelastoplastic media: Solitary porosity waves. *Journal of Geophysical Research: Solid Earth* 120 (7), 4843–4862.
- Zheng, L., May, D., Gerya, T., Bostock, M., 2016. Fluid-assisted deformation of the subduction interface: Coupled and decoupled regimes from 2-D hydromechanical modeling. *Journal of Geophysical Research: Solid Earth* 121 (8), 6132–6149.

Resolving thermo-mechanical coupling in two and three dimensions:
Spontaneous strain localisation owing to strain heating

Thibault Duretz^{1,2}, Ludovic Räss^{2,3}, Yury Y. Podladchikov^{2,3}, and Stefan M. Schmalholz²

¹Géosciences Rennes, Univ. Rennes 1, UMR CNRS 6118, France.

²Faculté des géosciences et de l'environnement, Institut des Sciences de la Terre, University of Lausanne, Lausanne, Switzerland.

³Swiss Geocomputing Centre, University of Lausanne, Lausanne, Switzerland.

Abstract

Numerous geological processes are governed by thermal and mechanical interactions. In particular, tectonic processes such as ductile strain localisation can be induced by the intrinsic coupling that exists between deformation, energy and rheology. To investigate this thermo-mechanical feedback, we have designed 2-D codes that are based on an implicit finite-difference discretisation. The direct-iterative method relies on a classical Newton iteration cycle, while the pseudo-transient method uses pseudo-time marching. We show that both methods are able to capture thermo-mechanical instability when applied to model thermally activated shear localisation; they exhibit similar temporal evolution and deliver coherent results both in terms of non-linear accuracy and conservativeness. The pseudo-transient method is an attractive alternative, since it can deliver similar accuracy to a standard direct-iterative method but is based on a much simpler algorithm and enables high-resolution simulations in 3-D. We systematically investigate the dimensionless parameters controlling 2-D shear localisation and model shear zone propagation in 3-D using the pseudo-transient method. Code examples based on the pseudo-transient and direct-iterative methods are provided in the supplementary material.

5.1 Introduction

Thermo-mechanical feedback represents a first-order multiphysics coupling for geodynamic processes. For instance, thermo-mechanical coupling plays a major role in initiating and regulating convection currents at the scale of the Earth’s mantle (McKenzie et al., 1974; Parsons and McKenzie, 1978; Pekeris, 1935) or in partially molten regions of the crust (Talbot, 1968). Thermal convection represents a type of Rayleigh-Bénard instability that is intrinsically linked to the temperature sensitivity of rock-forming mineral densities. Besides convection, thermally activated shear localisation is another, yet far less explored, example of thermo-mechanical coupling in geodynamics. However, these processes have been used to explain the initiation of subduction (Thielmann and Kaus, 2012), the generation of deep earthquakes (Ohuchi et al., 2017; Prieto et al., 2013), ductile strain localisation (John et al., 2009), or the formation of tectonic nappes (Jaquet and Schmalholz, 2017). Thermally activated shear localisation occurs when local temperature variations owing to shear heating (mechanical dissipation induced by irreversible deformation) are large enough not to be diffused away efficiently. Since ductile mineral strengths strongly depend on temperature (e.g. Carter and Ave’Lallemant, 1970), a local temperature increase results in softening, which can further induce the focussing of strain into a localised shear zone (Fleitout and Froidevaux, 1980; Kaus and Podladchikov, 2006). Since localisation is driven by a self-regulating feedback process, it can either rapidly vanish, be maintained stably, or evolve into a runaway instability given specific conditions (e.g. Braeck and Podladchikov, 2007; John et al., 2009; Rice and Fairbridge, 1975). Shear zones caused by shear heating have an inherent width (Duretz et al., 2014; Moore and Parsons, 2015) in which the strain is focussed although the thermal imprint may be diffused (Schmalholz and Duretz, 2015). Thermally activated shear localisation is generally not an exclusive mechanism and can occur in conjunction with other physical processes such as micro-structural evolution (Peters et al., 2015; Thielmann et al., 2015) and mineral reactions (Andersen et al., 2008) that can further promote strain localisation.

In the following, we first proceed to a dimensional analysis and parameter reduction for thermo-mechanical equations, which are further used to model thermally activated shear localisation. We introduce two numerical modelling approaches, namely a classic direct-iterative (DI) method and a less conventional, pseudo-transient (PT) approach. The PT method’s viability is demonstrated by providing a quantitative comparison with numerical solutions achieved with the standard DI method. We assess both the accuracy and performance of PT solutions. We provide a systematic parametric analysis of 2-D thermally activated shear localisation. Natural shear localisation always occurs in 3-D which is important for localisation caused by thermal softening, since thermal diffusion of local heat sources is more efficient in 3-D than in 2-D. Yet, there are very few efficient 3-D algorithms that allow one to accurately simulate thermally activated strain localisation in 3-D. Here, we show that the PT

method is well suited for the efficient and accurate simulation of 3-D shear zone formation by thermal softening. Finally, we discuss how different numerical treatments of non-linearities and time integration schemes can affect model predictions as well as performance. For reproducibility purposes, we provide the PT and DI numerical codes (MATLAB) used to solve thermo-mechanical problems.

5.2 The mathematical model

5.2.1 Thermo-mechanical coupling

The equations governing thermo-mechanics of slowly creeping incompressible fluids are:

$$\begin{aligned}
 \frac{\partial v_i}{\partial x_i} &= 0, \\
 \frac{\partial \tau_{ij}}{\partial x_j} - \frac{\partial P}{\partial x_i} &= 0, \\
 \tau_{ij} \dot{\epsilon}_{ij} + k \frac{\partial^2 T}{\partial x_i^2} &= \rho C_p \left(\frac{\partial T}{\partial t} + v_i \frac{\partial T}{\partial x_i} \right) \\
 \dot{\epsilon}_{ij} = \frac{1}{2} \left(\frac{\partial v_i}{\partial x_j} + \frac{\partial v_j}{\partial x_i} \right) &= \frac{1}{2} A \tau_{II}^{n_{\text{pow}}-1} \exp \left(-\frac{Q}{R(T_0 + T)} \right) \tau_{ij}
 \end{aligned} \tag{5.1}$$

where $v_{i,j}$ are components of the velocity vector in the $x_{i,j}$ spatial direction, P is the pressure, T is the temperature deviation from the initial temperature T_0 , ρ is the density, C_p is the specific heat, $\dot{\epsilon}_{ij}$ is the strain rate tensor, τ_{ij} and τ_{II} are the deviatoric stress tensor and the square root of its second invariant $\left(\tau_{II} = \frac{1}{2} (\tau_{xx}^2 + \tau_{yy}^2 + \tau_{zz}^2 + \tau_{xy}^2 + \tau_{yx}^2)^{\frac{1}{2}} \right)$, A is the pre-exponent, n is the stress exponent, Q is the activation energy and R is the universal gas constant.

Four independent scales

$$\begin{aligned}
 \bar{T} &= \frac{nRT_0^2}{Q} \\
 \bar{\tau} &= \rho C_p \bar{T} \\
 \bar{t} &= 2^{1-n} A^{-1} \bar{\tau}^{-n} \exp \left(\frac{Q}{RT_0} \right) \\
 \bar{L} &= \sqrt{\frac{k}{\rho C_p} \bar{t}}
 \end{aligned} \tag{5.2}$$

for temperature, stress, time and length, respectively, and their dependent combinations, such as the velocity scale: $\bar{V} = \bar{L}/\bar{t}$, are used to make all the variables dimensionless. Introducing

dimensionless variables in equations 5.1, without introducing specific symbols for dimensionless variables, results in the following dimensionless form of the governing equations:

$$\begin{aligned}
\frac{\partial v_i}{\partial x_i} &= 0, \\
\frac{\partial \tau_{ij}}{\partial x_j} - \frac{\partial P}{\partial x_i} &= 0, \\
\tau_{ij} \dot{\epsilon}_{ij} + \frac{\partial^2 T}{\partial x_i^2} &= \frac{\partial T}{\partial t} + v_i \frac{\partial T}{\partial x_i} \\
\dot{\epsilon}_{ij} &= \frac{1}{2} \left(\frac{\partial v_i}{\partial x_j} + \frac{\partial v_j}{\partial x_i} \right) = 2^{-n} \tau_{II}^{n-1} \exp \left(\frac{n T}{1 + \frac{T}{T_0}} \right) \tau_{ij}
\end{aligned} \tag{5.3}$$

The model parameters are the dimensionless initial temperature T_0 , the power law exponent n_{pow} as well as four parameters that arise from the initial and boundary conditions: the radius and amplitude of the circular thermal perturbation, the length of the square computational domain, L , and the boundary velocity, V_{BC} (Figure 5.2).

5.3 The numerical methods

The system of non-linear equations (Eq. 5.3) is discretised on a Cartesian staggered grid with regular grid-spacing. The time derivative of the heat equation is approximated by either a backward-Euler or a Crank-Nicolson scheme. The dimensionless viscosity is a non-linear function of both the temperature and the strain rate and is expressed, after Eq. 5.3, as:

$$\eta = \dot{\epsilon}_{II}^{\frac{1-n_{\text{pow}}}{n_{\text{pow}}}} \exp \left(-\frac{T}{1 + T_0 T} \right), \tag{5.4}$$

where $\dot{\epsilon}_{II}$ is the square root of the second invariant of the deviatoric strain rate $\left(\dot{\epsilon}_{II} = \frac{1}{2} (\dot{\epsilon}_{xx}^2 + \dot{\epsilon}_{yy}^2 + \dot{\epsilon}_{xy}^2 + \dot{\epsilon}_{yx}^2) \right)^{\frac{1}{2}}$.

Two methods are employed to solve for the flow, pressure and temperature fields. The first method relies on Newton iterations and uses a DI scheme thus requiring matrix assembly for each discrete operator. The second method uses a PT approach, which is fully iterative and matrix-free. Both numerical methods rely on a two-way coupling, since both the coupling term (shear heating) and rheology were treated implicitly. Since we will now mostly focus on small strains, we don't consider heat transport owing to advection.

5.3.1 The direct-iterative method

The discrete operator corresponding to the Jacobian matrix of the thermo-mechanically coupled system takes the form of:

$$\underbrace{\begin{bmatrix} \mathbf{J}_v & \mathbf{G} & \mathbf{H}_1 \\ -\mathbf{G}^T & \gamma^{-1}\mathbf{I} & \mathbf{0} \\ \mathbf{H}_2 & \mathbf{0} & \mathbf{J}_T \end{bmatrix}}_{\mathbf{J}_{\text{TM}}} \underbrace{\begin{bmatrix} \delta\mathbf{v} \\ \delta\mathbf{p} \\ \delta\mathbf{T} \end{bmatrix}}_{\delta\mathbf{x}} = - \underbrace{\begin{bmatrix} \mathbf{f}_v \\ \mathbf{f}_p \\ \mathbf{f}_T \end{bmatrix}}_{\mathbf{f}}. \quad (5.5)$$

The \mathbf{J}_v corresponds to the mechanical Jacobian matrix, which arises from the strain rate dependence of viscosity. The \mathbf{H}_1 block highlights the temperature-dependence of viscosity, and the \mathbf{H}_2 block arises from the linearisation of the shear heating term. The \mathbf{G} and \mathbf{J}_T respectively represent the gradient and Laplace discrete operators. The diagonal block $\gamma^{-1}\mathbf{I}$ ensures near-incompressible flow for large values of γ . The solution vector is composed of velocity corrections ($\delta\mathbf{v}$), pressure corrections ($\delta\mathbf{p}$) and temperature corrections ($\delta\mathbf{T}$). The right-hand-side vector contains the non-linear momentum, continuity and thermal residuals (\mathbf{f}_v , \mathbf{f}_p , \mathbf{f}_T). A detailed derivation of the entries of the analytical Jacobian matrix is provided in the supplementary material. Iterative Newton corrections are obtained by applying the inverse of the Jacobian matrix to the current non-linear residual vector:

$$\delta\mathbf{x} = \mathbf{J}_{\text{TM}}^{-1}\mathbf{f}. \quad (5.6)$$

This operation is achieved using a combined direct-iterative approach; details appear in the Appendices. Prior to solution update, we run a line search procedure to find the optimal globalisation parameter α ($0 < \alpha \leq 1$) that yields:

$$\min \|\mathbf{f} + \alpha \delta\mathbf{x}\|_{L_2}. \quad (5.7)$$

The non-linear iteration cycle is aborted once the following criteria $\|\mathbf{f}_u\|_{L_2} < \|\mathbf{f}_u\|_{L_2}^{\text{initial}} \text{tol}_{\text{nonlin}}$ is met. The main steps of the direct-iterative approach are summarised in Figure 5.1a. This code is written in MATLAB language; it is based on and made available as part of the M2Di routines (Räss et al., 2017) under the TM2Di moniker.

5.3.2 The pseudo-transient method

The PT or relaxation method allows one to iteratively solve non-linear problems in a single iteration loop in a matrix-free way. The PT method relies on introducing numerical time derivatives into steady state equations. Given a set of initial and boundary conditions, solu-

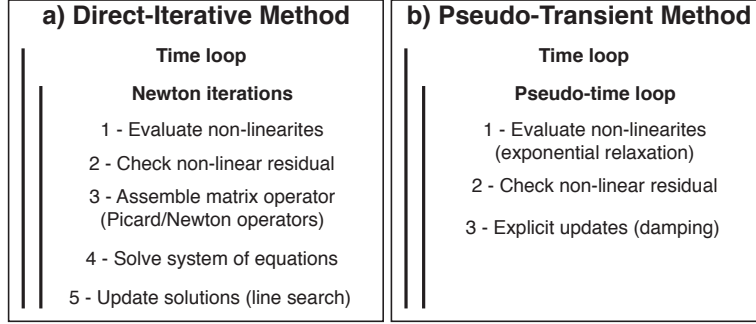


Figure 5.1: Algorithmic flowchart for both methods used in the study: (a) the direct-iterative method (TM2Di code) and (b) the pseudo-transient method.

tions can be found by integrating the equations forward in pseudo-time (τ) until steady-state is attained; i.e. the pseudo-time derivative vanishes. To this end, Eq. 5.3 is expressed as:

$$\begin{aligned}
 \frac{dP}{d\tau} &= \frac{\partial v_i}{\partial x_i}, \\
 \frac{dv_i}{d\tau} &= \frac{\partial \tau_{ij}}{\partial x_j} - \frac{\partial P}{\partial x_i}, \\
 \frac{dT}{dt} &= \frac{\partial^2 T}{\partial x_i^2} + \tau_{ij} \dot{\epsilon}_{ij}.
 \end{aligned} \tag{5.8}$$

The non-linear viscosity η is evaluated at each pseudo-transient iteration k using the current strain rate and temperature solution fields. The treatment of non-linearities is greatly facilitated by using an effective viscosity (η_{eff}), which we formulate as:

$$\eta_{\text{eff}}^k = \exp \left[\text{rel}_\eta \ln \left(\eta_{\text{eff}}^{k-1} \right) + (1 - \text{rel}_\eta) \ln \left(\eta^k \right) \right], \tag{5.9}$$

where rel_η ($0 \leq \text{rel}_\eta \leq 1$) corresponds to a relaxation factor. This approach is a continuation method, since the effective viscosity progressively relaxes towards the de facto physical viscosity ($\eta_{\text{eff}} \rightarrow \eta$) throughout the PT iterations.

The integration of the momentum and mass conservation equation necessitates the definition of individual pseudo-transient time-steps, $\Delta\tau_p$ and $\Delta\tau_{v_i}$. The pseudo-transient time-steps are formulated as:

$$\begin{aligned}
 \Delta\tau_p &= \text{rel}_p \frac{2.1 n_{\text{dim}} \eta_{it}^k (1 + \eta_b)}{\max(n_x, n_y)}, \\
 \Delta\tau_{v_i} &= \text{rel}_{v_i} \frac{\min(\Delta x, \Delta y)^2}{2.1 n_{\text{dim}} \eta_{it}^k (1 + \eta_b)},
 \end{aligned} \tag{5.10}$$

where η_b is a numerical analogy of bulk viscosity, Δx and Δy are grid-spacings, rel_p and rel_{v_i} are relaxation factors and n_{dim} is the number of dimensions. η_b is introduced in the normal

stress evaluation to balance the divergence-free formulation of the strain rates. It multiplies the pressure equation residuals and vanishes once the problem converges, since the pressure residuals tend towards 0. $\Delta\tau_{v_i}$ refers to the explicit CFL diffusive time-steps limitation. It is used in the pseudo-time iterations to allow optimal convergence of the transient problem using physics-based criteria. The use of $\Delta\tau_p$ expressed as nearly the inverse of $\Delta\tau_{v_i}$ provides optimal convergence of the Stokes problem, making the iteration strategy non-sensitive to the physical shear viscosity. We further highlight that η_{it}^k refers to entire fields (defined for every grid-point); thus, this pseudo-time-stepping method is analogous to the application of diagonal preconditioner in matrix-based solvers.

The use of damping allows one to greatly reduce the number of iterations needed for convergence of the pseudo-transient iterations (Choi et al. (2013); Yang and Mittal (2014)). Here, we apply damping on the velocity increments:

$$\Delta v_i^k = \Delta\tau_{v_i} f_v^k + \left(1 - \frac{\nu}{n_i}\right) \Delta v_i^{k-1} \quad (5.11)$$

where optimal values of ν reside within the range ($1 \leq \nu \leq 10$) and n_i is the number of cells in the direction i . The velocity field is computed at each iteration using the following update rule:

$$v_i^k = v_i^{k-1} + \Delta v_i^k. \quad (5.12)$$

The pseudo-transient iterations are performed until the following criteria $\|\mathbf{f}_v\|_{L2} < \|\mathbf{f}_v\|_{L2}^{\text{initial}} \text{tol}_{\text{nonlin}}$ is reached. An elastic analogy of this approach is described by Cundall and Strack (1979) and is successfully used in the FLAC geotechnical software (Cundall et al., 1993).

5.3.3 Time integration

For both the DI and PT methods, the integration of the heat equation occur in physical time t . An implicit (backward-Euler) or semi-implicit (Crank-Nicolson) solution is obtained by updating the heat fluxes and shear heating term at each non-linear or PT iteration. In the following examples, we use a physical time-step, Δt_T , which is proportional to the CFL time-step:

$$\Delta t_T = \xi \frac{\min(\Delta x, \Delta y)^2}{2.1 n_{\text{dim}}} = \xi \Delta t_{\text{exp}}, \quad (5.13)$$

where ξ corresponds to a time-step ratio, $\Delta t_T / \Delta t_{\text{exp}}$. Despite the use of an implicit scheme, we did not obtain successful time integration of the non-linear equations system for an arbitrary choice of time-step. Thus, we allow for time-step values that are proportional to those required for explicit integration of the heat equation (Δt_{exp}). In a following section, we systematically investigate for different spatial resolution which values of time-step can lead to successful time

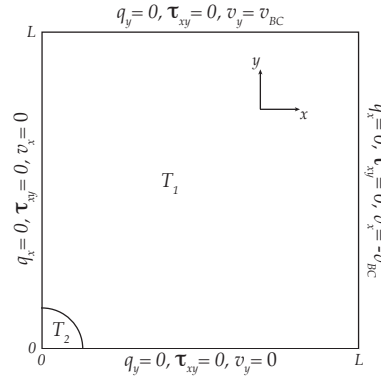


Figure 5.2: Schematic initial model configuration for 2-D calculations. T_1 stands for the initial temperature and T_2 indicates the locations where an initial temperature perturbation is prescribed.

integration. Implementations of the thermo-mechanical DI and PT solvers were performed in both MATLAB (see supplementary material) and C-CUDA languages (only for the PT method).

5.4 A comparison of the direct-iterative and the pseudo-transient methods

In this section, we demonstrate that both the DI method and the PT method can solve thermo-mechanical problems to the same accuracy level. We evaluate each method's performance on current personal computers (single CPU and single GPU).

5.4.1 The reference model's configuration

The numerical models were designed to study the propagation of shear zones owing to shear heating in a viscous medium subjected to far-field pure shear kinematics. For 2-D calculations, we consider a physical domain of dimensions $[0, L] \times [0, L]$. The normal boundary velocities are set to $v_x = -V_{BC}$ for $x = L$, $v_y = V_{BC}$ for $y = L$ and 0 elsewhere. Zero shear stress and zero heat flux boundary conditions are applied on all model sides. The initial temperature field, T_0 , is set to 16.4423 and a perturbation of radius equal to $0.0857L$ and amplitude equal to $0.1T_0$ is centred around the origin (Figure 5.2).

The reference model is run for a boundary velocity of 66.4437, a model length of 0.86038 and a stress exponent of 3. For the 3-D models, the model domain extends up to $z = L$, where a zero normal boundary velocity, shear stress and heat flux are applied. Thus, the first model embeds an initial cylindrical (along z) temperature perturbation and is similar to the 2-D model. In the second model, an initially spherical temperature perturbation is prescribed.

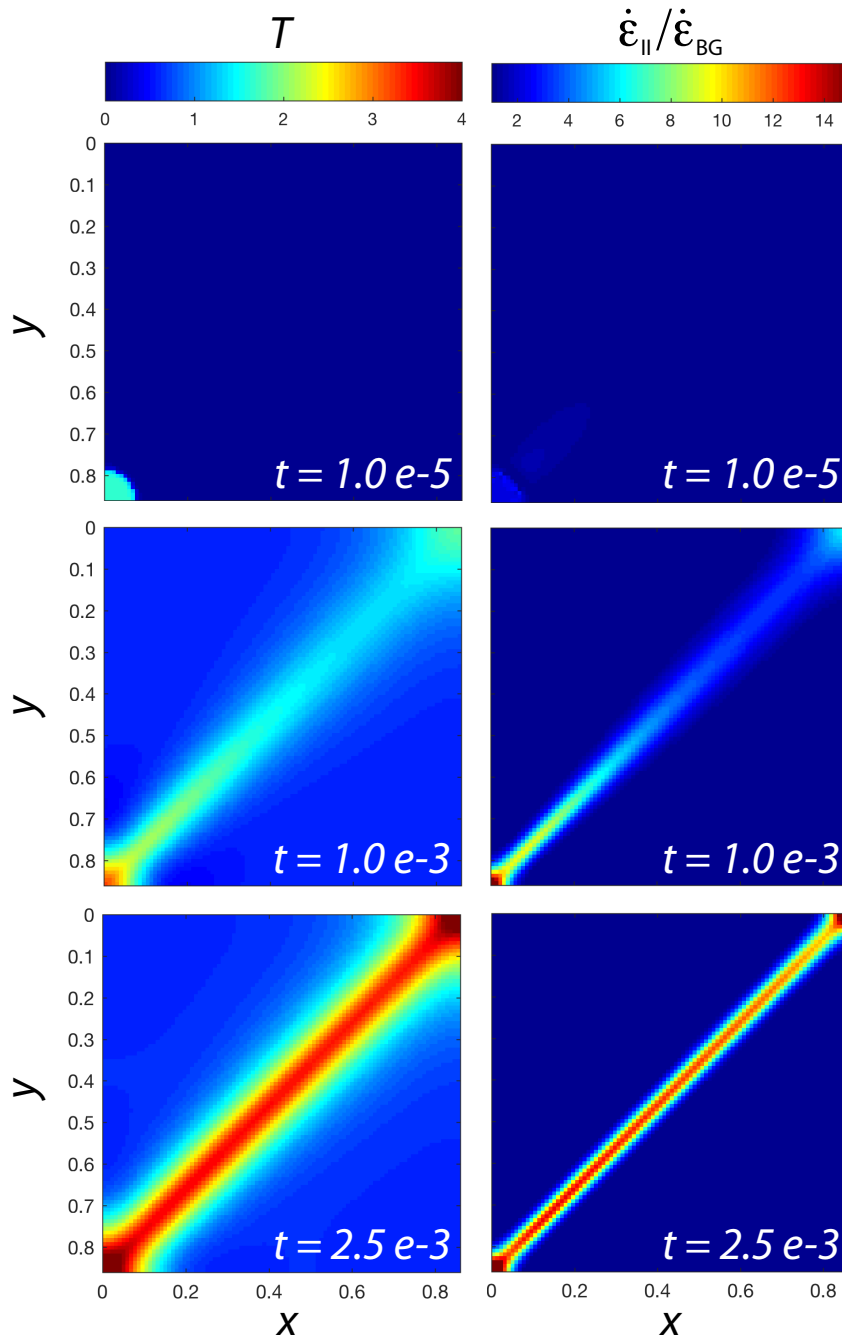


Figure 5.3: Thermo-mechanical activated shear localisation in 2-D. The model was run using the reference model parameter (see main text) and initiated with a circular temperature perturbation (10% increase of temperature). Pure shear was applied on boundaries normal to x (inflow) and y (outflow). All thermal boundary conditions were insulating (zero heat flow).

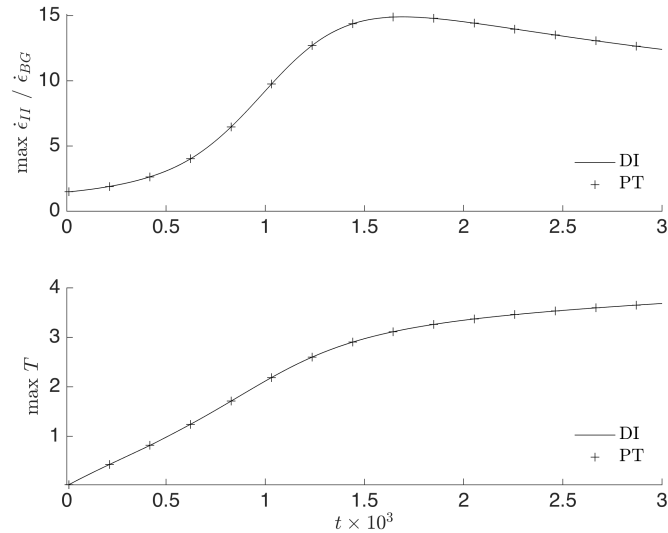


Figure 5.4: Strain rate amplification (upper panel) and temperature (lower panel) evolution in the shear zone (away from the model boundaries). Both PT and DI models were run with a relative tolerance of 10^{-9} and with backward-Euler time integration for the energy equation. For this example, PT models typically converge within about 10^5 iterations.

5.4.2 The temperatures and strain rates inside the shear zones

Thermally activated shear zones have inherent length scales that are proportional to material properties and loading conditions. Thus, it is possible to characterise dynamically evolving fields such as the temperature in such shear zones. If the numerical resolution is greater than the characteristic length scale, these measurements are essentially independent of the numerical resolution (e.g. Duretz et al., 2014). A typical model evolution is depicted in Figure 5.3, which shows the progressive focussing of strain rate and temperature with time. Since the shear bands have a finite length scale, it is possible to monitor the evolution of these quantities inside the shear band (Figure 5.4). The strain rate overcomes the background strain rate by an order of magnitude within 1.5×10^{-3} time units. The temperature increase follows a distinct evolution and tends towards a value of 3.5 for a model time of 3.0×10^{-3} . Again, the simulations computed with the DI and PT methods provide the same temperature and strain rate predictions.

5.4.3 The non-linear solvers' accuracy

To show the PT method's ability to handle non-linear thermo-mechanical problems, we present a quantitative analysis regarding its non-linear errors. A single time-step numerical solution was computed with the DI method using the previously described setup and a resolution of 94^2 numerical cells. The solution procedure was aborted once we attained ma-

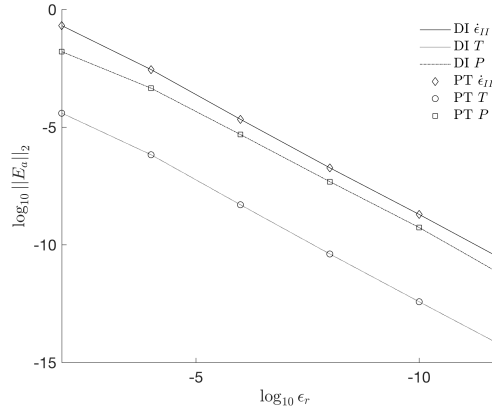


Figure 5.5: Non-linear accuracy PT and the DI method (TM2Di code). Errors in P , T and ϵ_{II} were computed for different relative tolerance (ϵ_r). The PT and the DI methods provide similar errors, and both converge linearly to the reference results with decreasing tolerance.

chine precision for non-linear residuals; the obtained effective strain rate, temperature and pressure serve as reference solution fields. We then computed a series of numerical solutions using larger non-linear tolerances (iteration exit criteria) with both the PT and the DI method.

The deviation of the numerical solutions with regard to the reference fields was calculated as:

$$\|E_a\|_{L2} = \|a^{\text{numerical}} - a^{\text{reference}}\|_{L2}, \quad (5.14)$$

where a is either ϵ_{II} , P , or T . For the same non-linear tolerance, the DI and PT provide the same deviation from the reference results (Figure 5.5). The deviations obtained with either the DI or the PT decrease as the non-linear tolerance is decreased. Thus, both methods converge towards the reference numerical solution with a linear trend. Non-linear numerical solutions obtained with the PT method can reach the same accuracy level as those obtained with the DI method.

5.4.4 The conservation of energy

For thermo-mechanical problems, considering a purely viscous rheology, energy conservation postulates that mechanical work should be fully converted into heat. The numerical simulations' accuracy depends on numerical schemes' ability to conserve energy and therefore fulfil the energy conservation equation. The work is evaluated over time and space, and is expressed as

$$W = \int_t \oint_{\Omega} \tau_{ij} v_i n_j \, dL dt, \quad (5.15)$$

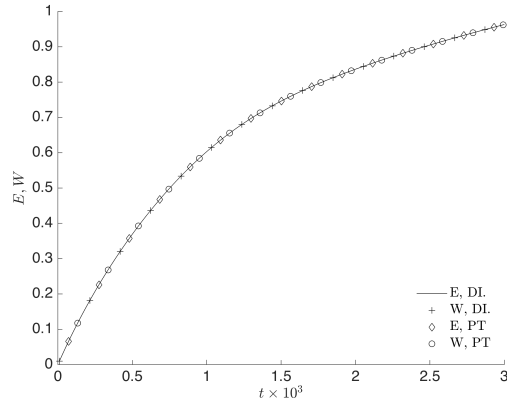


Figure 5.6: Evolution of mechanical work (W) and heat (E) in time. Both PT and DI models were run with backward-Euler time integration for the energy equation.

where n_j is the unit vector to the boundaries, and the thermal energy takes the form of:

$$E = \int_t \int_{\Omega} \frac{\partial T}{\partial t} d\Omega dt. \quad (5.16)$$

The time evolution of W and E for 2-D numerical simulations using the configuration described in Section 5.4.1 is depicted in Figure 5.6. Integrated work and heat computed from PT and DI simulations all follow the same trend. For both methods, the integrated work is equal to the integrated heat at any moment in time. Thus, the numerical solutions arising from the finite-difference discretisation are conservative, independent of the solving procedure.

5.4.5 Performance

We evaluate the performance of the solvers using two different metrics, effective memory throughput ($\text{MTP}_{\text{effective}}$) and wall-time. In the first, the MATLAB CPU-based and C-CUDA GPU-based pseudo-transient solver implementations are evaluated in terms of $\text{MTP}_{\text{effective}}$. In the second, the 2-D GPU-based pseudo-transient solver is compared to the direct-iterative TM2Di solver using the wall-time metric to time the convergence of a non-linear time-step.

Since the pseudo-transient solvers perform stencil operations in a matrix-free approach, the memory transfers bound the algorithm and floating-point operations (FLOPs) are for free. The used $\text{MTP}_{\text{effective}}$ metric (Omlin et al., 2017b) evaluates how efficiently data is transferred between the memory and the computation units, in GB/s:

$$\text{MTP}_{\text{effective}} = \frac{(n_x \cdot n_y) \cdot n_t \cdot \text{nIO} \cdot \text{precis}}{1e9 \cdot \text{time}_{n_t}}, \quad (5.17)$$

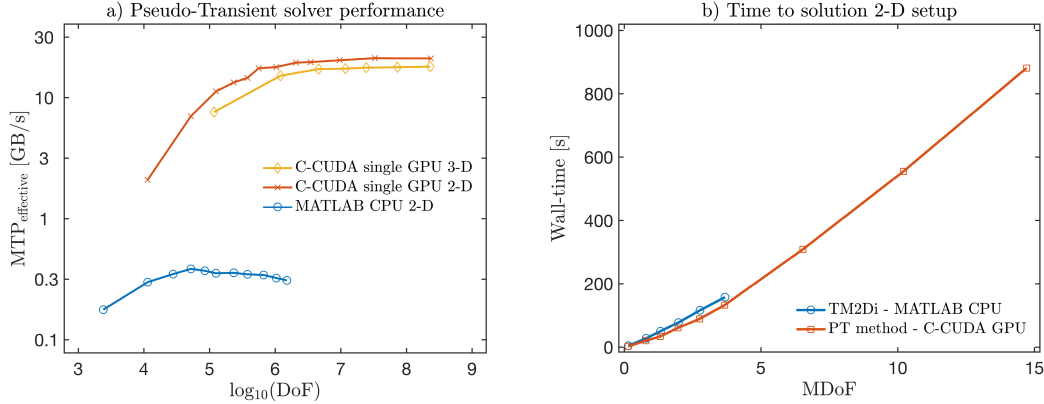


Figure 5.7: Performance evaluation of the thermo-mechanically coupled solvers. a) Effective memory throughput $MTP_{\text{effective}}$ in GB/s of the pseudo-transient implementations using an iterative and matrix-free approach. 2-D MATLAB running on an Intel i5 (2016) processor with 16 GB RAM is compared to 2-D and 3-D C-CUDA running on Nvidia Titan X (Maxwell) GPU. The DoF represent four variables in 2-D (v_x, v_y, P and T) and five variables in 3-D (v_x, v_y, v_z, P and T), multiplied by the respective number of grid-points. The $MTP_{\text{effective}}$ of the 2-D and 3-D GPU implementations saturate at about 20 GB/s. This is one order of magnitude lower than the MTP_{peak} (memory copy only) measured on the Titan X (Maxwell) GPU. The vectorised MATLAB implementation running on the Intel i5 CPU shows a close to two orders of magnitude discrepancy between peak and effective MTP. Two orders of magnitude $MTP_{\text{effective}}$ is observed between the GPU implementation and that of the CPU, both performing double-precision arithmetics. b) Time-to-solution converging a non-linear step to $\text{tol}_{\text{nonlin}} = 1e - 8$, comparing the pseudo-transient method implemented in C-CUDA running on a single Nvidia Titan X (Maxwell) GPU to the direct solver type using the TM2Di Newton MATLAB implementation executed on an Intel i5 (2016) CPU. 3.7 MDoF represent a 2-D domain of 960×960 grid-points and is the maximal resolution that TM2Di can handle while using less than 16 GB of RAM. 2-D domain resolution up to 6400^2 grid-points could be solved in 15 minutes using the matrix-free pseudo-transient GPU solver while using less than 12 GB of RAM (on the device).

where $(n_x \cdot n_y)$ is the grid resolution, n_t is the number of time-steps or iterations performed, $n\text{IO}$ is the number of memory accesses performed, precis is the floating-point precision (either 4 or 8 bytes), and time_{n_t} is the time (in seconds) needed to perform the n_t steps. The number of memory accesses ($n\text{IO}$) defines the minimum number of read-and-write or read-only operations required to solve the specific physics. For 2-D coupled thermo-mechanics, the read-and-write operations correspond to the updates of the DoFs (v_x, v_y, P, T), and two additional read-only operations for converging the non-linear viscosity; in our case, $n\text{IO} = 10$. All the performance benchmark runs are performed using double-precision floating-point arithmetic ($\text{precis} = 8$ bytes) for fair comparison in particular between MATLAB and C-CUDA implementations. The $MTP_{\text{effective}}$ values reported in Figure 5.7a represent the efficiency of memory transfers for the pseudo-transient solvers, for both vectorised MATLAB CPU and C-CUDA single-GPU implementations. The obtained numbers should be compared to the peak memory throughput values MTP_{peak} for the specific hardware, here an Intel i5 CPU and a Nvidia Titan

X (Maxwell) GPU. MTP_{peak} values are measured performing memory copy only without any computation. Values of MTP_{peak} are in the order of 20 GB/s for the Intel i5 CPU and in the order of 260 GB/s for the Titan X (Maxwell) GPU. The MATLAB CPU implementation runs at about 2% of the MTP_{peak} , while the C-CUDA GPU codes run above 10% of the MTP_{peak} . The optimised memory bandwidth as well as the inherent parallelism on the GPU chip could explain such differences. The resulting overall performance gain of the parallel GPU implementation vs. the serial CPU is more than two orders of magnitude. The GPU $MTP_{\text{effective}}$ values show that some optimisation steps could still be performed in order to achieve closer to MTP_{peak} values. Such considerations are beyond the scope of this study, but could include increased number of on-the-fly computation, kernel rearranging and register queues.

Although the effective memory throughput provides the efficiency of hardware utilisation for a specific implementation of the thermo-mechanical solver, a more relevant metric should be used to compare the memory-bounded stencil PT iterative approach to the DI solver TM2Di. Here, the wall-time metric is chosen to assess the overall time to solution of a non-linear step converged to $\text{tol}_{\text{nonlin}} = 10^{-8}$. The Newton-based DI solver TM2Di shows a close to linear increase of wall-time with increasing problem size (DoF). It is implemented in MATLAB, and an Intel i5 (2016) CPU on a system equipped with 16 GB of RAM is used for computations. The maximal 2-D problem size fitting in 16 GB RAM represents a numerical domain of 960^2 grid-points, solved in a wall-time close to 2.5 minutes. In comparison, 15 % less time was needed to converge the same problem using the C-CUDA GPU-based PT solver on a Nvidia Titan X (Maxwell). Nonetheless, the key benefit of this method is the maximal problem size that can be resolved using the available 12 GB of on-chip RAM of the GPU; 163 MDoF represents a numerical 2-D domain size of 6400^2 grid-points. In terms of wall-time, the PT GPU solver outperforms the Newton DI-based solver TM2Di for the investigated setup.

5.4.6 Explicit and implicit coupling strategies

The numerical solution of multiphysics problems can be achieved by means of various coupling strategies. For thermo-mechanical flow, a two-way coupling implies an implicit treatment of non-linear couplings terms (Kaus et al., 2016; Popov and Sobolev, 2008), namely the viscous dissipation term and the strain rate and temperature dependence of the viscosity. In the two-way coupling, the viscosity is thus a function of the strain rate and temperature evaluated at new time index: $\eta(\dot{\epsilon}_{II}^{t+\Delta t}, T^{t+\Delta t})$. One-way coupling represents an alternative coupling strategy commonly used in geodynamic modelling. One-way coupling resides in (1) obtaining a non-linear solution of the purely mechanical problem (thus only considering the strain rate dependence of viscosity) and (2) solving the energy equation using the mechanical dissipation obtained from the mechanical solution (Kaus and Podladchikov, 2006). In other words, one-

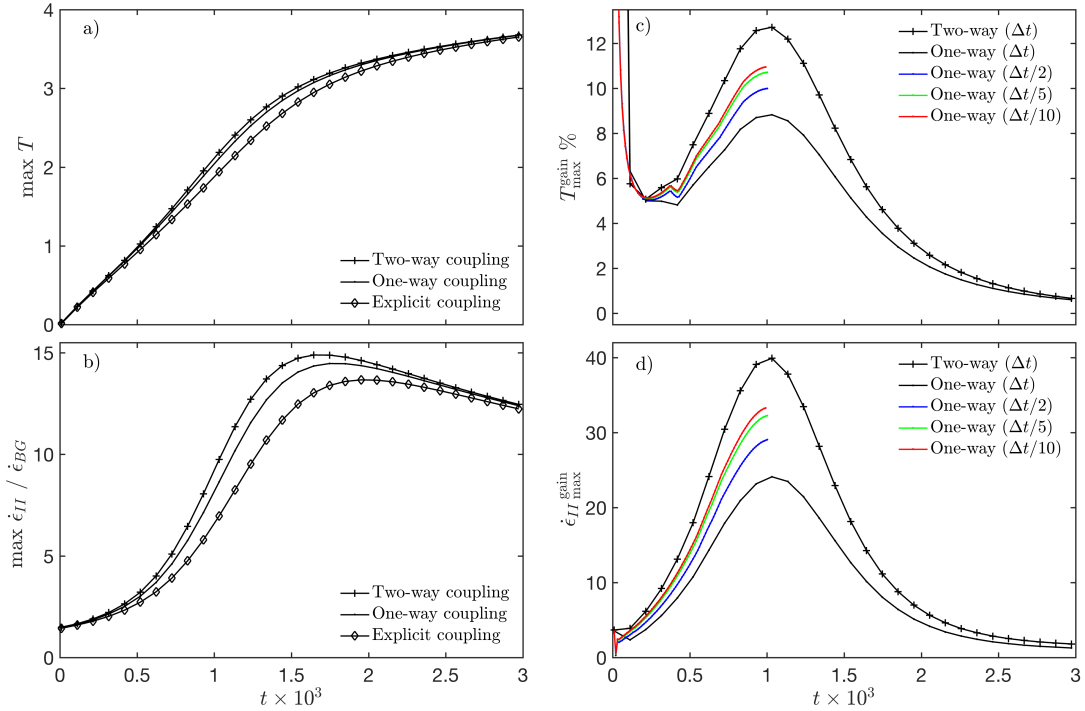


Figure 5.8: The impacts of different multiphysics coupling strategies (one-way coupling, two-way coupling and explicit coupling) on numerical solution. Panels a) and b) depict the evolution of the temperature increase and strain rate amplification in the shear zone for the different coupling strategies using the same constant physical time-step (Δt). Panels c) and d) show the gains in temperature and strain rate when using one-way coupling and two-way coupling in comparison to the explicit coupling (used as a reference here). We also report results obtained with the one-way strategy but with lower time-step values (colour lines). Backward-Euler time integration was used to integrate the energy equation.

way coupling uses strain rates at the new time index but temperature of the old time index to evaluate the viscosity, $\eta(\dot{\epsilon}_{II}^{t+\Delta t}, T^t)$. A fully explicit coupling strategy can also be envisaged (Gerya and Yuen, 2003, 2007). This approach relies on an explicit treatment of both coupling terms and rheological equations, which results in a linearised mechanical problem. With this approach, the viscosity is evaluated using solutions from the previous time index: $\eta(\dot{\epsilon}_{II}^t, T^t)$. To evaluate the impacts of the different coupling strategies, we have run our reference simulation (Section 5.4.1) with the different strategies. In general, explicit couplings can also lead to localisation, but with the least intensity. We have monitored the gains in strain rate amplification and temperature using the solutions obtained using explicit coupling as reference (Figure 5.8). For the same value of physical time-step, Δt , one-way coupling leads to an increase of 25% in strain rate amplification and two-way coupling results in a 40% increase in strain rate amplification. The impacts on maximum temperatures were less pronounced, since increments of 8% and 13% were obtained for one-way and two-way

coupling respectively. Refining the time-step can be used to improve the accuracy of the one-way coupling approach. For instance, twice smaller time-step led to a 30% gain in strain rate; however, with a smaller time-step, the gain in strain rate rapidly saturates (here, to about 32%) and does not catch up the values obtained with a two-way coupling.

5.4.7 Time integration

The choice of a time integration scheme is also critical when solving coupled non-linear transient equations. Using our configuration (Section 5.4.1), successful time integrations were not possible for arbitrary large time-step values. Time-step values were often required to be on the order of Courant-Friedrichs-Lewy criteria for diffusion despite the use of an implicit integration scheme (backward-Euler). This was especially true when using low grid resolutions (50^2 cells, $h = 1.7 \times 10^{-2}$). We have reported the range of time-step variation factors ξ that provided stable integration for various grid resolutions (Figure 5.9). Restrictions on time-step values usually decrease with increasing grid resolution. At high resolution (500^2 cells, $h = 1.7 \times 10^{-3}$), a time-step variation factor in the order of 50 was achievable using backward-Euler. The Crank-Nicolson scheme generally proved to have a larger stability domain, and time-step variation factors could reach 80 at high resolution. In practice, the combination of a Crank-Nicolson scheme with an adaptive time-stepping procedure (e.g. using time-step bisection based on the magnitude of non-linear residuals Duret et al., 2015; Popov and Sobolev, 2008) can allow for stable and flexible time integration.

5.5 Thermally activated shear localisation: Applications

Here we present applications computed with the PT approach that demonstrate the method's flexibility as well as its power.

5.5.1 Thermo-mechanical strain localisation in 2-D: A systematic study

We have studied the relative importances of the boundary velocity (V_{BC}) and bulk strain (ϵ) on shear zone development and evolution, performing 139 systematic 2-D simulations. Each simulation completed 1000 time-steps with a resolution of 190^2 cells and a time-step reduction factor T_{red} of 0.5. We have used a Crank-Nicolson time integration and relative non-linear tolerance of 10^{-5} . The entire systematic study was run sequentially on a single Nvidia GTX Titan X (Maxwell) GPU card. We have monitored the maximum temperature and the strain rate amplification factor in the evolving shear zone (Figure 5.10,a,b) using the model configuration described above (Section 5.4.1). Strain localisation occurred over the entire parameter space to a variable degree. Both the maximum temperature and strain

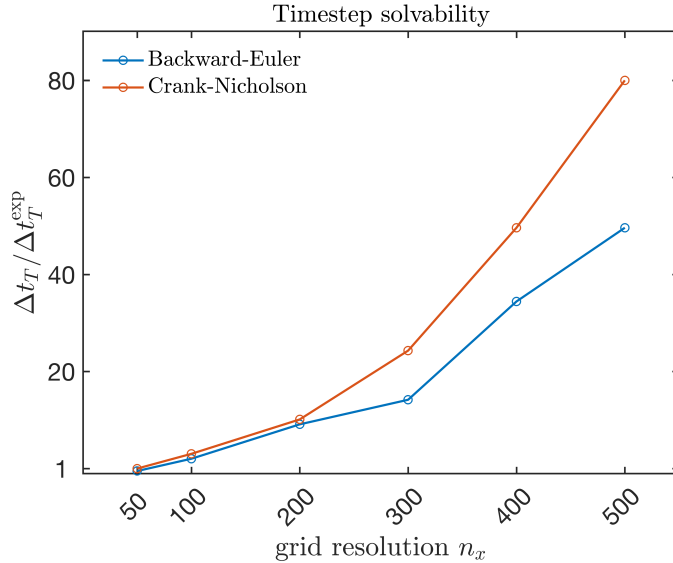


Figure 5.9: Solvability of the thermo-mechanical non-linear system (two-way coupling). Models were run for different values of $\Delta t_T / \Delta t_T^{\text{exp}}$ and various grid resolutions n_x . At larger resolutions, models with a larger physical time-step become more solvable. These results were obtained using the DI method. Models were run for the reference parameters until a final time of 3×10^{-3} . Simulations for which the DI solver failed to converge for the requested value of ξ are considered unsuccessful. In a general case, the time-step could be adapted through the simulations in case the linear or non-linear solves are unsuccessful.

rate amplification strongly depend on V_{BC} and ϵ . Weak shear localisation occurred for low boundary velocity and is characterised by a small strain rate amplification factor (< 5). Most intense shear localisation led to peak temperature (> 8) and strain rate amplification factor ($> 10^2$) and was achieved for a boundary velocity of 400.

In-depth analysis of this data set reveals that the model results can be collapsed using a single parameter $V_{\text{BC}} \log_{10} \epsilon$. Variations of this non-dimensional parameter allow one to predict the maximum temperature and strain rate amplification over the entire investigated parameter range (Figure 5.10,c,d). The consistent collapse for simulations with different bulk strains and significantly variable localisation intensities (different temperatures and strain rates in the shear zone) further show the approach's robustness, since the accuracy of numerical solutions is the same over the investigated parameter range.

5.5.2 The development of shear zones in 3-D

To demonstrate the flexibility of the presented pseudo-transient algorithm, we have extended our GPU code to study 3-D thermo-mechanical deformation. Two models characterised by different initial thermal conditions were performed. The models were run with a resolution of 158^3 and a relative tolerance of 10^{-5} was achieved at each time-step. Both simulations ran for

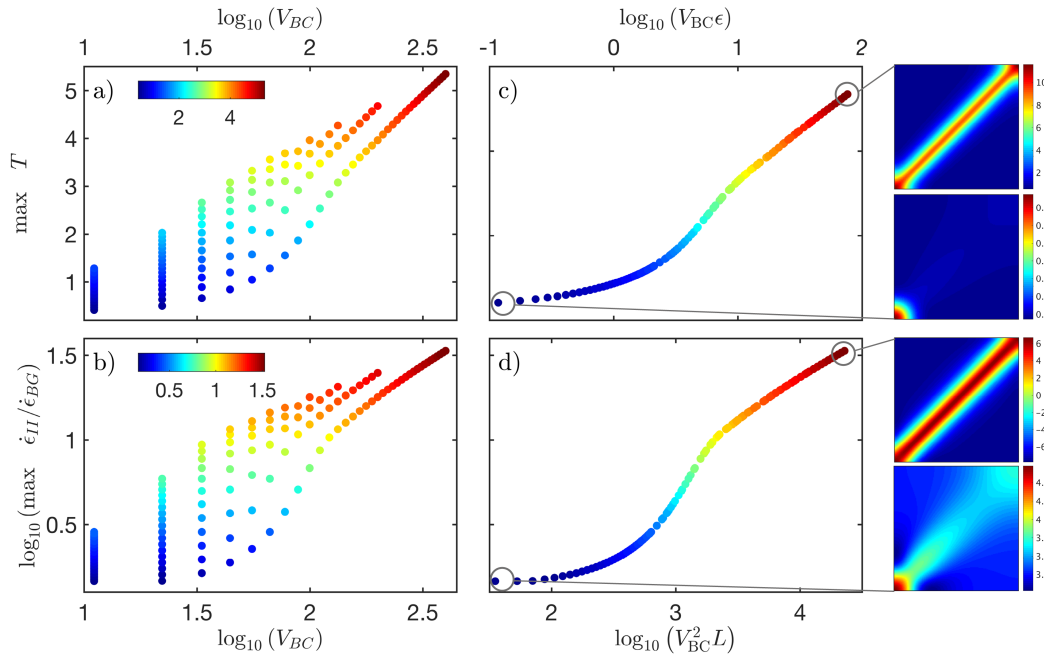


Figure 5.10: Systematic study of the relative importance of the boundary velocity (V_{BC}) on the maximum temperature and strain rate amplification reached in the shear zone. Panels (a) and (b) depict the maximum temperature and the strain rate amplification factor ($\log_{10} \max(\dot{\epsilon}_{II}/\dot{\epsilon}_{BG})$) achieved in the shear zone as a function of V_{BC} , respectively. Panels (c) and (d) show the data collapse for the maximum temperature as a function of $V_{BC}\epsilon$ and the strain rate amplification factor as a function of V_{BC}^2L . The rightmost subpanels depict temperature and strain rate fields associated to specific parts of the considered parameter space (indicated by the grey lines).

5,000 time-steps, and each took about a day on a single Nvidia GTX Titan X (Maxwell) GPU card. For both models, we applied zero shear stress on each side and only boundaries normal to the x and y axis had a non-zero normal velocity component. Thus, in the first setup, we considered a cylindrical initial thermal perturbation; this configuration is equivalent to the 2-D model discussed above (Section 5.4.1) and leads to the rapid development of a cylindrical shear zone (Figure 5.11a). The second model embedded spherical initial thermal perturbation. For such a configuration, more time is required to propagate the shear zone in 3-D (Figure 5.11b). Since more mechanical work is dissipated prior to localisation, the shear zone's walls experienced a higher temperature than in the cylindrical case. The maximum temperature in the centre of the shear zones was about 3.5 for both models, which is similar to what was obtained in the 2-D models (Figure 5.4).

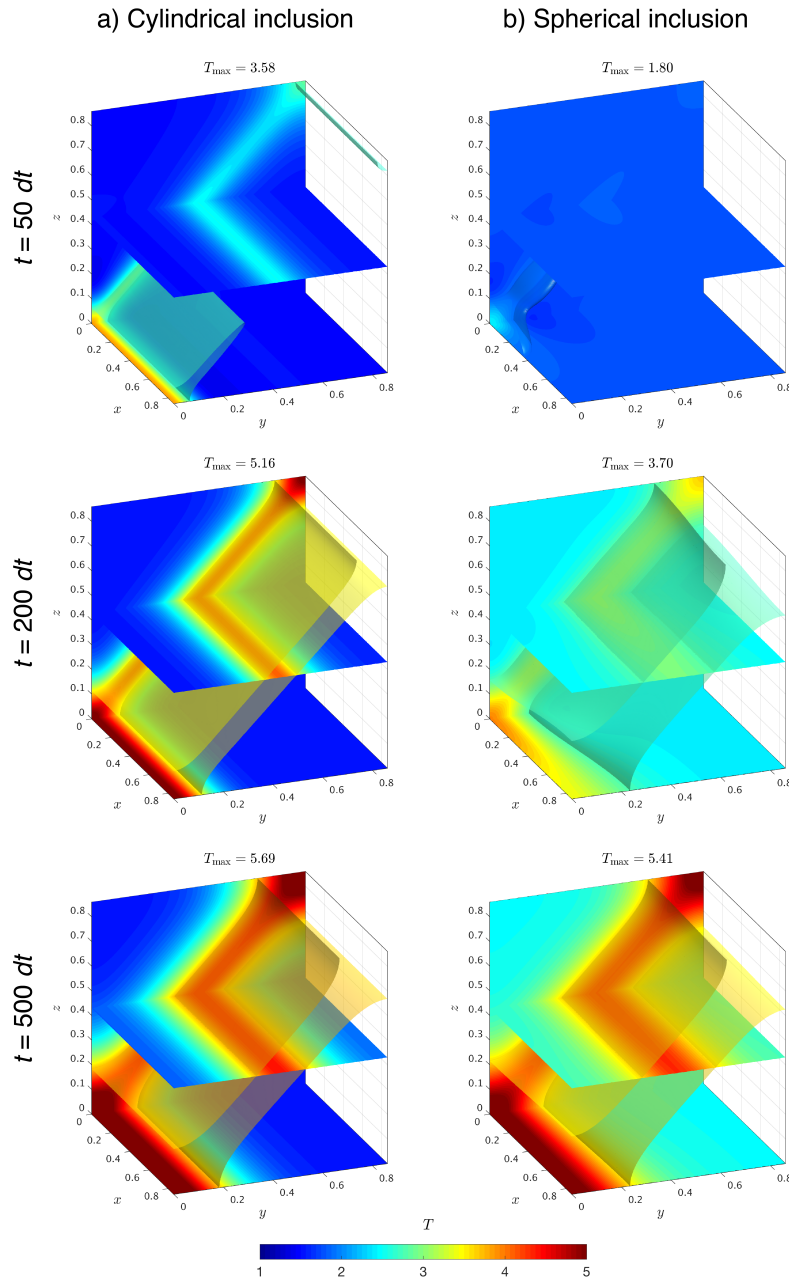


Figure 5.11: 3-D numerical models of thermo-mechanical shear localisation. Two different configurations were considered: a cylindrical initial thermal perturbation (a) and a spherical initial thermal perturbation. Both perturbations evolve into a single shear zone in response to the mechanical work exerted by the boundaries. Pure shear was applied on boundaries normal to y (inflow) and z (outflow); boundaries normal to x were free to slip. All thermal boundary conditions were insulating.

5.6 Discussion

5.6.1 Benefits of the pseudo-transient method and perspectives

The reported results confirm the PT method as performant alternative to a more classical DI solver type to address non-linear coupled problems in geodynamics. In this study, we proved that both methods are capable of resolving the complex non-linear physics and converge to an identical solution, even over a large number of time-steps. The DI solvers are robust and weakly sensitive to large contrasts in material properties (e.g. viscosity). However, they may require a long and non-trivial development phase. A performant Cholesky factorisation of the symmetrical and positive definite finite-difference matrix delivers acceptable time-to-solution for 2-D setups, but is inclined to hit the maximum available RAM memory already at low spatial resolutions for 3-D problems. We further report that implicit methods require physical time-step values close to CFL if significant non-linearities are involved.

In contrast, pseudo-transient solvers result from a simple implementation of the coupled system of equations. The inherent parallelism in PT iterative-based solvers enables a straightforward vectorisation, which shows promising implementation on multiple-core accelerators such GPUs. GPU-based PT solvers outperformed DI solvers regarding wall-time, even for 2-D setups. The reported solution of non-linear thermo-mechanical problems are identical when computed with either the PT or the DI solver types, and validates the robustness and accuracy of the PT solver implementation. Further, the PT algorithms are succinct codes that enhance readability and make them less error-prone. Besides faster times-to-solution, the benefits of PT stencil-based matrix-free solver approaches reside in lower memory footprint, optimal usage of actual hardware and straightforward parallelisation, since only neighbours' access is required. Since the investigation of large 3-D setups may require the use of more than a single-GPU accelerator, the GPU-based PT solver can readily be extended to run on a distributed-memory machine, via message-passing interface (MPI). Implementing an MPI point-to-point communication type for subdomain boundary exchange enables the PT solvers to scale on the largest supercomputers and show by construction a close to optimal parallel efficiency (Omlin et al., 2017a,c).

In this contribution, we focussed on small-strain limits and thus did not treat advection. In future applications, the PT method will be coupled to Eulerian (i.e. Upwind type) and Eulerian-Lagrangian (i.e. characteristics-based) advection solvers. Analogous to the treatment of non-linear couplings (see Section 5.4.6), the PT method will provide a simple framework for implementing explicit or implicit advection solvers (Furuichi and May, 2015).

5.7 Conclusions

In the perspective of quantifying and simulating fully coupled thermo-mechanical processes, such as ductile strain localisation owing to thermal softening, we have presented two numerical methods based on the finite-difference discretisation. The first method is a thermo-mechanical extension to the direct-iterative M2Di solver (Räss et al., 2017), and the second method is based on a fully matrix-free pseudo-transient method. Both methods can model thermo-mechanically activated shear localisation in 2-D and provide consistent results. For 2-D models on a standard desktop computer, the PT method is as accurate and can be as efficient (in terms of wall-time) as the DI approach. We also investigated the impacts of different non-linear coupling strategies and could show that no matter how much the time-step is decreased, solutions obtained with one-way coupling never achieves the accuracy of the two-way coupling.

The significant advantage of the PT method is that it can be extended for high-resolution 3-D numerical simulations without significant modification of the 2-D algorithm. We show that the pseudo-transient method is suitable to perform high-resolution 3-D simulations of thermo-mechanically activated shear localisation. Further, the efficiency of the thermo-mechanical codes makes it suitable for systematic analysis of the parameters that control the dynamics of shear zone development. Based on 139 2-D simulations, we show that a consistent data collapse of the shear zone temperature and strain rate can be established, which further demonstrate the PT method's robustness.

Acknowledgments

The authors acknowledge Daniel Kiss for constructive discussions and Samuel Omlin for his long-term partnership in the HPC code development.

Appendix

5.A The direct-iterative scheme

We seek a solution of the following linear system:

$$\underbrace{\begin{bmatrix} \mathbf{J}_v & \mathbf{G} & \mathbf{H}_1 \\ \mathbf{H} & \mathbf{J}_p & \mathbf{0} \\ \mathbf{H}_2 & \mathbf{0} & \mathbf{J}_T \end{bmatrix}}_{\mathbf{J}_{TM}} \underbrace{\begin{bmatrix} \delta \mathbf{v} \\ \delta \mathbf{p} \\ \delta \mathbf{T} \end{bmatrix}}_{\delta \mathbf{x}} = - \underbrace{\begin{bmatrix} \mathbf{f}_v \\ \mathbf{f}_p \\ \mathbf{f}_T \end{bmatrix}}_{\mathbf{f}}, \quad (5.A.1)$$

where the block matrix $\mathbf{H} = -\mathbf{G}^T$ and $\mathbf{J}_p = \gamma^{-1}\mathbf{I}$.

The linear residuals are defined as:

$$\begin{cases} \mathbf{r}_v = \mathbf{f}_v - \mathbf{J}_v \delta \mathbf{v} - \mathbf{G} \delta \mathbf{p} - \mathbf{H}_1 \delta \mathbf{T} \\ \mathbf{r}_p = \mathbf{f}_p - \mathbf{H} \delta \mathbf{v} - \mathbf{J}_p \delta \mathbf{p} \\ \mathbf{r}_T = \mathbf{f}_T - \mathbf{H}_1 \delta \mathbf{v} - \mathbf{J}_T \delta \mathbf{T} \end{cases} \quad (5.A.2)$$

The solutions are found iteratively:

$$\begin{cases} \delta \mathbf{v}^{i+1} = \delta \mathbf{v}^i + \delta \delta \mathbf{v} \\ \delta \mathbf{p}^{i+1} = \delta \mathbf{p}^i + \delta \delta \mathbf{p} \\ \delta \mathbf{T}^{i+1} = \delta \mathbf{T}^i + \delta \delta \mathbf{T}, \end{cases} \quad (5.A.3)$$

where $\delta \delta \mathbf{v}$, $\delta \delta \mathbf{p}$, and $\delta \delta \mathbf{T}$ are iterative corrections and i is the iteration count.

The iterative velocity correction is obtained by solving:

$$\delta \delta \mathbf{v} = \bar{\mathbf{J}}_v^{-1} \bar{\mathbf{r}}_v, \quad (5.A.4)$$

where $\bar{\mathbf{J}}_v = \mathbf{J}_v - \mathbf{G} (\mathbf{J}_p^{-1} \mathbf{H})$ and $\bar{\mathbf{r}}_v = \mathbf{r}_v - \mathbf{G} (\mathbf{J}_p^{-1} \mathbf{r}_p) - \mathbf{H} \delta \mathbf{T}$. Applying the inverse of \mathbf{J}_p is a trivial operation, since \mathbf{J}_p is a diagonal block matrix. However, applying the inverse of $\bar{\mathbf{J}}_v$ is a cumbersome task, since $\bar{\mathbf{J}}_v$ may not be a symmetrical matrix. Here, we use an iterative Krylov subspace solver (generalized conjugate residuals, Eisenstat et al. (1983)) where the Cholesky factors of the symmetrical operators resulting from a Picard linearisation are used for preconditioning. This approach is described in detail by Räss et al. (2017).

Subsequently, the iterative pressure correction is obtained in a trivial way by evaluating:

$$\delta \delta \mathbf{p} = \mathbf{J}_p^{-1} (\mathbf{r}_p - \mathbf{H} \delta \delta \mathbf{v}). \quad (5.A.5)$$

Finally, the iterative temperature correction is calculated as follows:

$$\delta \delta \mathbf{T} = \mathbf{J}_T^{-1} (\mathbf{r}_T - \mathbf{H}_2 \delta \delta \mathbf{v}). \quad (5.A.6)$$

Here, the \mathbf{J}_T block is a symmetrical positive definite matrix and its inverse can be efficiently applied using pre-computed Cholesky factors. The iteration is repeated until the L_2 norm of all linear residual vectors has decreased below a given threshold value.

Bibliography

- Andersen, T. B., Mair, K., Austrheim, H., Podladchikov, Y. Y., Vrijmoed, J. C., 2008. Stress release in exhumed intermediate and deep earthquakes determined from ultramafic pseudotachylyte. *Geology* 36 (12), 995.
- Braeck, S., Podladchikov, Y. Y., 2007. Spontaneous Thermal Runaway as an Ultimate Failure Mechanism of Materials. *Phys. Rev. Lett.* 98, 095504.
- Carter, N. L., Ave'Lallemant, H. G., 1970. High temperature flow of dunite and peridotite. *GSA Bulletin* 81 (8), 2181.
- Choi, E., Tan, E., Lavier, L. L., Calo, V. M., 2013. Dynearthsol2d: An efficient unstructured finite element method to study long-term tectonic deformation. *Journal of Geophysical Research: Solid Earth* 118 (5), 2429–2444.
- Cundall, P., Coetzee, M., Hart, R., Varona, P., 1993. *FLAC users manual*. Itasca Consulting Group, USA.
- Cundall, P. A., Strack, O. D., 1979. A discrete numerical model for granular assemblies. *geotechnique* 29 (1), 47–65.
- Duretz, T., Schmalholz, S. M., Podladchikov, Y. Y., 2015. Shear heating-induced strain localization across the scales. *Philosophical Magazine* 95 (28–30), 3192–3207.
- Duretz, T., Schmalholz, S. M., Podladchikov, Y. Y., Yuen, D. A., 2014. Physics-controlled thickness of shear zones caused by viscous heating: Implications for crustal shear localization. *Geophysical Research Letters* 41 (14), 4904–4911.
- Eisenstat, S. C., Elman, H. C., Schultz, M. H., 1983. Variational iterative methods for nonsymmetric systems of linear equations. *SIAM Journal on Numerical Analysis* 20 (2), 345–357.
- Fleitout, L., Froidevaux, C., 1980. Thermal and mechanical evolution of shear zones. *Journal of Structural Geology* 2 (12), 159–164, shear zones in rocks.
- Furuichi, M., May, D. A., 2015. Implicit solution of the material transport in stokes flow simulation: Toward thermal convection simulation surrounded by free surface. *Computer Physics Communications* 192, 1 – 11.
- Gerya, T. V., Yuen, D. A., 2003. Characteristics-based marker method with conservative finite-difference schemes for modeling geological flows with strongly variable transport properties. *Physics of the Earth and Planetary Interiors* 140 (4), 293–318.

- Gerya, T. V., Yuen, D. A., 2007. Robust characteristics method for modelling multiphase visco-elasto-plastic thermo-mechanical problems. *Physics of the Earth and Planetary Interiors* 163 (1), 83–105.
- Jaquet, Y., Schmalholz, S. M., 2017. Spontaneous ductile crustal shear zone formation by thermal softening and related stress, temperature and strain rate evolution. *Tectonophysics*.
- John, T., Medvedev, S., Rupke, L. H., Andersen, T. B., Podladchikov, Y. Y., Austrheim, H., 2009. Generation of intermediate-depth earthquakes by self-localizing thermal runaway. *Nature Geoscience* 2 (2), 137–140.
- Kaus, B. J., Popov, A. A., Baumann, T., Püsök, A. E., 2016. Forward and inverse modelling of lithospheric deformation on geological timescales. In: *Proceedings NIC Symposium*.
- Kaus, B. J. P., Podladchikov, Y. Y., 2006. Initiation of localized shear zones in viscoelasto-plastic rocks. *Journal of Geophysical Research: Solid Earth* 111 (B4).
- McKenzie, D. P., Roberts, J. M., Weiss, N. O., 1974. Convection in the earth's mantle: towards a numerical simulation. *Journal of Fluid Mechanics* 62 (3), 465–538.
- Moore, J. D., Parsons, B., 2015. Scaling of viscous shear zones with depth-dependent viscosity and power-law stress – strain-rate dependence. *Geophysical Journal International* 202 (1), 242–260.
- Ohuchi, T., Lei, X., Ohfuji, H., Higo, Y., Tange, Y., Sakai, T., Fujino, K., Irifune, T., 2017. Intermediate-depth earthquakes linked to localized heating in dunite and harzburgite. *Nature Geoscience* 10.
- Omlin, S., Malvoisin, B., Podladchikov, Y. Y., 2017a. Pore Fluid Extraction by Reactive Solitary Waves in 3-D. *Geophysical Research Letters*.
- Omlin, S., Räss, L., Podladchikov, Y. Y., 2017b. Simulation of three-dimensional viscoelastic deformation coupled to porous fluid flow. *Tectonophysics*.
- Omlin, S., Räss, L., Podladchikov, Y. Y., 2017c. Simulation of three-dimensional viscoelastic deformation coupled to porous fluid flow. *Tectonophysics*.
- Parsons, B., McKenzie, D., 1978. Mantle convection and the thermal structure of the plates. *Journal of Geophysical Research: Solid Earth* 83 (B9), 4485–4496.
- Pekeris, C. L., 1935. Thermal convection in the interior of the earth. *Geophysical Journal International* 3, 343–367.
- Peters, M., Veveakis, M., Poulet, T., Karrech, A., Herwegh, M., Regenauer-Lieb, K., 2015. Boudinage as a material instability of elasto-visco-plastic rocks. *Journal of Structural Geology* 78 (Supplement C), 86 – 102.

- Popov, A., Sobolev, S., 2008. Slim3d: A tool for three-dimensional thermomechanical modeling of lithospheric deformation with elasto-visco-plastic rheology. *Physics of the Earth and Planetary Interiors* 171 (1–4), 55 – 75, recent *Advances in Computational Geodynamics: Theory, Numerics and Applications*.
- Prieto, G. A., Florez, M., Barrett, S. A., Beroza, G. C., Pedraza, P., Blanco, J. F., Poveda, E., 2013. Seismic evidence for thermal runaway during intermediate-depth earthquake rupture. *Geophysical Research Letters* 40 (23), 6064–6068.
- Räss, L., Duretz, T., Podladchikov, Y. Y., Schmalholz, S. M., 2017. M2Di: Concise and efficient MATLAB 2-D Stokes solvers using the Finite Difference Method. *Geochemistry, Geophysics, Geosystems* 18 (2), 755–768.
- Rice, A., Fairbridge, R., 1975. Thermal runaway in the mantle and neotectonics. *Tectonophysics* 29 (1), 59 – 72, recent *crustal movements*.
- Schmalholz, S. M., Duretz, T., 2015. Shear zone and nappe formation by thermal softening, related stress and temperature evolution, and application to the Alps. *Journal of Metamorphic Geology* 33 (8), 887–908.
- Talbot, C. J., 1968. Thermal convection in the archaean crust? *Nature* 220 (5167), 552–556.
- Thielmann, M., Kaus, B. J., 2012. Shear heating induced lithospheric-scale localization: Does it result in subduction? *Earth and Planetary Science Letters* 359-360 (0), 1–13.
- Thielmann, M., Rozel, A., Kaus, B., Ricard, Y., 2015. Intermediate-depth earthquake generation and shear zone formation caused by grain size reduction and shear heating. *Geology* 43 (9), 791.
- Yang, X. I., Mittal, R., 2014. Acceleration of the Jacobi iterative method by factors exceeding 100 using scheduled relaxation. *Journal of Computational Physics* 274, 695–708.

CHAPTER 6

Chimneys, channels, pathway flow or water-conducting features: An explanation from numerical modelling and implications for CO₂ storage

Ludovic Räss¹, Viktoriya M. Yarushina², Nina S. C. Simon^{2,3,4}, and Yury Y. Podladchikov¹

¹Faculté des géosciences et de l'environnement, Institut des Sciences de la Terre, University of Lausanne, Lausanne, Switzerland.

²Institute for Energy Technology (IFE), PO Box 40, 2027 Kjeller, Norway.

²UNIK - Universitetsenteret på Kjeller, PO Box 70, 2027 Kjeller, Norway.

⁴University of Oslo, PO Box, 1047 Blindern, 0316 Oslo, Norway.

Abstract

Large amounts of CO₂ must be captured, transported, injected and safely stored in the subsurface in order to counteract increasing atmospheric CO₂ concentrations owing to steadily high consumption of energy from fossil fuels. The injection of gigatons of carbon dioxide poses challenges for pressure management and the mechanical integrity of the storage complex. Optimising the injection strategy, controlling deformation, preventing leakage and assuring safe long-term containment require reliable and predictive hydromechanical modelling. Based on a newly derived thermodynamically consistent set of equations, we have developed fully coupled codes in one, two and three dimensions. In accordance with field observations and laboratory measurements, stress-dependent poro-visco-elasto-plastic deformation is considered. Our simulations predict the spontaneous formation of self-localising high-porosity channels (or pathway flow) under conditions applicable to CO₂ storage in reservoirs. These channels form owing to mechanical instabilities that occur as a natural outcome of buoyancy-driven flow in visco-plastically deforming rocks. Our results indicate that viscous deformation may explain the formation of chimneys such as those observed at the Sleipner pilot, and that non-linear effects strongly impact on the velocity and distribution of the fluid as well as on stress and deformation of the rock matrix. Thus, complex rheology and non-linear coupling between porosity, permeability, pressures and stresses should be included in state-of-the-art reservoir simulation software in order to determine safe injection and storage conditions and correctly model observations and monitoring results.

6.1 Introduction

6.1.1 The need for numerical modelling

To remediate greenhouse gas emissions, enormous amounts of CO₂ must be captured and stored underground, and correspondingly large amounts of pore space are required to accommodate the CO₂ (IEA, 2013). Norway may be able to provide a significant proportion of suitable pore space in its offshore saline aquifers and depleted oil and gas fields (Halland et al., 2011, 2013). According to EU DIRECTIVE 2009/31/EC, the following requirements must be met for transfer of responsibility from the operator of a CO₂ storage site to the authorities at site closure: 1) there is no detectable leakage; 2) the observed behaviour of the injected CO₂ conforms with the modelled behaviour; and 3) the site is evolving towards long-term stability. Thus, reliable predictive models are a prerequisite for industrial scale CO₂ storage. However, existing reservoir simulation tools are struggling to provide good predictions, particularly owing to a shortage of available data (e.g. A. Chadwick, 2013; Cavanagh and Haszeldine, 2014). This problem is likely to be aggravated for the needed – very large-scale – storage operations (Gt of CO₂). In fact, experience with such large-scale injection operations for any fluid type is limited. CO₂ injection also differs from oil and gas operations and geothermal energy generation, because injection is not (directly) balanced by withdrawal. This represents a challenge for controlling pressures and preventing unwanted deformation. Such deformation may lead to the occurrence of (felt) seismicity, surface uplift or subsidence, changes in ground water flow or CO₂ leakage out of the intended storage complex. Thus, pressure and stress monitoring and management will be crucial in large-scale injection and storage operations, and correct and reliable hydromechanical models are a prerequisite. However, existing mathematical models often only qualitatively match field data or experimental results (see e.g. Rutqvist (2012) for an extensive review on the modelling of CO₂ injection and storage, and Figure 12b in Harrington et al. (2009) for an example of modelling of experimental gas flow through shale).

6.1.2 The Sleipner example

One of the best documented CO₂ storage operations is the injection of about 1 million tons of CO₂ per year since 1996 into the Utsira formation at Sleipner in the Norwegian North Sea. Geophysical monitoring indicates that the CO₂ is safely contained below the main caprock, and pressure at the well-head is stable. While attempts have been made to history-match the observations at Sleipner using conventional reservoir simulations, these have failed to capture first-order observations, such as the facile vertical flow of CO₂ through low-permeability shale layers, the formation of focussed flow channels or chimneys, and rapid lateral spreading underneath the caprock shale (Chadwick and Noy, 2010). These authors concluded that vertical

CO₂ migration at Sleipner occurs "via some form of pathway flow, the pathways becoming more effective, or more numerous with time" and stated that "The nature of these pathways is uncertain however". Such pathway flow is also often observed in experiments conducted on shale for nuclear waste or CO₂ storage purposes (e.g. Harrington et al., 2009; Horseman et al., 1999). To date, there are no numerical models that can predict the spontaneous formation and dynamic evolution of such pathways in an initially intact rock.

6.1.3 Localised fluid flow

Observations on fluid flow in the Earth's crust and in reservoirs generally show that fluid flow tends to be localised in space and time, requiring that permeability change dynamically during fluid flow (e.g. Chadwick and Noy, 2010; Harrington et al., 2009; Ingebritsen and Manning, 2010; Main et al., 2006; Ortiz R et al., 2011). Such localisation is predicted from theory and experiments owing to instabilities that arise from a strong coupling between fluid flow and deformation (Baisch et al., 2010; Connolly and Podladchikov, 2000; Kong et al., 2009; Nermoen et al., 2010; Rozhko et al., 2007; Yarushina, 2009).

6.1.4 Reservoir rheology

However, quantitative investigation of the potentially major effects of physical coupling of deformation and fluid flow only began recently (Appold and Nunn, 2002; Elsworth and Yasuhara, 2006; Le Guen et al., 2007; Tantserev et al., 2009). Further, the rheology of reservoirs may be more complex than generally assumed. Shallow reservoirs are mostly considered to behave elastically and fail by frictional plasticity. However, recent experiments show that reactions involving reactive fluids (as in CO₂ storage) are rapid (i.e. they occur at laboratory time-scales of hours to weeks) and under load lead to pressure solution and effectively viscous deformation (Elsworth and Yasuhara, 2006; Le Guen et al., 2007). These experiments suggest that viscous deformation may play a key role in reservoirs at time-scales relevant for CO₂ sequestration (days to 10,000 years); thus, we must consider a visco-elasto-plastic rheology (Yarushina and Bercovici, 2013). Even without actively flowing fluids, sedimentary rocks in reservoir and caprock sequences deform in both brittle (elasto-plastic) and ductile (viscous) manner (e.g. Hagin and Zoback, 2004b; Sone et al., 2011; Zoback and Gorelick, 2012). Implementation of such realistic complex rheology into the model is needed to simulate observed compaction in reservoirs (e.g. Zoback, 2010), and may be the key to explain the pathway flow observed at the Sleipner CO₂ injection site (Norwegian North Sea), and in experiments (Simon and Podladchikov (2013b) and references therein). In this contribution, we study the large-scale consequences of both complex visco-elasto-plastic rock rheology and the effects of non-linearity for dynamically evolving permeability in different reservoir rock types. This work is an extension of Simon et al.'s (Simon, 2012; Simon and Podladchikov,

2013a; Simon, 2013) 2-D results, which were also based on the simplified assumption of a lithostatic stress state. The new model we present here includes full mechanics, which allows us to investigate flow and deformation in a heterogeneously stressed crust with non-linear poro-visco-elasto-plastic rheology.

6.2 Model equations

6.2.1 Basic formulation

A system of equations for poro-visco-elasto-plastic deformation and flow was derived in (Yarushina, 2009; Yarushina and Podladchikov, 2014). The model generalises Biot's theory of poro-elasticity to large poro-visco-elasto-plastic deformations, and is consistent with Gassmann's equations and the elastic effective stress law (Tantserev et al., 2009; Yarushina, 2009). The closed system of equations describing fluid flow in porous visco-elasto-plastic media consists of the following minimum set of equations that represent mass balance:

$$\frac{1}{\rho_s} \frac{d^s \rho_s}{dt} - \frac{1}{1-\phi} \frac{d^s \phi}{dt} + \nabla_j v_j^s = 0, \quad (6.1)$$

$$\frac{\phi}{\rho_f} \frac{d^f \rho_f}{dt} + \frac{d^s \phi}{dt} + \phi \nabla_j v_j^s + \nabla_j q_j^D = 0, \quad (6.2)$$

force balance:

$$\nabla_j (\bar{\tau}_{ij} - \bar{p} \delta_{ij}) - g \bar{\rho} \hat{z}^i = 0, \quad (6.3)$$

$$-\frac{k}{\eta_f} \left(\nabla_i p^f + g \rho^f \hat{z}^i \right) = q_i^D, \quad (6.4)$$

and closure relations:

$$\epsilon_{ij} = \frac{1}{2G} \frac{d^s \bar{\tau}_{ij}}{dt} + \frac{\bar{\tau}_{ij}}{2\eta_s}, \quad (6.5)$$

$$\frac{d^s \phi}{dt} = \frac{1}{K_\phi} \left(\frac{d^f p^f}{dt} - \frac{d^s \bar{p}}{dt} \right) + \frac{1}{\eta_\phi} (p^f - \bar{p}), \quad (6.6)$$

$$\nabla_k v_k^s = -\frac{1}{K_{dry}} \left(\frac{d^s \bar{p}}{dt} - \alpha \frac{d^f p^f}{dt} \right) - \frac{\bar{p} - p^f}{(1-\phi)\eta_\phi}, \quad (6.7)$$

$$\nabla_k q_k^D = \frac{\alpha}{K_{dry}} \left(\frac{d^s \bar{p}}{dt} - \frac{1}{B} \frac{d^f p^f}{dt} \right) + \frac{\bar{p} - p^f}{(1-\phi)\eta_\phi}. \quad (6.8)$$

Here, ρ_s, ρ_f are solid and rock densities, v_i^s and q_i^D are the components of solid velocity and Darcy's flux, ϕ is the porosity, \bar{p}, p^f are the total and fluid pressures, k is the porosity-dependent permeability, $\bar{\tau}_{ij}$ are the total stress deviators, K_{dry} is the dry bulk modulus, K_ϕ, η_ϕ are the effective bulk modulus and viscosity, α is the Biot-Willis coefficient, and B is

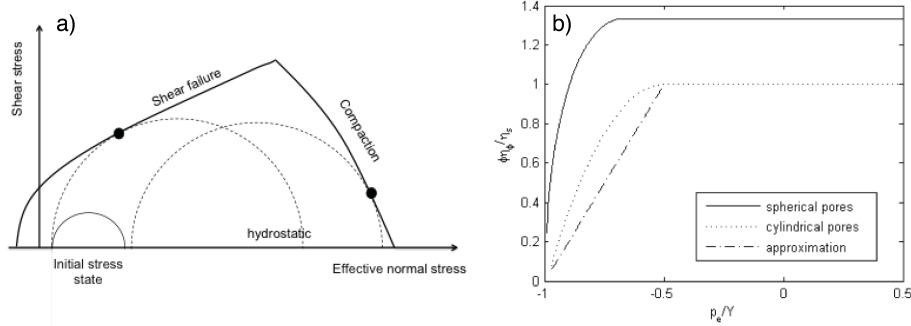


Figure 6.1: (a) Failure envelope for visco-elasto-plastic rocks. Inside the envelope material, the behaviour is visco-elastic. During injection, the stress state changes from its initial state and eventually reaches shear failure or the compaction line. At this point, decompaction weakening, as shown on the right, begins. (b) Effective viscosity η_ϕ of visco-plastic porous rock normalised to the shear viscosity of the solid rock frame η_s and porosity ϕ as a function of ratio p_e/Y of effective pressure to the yield strength Y of the rock frame. In the compaction regime ($p_e > 0$), effective viscosity doesn't depend on the effective pressure, while in the decompaction regime ($p_e < 0$), viscosity exhibits near-linear dependence on effective pressure after failure is initiated at $p_e = -(1 - \phi)Y/2$. At $p_e = -(1 - \sqrt{\phi})Y$, the material loses its integrity (full pore collapse), and effective pressure build up cannot be supported by the solid rock frame.

the Skempton's coefficient. Equation (6.5) relates shear strain rates to shear total stresses in a standard Maxwell visco-elastic manner. Equation (6.6) shows that changes in porosity and therefore permeability are caused by the difference between total and fluid pressures ($\bar{p} - p^f$). Equation (6.7) indicates that the total volumetric deformation of the rock is driven by effective stress with a Biot-Willis factor, and that it consists of elastic (first-term) and viscous (second-term) contributions. We assume here that solid rock grains are elastically compressible. Equation (6.8) shows that the flow is affected by total pressure as well as by fluid pressure, again with elastic and viscous components. In the purely elastic limit, equations (6.7) and (6.8) reduce to Biot's classical poro-elastic relationships.

The model is for now restricted to one fluid phase in the pore space since we focus is on hydromechanical interactions.

6.2.2 Model parameters

Constitutive equations (6.1) to (6.8) have a number of material parameters that depend on the stress state in terms of the first and second stress invariants. Effective bulk modulus K_ϕ and effective viscosity η_ϕ were obtained using methods of effective media theory, as averaged

properties of the representative volume element. They depend on solid elastic and/or viscous moduli as well as on porosity:

$$\begin{aligned} K_\phi &= m \frac{G_s}{\phi}, \\ \eta_\phi &= m \frac{\eta_s}{\phi}, \end{aligned} \quad (6.9)$$

where m is a geometric factor. It is equal to 1 for cylindrical pores and significantly reduces for elongated pores. Solid shear viscosity η_s is often assumed to depend on the equivalent shear stress in the following manner:

$$\eta_s = \frac{\eta_0}{1 + \left(\frac{\tau_{II}}{\tau_b}\right)^{N-1}}, \quad (6.10)$$

where τ_{II} is the second stress invariant, τ_b is a breakdown stress level, and N is a power law exponent with typical value $N = 3$. This expression captures non-Newtonian power law creep rheology. When stresses reach the yield limit, effective bulk modulus and viscosity drop significantly, exhibiting a strong dependence on effective pressure and a (de)compaction asymmetry (Figure 6.1).

Other mechanical parameters are related to the bulk moduli K_s and K_ϕ as follows:

$$\frac{1 - \phi}{K_{dry}} = \frac{1}{K_\phi} + \frac{1}{K_s}, \quad (6.11)$$

$$\alpha = 1 - \frac{K_{dry}}{K_s}, \quad (6.12)$$

$$B = \frac{\frac{1}{K_{dry}} - \frac{1}{K_s}}{\frac{1}{K_{dry}} - \frac{1}{K_s} + \phi \left(\frac{1}{K_f} - \frac{1}{K_s} \right)}. \quad (6.13)$$

Equation (6.11) is analogous to the first Gassmann's relation (Yarushina, 2009), equation (6.12) is a definition of the Biot-Willis coefficient, and (6.13) is a definition of the Skempton's coefficient (Wang, 2000). Numerous laboratory measurements on fluid flow in porous rocks indicate that permeability changes during compaction/decompaction as a function of porosity (David et al., 1994; Dong et al., 2010):

$$k = k_0 \left(\frac{\phi}{\phi_0} \right)^n, \quad (6.14)$$

where k_0 and ϕ_0 are background values of the permeability and porosity, respectively. The extent to which permeability depends on porosity is controlled by exponent n . n is a material parameter, which is usually taken to be between 3 and 5 for sandstones, but can be as high as 25 for shales (Dong et al., 2010).

6.2.3 Flow instability and chimney formation

Poro-visco-elastic equations have been previously used in the literature for modelling of melt ascend in deep Earth (McKenzie, 1984), petroleum migration from source rocks (Appold and Nunn, 2002), and compaction and fluid expulsion in sedimentary basins (Audet and Fowler, 1992; Connolly and Podladchikov, 2000). An astonishing result of these studies is the generation of a special fluid flow instability type that leads to the formation of high-porosity, high-permeability domains that can self-propagate upwards owing to the interplay between buoyancy and viscous resistance of the deforming porous rock matrix. This instability was named a porosity wave, owing to its resemblance to solitary waves known in fluid dynamics if porosity is plotted as a function of depth (Barcilon and Richter, 1986). As instability, porosity waves don't form everywhere. They require that special conditions be met. A first and key requirement is the solid rock frame's ability to undergo time-dependent deformation such as purely viscous, visco-elastic or visco-plastic deformation.

The appearance of porosity waves strongly depends on the rock rheology type. In viscous and visco-elastic rocks, they would form more or less spherical fluid-rich blobs that propagate upwards without changing their shape (Figure 6.2). Plasticity and the difference between compaction and decompaction responses lead to focussing of the porosity wave and the formation of vertical self-propagating channels (Figures 6.2 and 6.5). A second requirement for the generation of porosity waves is a non-linear dependence of permeability on porosity, i.e. the exponent in the power law for permeability (equation (6.14)) must be $n > 1$. Finally, the injection rates must locally exceed the Darcy flow rate so that fluid diffusion through porous rock cannot prevent a local buildup of fluid pressures in the CO₂ plume.

All these conditions are likely to be met at CO₂ injection sites. Indeed, the viscous rheology of sandstones and shales comprising typical reservoirs is well documented (e.g. Hagin and Zoback, 2004a; Sone and Zoback, 2014), as is the non-linearity of these rocks' porosity-dependent permeability (e.g. David et al., 1994; Dong et al., 2010). Thus, upward-propagation of CO₂ owing to buoyancy and channel-formation is unsurprising. In the following chapters, we will numerically investigate the generation of porosity waves using in-house developed visco-elasto-plastic numerical codes. Previous research showed that many features of 3-D porosity waves are captured in 1-D calculations, which represent vertical cross-sections of the wave.

6.3 Numerical implementation

A particular challenge for hydromechanical models is the issue of how to model the coupling between flow and deformation in numerical codes. These two processes are inherently coupled. However, numerical implementation of the full coupling is challenging and computationally

expensive. Numerical modelling attempts are therefore largely restricted to one-way sequential coupling of two different codes (e.g. TOUGH-FLAC (Rutqvist, 2011, 2012)) where large number of iterations are required for accurate predictions (Prevost, 2014).

However, iterative solving of the non-linear problem may not be sufficient to capture the strong physical couplings between flow and deformation that are a main feature of the thermodynamically consistent system of equations, and linear elastic behaviour is clearly an oversimplification of the behaviour of porous reservoir rocks.

Thus, the previously described complex physics justify the development of new numerical algorithms. Since the equations are strongly non-linear and fully coupled, an explicit iterative finite-difference scheme is used. The steady state is reached by performing pseudo-transient non-linear iterations until convergence is reached. Then, the physical time is updated and the next time-step is solved. The advantages of this numerical method are the straightforward implementation of the equations as well as light and performing codes, which do not require heavy memory access or matrices storage. The major limitation is the requirement of a more restrictive time-step, compared to other implicit methods. The benefits of such an implementation don't significantly influence 1-D runs, but become very interesting and needed when going to 2-D or 3-D setups. In our models, high resolution in both space and time is essential to capture the multiscale and spontaneous fluid-focussing events caused by dynamic porosity and the accompanying permeability increases. Conventional resolution much lower than characteristic compaction length would simply miss these events. Such runs can only be produced on massively parallel supercomputing architectures, using the latest technologies, such as graphical processing units (GPUs) and multiple integrated core architectures (MICs). The inherent low-level parallelism of explicit methods justifies the development of new algorithms, scaling linearly and performing very well on all tested machines.

6.3.1 The numerical setup of the model

We investigate two different setups, in various spatial dimensions. The 1-D and 3-D runs have the same setup, while the 2-D runs explore a more complex geometry closer to a reservoir setting. The first setup, used in the 1-D and 3-D runs, is an initial Gaussian porosity perturbation located at 1/4 of the domain height, representing an injection pulse. Total pressure and fluid pressures are initialised in order to set effective pressure on the neutral line in the failure envelope.

The 2-D run (Figure 6.2) contains nine shale layers, reproducing Sleipner's geometry, but the properties of the layers differ in porosity and permeability only. Injection is performed from the bottom of the model. In the 1-D runs (Figure 6.3), we compare two major different rock types found in the Sleipner reservoir, with unconsolidated sandstones constituting the main reservoir rock and the shale forming the low-permeability layers. Values for important

Description	Shale	Sandstone	Units
Bulk viscosity	1e11	1e14	Pa.s
Permeability	2e-6	2	Darcy
Brine + CO ₂ viscosity	8e-4	8e-4	Pa.s
Brine + CO ₂ density	1020	1020	kg.m ⁻³

Table 6.1: Note: Values from Cavanagh (2013); David et al. (1994); Hagin and Zoback (2004b); Sone and Zoback (2014).

parameters used in this setup can be found in Table 6.1. Finally, the 3-D runs (Figures 6.4 and 6.5) focus on the non-trivial stress distribution and effect of horizontal shear stress on the wave propagation and geometry.

6.4 Results and discussion

6.4.1 Fluid flow in deforming rocks and channel-formation

Simon et al. (Simon and Podladchikov, 2013a; Simon et al., 2013) have presented 2-D simulation results on fluid injection into visco-elasto-plastically deforming rocks using a simplified mechanical approach following (Connolly and Podladchikov, 1998). The simplification is that total pressure is considered to be lithostatic. Further, solid velocities were assumed to be small compared to fluid velocities and set to 0. Stresses, particularly deviatoric stresses, were therefore not calculated, and the deformation of the solid matrix could not be simulated. Further, Biot poro-elasticity was not included. An example of a 2-D simulation of flow in a layered reservoir appears in Figure 6.2 (from Simon and Podladchikov (2013a)). The run is initialised with a high porosity and permeability background with nine interspersed low porosity and permeability layers, and some random heterogeneity. Initial pressure is uniform (lithostatic). The layers are discontinuous and the box is open at the sides, so fluid can escape sideways. Fluid injection occurs in the light blue squares at the bottom of the box. Fluid flow is driven by buoyancy and local pressure gradients that develop owing to fluid flow and deformation. High-porosity channels (porosity waves) develop spontaneously, and fluid breaches the initial low permeability layers (dark blue boxes, arrows). Note the strongly heterogeneous and dynamically changing pressure distribution, which differs significantly from pressure distribution predicted from flow simulations that don't include viscous deformation.

6.4.2 Model development, improvements and goals

Our new model includes full mechanics, as described in Section 6.2. Further, the code has been extended to three dimensions, see Section 6.3. These improvements allow to accurately model

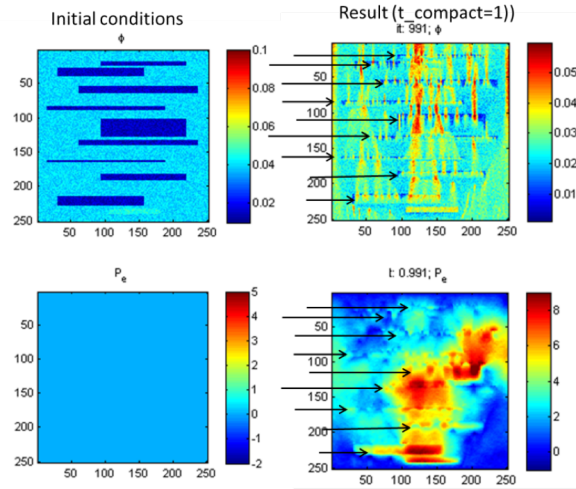


Figure 6.2: Example of a 2-D (X, depth) simulation of fluid flow through a high-permeability reservoir with interbedded low-permeability shales. The two left-hand panels show initial condition for porosity (top) and effective pressure $p_e = \bar{p} - p^f$ (bottom). The right-hand panels show results after one compaction time-scale. Arrows indicate the shale layers' locations. Fluid is injected at the bottom of the reservoir. Sand and shale differ in porosity and permeability only, but have the same bulk viscosity and compressibility. All parameters are dimensionless. The model resolution is 251 x 251 grid-cells. From Simon and Podladchikov (2013a).

fluid injection and flow into heterogeneously stressed rocks. Also, non-linear stress-dependent rheology is included, which may play key roles for mechanical weakening of the rock, the opening of pore space, and the onset of failure (Chhabra, 2007; Räss, 2013; Räss et al., 2013; Yarushina et al., 2013). Ultimately, the model will allow us to i) compute the speed and direction of fluid flow in a pre-stressed subsurface, the feedback on solid stresses and the deformation, including surface deformation, ii) explore the onset of failure of pre-existing and new faults and fractures, iii) determine the conditions for channelised flow, and iv) constrain operating parameters for CO₂ injection to assure storage containment and integrity over time. As we show in this paper, localised flow owing to visco-plastic deformation is likely to occur in reservoirs, and including complex rheology is crucial to predict localised flow phenomena besides brittle failure.

6.4.3 Porosity waves in 1-D and rock properties' effects

In this section, we explore fluid movement in two rock types that are common and representative of CO₂ storage aquifers and caprocks, respectively, namely loosely consolidated sand (such as the Utsira sand and Sleipner or the Mount Simon sandstone in Illinois) and shale. Mechanical and petro-physical properties of these rock types are taken from the literature; see Table 6.1. Figure 6.3 shows two examples of unconsolidated sandstone rheology and typical shale rheology. The high-porosity, high-permeability sandstone ($k_0 = 2$ Darcy) was chosen to

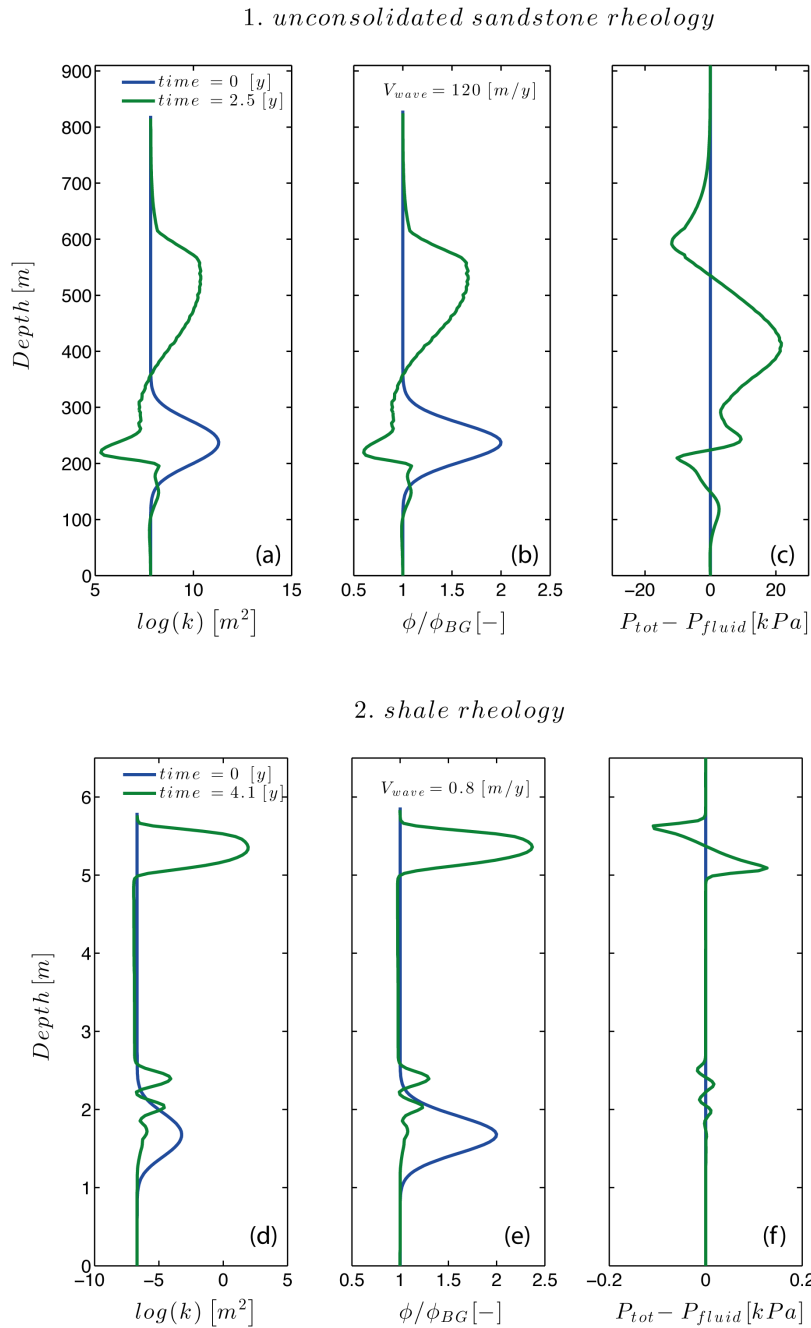


Figure 6.3: Formation and evolution of high-permeability regions travelling upwards in unconsolidated sandstone (upper panel) and shale (lower panel). Logarithmic permeability (a, d), porosity normalised to background porosity (b, e), and effective pressure $p_e = \bar{p} - p^f$ (c, f) are shown for the initial condition ($time = 0$, blue line) and some later time (green line; 2.5 years and 4.1 years for sandstone and shale, respectively). Else, both runs have identical initial and boundary conditions, as described in the text and shown in Table 6.1. Note the different scales for height of the wave, permeability and pressure in the two rock types.

have a power law exponent $n = 5$ for porosity-dependent permeability (equation (6.14)) and a solid viscosity $\eta_s = 1013$ Pa.s. In turn, the low permeability shale has $n = 15$ and $\eta_s = 1011$ Pa.s. The two runs were otherwise initialised identically, as described in Section 6.3.1.

Both runs result in the formation of a porosity wave that travels upwards, but the characteristic length and time-scales as well as the wave shapes differ significantly for the two rock types. The wave travels faster in the sandstone (120 m/yr vs. 0.8 m/yr in the shale; Figure 6.3b and Figure 6.3e), but is much more elongated (height ~ 250 m with a correspondingly large width), with maximum amplitudes in both porosity and permeability that are lower than the amplitude of the initial perturbation. In the shale, in contrast, the wave is much more focussed (height ~ 1 m, implying a similar or smaller width; see the 2-D and 3-D calculations). Further, the maximum amplitude of porosity and permeability increases during the upward travel of the fluid-filled perturbation in the shale. Thus, more fluid is concentrated in a smaller volume in the shale, while fluid is distributed over a larger depth range in the sandstone. In 3-D, the porosity wave would look more like a large blob or plume in the sandstone, while in the shale it looks more like a crack or channel.

The perturbations in effective pressure are significantly larger in the sandstone than the shale owing to the lower viscosity in the shale, i.e. less effective pressure is needed to open and close pore space in the shale because it is softer. This also implies that a pressure pulse associated to a porosity wave travelling through sandstone is easily large enough to cause deformation and pore opening in a soft shale that is interspersed in or overlying a sandstone. Since the fluid's velocity and the wave's amplitude are much higher in the sandstone than in the shale, we expect some lateral spreading of fluid underneath shale layers.

6.4.4 Examples of 3-D simulations

The results of the previous 2-D modelling (Simon and Podladchikov, 2013a) were confirmed and extended by 3-D calculations. Numerical runs with the newly developed 3-D hydromechanical simulator show that parallel GPU programming allows for fast runs of fully coupled numerical algorithms with high resolution in 3-D. Localised upward fluid propagation previously predicted with 2-D simulations was also observed in 3-D (Figures 6.4 and 6.5). Figure 6.4 shows the propagation of an initially spherical CO₂ plume in a visco-elastic porous rock subjected to background shear stresses. No flux boundary conditions are imposed. Buoyancy force generates high fluid overpressures at the top of the plume, leading to non-homogeneous distributions of fluid and total pressures (the left-hand columns in Figure 6.4). High fluid overpressures at the top dilate the pores pushing CO₂ upwards and generating local variations in shear stresses, as shown in the right-hand columns in Figure 6.4. Since viscosity is non-linearly related to shear stress, viscosity is reduced in high-stress regions around the traveling plume (Räss, 2013). This viscosity reduction leads to higher propagation speed,

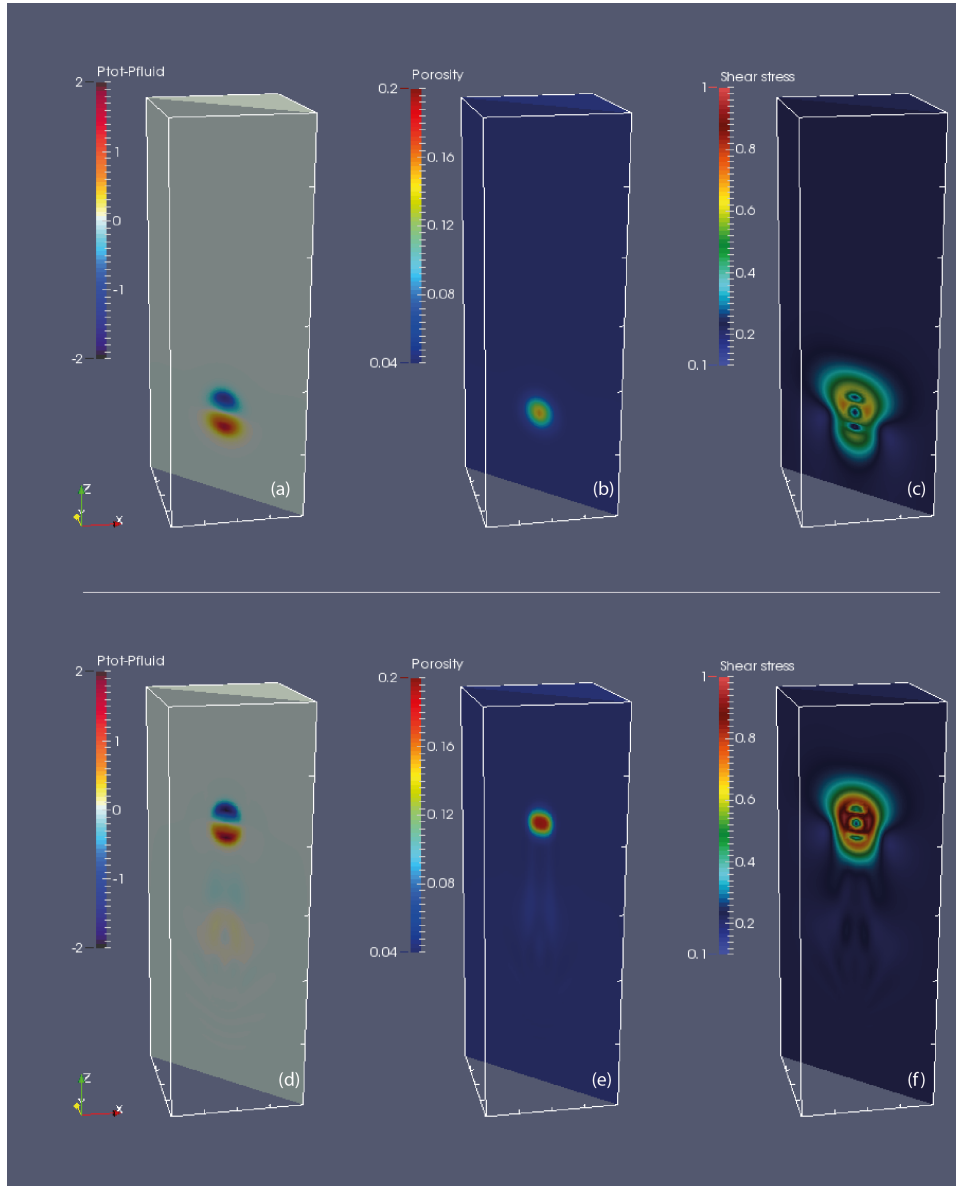


Figure 6.4: 3-D numerical simulation results of propagating porosity perturbation through non-linear viscous porous rock, exposed to background shear stress. Initial porosity perturbation is implemented as a 3-D Gaussian, located at $Lz/4$ and with an amplitude equal to three times the background porosity. Subplots shown for dimensionless time-steps 1 (a, b, c) and 80 (d, e, f) are the effective pressure $p_e = \bar{p} - p^f$ (a, c), the porosity distribution (b, d) and the shear stress invariant (c, e), respectively. All are dimensionless parameters.

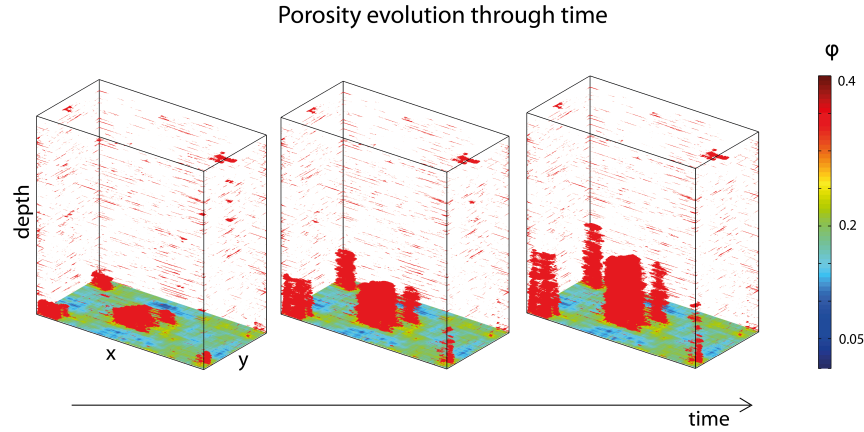


Figure 6.5: Porosity evolution from high-resolution 3-D simulation of focussing two-phase flow analogous to the 2-D simulation presented in Figure 6.2; 480 x 240 x 480 grid-points resolution in (x,y,z) dimensions, performed with C-CUDA and MPI on 4 GPUs. Full mechanics, bilinear viscosity and XY Gaussian trended background randomness (Räss et al., 2014).

even without invoking plasticity. However, variations in shear stress may eventually lead to failure or reactivation of pre-existing faults, when the critical yield stress is reached. This scenario is investigated in Figure 6.5, where we assume that effective viscosity reduces with decreasing effective pressure at the onset of failure (see Figure 6.1), and also shown in Figure 6.2. As a result, the reservoir rock’s viscosity differs between the top of the propagating plume and the bottom. Pores that were pushed open when the plume first reached them therefore don’t recover their initial volume. This leads to formation of vertical channels that are able to propagate upwards much faster than spherical blobs (Connolly and Podladchikov, 2007).

6.5 Conclusions

- We developed a new 3-D fully coupled numerical algorithm for fluid flow in deforming poro-visco-elasto-plastic rocks.
- The implemented rheology accounts for three different non-linearity types: Asymmetry in compaction and decompaction, porosity-dependent bulk properties, and viscosity that depends non-linearly on shear stresses.
- The new model predicts the formation of self-propagating high-porosity channels as a key feature.
- Resolving channel-formation requires high spatial and temporal resolution, which requires high-performance computing.

- Deduced time and length scales for CO₂ upward-migration are in agreement with observations from the Sleipner CO₂ storage pilot.
- Time-dependent rheology and non-linear porosity-dependent permeability strongly impact on deformation and flow. Thus, they must be included in numerical codes in order to obtain reliable simulations of CO₂ injection and storage operations.

Acknowledgments

This research has been funded by IFE strategic institute funds, by former WP3 (now WP2: Containment) in the CEER SUCCESS centre for CO₂ storage under grant 193825/S60 from the Research Council of Norway, and a PhD scholarship from UNIL to L.R.

Bibliography

- A. Chadwick, D. N., 2013. Achieving regulatory conformance: a study in prediction and verification at Sleipner. In: 7th TCCS, Trondheim, Norway.
- Appold, M. S., Nunn, J. A., 2002. Numerical models of petroleum migration via buoyancy-driven porosity waves in viscously deformable sediments. *Geofluids* 2 (3), 233–247.
- Audet, D. M., Fowler, A. C., 1992. A mathematical model for compaction in sedimentary basins. *Geophysical Journal International* 110 (3), 577–590.
- Baisch, S., Voros, R., Rothert, E., Stang, H., Jung, R., Schellschmidt, R., 2010. A numerical model for fluid injection induced seismicity at Soultz-sous-Forets. *International Journal of Rock Mechanics and Mining Sciences* 47 (3), 405–413.
- Barcilon, V., Richter, F., 1986. Nonlinear-waves in compacting media. *Journal of Fluid Mechanics* 164, 429–448.
- Cavanagh, A., 2013. Benchmark Calibration and Prediction of the Sleipner CO₂ Plume from 2006 to 2012. *Energy Procedia* 37, 3529–3545.
- Cavanagh, A. J., Haszeldine, R. S., 2014. The Sleipner storage site: Capillary flow modeling of a layered CO₂ plume requires fractured shale barriers within the Utsira Formation. *International Journal of Greenhouse Gas Control* 21 (0), 101–112.
- Chadwick, R. A., Noy, D. J., 2010. History-matching flow simulations and time-lapse seismic data from the Sleipner CO₂ plume. Geological Society, London, *Petroleum Geology Conference series* 7, 1171–1182.

- Chhabra, R. P., 2007. Bubbles, drops, and particles in non-Newtonian fluids, 2nd Edition. Vol. 1. Taylor and Franics, Boca Raton.
- Connolly, J. A. D., Podladchikov, Y. Y., 1998. Compaction-driven fluid flow in viscoelastic rock. *Geodinamica Acta* 11 (2-3), 55–84.
- Connolly, J. A. D., Podladchikov, Y. Y., 2000. Temperature-dependent viscoelastic compaction and compartmentalization in sedimentary basins. *Tectonophysics* 324 (3), 137–168.
- Connolly, J. A. D., Podladchikov, Y. Y., 2007. Decompaction weakening and channeling instability in ductile porous media: Implications for asthenospheric melt segregation. *Journal of Geophysical Research* 112 (B10), B10205.
- David, C., David, T.-F., Wong, W., Zhu, J., Zhang, 1994. Laboratory measurement of compaction-induced permeability change in porous rocks: Implications for the generation and maintenance of pore pressure excess in the crust. *Pure and applied geophysics* 143 (1-3), 425–456.
- Dong, J.-J., Hsu, J.-Y., Wu, W.-J., Shimamoto, T., Hung, J.-H., Yeh, E.-C., Wu, Y.-H., Sone, H., 2010. Stress-dependence of the permeability and porosity of sandstone and shale from TCDP Hole-A. *International Journal of Rock Mechanics and Mining Sciences* 47 (7), 1141–1157.
- Elsworth, D., Yasuhara, H., 2006. Short-Timescale Chemo-Mechanical Effects and their Influence on the Transport Properties of Fractured Rock. *Pure and Applied Geophysics* 163 (10), 2051–2070.
- Hagin, P. N., Zoback, M. D., 2004a. Viscous deformation of unconsolidated reservoir sands – Part 2: Linear viscoelastic models. *Geophysics* 69 (3), 742–751.
- Hagin, P. N., Zoback, M. D., 2004b. Viscous deformation of unconsolidated reservoir sands Part 1: Timedependent deformation, frequency dispersion, and attenuation. *geophysics* 69 (3), 731–741.
- Halland, E., Johansen, W., Riis, F., 2011. CO₂ Storage Atlas: Norwegian North Sea. The Norwegian Petroleum Directorate, Stavanger, Norway.
- Halland, E., Johansen, W., Riis, F., 2013. CO₂ Storage Atlas: Norwegian Sea. The Norwegian Petroleum Directorate, Stavanger, Norway.
- Harrington, J. F., Noy, D. J., Horseman, S. T., Birchall, D. J., Chadwick, R. A., 2009. Laboratory study of gas and water flow in the Nordland Shale, Sleipner, North Sea. Vol. 59 of AAPG Studies in Geology. pp. 521– 543.

- Horseman, S. T., Harrington, J. F., Sellin, P., 1999. Gas migration in clay barriers. *Engineering Geology* 54 (12), 139–149.
- IEA, 2013. Technology Roadmap - Carbon capture and storage, 2013 edition. Report.
- Ingebritsen, S. E., Manning, C. E., 2010. Permeability of the continental crust: dynamic variations inferred from seismicity and metamorphism. *Geofluids* 10 (1-2), 193–205.
- Kong, X.-Z., Kinzelbach, W., Stauffer, F., 2009. Migration of air channels: An instability of air flow in mobile saturated porous media. *Chemical Engineering Science* 64 (7), 1528–1535.
- Le Guen, Y., Renard, F., Hellmann, R., Brosse, E., Collombet, M., Tisserand, D., Gratier, J. P., 2007. Enhanced deformation of limestone and sandstone in the presence of high PCO₂ fluids. *Journal of Geophysical Research-Solid Earth* 112 (B5), B05421.
- Main, I. G., Li, L., Heffer, K. J., Papasouliotis, O., Leonard, T., 2006. Long-range, critical-point dynamics in oil field flow rate data. *Geophys. Res. Lett.* 33 (18), L18308.
- McKenzie, D., 1984. The Generation and Compaction of Partially Molten Rock. *Journal of Petrology* 25 (3), 713–765.
- Nermoen, A., Galland, O., Jettestuen, E., Fristad, K., Podladchikov, Y., Svensen, H., Malthesorensen, A., 2010. Experimental and analytic modeling of piercement structures. *J. Geophys. Res.* 115 (B10), B10202.
- Ortiz R, A. E., Renner, J., J, R., 2011. Hydromechanical analyses of the hydraulic stimulation of borehole Basel 1. *Geophysical Journal International* 185 (3), 1266–1287.
- Prevost, J. H., 2014. Two-way coupling in reservoir-geomechanical models: vertex-centered Galerkin geomechanical model cell-centered and vertex-centered finite volume reservoir models. *International Journal for Numerical Methods in Engineering* 98 (8), 612–624.
- Räss, L., 2013. Three-Dimensional GPU-Accelerated Modelling of Buoyancy-Driven Flow under Horizontal Far-Field Stress. Master Thesis.
- Räss, L., Omlin, S., Moulas, E., Simon, N. S., Podladchikov, Y., 2014. Multi-GPU Accelerated Simulation of Dynamically Evolving Fluid Pathways. In: *EGU General Assembly 2014*. Vol. Geophysical Research Abstracts Vol. 16.
- Räss, L., Omlin, S., Podladchikov, Y., 2013. Influence of intrinsic and extrinsic forces on 3D stress distribution using CUDA programming. *Geophysical Research Abstracts* 15, EGU2013–12637.
- Rozhko, A. Y., Podladchikov, Y. Y., Renard, F., 2007. Failure patterns caused by localized rise in pore-fluid overpressure and effective strength of rocks. *Geophysical Research Letters* 34 (L22304).

- Rutqvist, J., 2011. Status of the TOUGH-FLAC simulator and recent applications related to coupled fluid flow and crustal deformations. *Computers & Geosciences* 37 (6), 739–750.
- Rutqvist, J., 2012. The Geomechanics of CO₂ Storage in Deep Sedimentary Formations. *Geotechnical and Geological Engineering* 30 (3), 525–551.
- Simon, N., 2012. Compaction Driven Flow in Porosity Waves - A Threat to Caprock Integrity? In: Third EAGE CO₂ Geological Storage Workshop.
- Simon, N., Podladchikov, Y., 2013a. A consistent physical model for the formation of focused flow channels (chimneys) through intra-reservoir shales. In: The 7th Trondheim CCS Conference (TCCS-7), Trondheim, Norway.
- Simon, N., Podladchikov, Y., 2013b. A consistent physical model predicting the formation of focused flow channels-application to CO₂ injection at Sleipner. In: Second SES Conference, EAGE, Pau, France. p. 4.
- Simon, N. S. C., 2013. Fluid focusing and breaching of low permeability layers in reacting and visco-elasto-plastically deforming reservoir rocks. *Geophysical Research Abstracts* 15, EGU2013–5865.
- Simon, S., Räss, L., Podladchikov, Y., Souche, A., Yarushina, V., 2013. Predicting dynamically evolving permeability and localization of fluid flow in underground waste storage operations. In: International EAGE Workshop on Geomechanics and Energy.
- Sone, H., Zoback, M., et al., 2011. Visco-plastic properties of shale gas reservoir rocks. In: 45th US Rock Mechanics/Geomechanics Symposium. American Rock Mechanics Association.
- Sone, H., Zoback, M. D., 2014. Time-dependent deformation of shale gas reservoir rocks and its long-term effect on the in situ state of stress. *International Journal of Rock Mechanics and Mining Sciences* 69 (0), 120–132.
- Tantsev, E., Galerne, C. Y., Podladchikov, Y. Y., 2009. Multiphase Flow in Multi-Component Porous Visco-Elastic Media. In: Ling, H. I., Smyth, A., Betti, R. (Eds.), 4th Biot Conference on Poromechanics. Destech Publications, Inc, pp. 959–964.
- Wang, H. F., 2000. Theory of Linear Poroelasticity with Applications to Geomechanics and Hydrogeology. Princeton Series in Geophysics. Princeton University Press.
- Yarushina, V., 2009. (De-)compaction waves in porous viscoelastoplastic media. Thesis.
- Yarushina, V. M., Bercovici, D., 2013. Mineral carbon sequestration and induced seismicity. *Geophysical Research Letters* 40 (5), 814–818.

Yarushina, V. M., Bercovici, D., Oristaglio, M. L., 2013. Rock deformation models and fluid leak-off in hydraulic fracturing. *Geophysical Journal International* 194 (3), 1514–1526.

Yarushina, V. M., Podladchikov, Y. Y., 2014. (De)compaction of porous viscoelastoplastic media: 1. Thermodynamically admissible model formulation. *Journal of Geophysical Research*.

Zoback, M. D., 2010. *Reservoir geomechanics*, 2nd Edition. Cambridge University Press, Cambridge.

Zoback, M. D., Gorelick, S. M., 2012. Earthquake triggering and large-scale geologic storage of carbon dioxide. *Proceedings of the National Academy of Sciences of the United States of America* 109 (26), 10164–10168.

CHAPTER 7

The quantification of viscous creep's influence on caprock's storage capacity

Ludovic Räss¹, Roman Y. Makhnenko^{2,3}, Yury Y. Podladchikov¹, and Lyesse Laloui²

¹Faculté des géosciences et de l'environnement, Institut des Sciences de la Terre, University of Lausanne, Lausanne, Switzerland.

²Laboratory of Soil Mechanics, École Polytechnique Fédérale de Lausanne, EPFL ENAC IIC LMS, GC – Station 18, CH-1015 Lausanne, Switzerland.

³Department of Civil & Environmental Engineering, University of Illinois at Urbana-Champaign, 205 North Mathews Ave, Urbana, IL, 61801-2352, USA.

Abstract

In light of growing concerns for climate change, governments must encourage efficient capture and safe storage of large amounts of carbon dioxide in the subsurface. In this perspective, and in order to accurately predict a reservoir's short-term and long-term responses, a precise characterisation of the geomechanical properties must be carried out. Besides the classical poro-elastic properties, time-dependent deformation, such as viscous creep, should also be considered. A caprock's storage capacity may be seriously affected by local creep deformation allowing fast vertical fluid flow through an a priori very impermeable formation. In this study, we investigate the ease to creep of Opalinus clay (Jurassic shale) under shallow geological storage conditions and predict the propagation of high-porosity channels at operational time-scales. We infer the rock's effective poro-visco-elastic parameters are inferred from the novel laboratory experiments that allow evaluation of time-dependent deformation. The shale's bulk viscosity is found to be $\sim 10^{14} - 10^{15}$ Pa.s, and it decreases with rises of temperature and the ratio of pore fluid pressure to total mean stress. Further, the propagation speed of high-porosity channels (porosity waves) is calculated to be in the order of centimetres per year.

7.1 Introduction

Carbon dioxide (CO₂) storage security is largely influenced by caprock integrity, especially in the early stages after the start of injection. The caprock's lower boundary will then be in contact with CO₂-rich brine or pore fluid that consists almost of pure CO₂. Thermal and chemical interactions between the pore fluid and the caprock may change the latter's material properties. Geomechanical stability is also crucial for the caprock, since failure would potentially lead to a significant permeability increase and induced seismicity (IEAGHG, 2011). Considering clay-rich materials (e.g. shales) as potential seals has several advantages. In case reservoir overpressure is not very important, the thermal, chemical and inelastic deformations of the clay-rich ductile formation may not affect the caprock integrity. Another advantage of considering clay-rich materials as a potential seal is that the upward movement of CO₂ through the pore system is resisted by capillary pressure; the breakthrough pressure (CO₂ entry pressure) for shale is in the order of megapascals (Amann-Hildenbrand et al., 2013; Boulin et al., 2013; Makhnenko et al., 2017).

Although clay-rich formations show interesting self-sealing features, their ease to flow (or creep) may become a serious issue when assessing a reservoir's long-term storage integrity (Simon, 2012). Viscous (time-dependent) deformation of shales has been considered experimentally (e.g. Sone and Zoback, 2014; Yang et al., 2011; Zhang et al., 2007), but there has been little attention to material behaviour at high pore pressures, since it is in geological storage. Geomaterials, even partially saturated with water, generally have a non-linear rheology, and time-dependent behaviour of rock is a function of mean and differential stress, pore pressure, chemistry of a pore fluid, temperature and rock's microstructural properties, among others (e.g. Brantut et al., 2013; Bürgmann and Dresen, 2008; Elsworth and Yasuhara, 2006).

Viscous compaction of fluid-filled porous media allows a generation of a special fluid flow instability type that leads to formation of high-porosity, high-permeability domains that can self-propagate upwards owing to interplay between buoyancy and viscous resistance of the deforming porous matrix. This instability is known as a porosity wave (Connolly and Podladchikov, 2015; Yarushina et al., 2015); its formation is possible under conditions applicable to carbon dioxide storage in reservoirs and explains the creation of high-porosity channels and chimneys (Räss et al., 2014).

In this study, time-dependent or poro-visco-elastic processes are included in the constitutive equations by analogy to Biot's poro-elastic relationships. We present the experimental methods to measure the parameters relating to the model and the values of these parameters at in situ conditions for a caprock representative – Opalinus clay (Jurassic shale). We use the values obtained in the lab experiments to feed the numerical models in order to predict the time and length scale of possible porosity wave propagation in conditions relevant for caprock integrity.

7.2 Background

To predict the porosity evolution and therefore the possible formation of high permeability and porosity pipe structures in saturated porous media, we use the closed equation system proposed by (Yarushina et al., 2015), where time-dependent or creep effects are considered using the visco-elastic correspondence principle. The model reduces to Biot linear theory in the elastic limit (Wang, 2000) and verifies the viscous solution in the incompressible limit (Connolly and Podladchikov, 2007). The set of proposed equations forms a closed system that ensures thermodynamic consistency and non-negativity of entropy production. In this section, we highlight some relevant parts of the full derivation that can be found in (Yarushina et al., 2015).

The variable ϕ represents the interconnected porosity, and v^s and v^f are solid and fluid velocity, respectively. Fluid and solid pressures, p^f and p^s respectively, can be expressed through the fluid bulk modulus K_f , theunjacketed bulk modulus K'_s , and theunjacketed pore bulk modulus K''_s (Cheng, 2014). The main rheological assumption adopted here is Maxwell bulk visco-elasticity:

$$\nabla_k v_k^s = -\frac{1}{K_d} \frac{\partial \bar{p}}{\partial t} + \left(\frac{1}{K_d} - \frac{1}{K'_s} \right) \frac{\partial p^f}{\partial t} - \frac{\bar{p} - p^f}{(1 - \phi)\eta_\phi}. \quad (7.1)$$

Here, K_d is the drained bulk modulus and η_ϕ is the effective bulk viscosity, which reflects properties of porous rock, such as its pore structure and viscous and failure parameters of its mineral grains. The viscous part is governed by Terzaghi's effective stress: $p_e = \bar{p} - p^f$. Substituting equation (7.1) into the solid mass balance equation provides an expression for viscous and elastic evolution of the porosity (Cheng, 2014; Yarushina et al., 2015):

$$\frac{\partial \phi}{\partial t} = -\left(\frac{1 - \phi}{K_d} - \frac{1}{K'_s} \right) \frac{\partial p_e}{\partial t} + \phi \left(\frac{1}{K'_s} - \frac{1}{K''_s} \right) \frac{\partial p^f}{\partial t} - \frac{p_e}{\eta_\phi}. \quad (7.2)$$

The fluid content increment is recovered by substituting equation (7.1) into the sum of fluid and solid mass balance equations to eliminate the time derivatives of densities and the porosity and the divergence of solid velocity (Yarushina et al., 2015):

$$\nabla_j \left[\phi \left(v_k^f - v_k^s \right) \right] = \left(\frac{1}{K_d} - \frac{1}{K'_s} \right) \left(\frac{\partial \bar{p}}{\partial t} - \frac{1}{B} \frac{\partial p^f}{\partial t} \right) + \frac{p_e}{(1 - \phi)\eta_\phi}. \quad (7.3)$$

where B is Skemton's (Cheng, 2014; Skempton, 1984) coefficient:

$$B = \frac{\frac{1}{K_d} - \frac{1}{K'_s}}{\frac{1}{K_d} - \frac{1}{K'_s} + \phi \left(\frac{1}{K_f} - \frac{1}{K''_s} \right)}. \quad (7.4)$$

7.3 Methods

7.3.1 Experimental technique

The parameters introduced in Section 7.2 that govern poro-elastic behaviour of isotropic fluid-saturated rock (i.e. the drained bulk modulus K_d , the unjacketed bulk modulus K'_s , and Skempton's coefficient B) can be measured experimentally under three limiting conditions: drained, unjacketed, and undrained (Skempton, 1984). Another unjacketed parameter – K''_s – is rarely reported, because its measurements are associated with very small pore volume changes under constant effective stress, although it can be calculated from equation (7.4) if other parameters are known.

K'_s is measured under the unjacketed boundary conditions, which are achieved in hydrostatic ($\sigma_1 = \sigma_2 = \sigma_3 = \bar{p}$) compression experiments (Makhnenko and Labuz, 2016). A prismatic specimen (50 35 35 mm) with strain gage rosettes on its sides is saturated with the confining fluid (hydraulic oil), which seemed to have no chemical effect on the tested rock in a short-term. After at least 10 days of gradual increase of pore pressure up to 60 MPa, unjacketed unloading ($\bar{p} = p^f$ and $d\bar{p} = dp^f$) is performed.

Drained (constant pore pressure) and undrained (constant fluid content) compression experiments are conducted on cylindrical specimens (height = 100 mm, diameter = 50 mm) in the GDS Advanced triaxial cell at the EPFL. The setup is calibrated for testing of fluid-saturated rock at elevated temperatures (Figure 7.1). The back-pressure saturation technique (described in Makhnenko et al., 2013) is implemented: the increments of pore (or back) pressure are applied while keeping the effective mean stress approximately the same. Then, so-called B -checks are performed, and the achievement of constant value of B independent of the magnitude of the pore pressure indicates full saturation. Measured Skempton's B coefficient values are corrected to consider the contribution of the *dead* volume and the compressibility of the pore pressure measuring system. Drained bulk modulus K is calculated directly from the measured axial and radial displacements and indirectly from the volume of the fluid that escaped the specimen during compression under constant pore pressure. Knowledge of K'_s can then provide a proper evaluation of K (Cheng, 2014).

Equation 7.1 provides the following method for calculating the bulk viscosity under constant mean stress, $d\bar{p}/dt = 0$, and drained boundary conditions, $dp^f/dt = 0$, which can be referred to as the *direct* method,

$$\eta_\phi = -\frac{\bar{p} - p^f}{(1 - \phi)\nabla_k v_k^s}. \quad (7.5)$$

Here, $\nabla_k v_k^s$ can be treated as the volume strain rate, and considering the accuracy of volume strain measurements ($1 \cdot 10^{-5}$) and the level of applied effective mean stresses (\sim MPa), the observation time for calculating the bulk viscosity with two significant figures is $\sim 10^5$

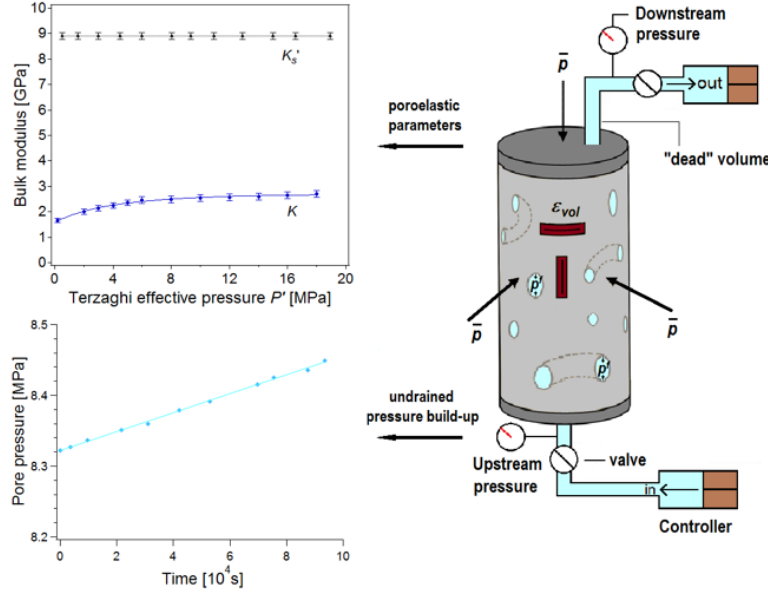


Figure 7.1: Experimental setup in the Advanced triaxial cell at the EPFL with indication of performed measurements; precise stress and strain measurements at different limiting regimes allow for the calculation of poro-elastic parameters and the observation of undrained pore pressure buildup for fully saturated specimens provides the evaluation of the material's bulk viscosity.

seconds. The time-scales should be even longer, to compensate for the effects of temperature and pressure perturbations; thus, the bulk viscosity of shallow rock is rarely reported.

For porous materials, the degree of saturation is the critical parameter to govern their viscous response: if saturation is not full, pore pressure does not increase significantly under the undrained condition, but rather decreases while the air bubbles dissolve in pore water. However, when full saturation is achieved and material deformation can be considered poro-visco-elastic, then equation (7.3) predicts pore pressure buildup over time at constant total stress conditions. Since changes in pore pressure for the fully saturated specimens can be measured more accurately than volume strain, they can be used as the monitoring parameter for viscous behaviour and for the calculation of bulk viscosity. The simplified form of equations (7.2) and (7.3) for the case of undrained deformation – no flow condition: $\nabla_j [\phi (v_k^f - v_k^s)]$ – at constant mean stress ($d\bar{p}/dt = 0$) leads to another method (referred to as *indirect*) of evaluating η_ϕ ,

$$\eta_\phi = - \frac{B (\bar{p} - p^f)}{(1 - \phi) \frac{dp^f}{dt} \left(\frac{1}{K_d} - \frac{1}{K_s^f} \right)}. \quad (7.6)$$

The bulk viscosity calculation then requires accurate measurements of poro-elastic parameters. However, owing to the accuracy of pore pressure measurements, this method is significantly less time-consuming ($\sim 10^4$ seconds).

7.3.2 Numerical methods

Numerically, the system of partial differential equations is solved on a 3-D staggered grid with regular grid spacing, using a finite-difference (FD) discretisation. Pressures and material properties are defined at the cell centres, while the Darcy fluxes and solid velocities are defined at the cell mid-faces. Shear components are located at the cell corners. The 3-D model is written in C language with CUDA features and is solved on many graphical processing units (GPUs) in parallel, using the standard message-passing interface (MPI) routine for inter-process communications.

An iterative pseudo-transient (thus, matrix-free) scheme is used to solve the system of partial differential equations. The advantages of using this approach are the lowest possible memory usage that scales $O(n)$, while only local stencil operations to update variables and minimum point-to-point communication between parallel processes are needed. Thus, such an algorithm scales linearly with a number of parallel processors owing to and ensured by its minimalistic construction.

The algorithm's workflow can be summarised in the following steps, which will be repeated in the time-step loop: 1) update values of total and fluid pressures and porosity solving for their time derivatives in the equations (7.1), (7.2), and (7.3); 2) compute the non-linear visco-elastic rheology as a function of the updated porosity and pressures fields; 3) solve the momentum equation (force balance) for the solid velocities; and 4) verify the non-linear residual of the momentum equation and the errors of the equations (7.1) to (7.3) and of the non-linear rheology. Once step 4 is verified and all errors are converged to targeted non-linear tolerance, the porosity can be explicitly advected using a flux-limiting upwind scheme (Räss et al., 2016).

The non-linear nature of the poro-visco-elastic equations sets important challenges in terms of numerical solutions. Strong localisation in space and time may spontaneously occur, and a wide range of length scales are involved. To overcome this and to resolve the instabilities, a very high resolution in space and time is required to predict accurate system evolution over time. Thus, we employ a numerical resolution of more than $2.5 \cdot 10^8$ grid-points in order to have 500 x 500 x 1,000 cells in X, Y and Z directions, respectively. The GPUs accelerators efficiently speed up the algorithm execution, allowing us to run the full 3-D simulation in not more than a five-day wall-time on our in-house high-performance computing GPU cluster octopus¹, designed by the Scientific Computing Group at the Earth Sciences Institute and hosted by the University of Lausanne.

¹Scientific Computing Group, specification of the *octopus* GPU cluster. 2015: <http://wp.unil.ch/geocomputing/computing-systems/octopus/>

7.3.3 Material

Opalinus clay (shaly facies) is the Jurassic shale we study as the caprock representative. The shale contains 55 to 60 % of clay (illite, kaolinite, chlorite and smectite), 25 to 30 % carbonate, 5 to 10 % quartz, and 10 to 15 % organic matter (Bossart, 2011). Interconnected porosity is 0.12, dominant pore throat diameter ~ 30 nm, and intrinsic permeability $\sim 10^{-21} - 10^{-20}$ m² (Makhnenko et al., 2017). If properly preserved after coring, the shale specimens have 80 to 90 % brine saturation, so the natural brine (Pearson, 2002) was used as the pore fluid to minimise the chemical effect, and its bulk modulus K_f is found to be 2.0 GPa, slightly less than that for pure water.

The characteristic dissipation time of the induced pore pressure in a specimen of length L drained at the two ends is in the order of $L^2/4c$, where c is the diffusion coefficient (Zimmerman, 1990), which can be expressed from the permeability k , fluid viscosity μ and the poro-elastic parameters:

$$c = \frac{kB}{\mu \left(\frac{1}{K_d} - \frac{1}{K'_s} \right)}. \quad (7.7)$$

Values of c for the tested shale are $\sim 10^{-8}$ m²/s for the case of brine saturation. The characteristic time-scale for equilibration of the pore pressure inside the rock at the range of stresses applied is in the order of 10^{-5} seconds for 100 mm long specimens (used in drained tests) and in the order of 10^{-4} seconds for the 35 mm long specimen (used in the unjacketed test). In the latter case, though, oil has partially penetrated into the unjacketed sample and has increased the viscosity of the pore fluid, and therefore the characteristic time-scale for pressure dissipation. Finally, each new step in the unjacketed test required a 24-hour waiting period, and the whole test took 15 days. At least 72 hours were spent between the consecutive steps during the drained loading.

7.4 Results and discussion

The unjacketed compression test provided constant (stress-independent) value of $K'_s = 8.9$ GPa for Opalinus clay after 15 days of gradual unloading from 60 MPa. Three different conventional triaxial test types were performed on the cylindrical shale specimens cored perpendicular to the bedding planes to measure the poro-elastic parameters of the rock and evaluate its bulk viscosity. One specimen was tested at 24 °C under low mean stresses and pore pressures (around 2 MPa), approximately corresponding to the in situ conditions at the Mont Terri underground rock laboratory from where the rock was recovered (Bossart, 2011). In this case, full brine saturation took about 75 days. Another specimen was gradually loaded to total isotropic stress of 10 to 30 MPa and saturated at pore fluid pressure of 8 MPa in 15 days, and its poro-visco-elastic parameters were measured at 24 °C and 40 °C. Drained bulk

Testing conditions	ϕ [-]	k [m ²]	K_d [GPa]	K'_s [GPa]	K_f [GPa]	B [-]	η_ϕ [Pa.s]
24 °C, $\bar{p} = 1.8$ MPa, $p^f = 1.6$ MPa	0.12	$3.0 \cdot 10^{-20}$	1.65	8.9	2.0	0.93	$2.2 \cdot 10^{14}$
24 °C, $\bar{p} = 15.5$ MPa, $p^f = 12.8$ MPa	0.12	$0.9 \cdot 10^{-20}$	2.20	8.9	2.0	0.90	$9.5 \cdot 10^{14}$
40 °C, $\bar{p} = 11.2$ MPa, $p^f = 8.7$ MPa	0.12	$0.5 \cdot 10^{-20}$	2.20	8.9	2.0	0.90	$4.6 \cdot 10^{14}$

Table 7.1: Note: Material properties, poro-elastic parameters, and bulk viscosity for the largest achieved p^f/\bar{p} ratios for three studied cases.

modulus K and Skempton's B coefficient showed weak stress-dependence: $K = 2$ to 3 GPa and $B = 0.81$ to 0.93 for $p_e = 2$ to 20 MPa. Further, brine permeability of shale was measured by steady-state flow method and was found to be strongly stress-dependent, changing by an order of magnitude for $p_e = 0.2$ to 5 MPa from $\sim 10^{-20}$ m² to $\sim 10^{-21}$ m².

Opalinus clay's response was monitored after each B -check, while a constant isotropic total stress was acting on the specimens. If the rock's behaviour is purely poro-elastic, application of constant total stress should not produce any pore fluid pressure perturbations. However, the pore pressure buildup occurred for fully saturated specimens at different initial total and pore pressures for all three tested cases (schematically shown in Figure 7.1). Notably, during the undrained loading when all-round stress is applied to the specimen, it is assumed that it affects the pore pressure immediately and equally inside all the pores. For the tested shale, it was found that pore pressure dissipation in the system takes a few tens of minutes, and all further pore pressure changes should be associated with the time-dependent material behaviour.

The observation times for the pore pressure buildup ranged from $4 \cdot 10^4$ to $1.5 \cdot 10^5$ seconds and provided an approximately linear response, given that the perturbations of total stress and temperature imposed by the loading system were very small. The effective stress does not appear to be the only governing parameter for the bulk viscosity for a number of sedimentary rock representatives; rather, it is the ratio between the pore pressure and total (isotropic) stress p^f/\bar{p} . The shale's bulk viscosity η_ϕ is calculated to be in the order of 10^{14} to 10^{15} Pa.s and has a decreasing trend with increasing p^f/\bar{p} ratio (Figure 7.2). A temperature increase from 24 °C to 40 °C is found to have an insignificant effect on poro-elastic parameters, but reduces the permeability by 40 % and the bulk viscosity by a factor of 2. Also, for the shale tested at low pressure, η_ϕ trend differs from the other two cases, with a steeper decrease at p^f approaching \bar{p} , which may relate to the fact that the shale was subjected to lower than in situ stresses and behaved like under-consolidated material. Values of the bulk viscosity corresponding to the largest achieved p^f/\bar{p} ratios for the three considered cases (low-pressure and high-pressure hydrostatic compression at 24 °C and high-pressure compression at 40 °C) along with the poro-elastic parameters used for calculation appear in Table 7.1.

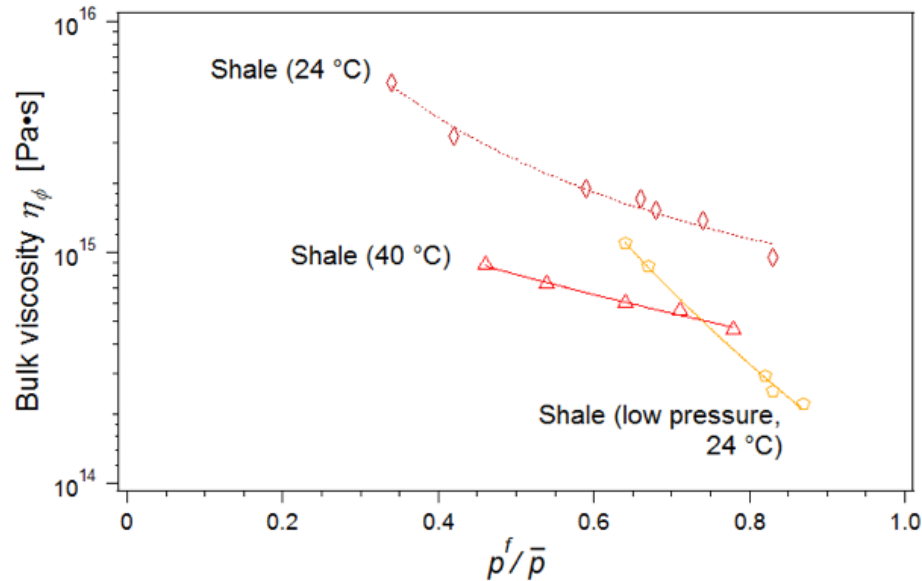


Figure 7.2: Calculated values of the bulk viscosity of shale plotted as functions of p^f/\bar{p} ratio for the three considered cases: low pressure at 24 °C (orange pentagons), high pressure at 24 °C (maroon diamonds), and high pressure at 40 °C (red triangles).

Further, the bulk viscosity calculated for the shale at high pressure at 24 °C is plotted against the viscosity trends for two other sedimentary rocks: Berea sandstone and Apulian limestone, tested at the same temperature (Figure 7.3). Increasing pore pressure at constant mean stress should lead to an increase in porosity if a geomaterial is deforming poro-elastically. However, all the tested specimens experienced time-dependent compaction, and measured volume strains were in agreement with porosity changes predicted by the presented poro-visco-elastic relationships, which can be viewed as the model validation.

The measurements inferred from the lab are then used to constrain the numerical model's key parameters. The initial setup (Figure 7.4) used for the numerical simulation is a 3-D cubic domain of visco-elastically deforming porous media saturated with pore fluid subject to gravity acceleration in the Z (depth) coordinate. A high-porosity horizontal ellipsoid is located at the first quarter of the total depth, with porosity values twice higher than the background value. This setup should represent the analogy of a buoyant fluid plume, thus an elevated porosity anomaly, located in a less permeable and less porous reservoir. Porosity evolution over time can be predicted and used to estimate the time and length scales representative for this wave propagation phenomenon.

The outcome of the numerical simulations shows elongated pipe features developing over time owing to highly focused fluid flow through the deforming porous media (Figure 7.5). The channel-formation and therefore asymmetry in decompaction vs. compaction rates is the result of viscosity dependence on the p^f/\bar{p} ratio. The effective viscosity drops in a region

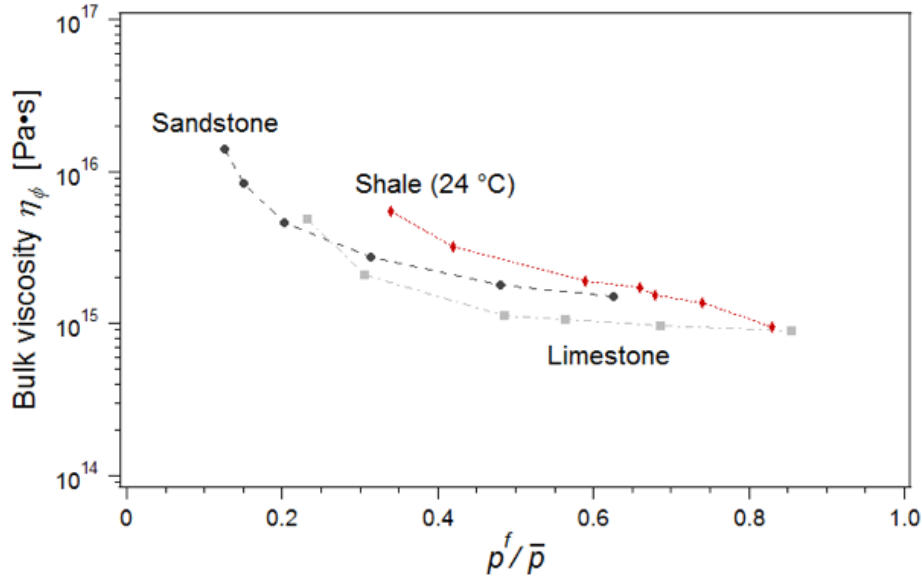


Figure 7.3: Bulk viscosity of Opalinus clay (maroon diamonds) compared to the trends of measured viscosities for Berea sandstone (dark grey circles) and Apulian limestone (light-grey squares), all tested at 24 °C and plotted as functions of p^f/\bar{p} ratio.

in which the pore fluid pressure is closer to the total stress (the red areas on the channel tip in Figure 7.5). The created channels are referred to as porosity waves, since the solid grains are only displaced very locally, allowing the fluid to go through the porous media in a wave-like motion. The associated fluid pressure (Figure 7.5) and its gradient will tend to move fluid from the near channel region into the channels. This mechanism enhances the porosity wave's self-sustainability by allowing a significant amount of surrounding fluid to flow into the channel. The surrounding fluid being expelled from the near-channel areas, the pipe's walls compact as a result of mass balance. The resulting channels' wall bulk and shear viscosities increase, freezing their shape over time. The expression of this mechanism in a natural system such as a shallow reservoir can be related to seismic chimneys visible on seismic surveys' cross-sections (Räss et al., 2016, 2014).

Using the laboratory data on shale behaviour, we can scale the numerical simulation in order to predict propagation velocities of the high-porosity (thus, high-permeability) channels. Permeability increase inside the channels is more than three orders of magnitude, enabling pore fluid or brine to travel with a vertical speed proportionally to permeability increase (i.e. three orders of magnitude), instead of the background Darcian flow regime. The characteristic time t^* and length L^* are given by:

$$t^* = \sqrt{\frac{\eta_\phi \mu}{k}} (\Delta \rho g)^{-1}, \quad (7.8)$$

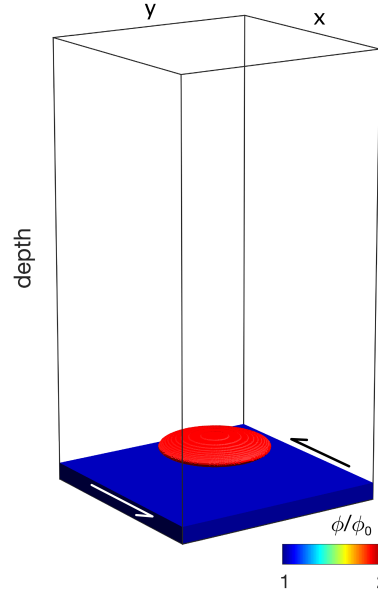


Figure 7.4: The setup used to model two-phase flow. The resolution is 500 x 500 x 1,000 grid-points in X, Y and X (depth) dimensions, respectively. The domain was decomposed into 64 subdomains, each computed on one Nvidia Titan X GPU.

$$L^* = \sqrt{\frac{\eta_\phi k}{\mu}}. \quad (7.9)$$

The travelling velocity for the porosity waves through the domain (in metres per year) can be computed as:

$$V_{porosity\ wave} = \frac{L_{run} \cdot L^*}{t_{run} \cdot t^*} 3600 \cdot 24 \cdot 365, \quad (7.10)$$

where L_{run}/t_{run} is the dimensionless velocity obtained from the numerical simulation. Finally, the porosity wave velocity calculated using the poroviscoelastic properties of Opalinus clay appears to be in the order of centimetres per year for a very low permeable (~ 10 to 20 m^2) formation.

7.5 Conclusions

We show that the viscous effect should not be excluded when assessing long-term behaviour of clay-rich materials, such as shales. The modelling results using parameters from the laboratory experiments on low-permeable shale predict that non-linear porosity-dependent permeability can increase up to three orders of magnitude in the porosity waves. Thus, long-term projections for storage behaviour should include time-dependent (viscous) deformation of the potential caprock.

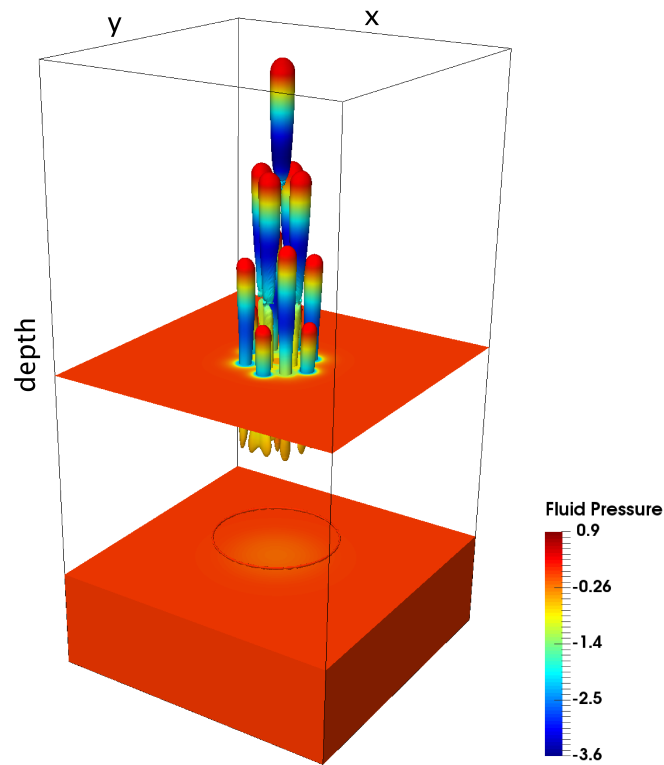


Figure 7.5: Fluid pressure values plotted on top of the isosurface values of normalised porosity equal to 4 as evolving from the initial high-porosity ellipsoid after a dimensionless time of 0.024. Low fluid pressure values are observed in the high-porosity channels. Box dimensions are 30 x 30 x 60 compaction lengths in X, Y and Z directions respectively, or a numerical resolution of 500 x 500 x 1,000 grid-points. The visualisation is performed in parallel on 64 Titan X GPUs using the ParaView software in a remote client-server configuration on the octopus GPU cluster.

Laboratory measurements performed to obtain both the permeability and viscosity values for the clay-rich rock types dramatically influence the prediction of the relevance of in-channel formation and propagation. Orders of magnitude changes in permeability will lead to proportionally faster or slower propagation velocities, since this quantity scales the model's dimensionless velocity. Significantly low effective viscosity values obtained from the laboratory experiments dramatically decrease the characteristic propagation time of the fluid focusing instabilities. This may lead to the generation and propagation of high-permeability tubular features in an operational time-scale. Thus, the viscous or creep effect should be considered while assessing storage integrity, especially for systems where clay-rich caprock formations are investigated. Under certain conditions, creeping ductile rock may locally flow away, leading to the formation of vertical pipes of high permeability and porosity.

Acknowledgments

Opalinus clay cores were provided by Swisstopo in the framework of Mont Terri Project, CS-C experiment. R. Makhnenko acknowledges support from SCCER-SoE (Switzerland) grant KTI.2013.288 and the Swiss Federal Office of Energy (SFOE) project CAPROCK #810008154.

Bibliography

- Amann-Hildenbrand, A., Bertier, P., Busch, A., Krooss, B. M., 2013. Experimental investigation of the sealing capacity of generic clay-rich caprocks. *International Journal of Greenhouse Gas Control* 19, 620–641.
- Bossart, P., 2011. Characteristics of the Opalinus Clay at Mont Terri. Mont Terri Project, Wabern Switzerland.
- Boulin, P., Bretonnier, P., Vassil, V., Samouillet, A., Fleury, M., Lombard, J., 2013. Sealing efficiency of caprocks: experimental investigation of entry pressure measurement methods. *Marine and Petroleum Geology* 48, 20–30.
- Brantut, N., Heap, M., Meredith, P., Baud, P., 2013. Time-dependent cracking and brittle creep in crustal rocks: A review. *Journal of Structural Geology* 52, 17–43.
- Bürgmann, R., Dresen, G., 2008. Rheology of the lower crust and upper mantle: Evidence from rock mechanics, geodesy, and field observations. *Annual Review of Earth and Planetary Sciences* 36.
- Cheng, A. H.-D., 2014. Fundamentals of poroelasticity. *Analysis and Design Methods: Comprehensive Rock Engineering: Principles, Practice and Projects* 2, 113.

- Connolly, J., Podladchikov, Y., 2007. Decompaction weakening and channeling instability in ductile porous media: Implications for asthenospheric melt segregation. *Journal of Geophysical Research: Solid Earth* 112 (B10).
- Connolly, J. A., Podladchikov, Y. Y., 2015. An analytical solution for solitary porosity waves: dynamic permeability and fluidization of nonlinear viscous and viscoplastic rock. *Geofluids* 15 (1-2), 269–292.
- Elsworth, D., Yasuhara, H., 2006. Short-timescale chemo-mechanical effects and their influence on the transport properties of fractured rock. *Pure and applied geophysics* 163 (10), 2051–2070.
- IEAGHG, 2011. Caprock Systems for CO₂ Geological Storage. Report.
- Makhnenko, R., Labuz, J., et al., 2013. Saturation of porous rock and measurement of the B coefficient. In: 47th US Rock Mechanics/Geomechanics Symposium. American Rock Mechanics Association.
- Makhnenko, R., Vilarrasa, V., Mylnikov, D., Laloui, L., 2017. Hydromechanical aspects of CO₂ breakthrough into clay-rich caprock. *Energy Procedia* 114, 3219–3228.
- Makhnenko, R. Y., Labuz, J. F., 2016. Elastic and inelastic deformation of fluid-saturated rock. *Phil. Trans. R. Soc. A* 374 (2078).
- Pearson, F., 2002. PC experiment: recipe for artificial pore water. Mont Terri Project. Tech. rep., Technical Note 2002-17.
- Räss, L., Yarushina, V., Duretz, T., Podladchikov, Y., 2016. High-resolution Numerical Modelling to Resolve the Dynamics of Pipe Structures in Porous Media. In: ECMOR XV-15th European Conference on the Mathematics of Oil Recovery.
- Räss, L., Yarushina, V. M., Simon, N. S., Podladchikov, Y. Y., 2014. Chimneys, channels, pathway flow or water conducting features-an explanation from numerical modelling and implications for CO₂ storage. *Energy Procedia* 63, 3761–3774.
- Simon, N., 2012. Compaction Driven Flow in Porosity Waves - A Threat to Caprock Integrity? In: Third EAGE CO₂ Geological Storage Workshop.
- Skempton, A., 1984. The pore-pressure coefficients A and B. In: Selected papers on soil mechanics. Thomas Telford Publishing, pp. 65–69.
- Sone, H., Zoback, M. D., 2014. Time-dependent deformation of shale gas reservoir rocks and its long-term effect on the in situ state of stress. *International Journal of Rock Mechanics and Mining Sciences* 69, 120–132.

- Wang, H. F., 2000. Theory of Linear Poroelasticity with Applications to Geomechanics and Hydrogeology. Princeton Series in Geophysics. Princeton University Press.
- Yang, D., Bornert, M., Chanchole, S., Wang, L., Valli, P., Gatmiri, B., 2011. Experimental investigation of the delayed behavior of unsaturated argillaceous rocks by means of Digital Image Correlation techniques. *Applied Clay Science* 54 (1), 53–62.
- Yarushina, V. M., Podladchikov, Y. Y., Connolly, J. A., 2015. (De)compaction of porous viscoelastoplastic media: Solitary porosity waves. *Journal of Geophysical Research: Solid Earth* 120 (7), 4843–4862.
- Zhang, C.-L., Rothfuchs, T., Su, K., Hoteit, N., 2007. Experimental study of the thermo-hydro-mechanical behaviour of indurated clays. *Physics and Chemistry of the Earth, Parts A/B/C* 32 (8), 957–965.
- Zimmerman, R. W., 1990. Compressibility of sandstones. Vol. 29. Elsevier.

CHAPTER 8

Perspectives

8.1 Summarising discussion

The main objectives of this work, as presented in Section 1.2, were: (1) to develop numerical models capable of resolving sudden localisation of fluid flow and strain on various temporal and spatial ranges, and (2) to make optimal use of current supercomputers, ensuring that algorithms perform close to hardware limits. In this framework, I have made efforts to provide at least partial answers to a number of research questions, raised in Section 1.2.2. In this final chapter, I will summarise the major results of each thesis chapter (Chapters 2 to 7). In the final section, I will highlight possible future developments in the field of coupled models that efficiently utilise HPC resources.

8.1.1 Fluid flow localisation arising from multi-physics coupling

Localised fluid flow is of particular importance in the Earth Sciences, since most geological observations suggest focused flow patterns that can be traced from shallow sedimentary environments (e.g. Judd and Hovland, 2007) to mantle conditions and subduction-related environments (e.g. Bouilhol et al., 2011). The modelling results I obtained in this thesis show new insights into the dynamics of flow localisation in fluid-filled porous media and strain localisation owing to hydro-mechanical (Chapter 4) and thermo-mechanical couplings (Chapter 5). They address important next steps after the computation of 3-D spherically shaped (Wiggins and Spiegelman, 1995) and 2-D channel-like porosity waves (Connolly and Podladchikov, 2007). The main results from Chapters 2 and 4 suggest focussed buoyant fluid rise that exhibits propagation velocities up to three orders of magnitude higher than those expected in a Darcian regime. The results were obtained by coupling a non-linear Darcy flow-solver to a Stokes solver that accounts for viscous activated bulk and shear rheology in the matrix (Yarushina and Podladchikov, 2015). A power law relationship that fits the data collapse further highlights decompaction weakening's strong influence on the vertical ascent velocities. In this context, none of the previous models have shown 3-D high-resolution results of flow localisation, including simultaneously viscous shear deformation of the matrix, decompaction weakening as a focussing mechanism, or a laboratory-verified effective viscous bulk rheology (Chapter 7) for the fluid-saturated porous matrix.

Porosity waves are solitons that occur in a specific fluid flow regime coupled to viscous matrix deformation. They provide a self-sustaining mechanism that permits enhanced vertical fluid transfers in various lithology types (Chapter 2). Their characteristic length scale, i.e. their compaction length (McKenzie, 1984), depends on the square root of the fluid transmissivity multiplied by the bulk compaction viscosity. Chapter 4's results confirm recent studies (Omlin et al., 2017a) that show a clear trend in increasing flow-rates with the drop of decompaction viscosity values owing to effective pressure. For the three major reservoir rock types tested

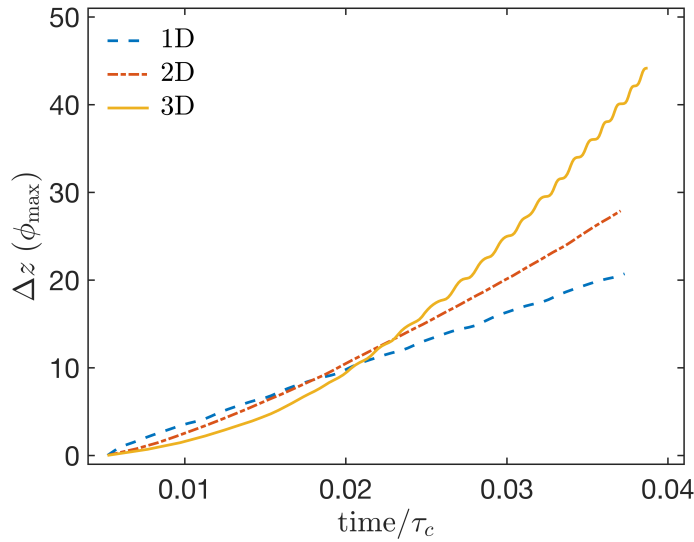


Figure 8.1: Discrepancy in effective wave velocities as a function of a number of spatial dimensions. Evolution plot of the vertical position of the largest channel as a function of dimensionless time. The largest channel is the one with the higher porosity (ϕ_{\max}). The three curves correspond to 1-D, 2-D and 3-D calculations, in which all the other physical parameters are the same. Notably, the slope of these curves is the vertical velocity at the channel top. Adapted from Omlin et al. (2017a).

at the Laboratory of Soil Mechanics (EPFL), clay-rich formations such Opalinus clay showed the most significant response to effective pressure, resulting in lowest effective bulk viscosity values, enhancing creep (Chapter 7). The low effective bulk viscosity values imply important contrasts between compaction and decompaction regimes, leading to the formation of highly localised and narrow fluid escape pipes and to significant variations in material properties (such as viscosity and permeability) in space. Both set important requirements in the numerical grid resolution, in order to resolve with accuracy the propagating channels' narrow top part. Decompaction weakening may result in significant focussing of the flow at locations unknown in advance within the numerical domain. This, it is mandatory to utilise a sufficient number of grid-points in all spatial dimensions to resolve the features in detail. Accuracy in resolving of the flow focussing owing to decompaction weakening in deformable porous media significantly influence the number of spatial dimensions utilised in the model (Figure 8.1). For a given reference setup (Section 4.3), varying only the number of spatial dimensions while keeping all other physical parameters identical results in non-negligible discrepancies in propagation velocities (Figures 4.6a and 4.6e), resulting in strong agreement with recent studies (Omlin et al., 2017a). Notably, a supercomputing approach is mandatory when computing 3-D setups at resolutions needed for comparison purposes with 2-D and 1-D setups.

8.1.2 Applicability of two-phase models to shallow environments

The modelled physical two-phase processes may address the non-linear behaviours observed in a variety of sedimentary basins (Berndt, 2005; Cartwright and Santamarina, 2015; Cathles et al., 2010; Hustoft et al., 2010; Løseth et al., 2011; Mazzini et al., 2017, e.g.), and provide a physical explanation for the formation of reported seismic chimneys in loosely consolidated reservoirs, and can be useful in further applications in the domains of energy and risk assessment (Chapters 2 and 6). Scientists and reservoir engineers are struggling to find a viable explanation that explains the spontaneous formation of high-permeability pathways through impermeable shale formations (Foschi et al., 2014), such as the Nordland shale layers present in the Utsira sand formation in the Sleipner field. Observations report well-defined structures common to many two-phase environments. Typical seismic chimneys usually show sharp intrusion in various sedimentary lithology types. The root zone is often defined as fairly diffuse. The channels' rims show signs of compaction, owing to the slightly downward bending of the seismic reflectors when approaching the inside/outside chimney transition area. Finally, the paleo-chimney structures are still visible and intact even though the system is no longer active.

These major observations are well captured by the two-phase model I proposed in this thesis. The high-resolution 3-D model results suggest spontaneous flow localisation owing to two-phase coupling and decompaction weakening as a formation process of high-permeability chimneys, such as those imaged by seismic surveys. The porous matrix's ability to viscously deform locally permits episodic buoyant vertical fluid release. The fluid pressure gradient decreases from outside towards the inside of the channel, driving the fluid flux from the outside towards the inside, continuously collecting surrounding fluid. To ensure local mass balance, the regions near a channel become depleted in fluid, compacting. These regions show higher bulk viscosity values and are therefore less affected by future deformation and constitute the so-called chimney rims.

When applying this model to the Sleipner conditions, the developed hydro-mechanical model predicts a permeability increase greater than two orders of magnitude in channel-like features, showing propagation velocities of about two metres per year through impermeable shale (Table 6.1). Recent work by Cavanagh et al. (2015) on the history matching the Sleipner plume in its vertical spreading needs a low capillary entry pressure of 50 kPa in order to explain the fast vertical CO₂ brine migration. According to the study, 50 kPa leads to an effective permeability increase of two orders of magnitude (0.002 to 0.2 mili-Darcy). Thus, the results obtained in this work utilising parameters relevant for Sleipner lithologies (Nordland shale) are in strong accord with these authors' conclusions and propose a physical mechanism for upward fluid migration.

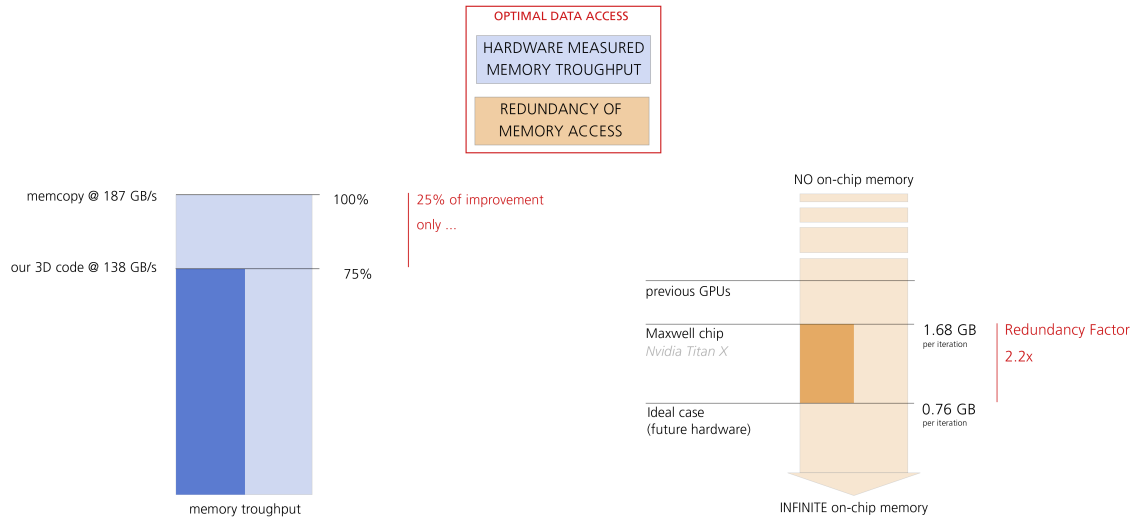


Figure 8.2: Optimal data access, combining hardware-measured memory throughput (in GB/s) and redundancy of memory access. Application of the performance evaluation to a single Nvidia GTX TITAN (Maxwell) GPU chip.

8.1.3 Supercomputing and algorithm performance

Over the past decades, a significant discrepancy between improvement in memory access speed and increased computational speed has appeared, owing to the development of parallel hardware (such as multicore CPUs and many-core GPUs). Thus, the ratio between floating point operations (FLOPS) performed per amount of numbers accessed in memory (bytes) – FLOPS to byte ratio – has continuously increased. However, most software packages only require few arithmetic operations (FLOPS) per accessed number (bytes). Thus, memory access speed totally determines the achievable performance as predicted by the memory wall in 1995 by Wulf, W. A. and McKee, Sally A. (1995). To achieve optimal performance on modern parallel hardware, tuning numerical algorithms mainly resides in avoiding, as much as possible, redundant as well as random memory accesses (e.g. Omlin et al., 2017b). FLOPS are thus “for free” and are therefore no longer a relevant metric to measure an algorithm’s performance. Hardware-measured memory access speed may also not be the most appropriate performance measure, since it may not deal with the redundancy of data access. Optimal data access measures combine hardware memory throughput measurements and data access redundancy (Figure 8.2) with target application to a single Nvidia GTX TITAN (Maxwell) GPU chip.

Optimal data access suggests maximising hardware-measured memory throughput while minimising data access redundancy. In other words, a memory bounded application performs optimally on actual multithread or many-thread hardware if the majority of the numbers mandatory for the calculations are accessed as little as possible, therefore residing close to

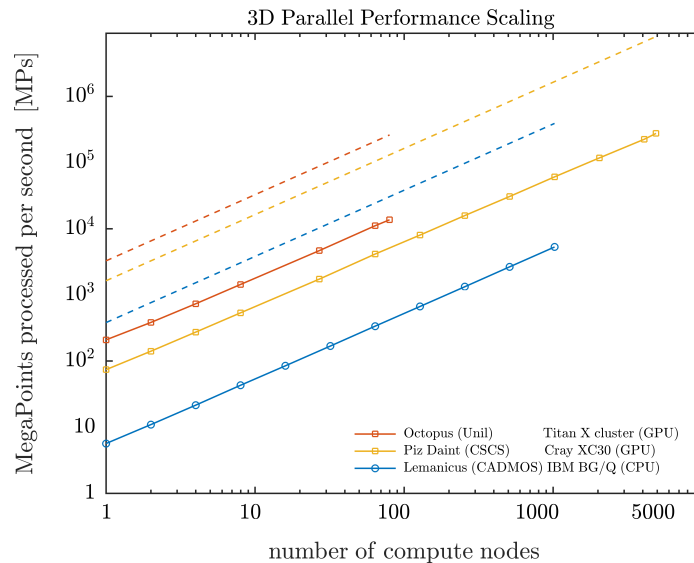


Figure 8.3: Weak scaling of the coupled two-phase 3-D algorithm on three supercomputers, two GPU-based machines, *Piz Daint* (a Cray XC30 hosting 5200 Nvidia Tesla Kepler GPUs) and *octopus* (an in-house-developed supercomputer that hosts 132 Nvidia GTX TITAN X Maxwell) and the CPU-based *Lemanicus* IBM BlueGene/Q. *Piz Daint* is, after an upgrade to a Cray XC50+Tesla P100 GPUs, the world’s 3rd largest supercomputer, and *Lemanicus* was available via the CADMOS project at EPFL until June 2016. The plain line represents the megapoints processed (thus) accessed per second (MPs) as a function of the increasing number of compute nodes. The dashed lines represent the corresponding maximal number of grid-points able to be processed per second if calculations would take no time.

the arithmetic units (on-chip memory). Also, their few accesses must be as optimal as possible, i.e. as close as possible to memory copy only throughputs (memcopy). The relevant numbers for the Nvidia GTX TITAN example (Figure 8.2) shows that the 3-D two-phase algorithm measured memory throughput (in gigabytes per second – GB/s) is 25 % below the hardware’s ability to perform memory copy only, without any computation. But the data access redundancy shows a redundancy factor of 2.2, reflecting the fact that the current on-chip memory is not sufficiently large to host the entire amount of numbers mandatory to perform on iteration, and propose some optimisation in this direction. Optimal data access infers the performance evaluation of a shared memory device, such as a single compute node or a single GPU. It does not ensure an optimal scaling of the algorithm when executed on distributed memory machines using MPI, such as HPC clusters or supercomputers. To assess the performance of a given algorithm on such machines, a weak scaling may be utilised (Figure 8.3). In such benchmarks, both the local problem size and the available resources are increased simultaneously. An optimal weak scaling would result in a constant and finite time-to-solution (Figure 8.4a), implying a parallel efficiency close to or equal to 1 (Figure 8.4b).

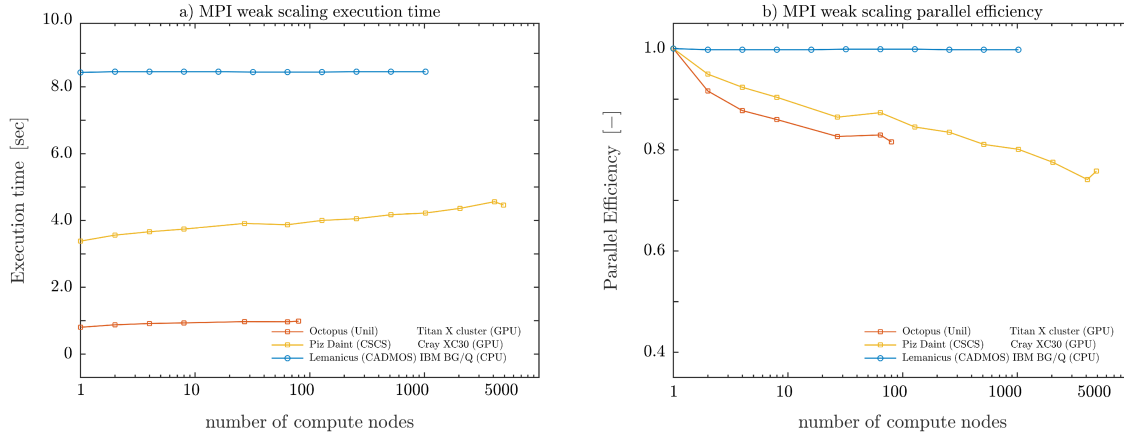


Figure 8.4: Weak scaling of the coupled two-phase 3-D algorithm on three supercomputers, two GPU-based machines, *Piz Daint* (a Cray XC30 hosting 5200 Nvidia Tesla Kepler GPUs) and *octopus* (an in-house-developed supercomputer that hosts 132 Nvidia GTX TITAN X Maxwell) and the CPU-based *Lemanicus* IBM BlueGene/Q. (a) Execution time (seconds) and (b) parallel efficiency, as functions of the number of compute nodes involved in the computation. The 3-D algorithm was written in C or C-CUDA, and the MPI standard was used to achieve inter-node communication. Note the algorithm’s close to 80 % of parallel efficiency while utilising the full *Piz Daint* machine; thus, 5200 GPUs.

In this thesis, with co-workers, I developed various implementations of GPU-based solvers that run in parallel at near peak performance on modern GPU-based supercomputers (Omlin et al., 2017a). The utilised machines were a Cray XC50 *Piz Daint*, hosted by the Swiss National Computing Centre (CSCS), a Supermicro-based *octopus* hosted by the University of Lausanne’s Institute of Earth Science, which was designed and assembled in the framework of this thesis and a CPU-based IBM BlueGene/Q *Lemanicus* available via the CADMOS project. Examples of the 3-D two-phase application (used in Chapters 4 and 7) show a close to linear weak scaling (Figure 8.3) on all three of the tested supercomputers. One notes the clear performance gain when utilising hardware accelerators such as GPUs. Interestingly, the maximum possible number of grid-points to process on the entire *octopus* (34 nodes – 136 GPUs) is more than three times larger compared to utilising all the 1024 nodes from the *Lemanicus*. Reasons for such a discrepancy are the approximately one order of magnitude slower processing speed and memory access rate of the older hardware (Figure 8.4a) installed in the IBM BG/Q. Parallel efficiency (Figure 8.4b) was obtained by normalising the execution time of every parallel execution within the weak scaling by the reference execution time for a single node. Optimal parallel efficiency was achieved for values close or equal to 1. The best parallel efficiency is obtained on the *Lemanicus*, with an impressive straight line at 1. The reason for this impressive parallel efficiency is the slow execution time owing to older processors. The consequences of this slow processing permit one to fully hide MPI communication time, resulting in a linear parallel efficiency. On faster hardware such as

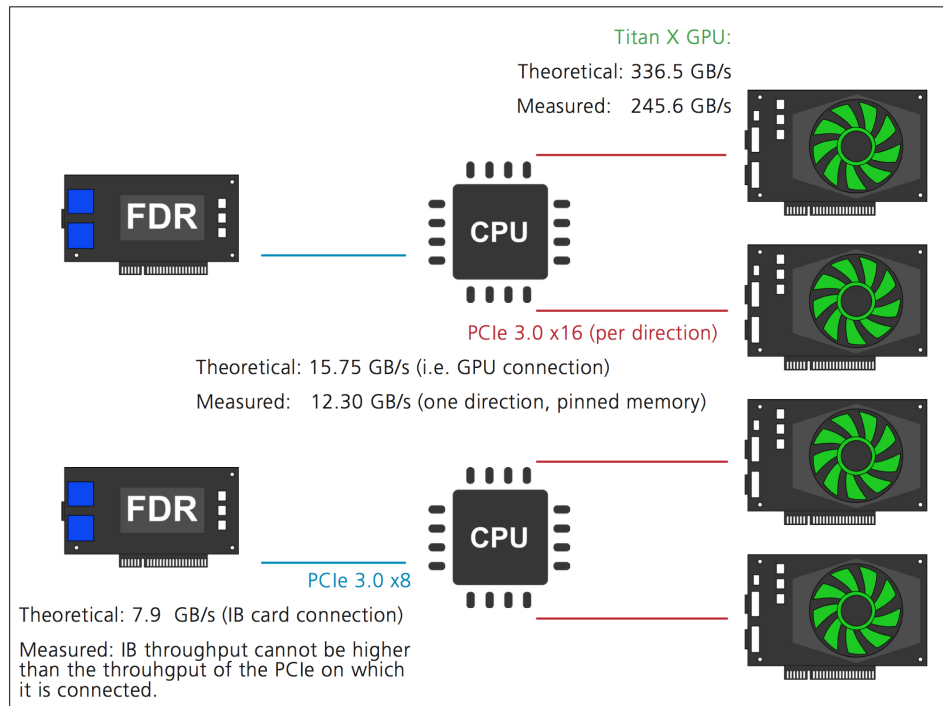


Figure 8.5: Intra-node configuration of the *octopus* supercomputer. FDR represents the two high-throughput Mellanox InfiniBand HCAs. The relevant throughput values are highlighted.

the GPU-based compute nodes populating the *Piz Daint* and the *octopus*, parallel efficiency drops by approximately 15 % with the increase in involved compute nodes. Notably, the values reported for the *Piz Daint* involving more than 200 compute nodes are biased owing to dynamic library loading at runtime.

The *octopus* supercomputer, although comprising one order of magnitude fewer compute nodes than *Piz Daint*, performed best in all the reported tests. This machine was designed and assembled as a long-term project running in parallel to this thesis. The objective was to assemble an inexpensive supercomputer capable of similar performance to the state-of-the-art existing machines, with the advantage of being in-house and fully available. This project's outcome is the *octopus*, which has 34 Supermicro dual-CPU nodes (Figure 8.5), each hosting two Intel Xeon E5-v3 2620 (Haswell), four Nvidia GTX TITAN (Maxwell) GPUs, 128 GB of RAM and 12 TB of scratch disk space. The 34 nodes are interconnected with dual-rail InfiniBand FDR high-speed interconnect from Mellanox. Owing to the high-density nodes (4 GPU accelerators per node), the inter-node communication needs maximal bandwidth in order to enable communication between processes at a rate that is fast as possible. The machine has been running since January 2016, and no significant issues have been listed to date, although high-end gaming cards (Nvidia Titan X) were used to perform the computations. The *octopus*

supercomputer enhanced a successful attempt to spread HPC in the Earth Sciences and has initiated several collaboration and transdisciplinary projects.

8.1.4 Outlook

In this thesis, I restricted the investigations of coupled physics to hydro-mechanical and thermo-mechanical processes. Thus, the approach to achieve an accurate and efficient solution that couples a mechanical solver to a diffusion solver can be further extrapolated to various additional couplings, including chemical effects or combining several processes. The coupling I addressed in this thesis are interesting starting points that will lead to various further investigations.

Up to this point, all numerical simulations utilised a high-porosity region as the initial condition idealising a porous reservoir surrounded by low permeable formations. However, porosity waves may also be generated naturally out of trended random red type of noise (Figure 8.6). Starting from a fluid-filled randomly distributed porosity domain that slowly compacts under gravity, channels generate spontaneously and without any prescription in space and time. The maximum normalised values of porosity and inverse of decompaction viscosity show a pulsating regime over time (Figure 8.7a). The corresponding fluid fluxes normalised by the background Darcian velocity and the solid strain rates' evolution over time confirm a pulsating mode (Figure 8.7b). The fluid fluxes are more than two orders of magnitude higher than

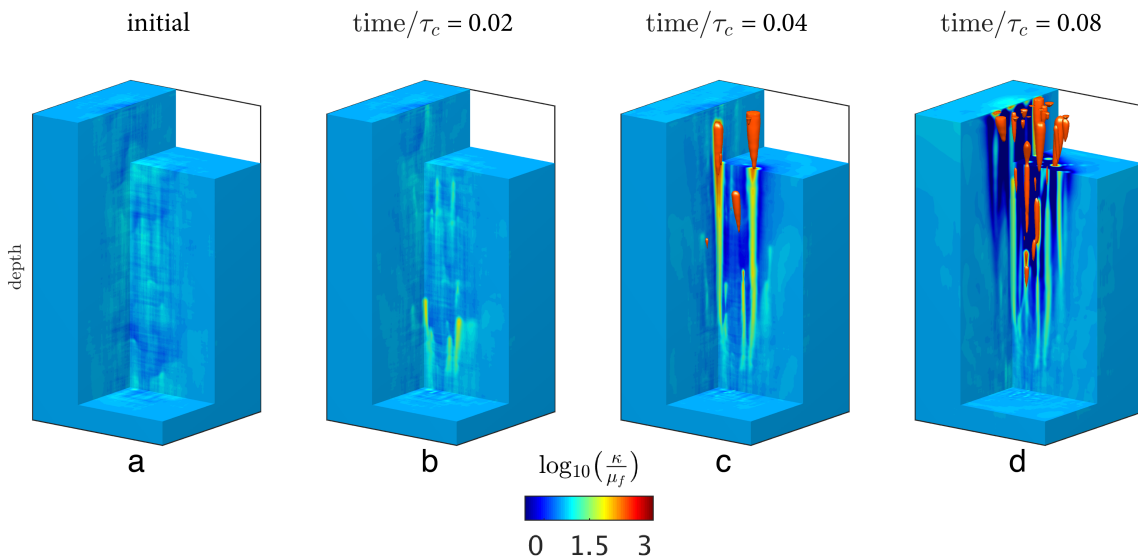


Figure 8.6: Spontaneous channel genesis out of initial red noise porosity distribution in 3-D. The values used in this calculation were listed in Chapter 4, with the exception of the initial configuration. (a), (b), (c) and (d) provide four snapshots in time of the upward-evolving high-porosity and permeability channels. The colour axis shows an up to three orders of magnitude permeability increase after a dimensionless time of 0.08.

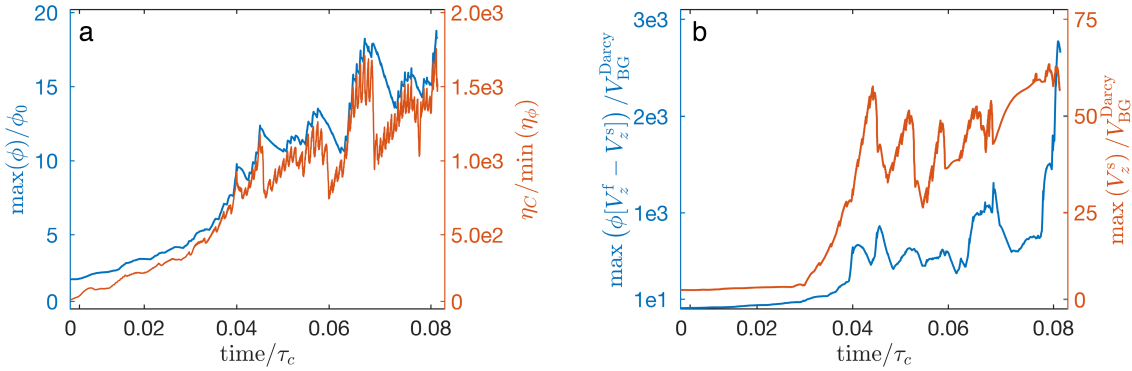


Figure 8.7: Evolution of maximal values as a function of dimensionless time. (a) Maximal normalised porosity values ($\max(\phi/\phi_0)$) and decompaction weakening ratio ($\eta_C/\min(\eta_D)$). (b) Maximal normalised fluid flux values over background Darcy flux ($\max(\phi[V_z^f - V_z^s])/V_{BG}^{Darcy}$) and matrix strain rates ($\max(V_z^s)/V_{BG}^{Darcy}$).

matrix strain rates, providing an efficient mechanism when addressing intermittent fast fluid migration events. Further investigation of such events' periodicity may have major implications for understanding and explaining, for instance, slow slip events and related tremors in locked subduction zones, such the Cascadia area, Northern U.S. (e.g. Rogers and Dragert, 2003; Wech and Bartlow, 2014).

8.2 Conclusion

In this thesis, I explored a supercomputing approach to resolve thermo-mechanically and hydro-mechanically coupled processes in porous rocks. The interaction between single-phase mechanics and fluid or heat diffusion considerably affect the deformation style and lead to spontaneous porous fluid and strain localisation in certain regimes. Porosity waves and decompaction weakening turn out to permit the formation of narrow high-porosity channels. These dynamically evolving features provide highly efficient pathways, allowing for fast buoyancy-driven vertical fluid transfers within saturated porous rocks. These chimneys reproduce the seismic chimneys observed in sedimentary basins all around the world strikingly well. Thus, the two-phase models provide a physical explanation on the genesis and evolution of such chimneys and allow us to predict their occurrence and characteristic lengths and time scales.

The developed numerical models converge with accuracy towards a fully coupled solution, and I suggest them as benchmarks for future implementation of thermo-mechanical and hydro-mechanical coupled models. Minor changes were required to successfully adapt the hydro-mechanically coupled codes to explore stain localisation owing to strain-heating in thermo-mechanically coupled physics. The direct-iterative and pseudo-transient parallel finite-difference-based algorithms provide robust and efficient tools to study spontaneous lo-

calisation in space and time in 2-D and 3-D. The GPU-based HPC algorithms further show close to linear weak scaling on the largest supercomputers, running close to peak performance.

This work lays an important basis for further studies on more complex couplings that combine several processes, since it systematically investigated the minimal requirements that lead to spontaneous localisation. In the context of geodynamics, applications of coupled models will become mandatory in future, more complete models for the entire lithosphere. In a more applied framework, accurate coupled models will provide reliable predictions on the mid-term to long-term evolution of various geosystem types such as engineered waste disposal. Preventing potential failures in such systems is vital to assess the risk for both society and the environment.

Bibliography

- Berndt, C., 2005. Focused fluid flow in passive continental margins. *Philosophical Transactions of the Royal Society of London A: Mathematical, Physical and Engineering Sciences* 363 (1837), 2855–2871.
- Bouilhol, P., Connolly, J. A., Burg, J.-P., 2011. Geological evidence and modeling of melt migration by porosity waves in the sub-arc mantle of Kohistan (Pakistan). *Geology* 39 (12), 1091–1094.
- Cartwright, J., Santamarina, C., 2015. Seismic characteristics of fluid escape pipes in sedimentary basins: Implications for pipe genesis. *Marine and Petroleum Geology* 65, 126–140.
- Cathles, L., Su, Z., Chen, D., 2010. The physics of gas chimney and pockmark formation, with implications for assessment of seafloor hazards and gas sequestration. *Marine and Petroleum Geology* 27 (1), 82–91.
- Cavanagh, A. J., Haszeldine, R. S., Nazarian, B., 2015. The Sleipner CO₂ storage site: using a basin model to understand reservoir simulations of plume dynamics. *First Break* 33 (June), 61–68.
- Connolly, J., Podladchikov, Y., 2007. Decompaction weakening and channeling instability in ductile porous media: Implications for asthenospheric melt segregation. *Journal of Geophysical Research: Solid Earth* 112 (B10).
- Foschi, M., Cartwright, J. A., Peel, F. J., 2014. Vertical anomaly clusters: Evidence for vertical gas migration across multilayered sealing sequences. *AAPG Bulletin* 98 (9), 1859–1884.
- Hustoft, S., Bünz, S., Mienert, J., 2010. Three-dimensional seismic analysis of the morphology and spatial distribution of chimneys beneath the Nyegga pockmark field, offshore mid-Norway. *Basin Research* 22 (4), 465–480.

- Judd, A., Hovland, M., 2007. *Seabed Fluid Flow*. Cambridge University Press, Cambridge.
- Løseth, H., Wensaas, L., Arntsen, B., Hanken, N.-M., Basire, C., Graue, K., 2011. 1000 m long gas blow-out pipes. *Marine and Petroleum Geology* 28 (5), 1047–1060.
- Mazzini, A., Svensen, H. H., Forsberg, C. F., Linge, H., Lauritzen, S.-E., Haffidason, H., Hammer, Ø., Planke, S., Tjelta, T. I., 2017. A climatic trigger for the giant Troll pockmark field in the northern North Sea. *Earth and Planetary Science Letters* 464 (May), 24–34.
- McKenzie, D., 1984. The Generation and Compaction of Partially Molten Rock. *Journal of Petrology* 25 (3), 713–765.
- Omlin, S., Räss, L., Podladchikov, Y. Y., 2017a. Simulation of three-dimensional viscoelastic deformation coupled to porous fluid flow. *Tectonophysics*.
- Omlin, S., Räss, L., Podladchikov, Y. Y., 2017b. Simulation of three-dimensional viscoelastic deformation coupled to porous fluid flow. *Tectonophysics*.
- Rogers, G., Dragert, H., 2003. Episodic tremor and slip on the Cascadia subduction zone: The chatter of silent slip. *Science* 300 (5627), 1942–1943.
- Wech, A. G., Bartlow, N. M., 2014. Slip rate and tremor genesis in Cascadia. *Geophysical Research Letters* 41 (2), 392–398.
- Wiggins, C., Spiegelman, M., 1995. Magma migration and magmatic solitary waves in 3-D. *Geophysical Research Letters* 22 (10), 1289–1292.
- Wulf, W. A. and McKee, Sally A., 1995. Hitting the memory wall. *ACM SIGARCH Computer Architecture News* 23 (1), 20–24.
- Yarushina, V. M., Podladchikov, Y. Y., 2015. (De)compaction of porous viscoelastoplastic media: Model formulation. *Journal of Geophysical Research: Solid Earth* 120 (6), 4146–4170.

Curriculum vitae

Education

- Ph.D., University of Lausanne, 2018 (defended on March 21st, 2018).
 - *Thesis title* Resolving thermo-hydro-mechanical coupling: Spontaneous porous fluid and strain localisation.
 - *Committee* Prof. Dr. Michel Jaboyedoff, Prof. Dr. Yury Y. Podladchikov, Prof. Dr. Stefan M. Schmalholz, Prof. Dr. Paul J. Tackley.
- Master in geoscience and environment, University of Lausanne, 2013.
- Bachelor in geoscience and environment, University of Lausanne, 2011.
- Secondary school graduation, Gymnase de Morges, 2007.

Fields of Research Interest

Geodynamics, Two-phase flow, THM coupling, CO₂ storage, Numerical modelling, High-Performance Computing, GPU.

Selected Scientific Publications

- Räss, L., Simon, N.S.C. and Podladchikov, Y. Y. (2018). Spontaneous formation of fluid escape pipes from subsurface reservoirs. *submitted to Nature Scientific Reports*

- Räss, L., Duretz, T. and Podladchikov, Y. Y. (2018). Resolving hydro-mechanical coupling in two and three dimensions: Spontaneous channelling of porous fluids owing to decompaction weakening. *submitted to Geophysical Journal International*
- Duretz, T., Räss, L., Podladchikov, Y. Y. and Schmalholz, S. M. (2018). Resolving thermo-mechanical coupling in two and three dimensions: Spontaneous strain localisation owing to strain heating. *submitted to Geophysical Journal International*
- Omlin, S., Räss, L. and Podladchikov, Y. (2017). Simulation of three-dimensional viscoelastic deformation coupled to porous flow. *Tectonophysics*. *Tectonophysics*. doi: <http://dx.doi.org/10.1016/j.tecto.2017.08.012>.
- Räss, L., Duretz, T., Podladchikov, Y. Y. and Schmalholz, S. M. (2017). M2Di: Concise and efficient MATLAB 2-D Stokes solvers using the Finite Difference Method. *Geochem. Geophys. Geosyst.*, 18, 755-768.
- Räss, L., Makhnenko, R. Y. and Podladchikov, Y. Y. (2017). Quantification of viscous creep influence on storage capacity of caprock. *Energy Procedia*, 114, 3237-3246. doi: <http://dx.doi.org/10.1016/j.egypro>.
- Räss, L., Yarushina, V. M., Simon, N. S., and Podladchikov, Y. Y. (2014). Chimneys, channels, pathway flow or water conducting features-an explanation from numerical modelling and implications for CO₂ storage. *Energy Procedia*, 63, 3761-3774.

Memberships and awards

- Member of the Swiss Geocomputing Centre SGC²
- Member of the European Geoscience Union (EGU)
- Member of the European Association of Geoscientist and Engineers (EAGE)
- Outstanding Student PICO and Poster award (OSPP) General Assembly EGU 2017, division Geodynamics (GD)

Teaching Experience

- BSc, Numerical Modelling, Unil since 2012.
- MSc, Advanced MATLAB as a language of scientific computation, Unil since 2010.
- MSc, MATLAB as a language of scientific computing, Unil since 2012.
- MSc, Physics as a basis for modelling, Unil since 2012.

- MSc, Physics modelling in environmental sciences, Unil since 2013.
- Doctoral school, CUSO – Introduction to HPC in Earth sciences, Unil since 2016.

Supercomputer design and assembly

The *octopus* GPU supercomputer design, assembly and partial maintenance (analogous to a Cray CS-Storm Cabinet).

Main characteristics:

- 136 Titan X GPUs
- 68 Intel Xeon E5 v3 CPUs (6 cores)
- 4.3 TB RAM
- Dual-rail Infiniband FDR High-speed interconnect

Publications in peer-reviewed scientific journals

- Räss, L., Simon, N.S.C. and Podladchikov, Y. Y. (2018). Spontaneous formation of fluid escape pipes from subsurface reservoirs. *submitted to Nature Scientific Reports*
- Räss, L., Duretz, T. and Podladchikov, Y. Y. (2018). Resolving hydro-mechanical coupling in two and three dimensions: Spontaneous channelling of porous fluids owing to decompaction weakening. *submitted to Geophysical Journal International*
- Duretz, T., Räss, L., Podladchikov, Y. Y. and Schmalholz, S. M. (2018). Resolving thermo-mechanical coupling in two and three dimensions: Spontaneous strain localisation owing to strain heating. *submitted to Geophysical Journal International*
- Yarushina, V. M., Makhnenko, R. Y., Räss, L. and Podladchikov, Y. Y. (2018). Poro-viscoelasticity of clay-rich rocks and caprock sealing integrity. *submitted to Geophysical Research Letters*
- Vaughan-Hammon, J., Räss, L. and Schmalholz, S. M. (2018). Buoyancy-driven ascent of viscous bodies and associated strain. *submitted to Tectonophysics*
- Omlin, S., Räss, L. and Podladchikov, Y. (2017). Simulation of three-dimensional viscoelastic deformation coupled to porous flow. *Tectonophysics*. doi: <http://dx.doi.org/10.1016/j.tecto.2017.08.012>.
- Räss, L., Duretz, T., Podladchikov, Y. Y. and Schmalholz, S. M. (2017). M2Di: Concise and efficient MATLAB 2-D Stokes solvers using the Finite Difference Method. *Geochem. Geophys. Geosyst.*, 18, 755-768.

- Räss, L., Makhnenko, R. Y. and Podladchikov, Y. Y. (2017). Quantification of viscous creep influence on storage capacity of caprock. *Energy Procedia*, 114, 3237-3246. doi: <http://dx.doi.org/10.1016/j.egypro>.
- Räss, L., Yarushina, V. M., Simon, N. S., and Podladchikov, Y. Y. (2014). Chimneys, channels, pathway flow or water conducting features-an explanation from numerical modelling and implications for CO₂ storage. *Energy Procedia*, 63, 3761-3774.

Contributions to international conferences

- Räss, Simon, N.S.C. and Podladchikov, Y. (2018). High permeability chimney genesis resolved in two-phase systems. *submitted to EGU General assembly 2018, Vienna, Austria*
- Räss, L., Duretz, T. and Podladchikov, Y. (2018). Resolving hydro-mechanical coupling in two and three dimensions. *submitted to EGU General assembly 2018, Vienna, Austria*
- Räss, L., Duretz, T. and Podladchikov, Y. (2017). Localised Two-Phase Flow: Application of Implicit Matrix-Free Pseudo-Transient Method. XV International Workshop on Modelling of Mantle and Lithosphere Dynamics. Putten, The Netherlands.
- Yarushina, V. M., Podladchikov, Y. Y., Minakov, A. and Räss, L. (2017). On the mechanism of stress-triggered seismic events during fluid injection. *Poromechanics VI* (pp. 795-800).
- Räss, L., Duretz, T., Schmalholz, S. and Podladchikov, Y. (2017). M2Di: MATLAB 2-D Stokes solvers using the finite difference method. *Geophysical Research Abstracts 19, EGU2017-18474. EGU General assembly 2017, Vienna, Austria.*
- Räss, L., Makhnenko, R. and Podladchikov, Y. (2017). High-performance coupled poro-hydro-mechanical models to resolve fluid escape pipes. *Geophysical Research Abstracts 19, EGU2017-18469. EGU General assembly 2017, Vienna, Austria.*
- Räss, L., Yarushina, V., Duretz, T. and Podladchikov, Y. (2016). High-resolution Numerical Modelling to Resolve the Dynamics of Pipe Structures in Porous Media. *ECMOR XV-15th European Conference on the Mathematics of Oil Recovery.*
- Yarushina, V., Räss, L. and Podladchikov, Y. Y. (2016). Geomechanical Origin of Focused Fluid Flow and Chimney Structures. *78th EAGE Conference and Exhibition 2016.*
- Räss, L., Yarushina, V. M., Simon, N. S. C. and Podladchikov, Y. Y. (2015). High Permeability Pathways Triggered by Subsurface Storage Operations. *Second Geomechanics and Energy Workshop 2015. GME, extended abstract. EAGE, Celle, Germany.*

-
- Räss, L., Omlin, S. and Podladchikov, Y. (2015). Use of High Performance and Massively Parallel GPU Computing to resolve nonlinear waves in poromechanics. PASC15 conference 2015, ETH Zrich, Switzerland.
 - Räss, L., Omlin, S., Simon, N. S. C. and Podladchikov, Y. (2015). Use of GPU HPC to resolve nonlinear waves in poromechanics. 2nd Frontiers in Computational Physics Conference: Energy Sciences 2015, Zrich, Switzerland.
 - Räss, L., Omlin, S., Simon, N. S. C. and Podladchikov, Y. (2015). Use of GPU Computing to Study Coupled Deformation and Fluid Flow in Porous Rocks. Geophysical Research Abstracts 17, EGU2015-132227. EGU General assembly 2015, Vienna, Austria.
 - Räss, L., Omlin, S., Yarushina, V., Simon, N. S. C. and Podladchikov, Y. (2015). Modeling of Multi-Scale Channeling Phenomena in Porous Flow. Geophysical Research Abstracts 17, EGU2015-12831. EGU General assembly 2015, Vienna, Austria.
 - Omlin, S., Räss, L. and Podladchikov, Y. (2014). Building a Terabyte Memory Bandwidth Compute Node with Four Consumer Electronics GPUs. Geophysical Research Abstracts 16, EGU2014-14438. EGU General assembly 2014, Vienna, Austria.
 - Räss, L., Omlin, S., Moulas, E., Simon, N. and Podladchikov, Y. (2014). Multi-GPU Accelerated Simulation of Dynamically Evolving Fluid Pathways. Geophysical Research Abstracts 16, EGU2014-15267. EGU General assembly 2014, Vienna, Austria.
 - Räss, L., Yarushina, V., Simon, N. S. C. and Podladchikov, Y. Y. (2014). The importance of poromechanics for CO₂ storage integrity. Fourth CO₂ storage Workshop 2014, extended abstract. EAGE, Stavanger, Norway.
 - Räss, L., Omlin, S., Podladchikov, Y. Y. and Simon, N. S. C. (2013). Solving three-dimensional non-linearly coupled hydro-mechanical two-phase flow on GPUs. 11th Swiss Geoscience Meeting 2013, Lausanne, Switzerland.
 - Simon, N. S. C., Räss, L., Podladchikov, Y. Y., Souche, A. and Yarushina, V. (2013). Predicting dynamically evolving permeability, localization of flow and breaching of low permeability barriers in waste storage operations. Geomechanics and Energy Workshop 2013. GME, extended abstract. EAGE, Lausanne, Switzerland.
 - Räss, L., Omlin, S., and Podladchikov, Y. (2013). Influence of intrinsic and extrinsic forces on 3D stress distribution using CUDA programming. EGU General Assembly 2013, Vienna, Austria.

Acknowledgements

First, I wish to thank my PhD advisor, Prof. Dr. Yury Podladchikov. Back in 2011, Yury started a modelling class at Unil with the challenging goal to programme the 2-D wave equation from scratch within two hours. This first experience with numerical modelling applied to Earth Sciences was the starting point of a long and enlightening journey. Yury shared his passion for geophysics and numerical modelling with the Scientific Computing Group, pushing the limits and exploring new paths. Yury's aim to laterally spread supercomputing in the Earth Sciences is a unique project that is leading to the democratisation of high-performance computing in geology and geophysics. As part of this project, we designed, tested and assembled the GPU-based *octopus* supercomputer here in Lausanne. This has been a great experience, and I am extremely grateful to be a part of this enterprise.

My gratitude also to Dr. Nina Simon, who co-advised my PhD. She allowed me to spend research time at IFE (Institute for Energy Technology) in Kjeller (Oslo, Norway), where she headed the environmental department. I could join her team for an internship at the start of my PhD and then for one month a year, to work on topics relating to safe CO₂ storage in geological formations. I am thankful for the time invested and the motivating projects, as well as her friendship and support during my thesis. Nina and IFE gave me a much-appreciated and instructive real-world collaboration.

My thanks to the experts on my thesis committee, Prof. Dr. Paul Tackley and Prof. Dr. Stefan Schmalholz, for agreeing to review my work. My gratitude to Stefan, who was always a good advisor concerning both scientific and administrative activities; thank you also for your continuous support as director of the Institute of Earth Sciences. A special thank you to Prof. Dr. Michel Jaboyedoff for presiding over my thesis defence and for long-term support since my undergraduate studies at Unil. Thank you for the good times, the apéros and the conducive study atmosphere.

I thank Dr. Samuel Omlin, my former PhD colleague, for the good times and very constructive interactions for more than five years. Samuel has been involved in the design of GPU-based parallel routines from the early stages. He showed me how to approach scientific computing in an efficient, concise and performant way, coaching me to become autonomous in programming.

I thank Philippe Logean, systems administrator of the computational infrastructure at our institute. Philippe always actively participated in our development activities, sharing his knowledge of system administration and hardware technicalities. With you, the *octopus* adventure would not have been the same. Thank you for investing time in stimulating discussions and for your great advice.

I acknowledge all those who made the *octopus* project happen. In particular, my thanks to Dr. Hamid Hussain-Khan for the early discussions regarding the supercomputer design, and the much-appreciated collaboration throughout the project. I learnt much regarding actual high-performance hardware, and collaborating was a pleasure. I thank Karine Rossier from the Decanat FGSE, who efficiently managed the budget-related parts of the *octopus* project and contributed to the project's success. I acknowledge Gautam Shah (Colfax Intl., Sunnyvale, CA), who helped us with the supercomputer's design as the main tech partner. I acknowledge the University of Lausanne and especially Daniel Henchoz for hosting the supercomputer and providing all the necessary help in improving its efficient exploitation.

I thank the IFE team members Viktoriya Yarushina, Magnus Wangen and Alban Souche for the great times in Norway during my internship, and recently during research visits.

My thanks to Dr. Roman Makhnenko, who joined the porosity wave project shortly after me. The novel high-quality laboratory experiment Roman conducted was a major step in more accurately constraining the complex rheology of two-phase systems. Thank you for the very rich and intense discussions. I thank Dr. Sasha Minakov for the motivating discussions and interesting ongoing projects, and Igor Podladchikov for the long-term collaboration on GPU and parallel computing-related topics.

I thank Isabelle and Yves Pigneur, Carole Graetzel and Josh for their help with the scientific writing of this manuscript.

My university journey may not have started without an enlightening discussion with Gérald Savary. Thank you for the early-days back office and your always-appreciated advice.

I deeply thank Dr. Thibault Duret and Dr. Evangelos Moulas for their scientific advice, the motivating projects we worked on and for the informal coaching throughout my PhD thesis. The discussions, the working sessions in remote places and the times together is much appreciated. You helped to broaden my vision of science.

My time in the office was enriched by office mates and friends. I thank Florian, Martin, Benjamin, Yoann, Annelore, Cindy and 'the boys' – Spitzberg, Lorenzo, Dani and Josh – for

good times, the non-constructive discussion about machine learning and Stokes equations, the refreshing beverages and much good and stimulating work. I also thoroughly enjoyed the non-work-related activities, which were and still are the best team-building one can ever have. I will miss you.

My deep and sincere gratitude to my family – Mama, Layla and Simone – for their continuous love and support. I dedicate this thesis to you.